Holographic Fourier domain diffuse correlation spectroscopy

Dr Edward James
BSc BVSc BEng MRes MRCVS

A thesis submitted in partial fulfilment
of the requirements for the degree of
Doctor of Philosophy
of
University College London

Department of Medical Physics and Biomedical Engineering
University College London

16th May 2022

‘I have no special talent. I am only passionately curious.’

Albert Einstein (1879 - 1955)
(1921 Nobel Prize in Physics)

Declaration

I, Edward James, confirm that the work presented in this thesis is my own. Where information has been derived from other sources, I confirm that this has been indicated in the thesis.

Abstract

Diffuse correlation spectroscopy (DCS) is a non-invasive optical modality which can be used to measure cerebral blood flow (CBF) in real-time. It has important potential applications in clinical monitoring, as well as in neuroscience and the development of a non-invasive brain-computer interface. However, a trade-off exists between the signal-to-noise ratio (SNR) and imaging depth, and thus CBF sensitivity, of this technique. Additionally, as DCS is a diffuse optical technique, it is limited by a lack of inherent depth discrimination within the illuminated region of each source-detector pair, and the CBF signal is therefore also prone to contamination by the extracerebral tissues which the light traverses.

Placing a particular emphasis on scalability, affordability, and robustness to ambient light, in this work I demonstrate a novel approach which fuses the fields of digital holography and DCS: holographic Fourier domain DCS (FD-DCS). The mathematical formalism of FD-DCS is derived and validated, followed by the construction and validation (for both *in vitro* and *in vivo* experiments) of a holographic FD-DCS instrument. By undertaking a systematic SNR performance assessment and developing a novel multi-speckle denoising algorithm, I demonstrate the highest SNR gain reported in the DCS literature to date, achieved using scalable and low-cost camera-based detection.

With a view to generating a forward model for holographic FD-DCS, in this thesis I propose a novel framework to simulate statistically accurate time-integrated dynamic speckle patterns in biomedical optics. The solution that I propose to this previously unsolved problem is based on the Karhunen-Loève expansion of the electric field, and I validate this technique against novel expressions for speckle contrast for different forms of homogeneous field. I also show that this method can readily be extended to cases with spatially varying sample properties, and that it can also be used to model optical and acoustic parameters.

Impact statement

Diffuse correlation spectroscopy (DCS) is a non-invasive optical modality which can be used to measure cerebral blood flow (CBF) in real-time. It has important potential applications in clinical monitoring and neuroscience, as well as in the development of a non-invasive brain-computer interface. Reducing the cost and enhancing the performance of such systems will allow for more widespread clinical use. There is currently an unmet need to develop such an instrument using a continuous, noninvasive, and portable bedside approach, and the research in this thesis addresses this important challenge.

DCS was first developed in 1997, and, until the last handful of years, developments in DCS have been fairly quiescent. However, since 2016, the investigation of novel approaches to improve the sensitivity of DCS to CBF has attracted interest from several research groups. Cognisant of this, in 2018 I began investigating a new approach to DCS that overcomes the limited light throughput of conventional single speckle detection techniques, and which makes use of holographic multispeckle detection. Not only does this approach demonstrate a significant signal-to-noise ratio (SNR) benefit, which opens the door to improved CBF sensitivity, but it also benefits from a 10-fold reduction in detector cost compared to conventional DCS, as well as operating without disturbance from ambient light, which increases its potential use and impact in real-world clinical settings. The *in vivo* feasibility of the approach is also demonstrated in this thesis. Furthermore, the reduction in detector cost results in ease of system scalability, which is an important consideration for achieving the end-goal of whole head coverage. The impact of the research described in this thesis is further increased as it can be adapted to include the work of other research groups (namely acousto-optic tomography (AOT) and long wavelength DCS approaches), and it therefore has significant potential for future applications.

Apart from the proof-of-concept validation of the novel approach to DCS that I present, a further key outcome of this thesis is the multispeckle denoising algorithm that I describe. This has allowed me to achieve an SNR gain of 36 using a detector that costs £500. The current state-of-the art in multispeckle DCS detection was published in 2020, and achieved an SNR gain of 32 using a detector that is two orders of magnitude more expensive. Another key outcome of this thesis is the development of a framework to simulate statistically accurate two-dimensional time-integrated dynamic speckle patterns (2D-TIDSPs). The measurement of such patterns for the purpose of CBF measurement using inexpensive low-frame rate cameras is an increasingly commonly performed task in the field of biomedical optics (indeed, the work presented in this thesis is one such example of this). Despite this, and despite literature on this dating from 2008, the generation of such a framework was an unsolved problem prior to this

thesis. I therefore expect these two theoretical components to have a significant impact on the biomedical optics community, specifically with regard to modelling and improving the SNR of time-integrated multispeckle detection for improved CBF sensitivity.

Publications and achievements

Peer reviewed journal articles

- **James, E.** & Powell, S. Fourier domain diffuse correlation spectroscopy with heterodyne holographic detection. *Biomedical Optics Express* **11,** 6755–6779 (2020).
- **James, E.**, Powell, S. & Munro, P. Simulation of statistically accurate time-integrated dynamic speckle patterns in biomedical optics. *Optics Letters* **46,** 4390–4393 (2021).
- **James, E.**, Powell, S. & Munro, P. Performance optimisation of a holographic Fourier domain diffuse correlation spectroscopy instrument. *Biomedical Optics Express* (in press - DOI: 10.1364/BOE.454346).

Conference proceedings

- **James, E.** & Powell, S. *Diffuse correlation spectroscopy in the Fourier domain with holographic camera-based detection* in *Dynamics and Fluctuations in Biomedical Photonics XVII* (eds Tuchin, V. V., Leahy, M. J. & Wang, R. K.) **11239** (SPIE, 2020), 29–35.
- **James, E.**, Powell, S. & Munro, P. *Simulation of time-integrated dynamic speckle patterns in biomedical optics* in *2021 IEEE Photonics Conference (IPC)* (2021).

Conference presentations

- **James, E.**, Powell, S. & Munro, P. *Simulation of statistically accurate time-integrated dynamic speckle patterns in biomedical optics* **[Invited]** in *Dynamics and Fluctuations in Biomedical Photonics XIX* (eds Tuchin, V. V., Leahy, M. J. & Wang, R. K.) **PC11959** (SPIE, 2022).
- **James, E.**, Powell, S. & Munro, P. *Performance characterisation of a holographic Fourier domain diffuse correlation spectroscopy instrument* in *Dynamics and Fluctuations in Biomedical Photonics XIX* (eds Tuchin, V. V., Leahy, M. J. & Wang, R. K.) **PC11959** (SPIE, 2022).

Prizes and other achievements

- $500 SPIE Family Care Grant - Photonics West 2020
- Nominated for Best Student Paper at IEEE IPC 2021
- 2021 Robert Speller Prize for Best Paper by a PhD Student in the UCL Medical Physics and Biomedical Engineering Department
- $500 SPIE Family Care Grant - Photonics West 2022
- $1000 SPIE Student Conference Support Award - Photonics West 2022

Acknowledgements

I would like to thank my primary supervisors, Samuel Powell and Peter Munro, for their continued patience and support in advising me through this research project. Sam provided an immensely interesting subject matter for me to explore, and I am thankful for his practical assistance. Thanks go to Peter for getting up to speed with my research when it was well beyond the halfway mark, and for giving me timely and constructive feedback on a huge amount of work in the closing stages. Peter has also provided me with excellent collaboration opportunities for which I am particularly grateful.

I would also like to thank my subsidiary supervisors, Simon Arridge and Jamie Guggenheim, for their immensely useful assistance. Simon's advice was indispensable when deriving the analytical framework for Fourier domain diffuse correlation spectroscopy, which is fundamental to this thesis. Thank you to Jamie for providing the optical resolution photoacoustic microscopy image that is used in this thesis.

Within the Medical Physics and Biomedical Engineering department, Gemma Bale and Konstantinos Papadimitriou were particularly helpful sources of practical inspiration. Thank you to Jem Hebden for regularly discussing my research goals with me, and for being a source of motivation and inspiration. Special thanks go to Jem, Peter Munro, and Nick Everdell for their excellent mentorship, and for encouraging me to persist with this PhD when the path ahead was not apparent.

I am particularly grateful to Michael Atlan, at the Digital Holography Foundation, who was generous enough with his time to spend an afternoon visiting my lab, and to share his hard-earned expertise in digital holography that he has acquired over the past two decades. Thank you also to Biju Cletus for his discussions, which were helpful in developing the model for the temperature dependent properties of intralipid optical tissue phantoms that is developed in this thesis.

This work is supported by the EPSRC-funded UCL Centre for Doctoral Training in Medical Imaging (EP/L016478/1). I would like to thank EPSRC and the Medical Imaging CDT for providing me with the opportunity to undertake this research project, and, in combination with funding from SPIE, to present my work to the international biomedical optics community.

Last, but not least, a heartfelt thank you to my wife, Polly, for letting me indulge my academic curiosity for far too long. Thank you for all the support throughout the highs and lows of this PhD, although I do agree that 13 years of higher education are probably enough!

Table of contents

List of abbreviations

2D	two-dimensional
2D-TIDSP	two-dimensional time-integrated dynamic speckle pattern
3D	three-dimensional
ABP	arterial blood pressure
AOM	acousto-optic modulator
AOM-DCS	acousto-optic modulated diffuse correlation spectroscopy
AOT	acousto-optic tomography
APD	avalanche photodiode
ARF	acoustic radiation force
ASL-MRI	arterial-spin labelling magnetic resonance imaging
BBB	blood-brain barrier
BF	blood flow
BFI	blood flow index
BOLD-MRI	blood oxygen level dependent magnetic resonance imaging
bpm	beats per minute
BS	beamsplitter
CA	cerebral autoregulation
CAD	computer-aided design
CBF	cerebral blood flow
CBV	cerebral blood volume
CCD	charge-coupled device
CEUS	contrast enhanced ultrasound
CHS	coherent haemodynamics spectroscopy
CMOS	complementary metal-oxide-semiconductor
$CMRO_2$	cerebral metabolic rate of oxygen consumption
CPP	cerebral perfusion pressure
CPS	count/s per second
CSF	cerebrospinal fluid
CT	computed tomography
CTF	coherent transfer function
CtOx	cytochrome oxidase
CUDA	compute unified device architecture
CVR	cerebrovascular resistance
CW	continuous wave
CW-DCS	continuous wave diffuse correlation spectroscopy

CW-NIRS	continuous wave near-infrared spectroscopy
DA	diffusion approximation
DC	direct current
DCS	diffuse correlation spectroscopy
DCT	diffuse correlation tomography
DFT	discrete Fourier transform
DHb	difference between oxyhaemoglobin and deoxyhaemoglobin
DLS	dynamic light scattering
DLSI	dynamic light scattering imaging
DOT	diffuse optical tomography
DP	diastolic pressure
DSCA	diffuse speckle contrast analysis
DSC-MRI	dynamic susceptibility contrast magnetic resonance imaging
DSPF	diffuse speckle pulsatile flowmetry
DWS	diffusing wave spectroscopy
EM	electromagnetic
FAIR-MRI	flow sensitive alternating inversion recovery magnetic resonance imaging
FD	frequency domain
FD-DCS	Fourier domain diffuse correlation spectroscopy
FD-NIRS	frequency domain near-infrared spectroscopy
FFT	fast Fourier transform
FINE	feedback induced noise eraser
fMRI	functional magnetic resonance imaging
fNIRS	functional near-infrared spectroscopy
GPU	graphics processing unit
HHb	deoxyhaemoglobin
HIE	hypoxic ischaemic encephalopathy
HPSD	heterodyne parallel speckle detection
HWHM	half width at half maximum
ICG	indocyanine green
ICP	intracranial pressure
iDCS	interferometric diffuse correlation spectroscopy
iDWS	interferometric diffusing wave spectroscopy
InGaAs	indium gallium arsenide
iNIRS	interferometric near-infrared spectroscopy
IR	inversion recovery
IRF	instrument response function

ISVS	interferometric speckle visibility spectroscopy
LASCA	laser speckle contrast analysis
LDF	laser Doppler flowmetry
LDH	laser Doppler holography
LLG	liquid light guide
LSCI	laser speckle contrast imaging
MAP	mean arterial pressure
MESI	multiple exposure speckle imaging
MiDWS	multi-exposure interferometric diffusing wave spectroscopy
MRI	magnetic resonance imaging
MTF	modulation transfer function
MVIM	multi-step Volterra integral method
NIR	near-infrared
NIRS	near-infrared spectroscopy
O_2Hb	oxyhaemoglobin
OR-PAM	optical resolution photoacoustic microscopy
PAD	peripheral arterial disease
PAT	photoacoustic tomography
PC	personal computer
PCT	perfusion computed tomography
PD	photodiode
PDE	photon detection efficiency
PDF	probability density function
PDT	photodynamic therapy
PET	positron emission tomography
PMT	photon multiplying tube
PR	photorefractive
PSD	power spectral density
QELS	quasi-elastic light scattering
RAM	random-access memory
RBC	red blood cell
ROI	region of interest
RTE	radiative transfer equation
SAP	systemic arterial pressure
sCMOS	scientific complementary metal-oxide-semiconductor
SCOS	speckle contrast optical spectroscopy
SCOT	speckle contrast optical tomography

SDS	source-detector separation
SHB	spectral hole burning
SNR	signal-to-noise ratio
SNSPD	superconducting nanowire single-photon detection
SP	systolic pressure
SPAD	single photon avalanche detector
SPECT	single photon emission computed tomography
SSD	sum of squared differences
StO_2	oxygen saturation of haemoglobin in brain tissue
SVD	singular value decomposition
SVS	speckle visibility spectroscopy
syMESI	synthetic multiple exposure speckle imaging
TCD	transcranial Doppler ultrasound
TD	time domain
TD-DCS	time domain diffuse correlation spectroscopy
TDF	thermal diffusion flowmetry
TD-NIRS	time domain near-infrared spectroscopy
TEM	transmission electron microscopy
THb	total haemoglobin
TOF	time-of-flight
TPSF	temporal point spread function
TTL	transistor-transistor logic
UMT/UMOT	ultrasound-mediated optical tomography
USB	universal serial bus
UTL	ultrasound tagging of light
WM-NIRS	wavelength modulated near-infrared spectroscopy
Xe-CT	xenon computed tomography

List of main symbols

$f / \Delta f$	frequency (shift)
$\omega / \Delta\omega$	radial frequency (shift)
μ_a	absorption coefficient
μ_s	scattering coefficient
μ_t	total attenuation coefficient
g	anisotropy factor
μ_s'	reduced scattering coefficient
μ_{tr}	transport attenuation coefficient
n	refractive index
Φ	radiance
t	time
D	optical diffusion coefficient
μ_{eff}	effective attenuation coefficient
∇	del operator
ρ	source-detector separation distance
r_1	distance between the detector and an approximated positive isotropic imaging source for a semi-infinite geometry
r_2	distance between the detector and an approximated negative isotropic imaging source for a semi-infinite geometry
K	speckle contrast
μ	mean
σ	standard deviation
G_1 / g_1	unnormalised/normalised electric field autocorrelation function due to dynamic and static scatterers
G_{1d} / g_{1d}	unnormalised/normalised electric field autocorrelation function due to dynamic scatterers only
λ	wavelength
k_0	wavenumber
τ	autocorrelation decay time
τ_c	sample decorrelation time
$\langle \Delta r^2(\tau) \rangle$	mean-square particle displacement
$\langle V^2 \rangle$	second moment of the speed distribution of scattering particles
D_b	effective Brownian diffusion coefficient of scattering particles
G_2 / g_2	unnormalised/normalised intensity autocorrelation function
α	fraction of scattering events due to dynamic, rather than stationary, scatterers
β	coherence factor

T	exposure time
$\mathcal{F}^{-1}/\mathcal{F}$	(inverse) Fourier transform
S_1/s_1	unnormalised/normalised first-order power spectral density of the electric field due to dynamic and static scatterers
S_{1d}/s_{1d}	unnormalised/normalised first-order power spectral density of the electric field due to dynamic scatterers only
N_f	number of camera frames
f_s	camera frame rate
ω_s	radial camera frame rate
H_C	camera plane hologram
H_R	reconstruction plane hologram
B	instrument response function of a heterodyne parallel speckle detection instrument
F_{Br}	Brownian factor
H	2D space-time matrix of camera plane holograms
R	2D space-time matrix of reconstructed multispeckle patterns
$\mathcal{M}$	degrees of freedom contained within a time-integrated speckle measurement
$\mathbf{\Omega}$	independent uniformly distributed variables on the interval $(-\pi, \pi)$
$\mathbf{U}$	electric field
$\hat{\mathbf{U}}$	Karhunen-Loève expansion coefficient of the electric field
$\mathbf{I}$	instantaneous intensity
$\mathbf{W}$	time-integrated intensity
λ_n	eigenvalues of the field autocorrelation function
$\mathbf{H}$	coherent transfer function
M	modulation depth
p	exponent of the electric field autocorrelation function for laser speckle contrast imaging

List of Figures

List of Tables

1 Introduction

1.1 Motivation

The ability to be able to monitor cerebral blood flow (CBF) in a medical setting is of crucial importance [1]. CBF, representing the perfusion of blood through the brain's tissue beds, needs to be maintained at an average resting value of 40 - 50 ml per 100g of brain tissue per minute [2]. This perfusion level is necessary in order to support the brain's relatively high demand of 20 % of the body's overall oxygen supply [3], as well as to remove the waste products of metabolism. The neurons of the brain require adenosine triphosphate in order to function, the production of which depends almost exclusively on oxidative processes [4]. Inadequate CBF, even if only for a few minutes, can lead to irreversible brain damage, ischaemic stroke, and death [1]. Excessive CBF can cause damage to the blood-brain barrier, which can cause seizures, headaches, encephalopathy, and stroke [5]. Durduran and Yodh therefore state that [3],

> 'CBF is an important biomarker of brain health and function. It is a critical physiological parameter linking metabolic demand to oxygen supply, oxygen supply to metabolic consumption, and metabolic consumption to byproduct clearance'.

CBF monitoring is critical in unconscious or anaesthetised patients, as it provides an indicator of the adequacy of the delivery of vital nutrients to the brain, as well as a commentary on the efficacy of cerebral autoregulation (CA). CA is the intrinsic homeostatic mechanism by which CBF is kept within tightly controlled bounds, in the face of variations in mean arterial pressure (MAP) and intracranial pressure (ICP) [2].

Cerebral perfusion pressure (CPP) is the net pressure gradient that drives CBF and causes the tissues of the brain to be perfused with blood. CPP can be calculated as the difference between MAP and ICP [5, 6]

$$\mathrm{CPP} = \mathrm{MAP} - \mathrm{ICP}. \tag{1}$$

MAP is also known as arterial blood pressure (ABP) or systemic arterial pressure (SAP). MAP in the brain is similar to the MAP anywhere else in the human body, and can be determined by intraarterial catheterisation. MAP can also be approximated noninvasively by

$$\mathrm{MAP} = \mathrm{DP} + \frac{\mathrm{SP} - \mathrm{DP}}{3}, \tag{2}$$

where SP is systolic pressure and DP is diastolic pressure.

ICP is the pressure within the rigid human skull, the volume of which, according to the Monro and Kellie doctrine, cannot change [7]. ICP is the sum of the partial pressures of brain tissue, cerebrospinal fluid (CSF), and cerebral blood volume (CBV) con-

tained within the skull, and thus may vary with any of these three partial pressures [2]. Changes in ICP can occur in the healthy patient due to arterial pulsations within the brain, changes in head and body positioning, or exercise, but may also occur due to the administration of drugs or various disease states, such as traumatic brain injury, intracranial haemorrhage or tumour, disorders of CSF circulation, and stroke [5, 7].

Analogous with Ohm's or Darcy's Law, CBF varies with CPP according to [5]

$$\mathrm{CBF} = \frac{\mathrm{CPP}}{\mathrm{CVR}}, \tag{3}$$

where CVR is total cerebrovascular resistance, and is associated with the entirety of the brain's vascular tree. Thus, one component of CA involves *pressure* autoregulation, by which varying degrees of vasoconstriction and vasodilation are used to affect changes in CVR. The other component of CA is *metabolic* autoregulation, in which CBF is adjusted according to metabolic needs of the tissue. This metabolic effect is primarily attributed to changes in brain tissue pH [2].

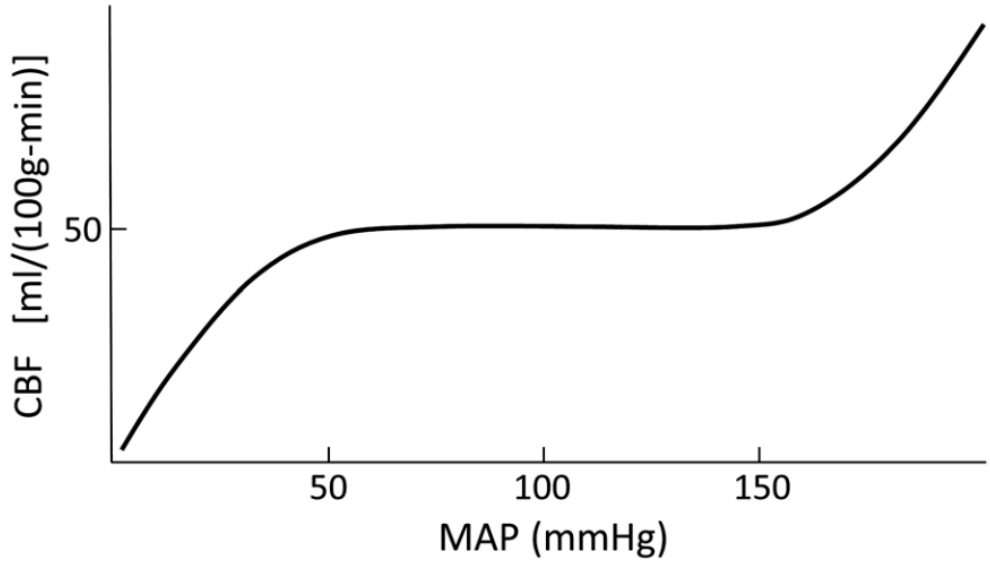

Figure 1.1: Within the autoregulatory range of 50 - 150 mmHg of mean arterial pressure (MAP), cerebral autoregulation is intact, with no correlation between MAP and CBF. Reproduced with permission from [5]. © 2016 Society of Photo-Optical Instrumentation Engineers (SPIE).

In order to assess CA in a continuous or semi-continuous manner in hospitalised patients, invasive measurements of ICP may be taken in order to calculate an estimate of CPP, which may be used as a surrogate for CA assessment [6]. For example, in the absence of CA, an increase in MAP will cause an increase in CPP [5]; alternatively, a decreased CPP can be viewed as an indicator of low CBF and impaired CA. This also allows clinicians to manage ICP directly, but has two disadvantages:

- in certain populations of patients, clinicians would prefer to avoid the risks of invasive continuous cerebral monitoring devices [8], such as the risk of bleeding, infection, and misplacement [9];

- a more accurate assessment of CA may be inferred from direct measurements of local CBF [3], and evaluation of its correlation with MAP, together with evaluation of clinical neurological signs. As shown in Figure 1.1, there should be no correlation between CBF and MAP when CA is operating effectively.

Indeed, raised ICP and low CBF are associated with ischaemia and poor outcomes following brain injury, and so many management protocols target these two parameters directly [7].

CBF measurements may also be used to distinguish between hypoxia and ischaemia, to avoid hyperperfusion injury, to characterise different types of hypoxic states, as well as to examine connections between vascular physiology and neurophysiology (i.e., neurovascular coupling) in healthy patients for neuroscience applications [4]. Finally, CBF monitoring also has applications in the development of a noninvasive brain-computer interface [10].

The motivation to measure local microvascular blood flow (BF) is by no means limited to the brain. Abnormal BF can be seen in a variety of medical conditions in the various tissues and organs of the human body, and the utility of its measurement has been demonstrated in conditions such as cancer and peripheral arterial disease (PAD), as well as in the monitoring of muscle disease, and normal exercise physiology. A few of these applications are briefly outlined below.

Worldwide, breast cancer is the most frequently diagnosed and primary cause of cancer-related mortality amongst women [11]. Therefore, every incremental improvement in breast cancer detection could have a significant impact on the detection of this disease. Previous studies have shown that BF in tissues affected by breast cancer is larger than in normal tissues [12, 13]. BF measurements have been used to monitor the response of:

- breast cancer to chemotherapy [13];

- head-and-neck cancer to chemoradiation therapy [14];

- prostate cancer to photodynamic therapy (PDT) [15].

It has also been demonstrated that BF measurement can be used in the prediction of the response of murine tumours to PDT [16], as well as in the real-time *in situ* monitoring of the response of prostate cancers to PDT [15].

Measurement of BF in skeletal muscles has important applications in exercise medicine and the furtherance of our knowledge of exercise physiology, as well as in the aiding of our understanding of diseases such as PAD, and how muscle function is affected by cardiovascular disease more generally [17]. There has also been recent interest in BF imaging of the heart to assess cardiac tissue for evidence of myocardial infarction (i.e., heart attack) [18], which would be especially useful in the emergency setting.

1.2 Project aims

Despite the importance of CBF monitoring, there is currently a vacant niche for an inexpensive, continuous, noninvasive, portable, bedside, and non-ionising imaging/sensing modality with which to measure CBF [19]. Indeed, Durduran and Yodh [3] state that 'clearly, an independent, versatile and noninvasive bedside monitor of local, microvascular CBF is desirable', and in this paragraph I offer a requirements capture of the idealised CBF measurement. Ideally this measurement would be performed in a continuous manner, with millimetre spatial resolution and centimetre depth penetration in order resolve regional flow differences throughout the entire brain [3]. The measurement would be obtained using an instrument that is non-ionising, noninvasive, and portable, and which adheres to any relevant safety standards [20]. Ease of use is also an important criterion, as is robustness to motion artefacts and ambient light, all of which are conducive to successful continuous long term monitoring in the clinical setting. The ability to be able to sample and contrast regional differences of CBF in the brain is important. Instrumentation and per measurement costs should kept as low as possible, and the measurement technique should be compatible with patients of all ages. The ability to be able to provide a range of functional diagnostic imaging information, with high sensitivity at the smallest physical scale possible, is also desirable. Finally, real-time operation with the millisecond temporal resolution that is required to capture *in vivo* sample dynamics would ideally be achieved [19].

Diffuse correlation spectroscopy (DCS), which was first developed in the 1990s [21], is a non-invasive optical imaging modality that can be used to measure CBF in real-time [22]. However, one of the limitations of DCS is that a trade-off exists between the signal-to-noise ratio (SNR) and imaging depth, and thus brain specificity, of this technique [23]. This is because an increase in imaging depth requires the use of larger source-detector separation (SDS) distances, which result in more photon losses due to absorption and scattering, and a subsequent decrease in SNR. Additionally, as DCS is a diffuse optical technique, it is limited by a lack of inherent depth discrimination within the illuminated region of each source-detector pair, and the CBF signal is therefore also prone to contamination by the extracerebral tissues which the light traverses [24]. Under

optical properties typical of biological tissues, DCS measurements are sensitive to flow at a depth approximately equal to one half to one third of the optical SDS distance [4, 8]. Thus, for a typical DCS setup with an SDS distance of 2 - 3 cm, attempts to measure CBF are limited to superficial cortical regions. To date, deep CBF has not been measured using DCS in human studies [4].

Given that the imaging of deep tissue perfusion is an important problem in the field of medical imaging research [25], the investigation of novel approaches to improve the sensitivity of DCS to CBF has recently attracted interest from several research groups. Techniques including multispeckle detection strategies [10, 26, 27], time-domain DCS (TD-DCS) [28], DCS in the short-wave infrared region [29, 30], interferometric approaches [23, 31, 32], and acousto-optic modulation [33] have all been proposed. Informed by these approaches, and placing a particular emphasis on scalability, affordability, and robustness to ambient light, in this thesis I propose to explore an approach which fuses the fields of digital holography and DCS: holographic Fourier domain DCS (FD-DCS). The potential benefits of holographic FD-DCS compared to conventional DCS are multiple: SNR that scales linearly with the square root of the number of camera pixels used, order of magnitude reduction in detector cost, robustness to the effects of ambient light, shot noise limited detection using off-axis holography [34], potential for detector scalability and sensor partitioning (which could facilitate tomographic and depth discrimination techniques [35, 36]), and suitability to a range of design wavelengths (which could confer a further SNR advantage [29]).

To explore the feasibility and potential advantages of holographic FD-DCS, the following key research objectives were pursued in this thesis:

1. Development of an FD-DCS analytical model.
2. Development of a holographic FD-DCS instrument suitable for *in vivo* pulsatile multispeckle detection.
3. Absolute validation of both of the above against conventional DCS.
4. Demonstration of SNR advantage and insensitivity to ambient light with respect to conventional DCS.
5. Demonstration of *in vivo* feasibility.
6. Rigorous characterisation and optimisation of system SNR performance.
7. Development of a simulation framework for a two-dimensional time-integrated dynamic speckle pattern (2D-TIDSP), which could be used to feed into a forward model for holographic FD-DCS.

8. Development of novel expressions for speckle contrast for various forms of electric field commonly encountered in biomedical optics.

1.3 Thesis overview and contribution

An overview of the literature pertinent to CBF is provided in Chapter 2. This includes a critical assessment of non-optical, optical, and hybrid methods, as well as a concise introduction to biomedical optics. DCS is the archetypal optical modality to measure flow beyond a few millimetres of the tissue surface, and it is suitable for continuous, noninvasive, portable, and real-time CBF measurement. However, the depth penetration and spatial resolution of DCS are fundamentally limited by the nature of diffuse optics, and, in Chapter 2, I review the various approaches that have been employed to overcome these limitations.

In Chapter 3, I introduce digital holography, and describe its previous applications to biomedical optics. I then propose how digital holography and DCS can be combined with a view to improving the SNR performance of DCS. In Chapter 3, I also describe some of the potential barriers to success and the fundamental limitations of this proposed technique.

Research objectives 1 - 5 are addressed in Chapter 4. The novel FD-DCS analytical model that I have derived is presented and numerically validated. This is followed by the development and validation of a holographic FD-DCS instrument that is suitable for *in vivo* pulsatile multispeckle detection. Both the analytical model and the instrument that I have developed are then validated against absolute conventional DCS measurements over a physiological temperature range in an intralipid optical tissue phantom. This validation required the development of not only a novel temperature dependent model for the properties of intralipid optical tissue phantoms, but also the development of a novel mixed motion DCS model. I also demonstrate the SNR advantage and relative insensitivity to ambient light that holographic FD-DCS offers compared to conventional DCS. The final contribution of Chapter 4 is a demonstration of the *in vivo* feasibility of holographic FD-DCS, through the measurement of pulsatile flow rates measured in the human forearm.

Research objective 6 is addressed in Chapter 5. The characterisation and removal of noise sources can be broadly subdivided into four investigations: the diagnosis and elimination of laser mode hopping, correction for the modulation transfer function (MTF) of a holographic FD-DCS instrument, using a singular value decomposition (SVD) spatiotemporal filtering approach to characterise and remove source noise, and the development of a novel multispeckle denoising algorithm to characterise and remove detector noise. By undertaking this rigorous and systematic SNR performance assessment, I demonstrate the highest SNR gain reported in the DCS literature to date, which has been achieved using scalable and low-cost camera-based detection.

Research objectives 7 and 8 are addressed in Chapter 6. The simulation of statistically accurate time-integrated dynamic speckle patterns using a physics-based model that accounts for spatially varying sample properties is yet to be presented in biomedical optics, and in this chapter I propose a solution to this problem based on the Karhunen-Loève expansion of the electric field. In Chapter 6, I also offer novel expressions for speckle contrast for various forms of electric field that are commonly encountered in biomedical optics. I then use these expressions to validate the novel time-integrated dynamic speckle pattern simulation framework that I have developed. Finally, I then show how the novel simulation framework can readily be extended to cases with spatially varying sample properties, that it can also be extended to include any form of electric field that results from various detection geometries, and that it can also include sample dynamic properties, as well as optical and acoustic parameters.

In Chapter 7, I conclude my findings by summarising the thesis and detailing the contribution to knowledge contained within. I then discuss the findings of my research within the context of similar work by other researchers, the limitations of the research, and the future work that could extend the investigations in this thesis.

I have published the research that was conducted for this thesis in two first author peer reviewed journal articles, one in Biomedical Optics Express and one in Optics Letters. For the former I was subsequently awarded the 2021 Robert Speller Prize for the best paper by a PhD student in the UCL Medical Physics and Biomedical Engineering Department. A third first author peer reviewed journal article has also recently been accepted for publication by Biomedical Optics Express. In addition to this, I have presented work from this thesis during four conference presentations at three international conferences: Photonics West SPIE BiOS 2020 and 2022, and IEEE IPC 2021. I presented an invited conference presentation at Photonics West SPIE BiOS 2022, and I was also nominated for the best student paper prize at IEEE IPC 2021. The work presented in this thesis therefore represents a distinct and significant contribution to biomedical optics.

2 Review of cerebral blood flow measurement methods

2.1 Chapter contribution

Many imaging modalities exist which attempt to measure cerebral blood flow (CBF), each of which has its own distinct advantages and disadvantages. These modalities may be broadly characterised by the various criteria described in Table 2.1. Within the more general context of tissue blood flow (BF) measurement, Yu *et al.* [19] state,

> 'The ideal BF measurement should provide quantitative information about macro- and microvasculature with millisecond temporal resolution. The measurements should be carried out continuously, noninvasively, and without risk to subjects. Furthermore, ideal measurements would not be limited to the tissue surface, i.e., it is desirable to probe BF in deep tissues. Unfortunately, no such ideal modality exists.'

This chapter contains a concise review and critical assessment of CBF measurement methods, and is divided into a treatment of non-optical, optical, and hybrid methods. Non-optical methods, which tend to not lend themselves well to continuous, non-invasive, and portable CBF monitoring, are reviewed at the beginning of the chapter. Having outlined a brief introduction to biomedical optics, both incoherent and coherent optical CBF measurement modalities are described, which have a range of imaging depths, spatial resolution, and measurement signal-to-noise ratio (SNR). Finally, the motivation for hybrid imaging methods, which make use of the interplay between optics and ultrasound, is described. Of the two hybrid modalities described, acousto-optic tomography (AOT) shows the most promise for deep and spatially resolved CBF measurement with a high enough measurement SNR to allow for clinically useful temporal resolution. However, there are many challenges that remain in making AOT methods an *in vivo* reality, and these are critically appraised at the end of this chapter.

2.2 Non-optical methods

With the notable exception of transcranial Doppler ultrasound (TCD), all the non-optical methods described in this section suffer from at least one of the following drawbacks: invasive measurement protocol, non-portability of equipment prohibiting bedside use and necessitating patient transport, single measurement rather than continuous monitoring, and high instrument cost, both in terms of the instrument itself and instrument time. This is supported by the observation by Durduran *et al.* [8] that local microvascular CBF is particularly difficult to measure at the patient's *bedside*.

Table 2.1: An outline of the salient features of current techniques used to measure CBF, adapted from [3, 5, 37, 38]. N.B. Table continues overleaf.

Method	**Technique**	**Invasiveness**	**Spatial extent**	**Absolute or relative**	**Snapshot or continuous**
Intravascular measurements	N_2O inhalation	Invasive	Global	Absolute	Snapshot
	Thermodilution	Invasive	Global	Absolute	Continuous
	Jugular bulb oximetry	Invasive	Global	Relative	Snapshot
Nuclear medicine	^{133}Xe, ^{85}Kr	Invasive	Regional	Absolute	Snapshot
	SPECT	Minimally invasive	Local	Relative	Snapshot
	PET	Minimally invasive	Local	Absolute	Snapshot
X-ray imaging	Xe-CT	Noninvasive	Local	Absolute	Snapshot
	PCT	Minimally invasive	Local	Absolute or relative	Snapshot
Magnetic resonance imaging	DSC-MRI	Minimally invasive	Local	Absolute or relative	Snapshot
	ASL-MRI	Noninvasive	Local	Absolute	Snapshot (repeatable)
Ultrasound	TCD	Noninvasive	Regional	Relative	Continuous
	CEUS	Minimally invasive	Regional/local	Relative	Snapshot (repeatable)
	Transit-time ultrasonic flowmetry	Invasive	Regional	Relative	Continuous
Thermal diffusion	TDF	Invasive	Regional/local	Absolute	Continuous
Biomedical optics	Qualitative NIRS	Noninvasive	Regional/local	Relative	Continuous
	Quantitative NIRS	Invasive	Regional/local	Absolute	Snapshot
	CHS	Noninvasive	Regional/local	Absolute	Continuous
	LSCI	Invasive	Local	Relative	Continuous
	MESI	Invasive	Local	Absolute	Continuous
	LDF	Invasive	Local	Relative	Continuous
	DLSI	Invasive	Local	Relative	Continuous
	DCS	Noninvasive	Regional/local	Relative	Continuous
	iNIRS	Noninvasive	Regional/local	Relative	Continuous
	SCOT/SCOS	Noninvasive	Regional/local	Relative	Continuous
	DSCA/DSPF	Noninvasive	Regional/local	Relative	Continuous

Method	Technique	Spatial resolution	Data acquisition time	Inter-scan time[a]	Instrument cost
Intravascular measurements	N_2O inhalation	N/A	15 - 20 min	30 min	Low
	Thermodilution			0 min	
	Jugular bulb oximetry				
Nuclear medicine	^{133}Xe, ^{85}Kr	4 - 6 mm	10 - 15 min	10 min	High
	SPECT				
	PET		5 - 9 min		
X-ray imaging	Xe-CT	4 mm	10 min	20 min	Moderate
	PCT	1 - 2 mm	40 sec	10 min	
Magnetic resonance imaging	DSC-MRI	2 mm	1 min	25 min	High
	ASL-MRI		5 - 10 min	0 min	
Ultrasound	TCD	N/A	10 -20 min	0 min	Low
	CEUS			10 - 60 min	
	Transit-time ultrasonic flowmetry	3 mm	> 1 μs	0 min	
Thermal diffusion	TDF	3 mm	> 1 μs	0 min	Low
Biomedical optics	Qualitative NIRS	10 mm	> 0.1 sec	0 min	Low
	Quantitative NIRS				
	CHS				
	LSCI	> 50 μm	> 10 ms		
	MESI				
	LDF				
	DLSI				
	DCS	10 mm	> 0.1 sec		
	iNIRS				
	SCOT/SCOS				
	DSCA/DSPF				

[a]Minimal time between two consecutive examinations.

2.2.1 Intravascular measurements

The Kety-Schmidt arteriovenous difference method [39] became the standard approach to global CBF measurement following its publication in 1945. This technique involves the inhalation of nitrous oxide (N_2O) by the patient, and the subsequent exploitation of its properties as an intravascular tracer that freely diffuses into the brain. Following inhalation, the time required to reach a steady state concentration of $[N_2O]_{arterial} = [N_2O]_{venous}$ (as determined from femoral artery and right internal jugular venous blood samples, respectively) is found to be inversely proportional to CBF, and this provides a snapshot quantitative bedside result [5]. This process is relatively time consuming, with a steady state concentration achieved in 10 - 15 minutes, during which CBF is assumed to remain constant. This technique is also invasive, not practical in a clinical setting [40], and is restricted to global CBF measurements.

Continuous jugular thermodilution is like the above method, but a cold miscible tracer is used as the intravascular marker instead. This typically requires catheterisation of an internal jugular vein to facilitate the injection of a suitable fluid tracer, as well as measurement of temperatures of the blood and its mixture with the tracer. Jugular BF can then be calculated by relating the rate of injection of the tracer fluid, the densities of blood and the tracer, the specific heat capacities of blood and the tracer, and the temperatures of blood, the tracer and their mixture [5]. Based on the assumption that the left and right internal jugular veins both drain the brain equally, and knowledge of total brain mass, CBF may then be inferred from jugular BF. A non-continuous double-indicator dilution technique has also been proposed, based on injections of indocyanine green (ICG) dye and iced water [41].

Jugular bulb oximetry is a form of intravascular measurement technique that involves measuring the oxygen content of paired arterial and jugular blood samples, and can provide information regarding the sufficiency of CBF relative to the metabolic demands of the brain. This procedure is invasive and technically demanding, as well as being prone to modelling errors regarding the proportion of the brain that is drained by either the left or right internal jugular veins [7]. This technique cannot calculate direct CBF measurements and assumes that cerebral autoregulation (CA) mechanisms are intact. As with all the intravascular measurement techniques, global CBF measurements will not be able to reflect regional ischaemic changes.

2.2.2 Nuclear medicine

The Kety-Schmidt technique can be further modified to exploit the radioactive properties of ^{133}Xe or ^{85}Kr. These gases may be administered to a patient via intraarterial, intravenous, or inhalation routes, after which point they are diffusible and inert within the body. Compared to N_2O, a major advantage of using these noble gases is that they

do not interfere with brain metabolism [40]. Measurement of the isotope's concentration clearance curve can then be undertaken at various regional locations over the brain's hemispheres, from which CBF can be calculated by modelling the observed clearance curve as an exponentially decaying function.

This technique has the obvious disadvantage of exposing the patient to a certain dose of ionising radiation, as well as giving measurements on a timescale of minutes [5] using 'bulky' equipment [7]. This technique is also susceptible to missing low CBF areas, due to the possibility of an adequately perfused region being superimposed upon an inadequately perfused region (the 'look-through phenomenon').

Single photon emission computed tomography (SPECT) and positron emission tomography (PET) are two further methods which require exposure to ionising radiation, and also additionally require arterial blood sampling for quantification of CBF [19]. PET can provide further diagnostic information, including cerebral blood volume (CBV), and information relating to both oxygen and glucose metabolism [5]. These two techniques are both associated with considerable cost (especially PET), patient administration of a radioactive nucleotide (which may limit suitability in certain clinical settings), limited clinical availability, patient discomfort, and unsuitability for long-term monitoring [8], particularly in a populations such as neonates [3]. It is of note that SPECT increases the total dose of radiation exposure due to the use of both a radioactive nucleotide and X-rays [40].

2.2.3 X-ray imaging

Xenon computed tomography (Xe-CT) involves the acquisition of a baseline computed tomography (CT) scan of a patient's brain, inhalation of a stable xenon gas mixture, followed by the acquisition of subsequent CT scans, and the sequential subtraction of the baseline values from xenon enhanced CT images. This yields a set of voxel-wise tracer accumulation curves, from which CBF in each voxel can then be calculated. Xe-CT suffers from particular susceptibility to patient motion artefacts [5], and, although noninvasive and providing an absolute measurement, the instrument and the gas required to perform this technique are both expensive [8], and its capability to measure CBF is limited to snapshot results at discrete time points.

Dynamic perfusion computed tomography (PCT) is a similar technique to Xe-CT and involves the acquisition of a no contrast baseline CT scan of a patient's brain, after which an iodine based contrast agent is administered intravenously. This is followed by a series of rapidly acquired CT scans to determine time-concentration curves of the contrast agent, from which CBF may be inferred. The acquisition time for this technique, although far from being real-time, is relatively short at 40 seconds, and PCT has a spatial resolution of $\sim$1.5 mm, and it is thus competitive with magnetic resonance imaging (MRI) in this regard [3, 19]. Like Xe-CT, PCT also suffers from patient movement

artefacts and is not suited to continuous monitoring.

2.2.4 Magnetic resonance imaging

MRI measurements of CBF may be made using dynamic susceptibility contrast MRI (DSC-MRI), a technique that is also known as perfusion-weighted imaging or bolus-tracking MRI. This technique requires the intravenous injection of a gadolinium-based contrast agent. Unlike the Kety-Schmidt technique, this contrast agent stays in the vascular space and does not cross the blood-brain barrier (BBB). The retention of the paramagnetic contrast agent in the vascular space creates a magnetic field gradient between the brain's capillaries and its surrounding tissues, which is the source of contrast for DSC-MRI measurements, and is affected by local CBF [5]. The use of a bolus injection renders this technique minimally invasive.

Other forms of MRI which are noninvasive (because they rely on endogenous contrast and do not require the use of an exogenous contrast agent) are arterial-spin labelling (ASL-MRI), flow sensitive alternating inversion recovery (FAIR-MRI), and blood oxygen level dependent (BOLD-MRI). BOLD-MRI, an example of a functional MRI (fMRI) modality, makes use of the endogenous contrast associated with the magnetic properties of deoxyhaemoglobin [42]. This can then be used to infer brain activity through the principle of neuro-vascular (or activation-flow) coupling [3, 43]. ASL-MRI is based on the premise of magnetically labelling water in the brain's arterial inflow in a labelling plane, and then measuring local CBF by quantifying the decrease in magnetisation in the imaging plane that is caused by the inflow of arterial blood, which carries a negative magnetisation (i.e., a magnetisation that is flipped by 180^0). Similarly, FAIR-MRI operates on the principle of obtaining two inversion recovery (IR) images: one with a slice-selective inversion pulse, and one with a non-slice-selective inversion pulse. The signal enhancement between the two images is then directly related to CBF [44].

These MRI techniques are capable of imaging the entire head, and produce images which can easily be registered to other fMRI and anatomical MRI techniques, with a spatial resolution of as little as 2 mm [8, 19]. MRI machines require strong magnetic fields, which may prohibit their use in certain clinical settings and in patients with metallic implants (e.g., pacemakers). Claustrophobic patients and neonatal patients are not well suited to this imaging modality, the latter of which may require sedation/anaesthesia or be required to be asleep to reduce patient motion. Further, ASL-MRI suffers from noise during low perfusion readings, as is often encountered with neonatal patients [4]. MRI technology is also expensive, requires patient transport, and is associated with a low patient throughput. Many patients tend to undergo MRI examination only once during their stay in hospital, during which time a snapshot measurement of CBF may be recorded during an intrascan time which can be up to one hour in length [8], and which is typically done in conjunction with a specific research protocol [19].

2.2.5 Ultrasound

Of all the imaging modalities outlined in Section 2.2, TCD is the 'only one non-optical method [that] is available for routine, non-invasive monitoring of cerebral haemodynamics at the bedside' [3]. This is achieved by measuring frequency shifts in reflected probing ultrasound pressure waves, that have been scattered by moving red blood cells (RBCs)[1]. When RBCs flow toward/away from a fixed ultrasound source, the frequency of the reflected ultrasound wave is increased/decreased due to the Doppler effect. The amount of Doppler shift (f_d) is related to the frequency (f) of the ultrasound source, the speed of the scattering RBCs (v, which can be positive or negative), the cosine of the angle of insonation (θ), and the speed of ultrasound in the medium (c_0), by the Doppler equation

$$f_d = \pm \frac{f v \cos\theta}{c_0}. \tag{4}$$

The Doppler signal is usually extracted from a localised range gate that processes only a segment of the received signal [46]. To improve frame rates, a colour Doppler image may be processed within a small colour box (i.e., region of interest) within a B-mode ultrasound image [5].

TCD is capable of measuring flow in large vessels with millimetre spatial and millisecond temporal resolutions, but is limited to be being performed through ultrasonic 'bone windows' and to measurement of the proximal portions of the basal brain arteries (posterior, middle, and anterior cerebral arteries) and the circle of Willis (Figure 2.1) [3]. This technique has achieved success when assessing patients with proximal arterial occlusions, but may be less useful in other important clinical applications, such assessment of stroke patients [8].

Steiner and Andrews describe this technique as 'easy to use and noninvasive' and that it 'can be used repeatedly' for serial bedside measurements [7]. The same authors state that TCD is 'the simplest way to noninvasively obtain repeated real-time estimates of CBF'. However, this is at odds with the findings of Lipnick *et al.* [48],

> 'Accurate TCD measurements and interpretation require the presence of adequate transcranial windows, a highly trained technician to perform the study, and a physician who can interpret the study. Measurements cannot easily be done continuously and may be subject to interference from electrical noise',

and

> 'Despite numerous scenarios where continuous CBF measurement could provide useful clinical information (e.g., vasospasm in subarachnoid patients or flow

[1] Blood contains 45 % RBCs by volume, and the remaining cellular component is contained within the buffy coat, which occupies less than 1 % of the blood by volume and is composed of white blood cells and platelets [45]. Hence, when considering the scattering effects of moving blood cells, the relevant literature focuses on the effects of RBCs.

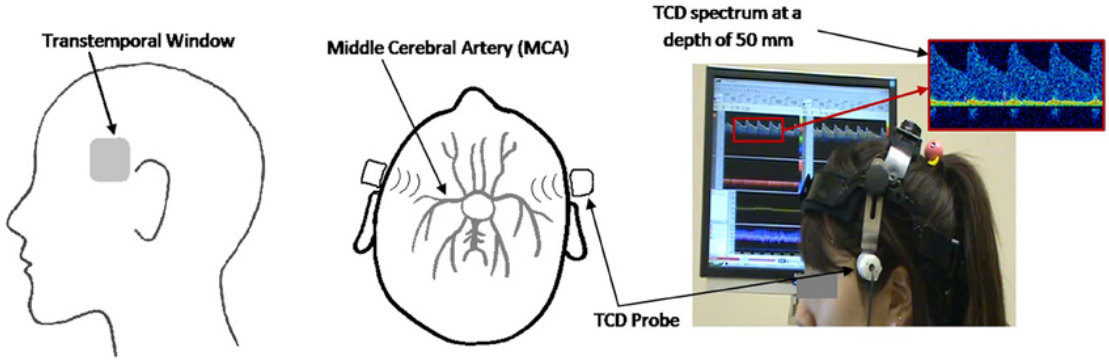

Figure 2.1: Transcranial Doppler ultrasound (TCD). Transtemporal bone window (left) and measurement of BF velocity in the left middle cerebral artery (middle). TCD spectrum (right) in which the x axis corresponds to time, the y axis corresponds to flow velocity, and colour corresponds to relative amplitude. Reproduced with permission from [47] under the terms of a Creative Commons Attribution 3.0 License. Copyright © 2014 Lu, Mamun, and Chau.

> monitoring during carotid endarterectomy), relatively few intensivists, anaesthesiologists, or intensive care unit nurses are proficient with TCD. Furthermore, even where trained personnel are available to provide TCD, continuous measurements for prolonged periods remain technically challenging'.

This highlights the operator dependence of TCD measurement in the clinical setting, and indicates that there is a need for a CBF measurement technique that requires less training, greater ease of use, and that is more robust to both patient and probe positioning, and therefore more conducive to continuous monitoring in the hospital.

It should also be noted that TCD only provides an estimate of CBF, and that, additionally, this technique measures *macrovascular* speed of BF. This can be related to CBF through knowledge of the diameter of the insonated blood vessel (as well as other factors such as RBC velocity spectrum and regional flow distribution [41]), assuming that this and the angle of insonation do not change throughout the examination, and that both can be measured accurately. This relationship introduces uncertainty when converting speed of BF (cm/s) into volumetric flow (ml/s), and knowledge of the mass of brain tissue perfused by the insonated vessel is then required to convert from relative to absolute CBF units [49]. Durduran and Yodh report that in some patients many arteries cannot be insonated, and that estimates of CBF from TCD can be 'problematic' if the diameter of the insonated artery is not measured with sufficient accuracy [3].

To provide information regarding tissue bed perfusion, ultrasound examination requires supplementation with an exogenous contrast agent, such as microbubbles [19]. This technique is known as contrast enhanced ultrasound (CEUS). Microbubbles flow into regions of interest, and tissue perfusion metrics can be obtained from measured contrast time-intensity curves [40]. The advantages of CEUS are that it can be performed

at the bedside, and that neither patient sedation nor ionising radiation is required. Furthermore, it has been postulated that CEUS could be used to screen for patients suffering from hypoxic ischaemic encephalopathy (HIE), on the basis that CBF is a useful biomarker for neonatal HIE [40]. Another potential advantage of this technique is that microbubbles can be targeted to specific cell receptors, and they can also be used for therapeutic purposes by loading them with drugs [46]. However, a recent case study reports that an ultrasonographer, with 20 years' experience, required 14 minutes to perform a brain CEUS scan [50]. CEUS, which is also invasive due to the required exogenous contrast, is therefore not suited to continuous long-term monitoring of hospitalised inpatients.

Transit-time ultrasonic flowmetry is an invasive surgical method that involves placing two ultrasound transducers on one side of a blood vessel, and an acoustic reflector on its other side [51]. By measuring transit times from one ultrasound transducer to the other, both with and against the direction of BF, volumetric BF (ml/s) can be calculated, which can be taken as a relative measure of CBF (analogous to the jugular thermodilution method) [5].

2.2.6 Thermal diffusion

Thermal diffusion flowmetry (TDF) can provide a continuous bedside measure of absolute focal CBF with excellent temporal resolution, but in a notably invasive manner. A probe is inserted through a burr hole in the skull and placed on or in a cortical region of the brain. CBF measurements can be calculated based on the principles of conduction of heat by brain tissue and the convective flow of heat by BF, within a 20 - 30 mm^3 volume of brain tissue [5]. The probe itself consists of two thermistors, one of which is heated, and there is then an inverse relationship between CBF and the temperature difference between the two thermistors.

This technique is contraindicated in feverish patients, and the modelling assumptions upon which it operates may break down if the probe is placed close to a large blood vessel. The probe must remain stationary to yield reliable results, and the use of an invasive probe may not be appropriate in certain populations of patients [3].

2.3 Optical methods

Light has the distinct advantage of having photon energies which match the electronic and vibrational energy levels of many biological compounds. This can be useful when detecting specific changes at the molecular level, which may then be used to calculate functional changes of physiological parameters [52] (e.g., blood oxygenation levels). Light therefore has the potential to both target and provide detailed information about

specific molecules in biological tissue. Compared with other imaging modalities, e.g., MRI or CT, optical imaging enables real-time assessment of patients with equipment that is relatively portable and inexpensive [53], with cost reductions that are in part due to the development of light guides for the telecommunications industry. As optical imaging devices are often lightweight and do not present significant physical restraints, they lend themselves well to the development of wearable devices which can be used to study a wide range of behaviours in a broad range of subjects [54]. Indeed, the first functional brain imaging study in infants in Africa, performed in a remote field station, is attributed to the field of functional near-infrared spectroscopy (fNIRS) [55]. Light sources can also be highly controlled and engineered (in terms of modulation frequency, focusing power, and transmission along optical fibres), and emit radiation that is non-ionising in the near-infrared (NIR) range of the electromagnetic (EM) spectrum [52].

2.3.1 Introduction to biomedical optics

Biomedical optics refers to the interaction of light and biological tissue, and how this interaction can be exploited for sensing, imaging, and therapy. Light in this context refers to visible wavelengths (380 - 750 nm), as well slightly shorter (ultraviolet) and longer (NIR) wavelengths. The concise introduction to biomedical optics that follows includes a discussion of optical absorption and scattering, light transport theory, modelling the time-resolved interaction of light with biological tissues, and autocorrelation functions of coherent light.

The field of diffuse biomedical optics can be broadly divided into incoherent and coherent methods. The aim of incoherent methods is to quantify tissue optical properties, from which oxygen saturation may be inferred. Near-infrared spectroscopy (NIRS) is an example of an incoherent method, and this is introduced in Section 2.3.2. The aim of coherent methods is to quantify sample dynamics directly by analysing spatiotemporal fluctuations of scattered coherent light. Surface sensitive coherent methods are introduced in Section 2.3.4, and coherent methods with deeper imaging sensitivity are introduced in Sections 2.3.5 - 2.3.9. NIRS is the most commonly used diffuse optical technique to measure cerebral haemodynamics at present. However, in this section, I outline the potential benefits that coherent methods offer, the challenges that are faced when using coherent methods, and recent approaches that have been investigated to overcome these challenges. This review of coherent methods serves to inform the novel approach to DCS that is subsequently investigated in this thesis.

2.3.1.1 Optical absorption and scattering

Molecules within biological tissue that *absorb* light are called chromophores, which are the parts of a compound responsible for its colour. For example, red objects appear red to the human eye as their chromophores strongly absorb all parts of the visible EM spectrum apart from red wavelengths, which may be reflected back to the observer. White objects appear so as they *reflect* all incident light, and black objects appear so as they *absorb* all incident light. Each of these chromophores has a specific absorption spectrum that is a function of the wavelength of incident light. During absorption, photon energy is converted into vibrational, electronic, or rotational energy in the absorbing chromophore.

Photons passing through biological tissue will also be *scattered* into directions away from their original path of propagation, due to random fluctuations in the refractive index of tissue at a cellular level. The amount of scattering tends to decrease with an increased wavelength of incident light. The amount of refraction depends on the refractive index, n, of the tissue, with typical values of n being in the range of 1.33 - 1.55 for water and fat, respectively [56]; however, the *bulk* refractive index of tissue is often considered to be constant on a macroscopic scale.

Absorption and scattering represent the main two categories of the interaction of light with biological tissue, both of which will place a limit on how far light can travel into it [53]. They can be characterised by two coefficients when considering light-tissue interactions:

- μ_a, the absorption coefficient (per unit length);
- μ_s, the scattering coefficient (per unit length).

The probability of a photon being absorbed whilst travelling a short distance dz within tissue is given by the product $\mu_a dz$. Alternatively, the absorption mean free path (or optical absorption depth) is simply the reciprocal of the absorption coefficient, and gives the average distance travelled by a photon before it is absorbed. This is also the distance over which a collimated beam will have its intensity reduced by a factor of $1/e$ ($\sim$37 %) due to absorption alone. Aside from melanin, water, collagen, and lipids, haemoglobin is one of the main endogenous optical absorbers in biological soft tissue, and is the chromophore that most influences functional optical imaging (in both its oxygenated and deoxygenated states).

Similarly, the probability of a photon being scattered whilst travelling a short distance dz within tissue is given by the product $\mu_s dz$. Typical values for μ_s in soft tissue are 100 - 1000 cm^{-1} at NIR wavelengths [57], with scatter being the most dominant light-tissue interaction in this part of the EM spectrum. The total attenuation coefficient can then be defined as

$$\mu_t = \mu_a + \mu_s, \tag{5}$$

which can be used to model the exponential decay of the intensity of light in the unscattered part of the beam (i.e., the part that remains *collimated*) due to both scattering and absorption. The average distance travelled by a photon before it is absorbed or scattered is known as the optical mean free path, which is the reciprocal of the total attenuation coefficient. This distance is also known as the optical penetration depth; beyond this depth limit a collimated beam is no longer collimated, and photons move out of the ballistic regime and closer to the diffuse or 'random walk' regime.

Compared to other wavelengths of light, the optical penetration depth is greatest in skin tissues for red and NIR light, where incident optical energy drops by a factor of $1/e$ at a depth of 1 - 3 mm [53]. For this reason, the wavelength range 650 - 1300 nm is referred to as the 'optical window', which comes about due to the relatively low levels of absorption by endogenous chromophores at these wavelengths.

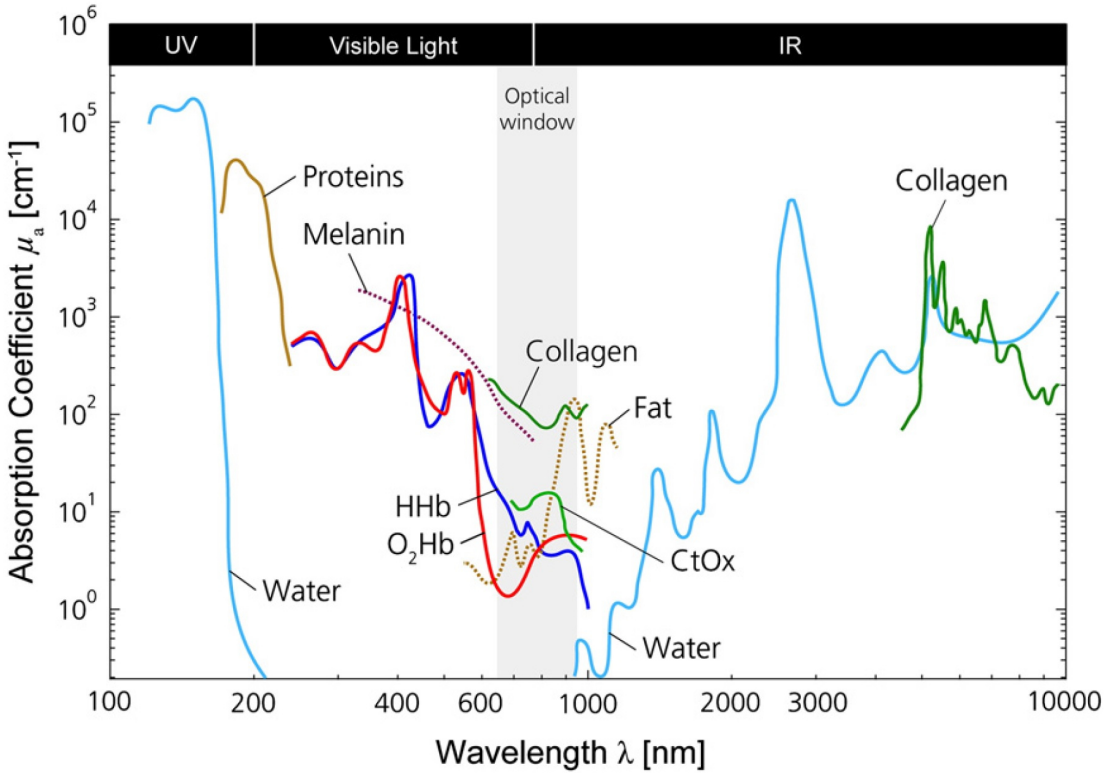

Figure 2.2: Absorption spectra for various endogenous chromophores in biological tissue: oxyhaemoglobin (O_2Hb), deoxyhaemoglobin (HHb), proteins, water, collagen, fat, and cytochrome oxidase (CtOx). Reproduced with permission from [58].

The scattering coefficient indicates how much light is scattered out of a collimated beam, but it does not offer any information on the direction of scattering. To include this angular information, we must consider a scattering *phase* function, which can be measured using a goniophotomoter, or goniometer. A commonly employed scattering phase function is the Henyey-Greenstein function [59], which is widely used for modelling tissue optics. Scattering phase functions makes use of the anisotropy factor, g, which is

defined as the average cosine of the scattering angle. Therefore g can take values anywhere in the range of $-1 \leq g \leq 1$, where positive values imply forward scattering and negative values imply back scattering. If the magnitude of g is large, then the scattering phase function is anisotropic; on the other hand, if $g = 0$, then the scattering phase function is isotropic. Typical values of g in biological soft tissue for NIR light are in the range of 0.69 - 0.99 [57], from which we can infer that tissue is highly forward scattering.

The reduced (or transport) scattering coefficient, μ_s', takes into account that a photon only loses 'knowledge' of its initial direction after $1/(1-g)$ scattering events,

$$\mu_s' = \mu_s(1-g). \tag{6}$$

The reciprocal of μ_s' therefore represents the mean distance between two effectively isotropic scattering events, and is known as the reduced photon-scattering length or random-walk step length [19]. Typical values of μ_s' in biological tissue are often in the order of 10 cm^{-1} [56].

As the reciprocal of μ_t (i.e., the optical mean free path) is a poor indicator of the penetration depths of light into tissue which is highly anisotropically scattering, there is therefore a need for the transport attenuation coefficient,

$$\mu_{tr} = \mu_a + \mu_s'. \tag{7}$$

2.3.1.2 Light transport theory

As well as being computationally intractable, absence of the knowledge of the refractive index distribution for tissue means that solving Maxwell's equations to model tissue scattering of light waves is not feasible. Instead transport theory is used, which is an intensity-based model that treats light as a flow of energy. The radiative transfer equation (RTE), also known as Boltzmann's transport equation, is an idealised representation of low energy photon transport. One method of deriving the RTE is to consider the conservation of energy for the propagation of light through a volume element of a medium, to derive the number of photons per unit volume, at a time t, at a position $\mathbf{x}$, whose velocity is in the direction of $\hat{\mathbf{s}}$. This expression for directional photon intensity, $\Phi_p(\mathbf{x}, \hat{\mathbf{s}}, t)$, is governed by consideration of the following terms [52]:

A. The net inflow of photons in the direction of interest into the volume (due to photons either entering or leaving).

B. The rate of generation of photons in the direction of interest within the volume (i.e., due to a source term).

C. The rate at which photons are scattered into the direction of interest within the volume.

D. The rate at which photons travelling in the direction of interest are absorbed within the volume.

E. The rate at which photons travelling in the direction of interest within the volume are scattered into a different direction.

The RTE may then be generated by equating the change in the number of photons in a volume element travelling in a given direction over a given time period to a function of the above terms: $[(A + B + C) - (D + E)]$. This yields a complex integro-differential equation, and the use of the RTE in this form in analytical solutions is restricted to simple geometries, and its use in numerical calculations is computationally expensive. As such it is often simplified by expression as a sum of spherical harmonics, which is truncated after N terms to produce the P_N approximations. However, it is of note that by ignoring the effects of scattering, the steady-state RTE reduces to Beer's law in one dimension (i.e., $\Phi(z) = \Phi_0 \exp[-\mu_a z]$, where Φ is radiance, which is the rate of energy flow per unit area per unit solid angle at time t at position $\mathbf{x}$ in direction $\hat{\mathbf{s}}$, Φ_0 is surface radiance, and z is depth).

Truncation after the first term leads to the P_1 approximation, and, after further simplification, also leads to the diffusion approximation (DA) to the RTE (or the photon diffusion equation)

$$\frac{1}{c}\frac{\partial \Phi}{\partial t} + \mu_a \Phi - \nabla \cdot (D\nabla)\Phi = q_0, \tag{8}$$

where c is the speed of light in the volume, q_0 is an isotropic source term, and the optical diffusion coefficient is defined as

$$D = \frac{1}{3\mu_{tr}}. \tag{9}$$

Care must be taken when solving and applying the DA, as it is derived under the assumption that photons are entirely diffuse, and therefore it will not be applicable close to optical sources or tissue boundaries. Its use is appropriate when the condition $\mu_a \ll \mu_s'$ is met (i.e., when scattering is assumed to be isotropic) [60]. The DA is the simplest approximation to the RTE, and its use is widespread within the context of biological tissue; however, it does show marked differences to higher order approximations, such as the *diffusive wave* approximation, which has applications for the time-resolved measurement of light in turbid media [61].

Equation 8 can be solved for arbitrary heterogeneous media using numerical techniques; however, solutions for homogeneous media can help to provide insight. By considering the steady state solution to Equation 8 we have

$$\mu_a \Phi - \nabla \cdot (D\nabla)\Phi = q_0. \tag{10}$$

For tissue with homogeneous optical properties, in which D is constant, we have

$$(\mu_a - D\nabla^2)\Phi = q_0. \tag{11}$$

The fundamental solution, or 3D Green's function, to Equation 11 is

$$G_0(\mathbf{x}, \mathbf{x}') = \frac{\exp(-\mu_{\text{eff}}|\mathbf{x} - \mathbf{x}'|)}{4\pi D|\mathbf{x} - \mathbf{x}'|}, \tag{12}$$

where the effective attenuation coefficient

$$\mu_{\text{eff}} = \sqrt{3\mu_a(\mu_a + \mu_s')}. \tag{13}$$

2.3.1.3 Temporal point spread functions

Contini *et al.* [62] presented solutions to the time-dependent DA (i.e., Equation 8) in a semi-infinite diffusing slab (i.e., infinite in the xy plane but bounded in the z axis), in which a normally incident light beam is represented by a delta function coaxial to the z axis, at time $t = 0$. The authors' notation is further described in Figure 2.3: ρ is the radial distance away from the light beam, and s is the thickness of the slab.

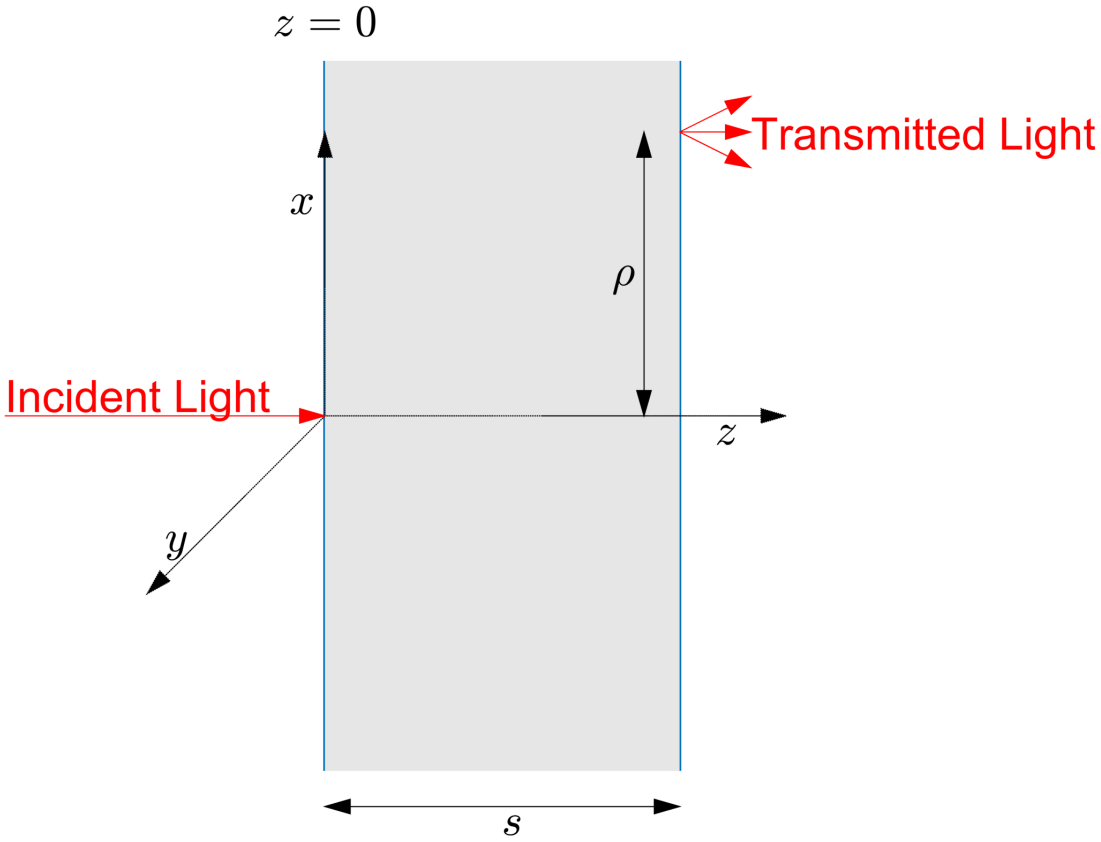

Figure 2.3: Semi-infinite slab geometry with a thin and collimated incident light beam coaxial to the z axis.

Two sets of boundary conditions were used in this study: a zero boundary condition, and an extrapolated boundary condition. The extrapolated boundary condition assumes that the average diffuse intensity is equal to zero at two extrapolated flat surfaces (shown by the green dashed lines in Figure 2.4). The distance of these extrapolated surfaces from the boundaries of the slab is given by [63, 64]

$$d = 2AD, \tag{14}$$

where A is a coefficient that is a function solely of n. This boundary condition takes into account refractive index mismatches between the diffusing slab and the surrounding medium, and is sufficient to solve the RTE in this geometry [62].

To adhere to this boundary condition, the authors used a system of an infinite number of positive and negative dipole sources in an infinite diffusing medium. The first three of these dipole sources, together with their characteristic equations, are shown in Figure 2.4. The authors found that the use of 7 such dipoles was sufficient to restrict truncation error to less than 0.1 % when using the optical parameters described in Figures 2.5 and 2.6, and also when $\rho < s$.

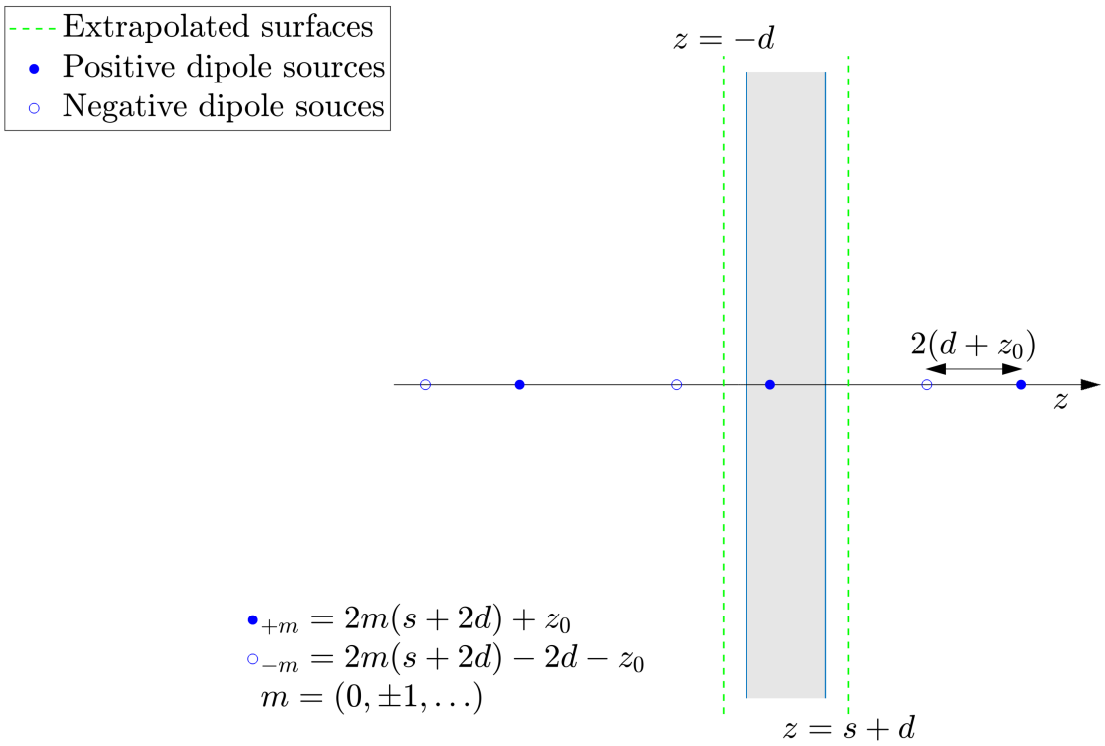

Figure 2.4: The two extrapolated surfaces and the first three of an infinite series of positive and negative dipole sources.

Alternatively, the zero boundary condition assumes that the average diffuse intensity is equal to zero on the boundary of the slab. This boundary condition is independent of the refractive index of the medium, but is still dependent upon its diffusion coefficient, D. In this scenario the extrapolation distance, d, is effectively zero. This condition

is not particularly physically realistic, as the effects of reflections at the boundary are not considered.

Using equations A2, A3, 36, 37, and 39 from Contini *et al.* [62], and a μ_a dependent optical diffusion coefficient (see Equations 7 & 9), both temporal point spread functions (TPSFs) from Figure 3 of this paper were reproduced. The time-resolved reflectance (Figure 2.5) represents the power reflected from the surface of the slab at $z = 0$, per unit area and per unit time, at a radial distance ρ from the light beam, with any exit angle. The authors note that a value of $n = 1.4$ is a typical value for the air-tissue interface.

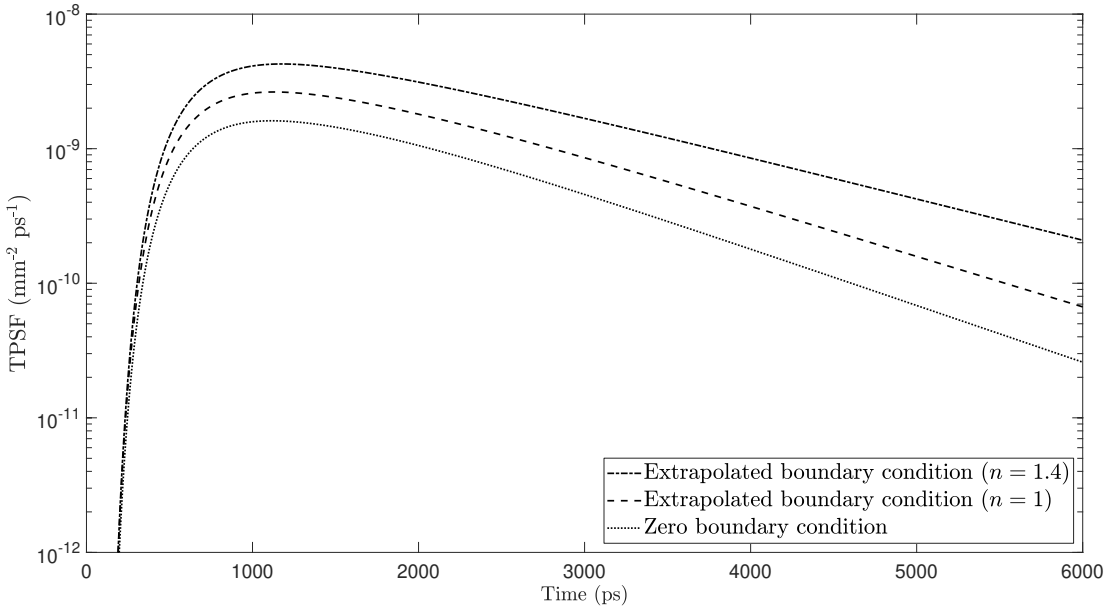

Figure 2.5: The time-resolved reflectance at ρ = 40 mm for a slab 40 mm thick, with μ_a = 0.0 mm^{-1} and μ_s' = 0.5 mm^{-1}.

The time-resolved transmittance (Figure 2.6) represents the power crossing and exiting the surface of the slab at $z = s$, per unit area and per unit time, at a radial distance ρ from the light beam, with any exit angle. This can be thought of as the non-reflected and non-absorbed diffuse light that is detectable on the other side of the slab, due to the incident beam.

Together these two temporal point spread functions (TPSFs) represent the relative likelihood that a single photon, which has entered the slab at the origin of the coordinate system at time $t = 0$, will leave the slab per unit time and per unit area, at time t, and at a radial distance p from the z axis. The time-resolved transmittance TPSF can be thought of as a measure of the rate of arrival of photons from a point source at a detector, through some biological tissue under examination, as a function of time. The early arriving photons will have taken a more direct route from source to detector, whereas the late arriving photons will have undergone multiple scattering events and will have taken a more indirect route from source to detector.

With reference to Figure 2.6, Contini *et al.* describe how two defining characteristics

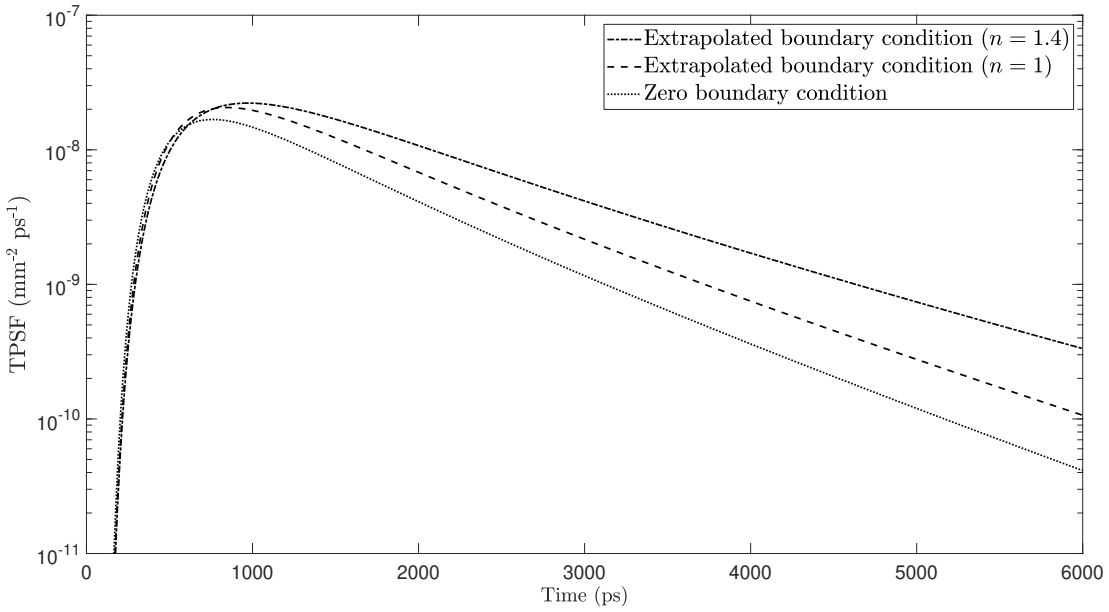

Figure 2.6: The time-resolved transmittance at ρ = 0 mm (i.e., coaxial to the z axis) for a slab 40 mm thick, with μ_a = 0.0 mm^{-1} and μ_s' = 0.5 mm^{-1}.

of this TPSF can be used to characterise the optical properties of the medium under examination: μ_s' can be inferred from its maximal peak, and μ_a can be inferred from its slope at long times [62]. Therefore, accounting for an extrapolated boundary condition (i.e., the effect of reflections and refractive index mismatches) as well as the use of an appropriate refractive index are important in this context.

2.3.1.4 Autocorrelation functions

Laser speckle is a random interference pattern that is produced by the coherent summation of a scattered laser beam of light, each component of which has travelled a slightly different pathlength due to scattering. Movement of scattering RBCs in biological tissue causes modifications to the intensity of this speckle pattern, in both the temporal and spatial domains [65]. Speckle ensemble methods use a high-pixel-count and typically low-frame rate detector to capture speckle patterns and infer sample dynamics through assessment of the spatial fluctuations of speckle [66].

Alternatively, temporal sampling methods record the intensity fluctuations of each pixel over time, typically using high-frame rate and single or few-mode detection [66]. When an incident coherent light beam interacts with a scattering particle, each particle develops an induced dipole moment. Each of these oscillating dipoles emits scattered light fields in all directions. The scattered light electric field at the detector, $E(t)$, is thus composed of the addition of all of these oscillating dipole contributions. Due to the movement of the scattering particles, the phases of these fields vary relative to each other, which results in fluctuations in the field and intensity over time. Temporal sampling methods access sample dynamics by considering the *autocorrelation* of such a

time-series of measurements, the rate and shape of the decay of which, correspond to the speed and the nature of scattering particles, respectively.

In practice the scattered normalised intensity temporal autocorrelation function, $g_2(\tau)$, at the detector is measured. This is more straightforward to measure than the electric field [3], which fluctuates at 0.23 - 0.46 PHz in the NIR optical window (650 - 1300 nm) and which light sensors are unable to detect. However, $g_2(\tau)$ is directly measurable as [19]

$$g_2(\tau) \equiv \frac{\langle I(t)I(t+\tau)\rangle}{\langle I(t)\rangle^2}, \tag{15}$$

where intensity $I(t) = |E(t)|^2$. An example of $g_2(\tau)$ is shown Figure 2.11. Assuming a zero mean Gaussian electric field, the Siegert relation can then be used to extract the electric field autocorrelation function, $g_1(\tau)$, from $g_2(\tau)$ using [67]

$$g_2(\tau) = 1 + \beta|g_1(\tau)|^2, \tag{16}$$

where [21]

$$g_1(\tau) = \alpha|g_{1d}(\tau)| + (1-\alpha), \tag{17}$$

where $g_1(\tau)$ is the field autocorrelation due to *both* dynamic and static scatterers, $g_{1d}(\tau)$ is the field autocorrelation due to dynamic scatterers *only*, and where $\alpha \in [0,1]$ and $\beta \in [0,1]$ are both unitless factors.

Sample motion may be inferred by fitting measured data to a theoretical model of $g_1(\tau)$ that incorporates mean-square particle displacement, $\langle \Delta r^2(\tau)\rangle$. For the case of deterministic convective motion of scatterers, $\langle \Delta r^2(\tau)\rangle = \langle V^2\rangle\tau^2$, where $\langle V^2\rangle$ ($\mathrm{cm}^2/\mathrm{s}^2$) is the second moment of the speed distribution of scattering particles. In the case of diffusive Brownian motion of scatterers $\langle \Delta r^2(\tau)\rangle = 6D_b\tau$, where D_b (cm^2/s) is the effective Brownian diffusion coefficient of scattering particles [68]. Other types of particle motion contribute toward the measured signal (e.g., rotation, shear flow, and turbulence) but the relevant literature focuses on these two effects.

α is an adaptation to biological tissue and refers to the fraction of scattering events due to dynamic, rather than stationary, scatterers. This factor is therefore the ratio of dynamic scatterers to the total number of scatterers in a sample. One must be careful when applying the Siegert relation to samples which have a large proportion of static scatterers; however, Durduran *et al*. concluded that 'one can routinely employ the Siegert relation in most tissue dynamics experiments, except perhaps those wherein the subject is exercising' [8]. If we make the assumption that a sample is composed entirely of dynamic scatterers, then Equation 17 can be simplified to

$$g_1(\tau) = |g_{1d}(\tau)|. \tag{18}$$

Similarly, if a sample is composed entirely of static scatterers, then we have

$$g_1(\tau) = 1. \tag{19}$$

β, the coherence factor, is a constant determined by the geometry and collection optics of the experiment and is equal to 1 ideally. β is inversely proportional to the number of detected speckles, and is also related to the coherence length, stability of the laser light source, stray light, detector stability, sample coupling, and polarisation state [21]; it can be determined from the y-intercept of $g_2(\tau)$ at $\tau = 0$.

2.3.2 Near-infrared spectroscopy

If a sample contains N known chromophores, then in principle it is possible to estimate the concentrations of each chromophore by making measurements of absorbance at N wavelengths. Under conditions of linear absorption, the total absorbance at each wavelength due to all chromophores of interest can be added, which results in a system of N simultaneous equations, which can then be solved to infer the concentrations of each chromophore, assuming a suitable condition number. NIRS is an incoherent method that uses this technique of spectroscopic inversion (or differential spectroscopy) to make measurements of tissue chromophore concentration within the illuminated region of a sample between a single source and detector pair.

The ability to describe how light travels through biological tissue is at the core of the field of biomedical optics. If this can be done with a certain degree of accuracy, then, using an array of optical sources to illuminate a volume of biological tissue, we can model the propagation of photons that enter the tissue, based on the knowledge of the spatial distribution of variations in the optical properties of the volume in question. This is known as the 'forward problem'.

Alternatively, with knowledge of the optical sources used, and based on *data* derived from surface measurements using an array of optical detectors, we can reconstruct a *solution* for the spatial distribution of optical properties within the volume. From this we can then infer the distribution of any pathology or functional physiological changes that we may be interested in. This is known as the 'inverse problem'.

One imaging modality which utilises the solution to this particular inverse problem, based on NIRS measurements acquired using an array of sources and detectors, is diffuse optical tomography (DOT), which is a bedside application that can be used for continuous monitoring. This noninvasive functional imaging technique uses measurements of light that is transmitted through patient tissues to generate 3D volumetric images, and is particularly useful in the study of haemodynamic and blood oxygenation changes in the new-born infant brain [56, 69] (including oxyhaemoglobin [O_2Hb], deoxyhaemoglobin [HHb], and total haemoglobin [THb] concentrations). Figure 2.7

shows one of the first DOT images of an entire infant's head, which was acquired during an evoked motor response [56].

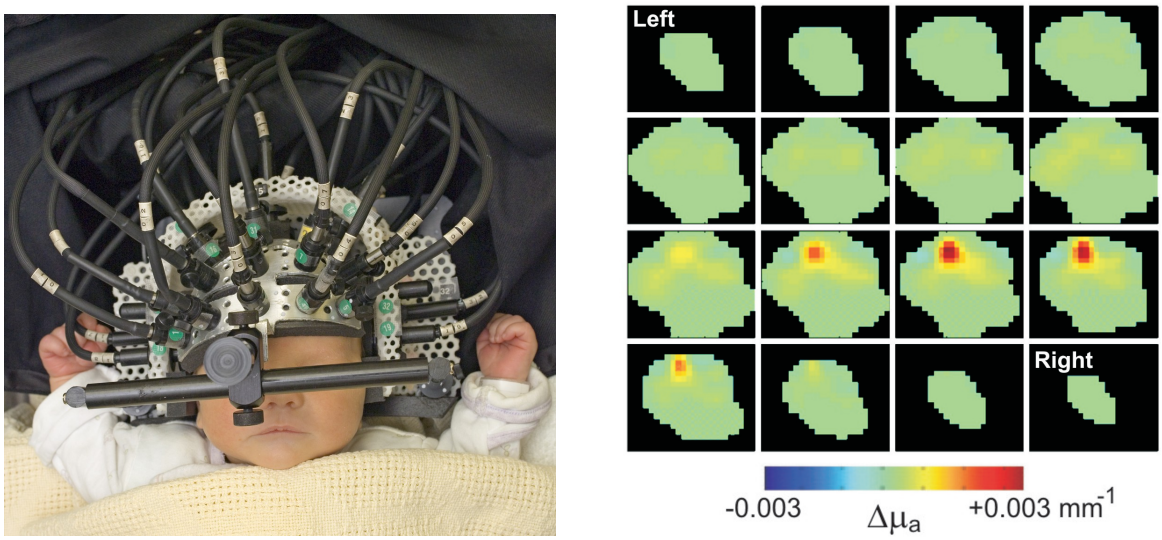

Figure 2.7: An array of optical fibres coupled to an infant's head (left). Para-sagittal slices across a 3D image of the absorption coefficient change (see Section 2.3.1.1) induced by passive movement of the left arm (right). Reproduced with permission from [56]. © 2012 by Taylor & Francis Group, LLC.

NIRS instruments can be divided into three categories [58, 70]:

- Frequency domain (FD) instruments, in which light intensity is modulated at a certain frequency through tissue, and the reduction in intensity and phase shift in the transmitted light are measured.
- Continuous wave (CW) instruments, in which light is modulated at a constant intensity through tissue, and only the reduction in intensity in the transmitted light is measured. This is analogous to an FD instrument in the limiting case of zero modulation frequency.
- Time domain (TD) instruments, in which an ultra-short pulse of light is transmitted through tissue, and the arrival times of transmitted photons are measured.

Multiplexing is a technique used in DOT to distinguish between signals arising from different sources and wavelengths, which are incident upon any one detector during any one sampling period. Time multiplexing, frequency multiplexing, code multiplexing, and spatial multiplexing have all been described [58]. Frequency multiplexing involves modulating each source with a distinct frequency, and the signal amplitude for each source may then be extracted using lock-in amplification techniques or Fourier domain analysis. Inspired by this frequency multiplexing strategy, a fourth category of NIRS *instrumentation* has recently been proposed: wavelength modulated NIRS (WM-NIRS) [71], in which the source *wavelength* is modulated at a fixed frequency. This mod-

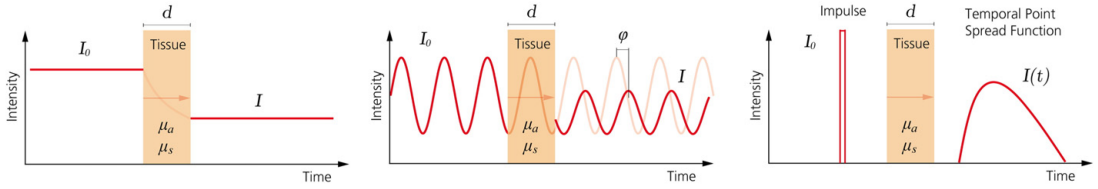

Figure 2.8: The three different NIRS techniques. CW-NIRS (left) involves modulating an incident light signal, I_0, at a constant intensity, and measuring the transmitted light signal, I, that has passed through tissue of thickness d. FD-NIRS (middle) modulates the incident light signal and then measures both I and the phase shift, φ, which corresponds to the time of flight. TD-NIRS (right) involves emitting an extremely short pulse of light into the sample, and measurement of the TPSF of the transmitted signal, $I(t)$. TD-NIRS offers the most information of all three techniques, but is also the most complex to implement. Reproduced with permission from [58]. Copyright © 2013 Elsevier Inc. All rights reserved.

ulation leads to variation in absorption, which in turn will lead to a modulation in detected intensity, and which can also be measured using lock-in amplification or Fourier analysis. A potential advantage of WM-NIRS is the ability to measure absolute changes in chromophores in the face of unknown changes in surface coupling losses. This could be especially useful when differentiating between haemorrhagic and ischaemic stroke in the emergency setting, for example.

DOT uses NIR light to ascertain the concentrations of haemoglobins, water, and lipids in biological tissue by interrogation of the optical absorption spectra of these chromophores (see Figure 2.2) at at least two wavelengths (this is usually achieved using discrete wavelengths; however, broadband NIRS approaches have also been implemented, which make use of light from a continuous portion of the EM spectrum [8, 58]). This allows the assignment of optical and physiological properties to voxels within a tissue sample. By using a high density of sources and detectors, a recent DOT study has demonstrated functional neuroimaging of the superficial cortex with images of a diagnostic quality similar to those of fMRI [72].

NIRS can be used in a qualitative sense to provide continuous relative CBF measurements. This can be done by making use of the following relationships [5]:

- $[O_2Hb] + [HHb] = [THb]$;
- $[O_2Hb]/[THb] = StO_2$, the oxygen saturation of haemoglobin in brain tissue;
- $[O_2Hb] - [HHb] = [DHb]$, the concentration difference between oxyhaemoglobin and deoxyhaemoglobin.

[DHb] and StO_2 are linked to CBF, but can only be used as a relative measure of CBF, and are also affected by other factors, including blood volume, haematocrit, capillary density, and metabolic rate of oxygen consumption.

By using a tracer agent, NIRS can also be used to obtain snapshot absolute CBF measurements. This can be done noninvasively by using endogenous oxyhaemoglobin, or minimally invasively by using an intravenous bolus injection of exogenous ICG. These absolute measurement techniques can introduce ambiguities and cannot be used continuously [3].

Due to the highly diffuse nature of light propagation in scattering biological tissue, the DOT image reconstruction problem is highly ill-posed and the resultant image offers relatively poor spatial resolution [60] with a limited penetration depth [73]. Fantini *et al.* state that the spatial resolution of this technique is on the order of 1 cm, with a maximum depth penetration of 2 - 3 cm [5]. This is in agreement with my previous findings [74], as demonstrated in Figure 2.9. NIRS measurements make use of at least two wavelengths of NIR light, and also require reference phantoms for quantification [4].

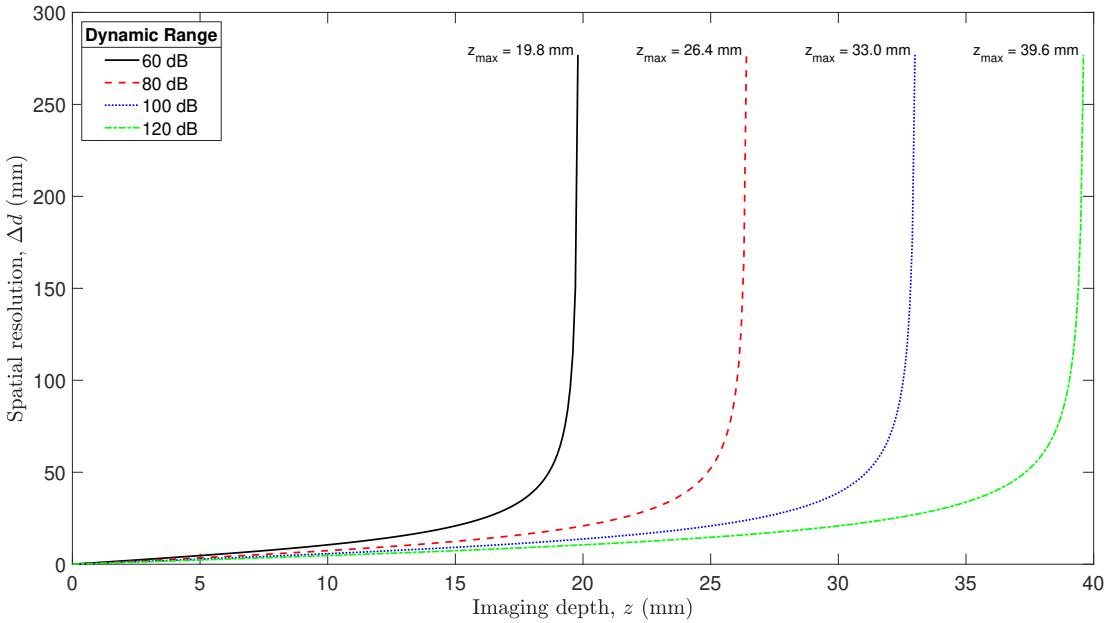

Figure 2.9: Spatial resolution in CW-NIRS as a function of imaging depth for various dynamic ranges of opto-electronic equipment, up to maximum imaging depth, $z_{\max}$ [74].

These fundamental shortcomings, in addition to the effects of superficial tissue, systemic physiological changes, measurement noise, and motion artefacts, all hinder the complete translation of NIRS from a research tool to a reliable and reproducible clinical modality [58, 75].

2.3.3 Coherent haemodynamics spectroscopy

Rather than being an imaging modality *per se*, coherent haemodynamics spectroscopy (CHS) is an additional data processing pipeline that can be applied to NIRS data, following physiological manipulation of the subject. The technique, which was developed

by Fantini *et al.* [5], can be used to translate cerebral haemodynamic measurements into physiological quantities. For example, CHS permits the translation of noninvasive qualitative NIRS data into continuous bedside regional/local measurements of absolute CBF. It should be noted that these measurements will therefore be limited by the spatial resolution and depth penetration of diffuse optical techniques.

CHS operates in either the frequency or time domains. In the frequency domain, oscillations in mean arterial pressure (MAP) are induced by paced breathing or cyclical thigh cuff inflations, which results in oscillations of cerebral [O_2Hb] and [HHb] that are in phase with any changes in MAP. These data may then be fit to a haemodynamic model, the fitting parameters of which relate to CBF and CBV.

Alternatively, in the time domain, a thigh occlusion cuff is suddenly released after a two minute occlusion of pressure that is sufficient to block arterial BF. This occlusion will have caused a temporary decrease in MAP, as well as [O_2Hb] and [HHb], which can then be fit to the time domain CHS haemodynamic model.

2.3.4 Surface sensitive imaging techniques

We now move to consider coherent imaging methods, which make use of the spatiotemporal analysis of scattered coherent light to infer sample dynamics. The following five surface sensitive coherent imaging techniques are used to measure microvascular flow in tissues within a few hundred microns of the surface [19]. Hussain *et al.* describe these methods as 'important tools in the clinic', but also iterate concerns regarding the superficial nature of flow detection, due to deterioration of resolution with tissue depth as a result of multiple scattering [76].

2.3.4.1 Laser speckle contrast imaging

Laser speckle contrast imaging (LSCI) (also known as laser speckle contrast analysis (LASCA), laser speckle flowmetry, speckle visibility spectroscopy (SVS), and speckle contrast spectroscopy) operates on the principle of analysing the temporal and spatial changes in intensity that occur when moving RBCs scatter coherent incident light [77, 78]. These intensity changes can be analysed by quantifying the localised spatial blurring that is caused by speckle movement in a single shot LSCI image, for a given imaging exposure time [79]. Spatial speckle contrast, K, is calculated according to

$$K = \frac{\sigma}{\mu}, \tag{20}$$

where σ is the standard deviation for exposure time T, and μ is the mean of the pixels, usually in a 7×7 pixel window [65]. K can also be calculated globally (i.e., over an entire single image), or through a spatiotemporal windowing approach over one or more frames. K takes a value from zero to one, with larger numbers indicating slower

fluctuations of scatterers [25]. In areas of increased BF, intensity fluctuations are more rapid, which results in increased speckle blurring, with a lower value of K. It has been shown that, over the physiological range, blood flow index (BFI) may be inferred as [80]

$$\text{BFI} = \frac{1}{K^2}. \tag{21}$$

Various other techniques of calculating speckle contrast exist, which make use of various combinations of spatial and temporal statistics, and which maximise temporal and spatial resolution, respectively [81].

These images are commonly captured on a charge-coupled device (CCD) sensor [19], and the application of this technique is limited to periods of open-skull surgery [8].

2.3.4.2 Multiple exposure speckle imaging

LSCI is able to measure *relative* flow, but cannot measure baseline absolute flow values. Additionally, LSCI is limited by the use of a single exposure time, which, due to the presence of static scatterers, can lead to systematic error and deviations from an appropriate model fit [82]. An adaptation to LSCI, multiple exposure speckle imaging (MESI) involves fitting speckle contrast images, acquired at a range of camera exposure times, to single scattering flow models to quantify *absolute* flow at shallow imaging depths [65, 83]. However, the serial acquisition of multiple exposure times reduces the temporal resolution of this technique, and therefore reduces the possibility of resolving fast changes in BF.

Initially, the multiple camera exposure times that MESI requires were achieved by modulating the laser duty cycle [65]. The same group recently presented a *synthetic* approach to MESI (syMESI), that makes use of spatial binning/averaging of single exposure LSCI images to synthesise MESI images [84].

2.3.4.3 Laser Doppler flowmetry

Laser Doppler flowmetry (LDF), sometimes known as scanning LDF or just laser Doppler (imaging), is a technique which quantifies the Doppler shifts in the spectrum of re-emitted light. When a photon scatters off a moving RBC, its carrier frequency is Doppler shifted. By analysing the Doppler shifts that occur in a distribution of photons, the dynamics of the particles scattering the light may be inferred. A perfusion value may be calculated as the first moment of the Doppler power spectrum [79], which is proportional to both the velocity and number of RBCs [5]. LDF can provide a continuous and relative measure of CBF.

A long coherence length NIR optical source (670 - 810 nm) and photodetector are placed in very close proximity (0.25 - 1.00 mm) on the subject's brain, and LDF therefore achieves a maximum penetration depth of $\sim$1 mm [25]. This technique therefore

requires removal of the scalp and skull over the region of interest, and is thus deemed an invasive method, which is limited to intraoperative measurements from a practical perspective. The photodetector detects scattered photons that emerge from the tissue, and the Doppler shift of this light is then fitted to a single scattering model, before being converted to a voltage that varies with time, which is proportional to CBF [5]. This technique could therefore be considered to be the Fourier counterpart of dynamic light scattering (DLS), which is discussed in Section 2.3.4.4.

In addition to being an invasive technique, LDF has the disadvantages of being prone to artefacts caused by patient motion and probe movement, as well as having limited depth penetration and repeatability [4]. Using a larger source-detector separation (SDS) may give a greater depth penetration [85] (which can be further facilitated using *pulsed* LDF [86], for example) and this has been shown to be effective in human skeletal muscle to a depth of 5 - 10 mm [87]. However, this is yet to be translated to noninvasive transcranial monitoring [8].

Surgically implantable monitors are available which use either LDF or TDF to measure CBF in a highly localised area [5, 88]. However, these probes are mainly restricted to experimental use as they 'suffer from all the limitations of any invasive procedure leaving the vulnerable patient at risk for additional pain, infection, bleeding, and the potential for dislodging probes during the routine care of the patient' [5]. Further, there is also a lack of information regarding whether their use has any impact on patient outcomes following brain injury.

2.3.4.4 Dynamic light scattering

As discussed above, the motion of tissue scatterers (e.g., RBCs) can lead to fluctuations in the speckle pattern of scattered light. Dynamic light scattering (DLS) involves the detection of scattered photons, from which hardware or software correlators compute the temporal autocorrelation function of the scattered intensity, $g_2(\tau)$. The motion of the scatterers, such as particles in a suspension, can then be inferred from the rate of decay of $g_2(\tau)$. The mathematical modelling employed by this technique requires that each photon be scattered at most once, and its use is therefore restricted to optically thin samples. This technique is sometimes also known as quasi-elastic light scattering (QELS).

DLS involves the use of a light beam with a long coherence length to illuminate a sample, and a point-like photon detector placed on the other side of the sample, at an angle θ to the incident beam. For independent particles with isotropic dynamics, the detected normalised electric field temporal autocorrelation function due to *dynamic*

scatterers, $g_{1d}(\tau)$, is [8, 21]

$$g_{1d}(\tau) \equiv \frac{\langle E^*(t)E(t+\tau)\rangle}{\langle |E(t)|^2\rangle} = \exp^{-q^2\langle \Delta r^2(\tau)\rangle/6}, \tag{22}$$

where the subscript d denotes the contribution from dynamic scatterers only, $q = \sqrt{2k_0^2(1-\cos\theta)}$ is the scattered wavenumber, $k_0 = 2\pi n/\lambda$ is the wavenumber of the incident light field, λ is the wavelength of the light field, $\langle \Delta r^2(\tau)\rangle$ is the mean-square particle displacement (which directly characterises the particle displacement) in autocorrelation decay time, τ, and $\langle \dots \rangle$ denotes a spatial ensemble-average (which is equivalent to a time-average for an ergodic sample [21]).

2.3.4.5 Dynamic light scattering imaging

Dynamic light scattering imaging (DLSI) is a technique that has recently been proposed, which makes use of *high-frame* rate full-field intensity measurements. The camera frame rates used in this technique typically exceed 20 kHz [80]. This high temporal resolution allows for the identification of the dynamic scattering regime at every pixel, which is assumed *a priori* in LSCI, MESI, LDF, and DLS, and which is a function of the amount of dynamic light scattering (and its relative proportion compared to static light scattering), the type of particle motion, and the approximate vessel size [89]. DLSI can be used with other methods to guide dynamic scattering model selection, or can it be used in isolation as a quantitative, full-field superficial flow detection technique. The high speed cameras that are required by DLSI are a key hardware limitation of this technique, and further research is required to characterise the noise arising from both high speed cameras and laser source instabilities [80].

2.3.5 Diffusing wave spectroscopy

We now move to a treatment of non-superficial coherent methods by firstly considering diffusing wave spectroscopy (DWS). DWS extends DLS to the multiple scattering limit, by modelling $g_{1d}(\tau)$ as an integral over photon paths, assuming uncorrelated motion at each scattering event [90]. In biological tissue, or more concentrated solutions, the incident light field is multiply scattered, and therefore the DLS theoretical model needed to be adapted to accommodate this. DWS, introduced before diffuse correlation spectroscopy (DCS), is equivalent to an integral formulation of DCS (see section 2.3.6) [91]; however, the name DCS has been chosen in the field of biomedical optics due to DWS having implications for both absorption and fluctuation spectroscopy [8].

Thus the DWS formulation of DLS, developed in the 1980s, allows for multiple scattering events to contribute to the measured $g_2(\tau)$ function. DLS and DWS use the same measurement hardware, but DWS permits the recovery of flow information at *depth* by

incorporating an SDS distance, ρ, into the measurement geometry, as is shown in Figure 2.10. The accumulated phase shift of many photon random walk paths through the sample is calculated for a range of delay times. Each scattering event from a dynamic scatterer contributes to the accumulation of the phase shift, and therefore the decay of the autocorrelation function. If scattering events within each random walk path are independent and uncorrelated, and when the DA is valid, $g_{1d}(\tau)$ is equal to the angle-averaged DLS signal due to a typical single scattering event, raised to the power N, where N is the number of steps in the random walk photon path.

The measured signal is then the integral of these single path signals over all possible photon paths. The field autocorrelation function from a single path is expressed as [19]

$$g_{1d}(\tau)_{\text{onepath}} = \exp^{-k_0^2 Y \langle \Delta r^2(\tau) \rangle / 3}, \tag{23}$$

where $Y = N \cdot (1 - \langle \cos\theta \rangle_N)$, and $\langle \cos\theta \rangle_N$ is the average value of the cosine of the scattering angle over N scattering events along any one path. When N is large, $\langle \cos\theta \rangle_N$ is equal to the ensemble average over all N, $\langle \cos\theta \rangle$, which is equivalent to the anisotropy factor, g, of the sample (see section 2.3.1.1).

The random-walk photon step length between two effectively isotropic photon scattering events is given by $l_s^* = 1/\mu_s'$, and the photon step scattering length is given by $l_s = 1/\mu_s$. If we let s represent the total pathlength associated with a particular photon path, then the total number of scattering events in this photon path is

$$N = \frac{s}{l_s}, \tag{24}$$

and the total number of isotropic random walk steps associated with the photon path is

$$Y = \frac{s}{l_s^*}. \tag{25}$$

By letting $P(Y)$ represent the probability of a photon path with a number of discrete random walk steps, Y, g_{1d} can then be calculated by integrating the contribution from each photon path of step length Y [19]

$$g_{1d}(\tau)_{\text{allpaths}} = \int_0^\infty P(Y) \exp^{-k_0^2 Y \langle \Delta r^2(\tau) \rangle / 3} \; dY. \tag{26}$$

In a highly scattering sample, this can be expressed as an integral over all allowed pathlengths by using the pathlength distribution, $P(s)$, [19]

$$g_{1d}(\tau)_{\text{allpaths}} = \int_0^\infty P(s) \exp^{-k_0^2 s \langle \Delta r^2(\tau) \rangle / 3 l_s^*} \; ds. \tag{27}$$

$P(s)$ can be derived from Monte Carlo simulation, analytical solutions to the DA,

and from experimental time-resolved spectroscopy measurements. Equation 27 can be solved for a particular geometry (e.g., infinite medium, semi-infinite medium, and slab) and experimental setup. DWS has been shown to be highly successful for modelling motions of scatterers in homogeneous and highly concentrated systems, such as colloids, foams, emulsions, and gels, but is less useful when modelling heterogeneous media, such as biological tissue [21].

2.3.6 Diffuse correlation spectroscopy

Boas and Yodh derived the correlation diffusion equation [21], which more accurately describes the propagation of the temporal electric field autocorrelation function in turbid biological tissue than its DWS counterpart does, and provides a natural framework for the study of tissue dynamics and tomography [19]. DCS is a differential formulation of DWS [90]. Analogous to Equation 8, the diffusion equation for photon electric field correlation (i.e., the correlation diffusion equation) can be derived, and, in a clinically relevant semi-infinite geometry (Figure 2.10) [22], the *unnormalised* solution for the autocorrelation function for dynamic scatterers is given by [21]

$$G_{1d}(\tau) = \frac{S_0}{4\pi D}\left[\frac{\exp^{-K(\tau)r_1}}{r_1} - \frac{\exp^{-K(\tau)r_2}}{r_2}\right]. \tag{28}$$

The *normalised* temporal electric field autocorrelation function is then [13]

$$g_{1d}(\tau) = \frac{G_{1d}(\tau)}{G_{1d}(\tau = 0)}, \tag{29}$$

where, in Equation 28,

- S_0 is the optical source intensity;
- D is the optical diffusion coefficient, $\frac{1}{3(\mu_a+\mu_s')}$;
- $K(\tau) = \sqrt{3\mu_a\mu_s' + \mu_s'^2 k_0^2 \langle \Delta r^2(\tau)\rangle}$ is the decay constant;
- $z_0 = 1/\mu_s'$ is the depth into the medium at which the collimated source is approximated as a positive isotropic source;
- ρ is the distance between the optical source and detector;
- $R_{\text{eff}} = -1.440n^{-2} + 0.710n^{-1} + 0.668 + 0.0636n$ is the effective reflection coefficient and accounts for the reflective index mismatch between air (n_{out}) and tissue (n_{in}), where $n = n_{\text{in}}/n_{\text{out}}$.
- $z_b = \frac{2z_0}{3}\frac{(1+R_{\text{eff}})}{(1-R_{\text{eff}})}$, $-z_b$ is the position at which there should be a signal size of zero to fulfil the extrapolated boundary condition [63];

- $r_1 = \sqrt{z_0^2 + \rho^2}$ is the distance between the detector and an approximated positive isotropic imaging source;
- $r_2 = \sqrt{(2z_b + z_0)^2 + \rho^2}$ is the distance between the detector and an approximated negative isotropic imaging source located at position $z = -(z_0 + 2z_b)$.

A value for $\langle \Delta r^2(\tau) \rangle$ can be extracted from measured data, by fitting to either a Brownian or a convective motion model of Equation 29, or a linear combination of the two, assuming that [92]

$$\langle \Delta r^2(\tau) \rangle = 6D_b\tau + \langle \Delta V^2(\tau) \rangle \tau^2. \tag{30}$$

Figure 2.10 describes the method of images and the notation that is used in a semi-infinite DCS geometry model when ensuring an extrapolated-zero boundary condition (see Section 2.3.1.3).

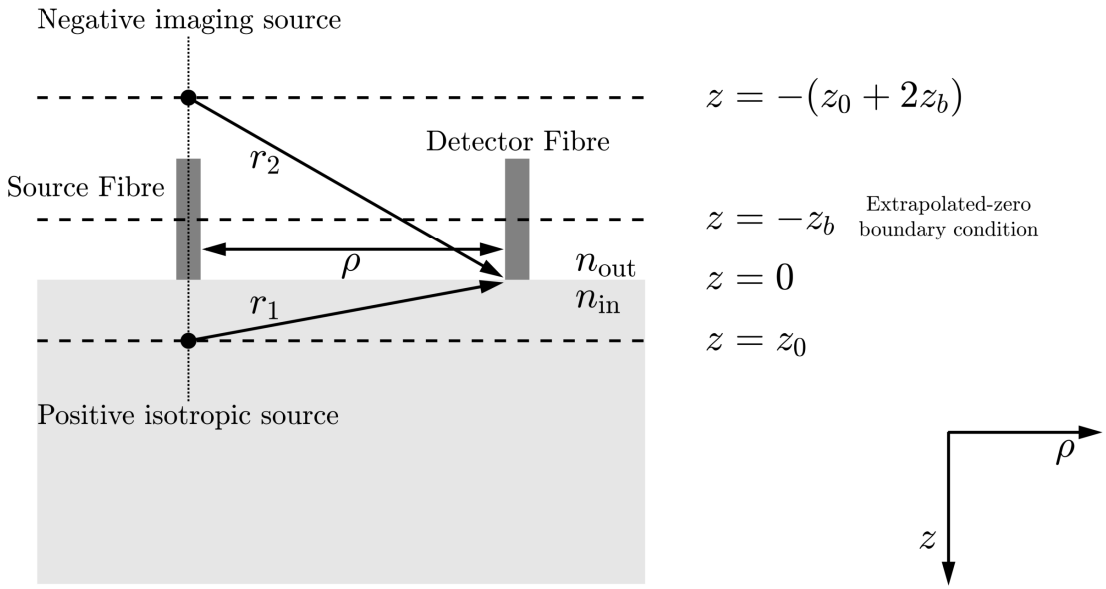

Figure 2.10: Semi-infinite geometry model and notation used in DCS measurements. Adapted from [19].

Diffusing light is primarily absorbed when crossing large arteries and veins, and therefore DCS is most sensitive to the motion of scatterers in the *microvasculature* (capillaries, arterioles, and venules) rather than macrovasculature [8]. Microvasculature is convoluted and the distribution of the direction of velocities of RBCs can therefore be assumed to be isotropic. Previous authors have found that the Brownian model fits observed data more precisely than the convective flow model in many biological tissues [19].

D_b can be used as a BFI parameter, although it has units of cm^2/s, rather than the more commonly encountered blood perfusion unit of ml/100g/min. D_b is also a relative, rather than an absolute, measure. Relative change in BF, $r\text{BF} = \text{BFI}/\text{BFI}_0$, where BFI_0 is the baseline measurement of BFI, acquired by DCS measurement has been shown

to agree with relative changes in absolute BF as measured by gold standard techniques, such as ASL-MRI [4]. Additionally, the use of DCS/NIRS hybrid systems, to measure NIRS derived StO_2 and DCS derived CBF, can be utilised to provide quantitative measurement of cerebral metabolic rate of oxygen extraction ($CMRO_2$), and its continuous noninvasive inference in this context relies on fewer assumptions than when using NIRS alone [8]. Local $CMRO_2$ is an important physiological parameter to monitor, as it is a function of oxygen saturation of arterial and venous ends of the local cerebral circulation, as well as CBF itself. Overall, this provides a more robust picture of brain health [4]. Validation studies show that DCS measurements of BF are in close agreement with results obtained by theoretical expectation, computational simulation, and other biomedical imaging modalities [19].

A typical DCS system requires only one wavelength of NIR light to operate (commonly ∼785 nm), and can be made to be very compact due to the advent of solid state laser technology. A long coherence length (∼10m) laser light source is delivered through a multimode source fibre. Single-mode or few-mode optical fibres are used to collect photons from a single/few speckles, as far away as 2.5 - 3.5 cm. Fast photon-counting avalanche photodiodes (APDs) can be used as detectors, as can photon multiplying tubes (PMTs), or single photon avalanche detectors (SPADs). A correlator board receives the intensity output from the photodetector and then computes $g_2(\tau)$, typically using the multi-tau autocorrelation algorithm [19]. A schematic of the entire DCS measurement process is shown in Figure 2.11.

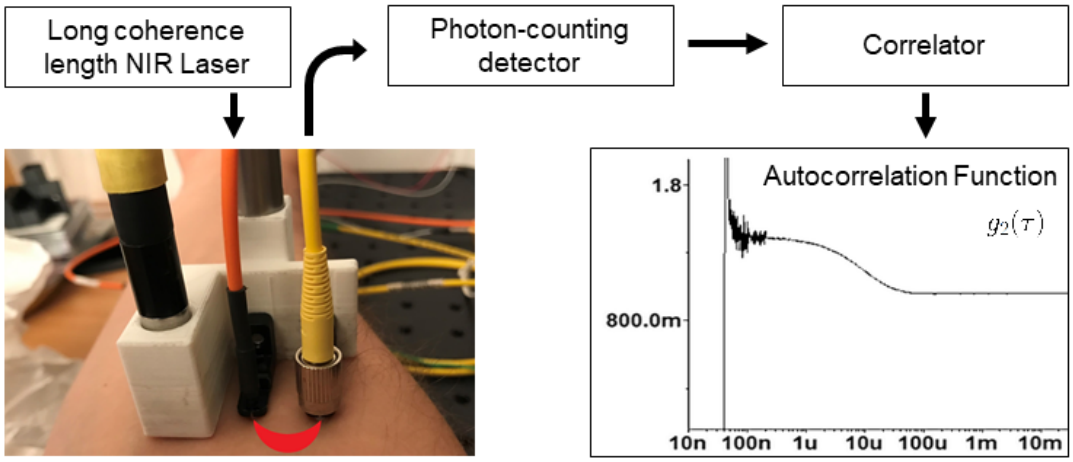

Figure 2.11: Schematic overview of a DCS system and measurement pipeline.

2.3.6.1 Key limitations

The conventional implementations of DCS that have been described typically employ single-mode photon counting techniques, with an associated high cost of detection components. Such methods are limited by low light throughput [4] in a single-mode, placing

a minimum limit on the detection time [93]. Increasing penetration depth requires the use of larger SDS distances, which will decrease the available SNR further (by increasing the number of absorption and scattering events, since the attenuation of NIR light by these two mechanisms is in the order of 10 dB/cm [94]), and this can be worsened by the presence of hair or darkly pigmented skin.

Increasing acquisition time can ameliorate this situation but leads to a reduction in temporal resolution. Taking the average of many single-mode detection fibres bundled together is an expensive option that requires many photon counting detectors and can increase complexity of system integration. Improved collection optics, the use of few-mode detection fibres, and increasing the amount of light delivered to the tissue can also help to improve SNR [4, 95, 96]. However, patient safety limits [20] must be adhered to, which necessitates an optical source of sufficiently large diameter and low power rating. All the above characteristics limit the applicability of conventional homodyne DCS in portable continuous monitoring applications to which optical methods are otherwise well suited.

Light collection efficiency and SNR increase with the effective number of detected modes, N. SNR also increases with β, but this quantity scales as $1/N$ for each detected mode due to the loss of coherence of g_1. In typically non-ideal situations, SNR may be optimised by using a single-mode detector fibre; however, if the optimisation of temporal resolution is of interest, then a few-mode detector fibre can be used [97]. The use of a single-mode fibre in a conventional DCS experiment will lead to a maximum β value of 0.5, due to the two orthogonal electric field components collected by the fibre. The recorded value of β will likely be less than this due to variations in light coherence, laser stability, stray light, detector stability, and fibre-tissue coupling [68]. This value of β can be doubled by placing a polariser in front of the detector fibre.

DCS offers the ability to be able to perform safe, noninvasive, and continuous bedside measurements of superficial microvascular CBF, with a relatively high temporal resolution (up to 100 Hz) [19]. However, it suffers from poor spatial resolution (which worsens with depth) and depth penetration (a general rule of thumb in diffuse optics is that a banana-shaped region of depth equal to one half to one third of the optical SDS distance is sampled [4, 8]). The main limitation of DCS is that a trade-off exists between the SNR and imaging depth, and thus brain specificity, of this technique [23]. Additionally, DCS is also susceptible to superficial extra-cerebral signal contamination, and the measurement of absolute CBF with this technique still remains challenging [5]. DCS also depends on the accurate measurement of μ_a and μ_s' to provide a precise assessment of CBF, and it is also limited by low SNR due to single-mode detection (especially when using large SDS values, in the presence of hair, and in patients with dark skin) and susceptibility to motion artefacts.

Despite these disadvantages, DCS has important potential applications in clinical

monitoring [36], as well as in neuroscience and the development of a noninvasive brain-computer interface [10]. Previous authors have noted that improvements to increase SNR, depth penetration, and both spatial and temporal resolution will assist the development of DCS functional experiments, as well as expand the range of uses for DCS in clinical monitoring [4]. The utility of high-frame rate ($\sim$20 Hz) DCS measurements, compared to the frame rates of 0.3 to 1 Hz that are currently used, has also been discussed [22]. These benefits include improved monitoring of cerebrovascular autoregulation dynamics, more robust identification of motion artefacts, and increased throughput that could enable high spatial resolution with fewer detectors.

The investigation of novel approaches to improve the sensitivity of DCS to CBF has therefore recently attracted interest from several research groups. Techniques including multispeckle detection strategies [10, 26, 27], time-domain DCS (TD-DCS) [28], DCS in the short-wave infrared region [29, 30], interferometric approaches [23, 31, 32], and acousto-optic modulation [33] have all been proposed. The remainder of Section 2.3.6 is therefore dedicated to the introduction of the wide variety of these approaches that have recently been published, which serves to inform the novel approach to DCS which is investigated in subsequent chapters of this thesis.

2.3.6.2 Multispeckle approaches

As described above, it has generally been accepted in the field of DCS that as the number of modes per detection fibre increases, the resulting gain in SNR due to increased photon intensity is negated by the subsequent loss of coherence and reduction in β. However, closer inspection of the DCS noise model [35] reveals one term in which the photon count has a higher weighting than β. Carp therefore proposed that the use of few-mode detection, rather than single-mode detection, could confer a slight SNR advantage at low photon count rates, and demonstrated a 20 % reduction in the standard deviation of relative BFI when switching from single-mode to few-mode detection, when making DCS measurements on an intralipid phantom with an SDS distance of 3 cm [98].

The SNR benefit that results from integrating multiple mutually incoherent speckle grains on the same photodetector does not persist beyond few-mode detection, and DCS therefore clearly benefits from a parallelised detection strategy, in which the detection of N speckle grains on multiple independent photodetectors will result in a $\sqrt{N}$ improvement in SNR, under the assumption of shot noise [27]. Dietsche *et al.* validated this approach by bundling together 28 stand-alone SPADs, which yielded a $1/\sqrt{28}$ reduction in noise [95]. Johansson *et al.* demonstrated a more compact approach by developing a 5×5 SPAD array for DCS detection, which resulted in improved SNR [99]. Subsequently, a 32×32 SPAD array was used for DCS detection by two groups [10, 27], which allowed Sie *et al.* to demonstrate a 32-fold increase in SNR with respect to traditional single speckle DCS, for $g_2(\tau = 4\mu\text{s})$ [10].

A third approach to multispeckle detection is to use conventional camera array detectors; however, current camera technology is limited by noise performance (when compared to SPADs) and by detection times, which are not short enough to fully characterise g_2 at very short lag times. By making use of the relationship [77, 100]

$$K = \left[\frac{2\beta}{T} \int_0^T \left(1 - \frac{\tau}{T}\right) \left[g_1(\tau)\right]^2 \, d\tau \right]^{1/2}, \tag{31}$$

where T is camera exposure time, Murali *et al.* demonstrated that by making measurements of K for various values of T, it is possible to recover $g_1(\tau)$ using low-cost and low-frame rate cameras [26, 83, 101]. With regard to compensating for camera noise performance, interferometric approaches have recently been proposed, and these are discussed in Section 2.3.6.4. Care must be taken when using multimode fibres for detection, as these fibres are sensitive to motion caused by environmental vibrations, for example [98].

2.3.6.3 Long wavelength approaches

Compared to a more commonly used wavelength of 785 nm, using a design wavelength of 1064 nm confers an SNR advantage in DCS systems. Light suffers from less optical scattering events at this wavelength, where a local minimum in water absorption combined with lower haemoglobin absorption also occurs, which results in an increase in photon availability [102]. Maximum permissible exposure limits are also higher at 1064 nm, meaning that roughly 2.5 - 4 times more optical power can be used [98]. The decrease in scattering also results in a slower decay of the autocorrelation curve, which moves g_1 into longer and less noisy timescales. By considering this overall photon budget, Carp *et al.* demonstrated that at 1064 nm, 13, 10.5, and 7 times more photons will be detected than at 765, 785, and 850 nm, respectively [29]. These authors note that the reduction in scattering that occurs at 1064 nm results in a *reduced* sensitivity to motion; however, this is more than compensated for by the advantageous photon budget at this wavelength. It is of note that the low haemoglobin absorption that occurs at 1064 nm makes this choice of wavelength impractical for NIRS experiments.

The main limitation that prevents the implementation of DCS at 1064 nm is a lack of suitable detector technology. For example, silicon SPADs have a photon detection efficiency (PDE) of 64 % and 54 % at 765 and 850 nm, respectively, but which drops to 3 % at 1064 nm [29]. Alternatively, InGaAs SPADs have a PDE of $\sim$32 % at 1064 nm; however, these detectors have unacceptably long afterpulsing in the region where g_2 starts to decay (i.e., 1 - 10 μs) [30]. Potential solutions to this afterpulsing problem include custom detector designs, and cross-correlation approaches using two detectors [29, 32, 103]. A second detector technology that is suitable for 1064 nm is superconducting nanowire single-photon detection (SNSPD). SNSPD detectors possess several

advantages over InGaAs SPADs, including shorter dead time (<50 ns), better timing resolution (<80 ps), an extremely favourable dark count rate of 1 count per second (CPS), a PDE of >80 % at 1064nm, and no afterpulsing issues. Ozana *et al.* achieved an SNR gain of 16, for $g_2(\tau = 4\mu s)$, when making *in vivo* measurements on the forehead of 11 human subjects with an SDS distance of 25 mm, compared to DCS at 850 nm using silicon SPAD detection [30]. However, SNSPD detectors are expensive, bulky, and loud, require cryostats to achieve an operating temperature of 2 - 3.1 K, and have a turn-on time of several hours, which limits their clinical application at present.

2.3.6.4 Interferometric approaches

The theory of DCS that has been considered so far has been restricted to homodyne detection (i.e., the self-interference of changing light fields) in which $g_2(\tau)$ is related to the motion of the sample by the Siegert relation (Equation 16). An interferometric DCS (iDCS) system may be constructed by modifying a homodyne DCS setup with a pair of fibre couplers, to create a Mach-Zehnder interferometer. iDCS works by using the reference arm of the interferometer to coherently amplify the speckle fluctuations of the sample arm, and the expression for $g_2(\tau)$ can then be found as [32]

$$g_2(\tau) = 1 + \beta \left(1 - \frac{I_R}{I_T}\right)^2 [g_1(\tau)]^2 + 2\beta \frac{I_R}{I_T} \left(1 - \frac{I_R}{I_T}\right) g_1(\tau), \tag{32}$$

which can be simplified to

$$g_2(\tau) = 1 + \beta_1 [g_1(\tau)]^2 + \beta_2 g_1(\tau), \tag{33}$$

where I_R is the reference intensity, and I_R / I_T is the fractional reference intensity, where $I_T = I_s + I_R$ is the total intensity, and I_S is the sample arm intensity. A caveat of this technique is that any laser intensity instability will have a larger influence on $g_2(\tau)$ for an interferometric measurement [98]. Using silicon SPADs and a 785 nm laser, Robinson *et al.* used iDCS to demonstrate an improvement in the SNR of $g_1(\tau)$ by approximately a factor of 2 at each time lag [32]. These authors also showed an up to 80 % reduction in the variability of measured BFI using this technique.

Interferometric techniques are beneficial in that they can compensate for detector nonidealities (e.g., afterpulsing, read noise, and dark noise) [32], they are robust to environmental noise (such as ambient light that is present in the clinical environment) [98], and they allow for effective measurement even in the presence of very low signal levels, allowing for the measurement of CBF within short acquisition times in low-light conditions [37]. This means that less expensive detectors with sub-optimal noise characteristics can be used for interferometric detection.

As such, an interferometric diffusing wave spectroscopy (iDWS) system has recently

been described which makes use of multimode fibre detection and a high speed line-scan CMOS camera capable of operating at 333 kHz [31]. The use of camera-based detection is conducive to multispeckle detection and the SNR advantage that this confers, and this system is capable of measuring ∼96 speckles simultaneously, meaning that clear BFI traces can be obtained using an SDS distance of 35 mm on the adult human head with an integration time of 0.1 s [24]. Although this technique is robust to the effects of ambient light, its sample rate is considerably slower than a conventional DWS system (which is typically in the order of ∼10 MHz) and it cannot resolve sample decorrelations shorter than 3 μs. Additionally, this approach does not have the temporal resolution necessary to sufficiently resolve ultrasound tagged photons (see Section 2.3.6.7 & Section 2.4.1), which are typically modulated by ultrasound pressure fields fluctuating in the range of 1 - 5 MHz [93].

The authors of the iDWS technique have also recently proposed multi-exposure iDWS (MiDWS), which makes use of a low-frame rate 2D CMOS sensor, and which measures brain BFI using an SDS of 30 mm and an integration time of 0.096 s, at a lower cost per pixel than iDWS [23]. BFI measurement using holographic approaches, which are inherently interferometric, have also been documented, and these are introduced in Chapter 3.

2.3.6.5 Depth discrimination techniques

As DCS is a diffuse optical technique, it is limited by a lack of inherent depth discrimination within the illuminated region of each source-detector pair, and the CBF signal is therefore also prone to contamination by the extracerebral tissues which the light traverses. If robustness to extracerebral contamination is the main concern, then the measurement of BFI (i.e., DCS), rather than haemoglobin concentration (i.e., NIRS), will, in theory, provide a more effective signal. This is because optical fluctuations achieve 3 - 5 times better brain specificity than optical absorption, as brain BFI exceeds extracerebral BFI by 6 - 10 times, while the corresponding ratio for haemoglobin concentration is 2.5 times [24]. However, this analysis relies on the SNR of DCS and NIRS being comparable [29]. NIRS, which does not rely on coherence, can measure many incoherent modes using large detectors, and this technique can therefore more easily achieve a higher SNR than DCS. Therefore, changes to improve the SNR of DCS will help to realise this theoretical like-for-like advantage that DCS has over NIRS.

One method to account for extracerebral tissue is to switch from the traditional semi-infinite geometry model, which is commonly used in DCS, to a multi-layered (typically two or three layered) geometry model [104]. Although this is an effective technique, these models rely on accurate prior knowledge of the optical properties and thickness of each layer. Alternatively, Selb *et al.* proposed to remove the contribution of extracerebral contamination via a superficial regression technique, in which a fraction of the BFI of

a short SDS pair is subtracted from the BFI of a corresponding long SDS pair [36]. These authors removed a fixed contribution of 70 % of the short SDS BFI (i.e., CBF = BFI_{long} - 0.7 $\times$ BFI_{short}), and noted that this technique could be optimised through further measurements and modelling studies, and also by optimisation of the DCS probe location based on observation of a patient's prior CT or MRI scans. A natural extension of this technique is the principle of diffuse correlation tomography (DCT), in which a 3D volumetric image of BFI may be reconstructed based on intensity measurements acquired using arrays of sources and detectors [35]. This is analogous to the extension of NIRS to DOT, the technique described in Section 2.3.2, which reconstructs 3D volumetric images of haemoglobin concentration changes.

Probe pressure modulation is an alternative technique which makes use of a two-layer model (i.e., extracerebral and cerebral layers), with measurements acquired at multiple optical probe pressures and multiple SDS distances, and which does not require prior anatomical information [105]. By exploiting the fact that variations in optical probe pressure will induce variations in extracerebral BFI, whilst cerebral BFI remains constant, these authors were able to isolate the contribution to BFI of the cerebral layer.

Other depth discrimination approaches have also been proposed, including TD-DCS (see Section 2.3.6.6) and acousto-optic techniques, which make use of the ultrasound tagging of light (see Section 2.3.6.7 & Section 2.4.1).

2.3.6.6 Time-domain approaches

Aside from contamination by extracerebral tissue, one of the other major limitations of DCS is the need to know the optical properties of tissue to accurately quantify BFI. TD-DCS is a time-of-flight (TOF) resolved method that enables deep tissue BFI measurement with depth discrimination at short SDS distances, whilst simultaneously acquiring tissue optical properties [28]. In this technique, each detected photon is associated with two measurements: the TOF from source to detector to obtain the TPSF, and the absolute arrival time to obtain g_2. Optical properties can be extracted from the characteristic properties of the TPSF (see Section 2.3.1.3). Then, by using a train of long coherence length laser pulses, autocorrelation functions can be evaluated at different time gates of the TPSF, and flow parameters can then be fit to measured g_2 functions arising from early and late arriving photons (i.e., short and long photon paths, respectively), which thus provides depth discrimination. Due to the decreased SDS distances that are used, TD-DCS affords both better depth sensitivity and improved spatial resolution than continuous wave DCS (CW-DCS) [98].

Compared to CW-DCS, the measurement duty cycle of TD-DCS is decreased by a factor of 50, due to the need for pulsed illumination [28]. Additionally, the intrinsically lower coherence of a pulsed source results in lower SNR. TD-DCS performance is strongly impacted by the system instrument response function (IRF), the selection of

time gates that are used, and the temporal shape of the pulsed laser source [106]. Satisfying the TD-DCS requirements of a picosecond pulsed laser with a long coherence length, adequate illumination power, and a narrow IRF remains challenging [107].

An alternative technique, interferometric near-infrared spectroscopy (iNIRS), also quantifies TOF resolved dynamics, and this is introduced in Section 2.3.7.

2.3.6.7 Other approaches

Robinson *et al.* have presented an approach toward enabling quantitative depth selective flow measurements in DCS by using acousto-optic modulation (AOM-DCS) [33]. This is a hybrid technique that allows for improved spatial resolution of the optical signal based on knowledge of the area that is insonified by ultrasound, owing to the ultrasound tagging of light (UTL). These authors presented a quantitative model for flow detection using CW ultrasound, based on the principle that both $g_2(\tau)$ and the amplitude of the modulation of $g_2(\tau)$ decay with time [108]. More complex spatiotemporal distributions of ultrasound (e.g., focused, pulsed, encoded, or overlapping pressure fields using two ultrasound transducers) are required to resolve flow with both better spatial and temporal resolution. AOM-DCS is part of a broader group of methods, known as AOT, which is discussed more fully in Section 2.4.1. The interaction of the ultrasound generated acoustic radiation force (ARF) and the DCS signal has also been investigated [109].

With a view to developing a low-cost and wearable DCS system, Biswas *et al.* have recently presented a portable DCS system which makes use of a small-form factor and fibre-less embedded diode laser [110]. The same group has also developed a system to obtain pathlength resolved DCS measurements (similar to TD-DCS and iNIRS) by using a Mach-Zehnder interferometer with a reference arm that has an adjustable length [111]. By scanning the length of the reference arm, $g_2(\tau)$ may be evaluated for various photon pathlengths. Additionally, the average intensity as a function of pathlength can be used to generate a TPSF, from which tissue optical properties may be obtained.

Deep learning techniques have recently been employed with a view to reducing the computational demand of DCS experiments [112]. Fitting measured $g_2(\tau)$ data to analytical or Monte Carlo models to extract BFI can be computationally demanding and suffers from inaccuracy in low SNR environments. These authors used a deep learning model that resulted in a 23-fold increase in the speed of BF quantification, which further enables the real-time and accurate quantification of BFI using DCS. DCS denoising algorithms, including the use of support vector regression, have also been explored [113]. Within the context of DCT image reconstruction, learning approaches have also been employed to compensate for the decreased spatial resolution resulting from the ill-conditioned and ill-posed nature of the inverse problem, resulting in an imaging depth of 5 mm at 2.5 Hz using a 32×32 SPAD array [114].

2.3.7 Interferometric near-infrared spectroscopy

FD-NIRS and DCS instruments can be combined into one instrument to concurrently measure both optical and dynamical properties; however, this technique cannot provide TOF resolved DCS measurements. To overcome this limitation, iNIRS combines TD-NIRS and DCS into a single modality to simultaneously extract sample optical properties and TOF resolved sample dynamics. This is achieved through the analysis of a spectral interference fringe pattern, which is measured using a Mach-Zehnder interferometer with a frequency-swept narrow linewidth laser [115]. Photons with shorter pathlengths will produce a lower frequency fringe pattern, and arrive at the detector earlier than photons with longer pathlengths, which will produce a higher frequency fringe pattern.

The TOF difference between light propagating through the sample arm and the reference arm of the interferometer can be obtained by Fourier transforming the frequency resolved interference signal. This yields a complex mutual coherence function, $\Gamma_{rs}(\tau_s, t_d)$, between the sample and reference fields, where τ_s is TOF and t_d is delay time. From a time series in t_d, a 2D TOF resolved optical field autocorrelation function, $G_1^{\text{iNIRS}}(\tau_s, \tau_d)$, can be obtained

$$G_1^{\text{iNIRS}}(\tau_s, \tau_d) = \langle \Gamma_{rs}^*(\tau_s, t_d)\Gamma_{rs}(\tau_s, t_d + \tau_d)\rangle_{t_d}, \tag{34}$$

where τ_d is time lag. The measured $G_1^{\text{iNIRS}}(\tau_s, \tau_d)$ is related to the intrinsic $G_1(\tau_s, \tau_d)$ by convolution with the system IRF,

$$G_1^{\text{iNIRS}}(\tau_s, \tau_d) = G_1(\tau_s, \tau_d) * \text{IRF}(\tau_s). \tag{35}$$

$G_1^{\text{iNIRS}}(\tau_s, 0)$ is equivalent to the TPSF that is measured from TD-NIRS. $G_1^{\text{iNIRS}}(\tau_s, \tau_d)$ provides TOF resolved dynamics, which, when integrated over τ_s and normalised, yields $g_1(\tau_d)$, as per a conventional DCS experiment.

Therefore $G_1^{\text{iNIRS}}(\tau_s, \tau_d)$ is a rich data set which provides both sample optical properties and TOF resolved sample dynamics, and the authors of this technique argue that it is the most informative diffuse optical method to date. Advantages of iNIRS, when compared to TD-DCS for example, are that iNIRS does not require pulsed lasers (which result in a reduced coherence factor) or single photon counting detectors, and TD-DCS is also sensitive to ambient light. iNIRS also accesses the field autocorrelation directly, therefore obviating the Siegert relation, and the constraints therein. The main drawback of iNIRS, when compared to incoherent TD-NIRS for example, is that iNIRS is a coherent modality which, like DCS techniques, suffers from moderate light throughput.

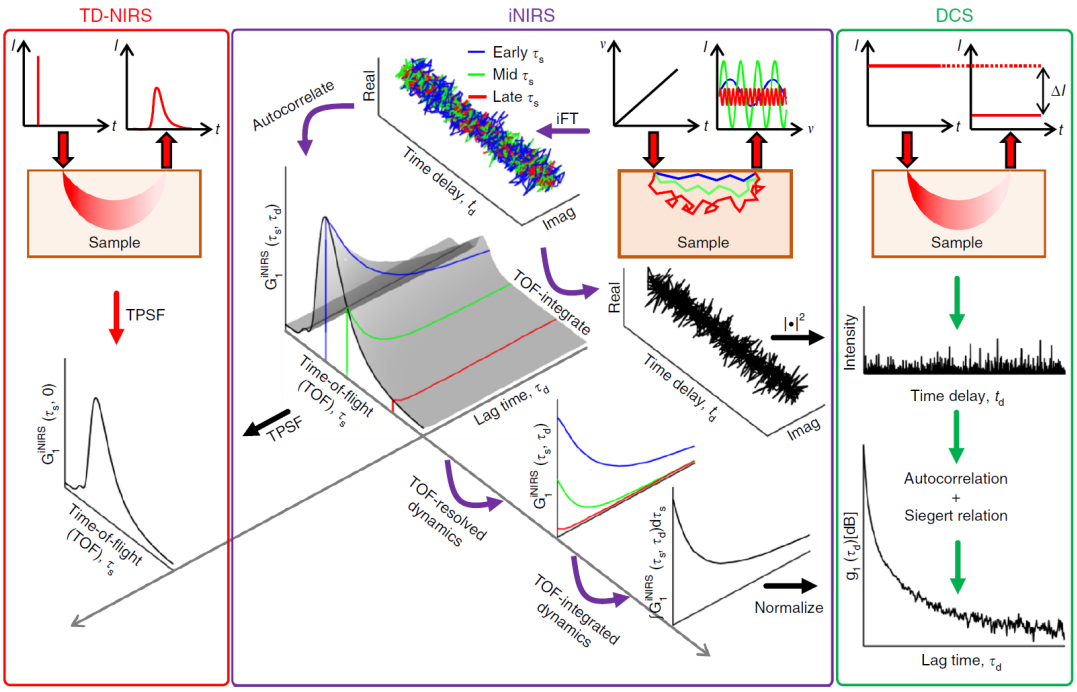

Figure 2.12: Due to the fact that the laser frequency is swept, photons travelling deeper into tissue, which take a longer time to travel through the sample arm of the interferometer, generate a larger beat frequency upon interference with the reference arm. Therefore, iNIRS encodes TOF, τ_s, as beat frequency. Autocorrelation of a time-series of mutual coherence functions yields $G_1^{\text{iNIRS}}(\tau_s, \tau_d)$, which can be used to obtain both TPSFs and TOF resolved dynamics. Reproduced with permission from [116] under the terms of a Creative Commons Attribution 4.0 License. © Kholiquov, Zhou, Zhang, Du Le, and Srinivasan 2020.

2.3.8 Speckle contrast optical tomography

Analogous to the extension from DCS to DCT, LSCI (Section 2.3.4.1) can be extended to speckle contrast optical tomography (SCOT). SCOT is a technique that enables deep BF measurements based on changes in laser speckle contrast over large channel counts [25], and merges the deep imaging capability of DCS with the low cost and high-frame rate detectors used in LSCI, enabling improved SNR and a broad field-of-view when compared with DCT, without being prohibitively expensive. Speckle contrast optical spectroscopy (SCOS) extends SCOT in one of three ways: using a fixed camera exposure time and varying the SDS distance, using a fixed SDS distance and varying the camera exposure time, or by varying both camera exposure time and SDS distance simultaneously [117].

In the implementations that have been described in the literature, SCOT is limited by the requirement of frame averaging, which typically requires 200 camera exposures, with a resulting temporal resolution in the order of ∼0.5 Hz [82]. Also, to obtain spatially coherent information (i.e., imaging rather than illumination), detector arrays must be mounted close to the sample to make use of free space detection. This is also prob-

lematic when hair occludes the field of view. Alternatively, expensive spatially coherent fibre bundles can be used to transmit light from the sample to the detector, to decrease the form-factor on the detection side of the instrument, and also to comb through hair. However, fibre bundles suffer from fragility and tend to accumulate dead pixels over time.

2.3.9 Diffuse speckle contrast analysis

Diffuse speckle contrast analysis (DSCA) can be thought of as a modality that combines DCS and LSCI, and which is sensitive to deep flow [118]. DSCA differs from LSCI in that an SDS distance is specified, which enables deep flow measurement, and DSCA differs from DCS in that low-frame rate camera detection is used.

Due to the single-mode detection that is used in DSCA, only one speckle is captured per camera frame, and speckle contrast must be calculated temporally over $\sim$60 camera frames. This yields a flow measurement frame rate that is 1/60 of the camera frame rate. By switching to multimode detection, the same authors developed diffuse speckle pulsatile flowmetry (DSPF), which allows speckle contrast to be calculated spatially, rather than temporally, within each camera frame [100]. This means that the flow measurement frame rate is increased by a factor of 60 compared to DSCA, and is equal to the camera frame rate, which was 300 Hz in the paper that describes DSPF.

Multimode fibres may be less likely to be used for coherent detection due to problems with movement artefacts, and the non-ideality of the output speckle pattern. Bi *et al.* corrected for this latter effect by normalising each speckle pattern by the average background intensity profile of the multimode fibre tip over 6000 camera frames, a process requiring about 20 seconds [100]. The authors note that this average image would need to be recalibrated each time the multimode fibre moves.

2.4 Hybrid methods

The desire to simultaneously exploit the depth penetration and spatial resolution of ultrasound, whilst also making use of the high levels of contrast, spectroscopic specificity, and functional imaging information available with optical techniques, has led to the recent development of 'coupled-physics' or 'hybrid' imaging techniques. Two hybrid modalities have emerged that make use of the interplay between sound and light: acousto-optic tomography (AOT) and photoacoustic tomography (PAT). Both of these imaging techniques aim to improve upon either solely optical or ultrasound methods, and combine the two modalities to attempt to reduce the effects of the constraints associated with each method, namely weak contrast and limited specificity in the case of ultrasound, and poor depth penetration and spatial resolution in the case of diffuse optical imaging (as has been described in Section 2.3). The specific application of AOT to

enhance DCS measurements [33, 108] was introduced in Section 2.3.6.7. The purpose of Section 2.4.1 is therefore to introduce AOT approaches within a more general context.

2.4.1 Acousto-optic tomography

AOT, also known as ultrasound-modulated or ultrasound-mediated optical tomography (UMT/UMOT), ultrasound assisted optical tomography, acousto-photonic imaging, or acousto-optic imaging, aims to achieve increased spatial resolution sensitive to optical absorption by creating an artificial ultrasound marker at some axial depth in the sample [93]. This marker is brought about by imposing a focused ultrasound beam on the sample under examination, meaning that the spatial resolution and sensitivity of this technique will be greatest in the region of the ultrasound focus. Photons which pass through the ultrasound beam are 'tagged' as their frequency is shifted away from the main optical carrier frequency. By recording the intensity of photons arriving at an optical detector that are modulated at the acoustic frequency, the relative number of photons that have travelled through the focus of the ultrasound beam can be calculated, and thus photon localisation in turbid tissue is achieved. AOT therefore improves upon diffuse optical imaging methods in terms of *spatial resolution*; improvements related to increasing depth penetration and SNR are discussed below.

Ultrasound tagging of light (UTL) was initially developed to provide 3D imaging of breast tumours by Marks *et al.* [119]. If a sample is illuminated with a laser of sufficiently long coherence length (dependent upon tissue thickness and optical scattering properties), then the intensity distribution measured at a photodetector will be a speckle pattern, as discussed in Section 2.3.1.4. When an ultrasound beam is focused into the tissue, this speckle pattern will become blurred (see Figure 2.13) due to the periodic compression and rarefaction of the tissue, which leads to changes in the optical pathlengths that are caused by two coherent mechanisms [93]:

- the local index of refraction, n, of the tissue is changed by periodic compression and expansion by the ultrasound beam, and photons diffracted by this refractive index grating will be shifted in frequency;
- the oscillation of optical scatterers, caused by propagation of the ultrasound beam, will mean that photons undergoing Rayleigh scattering will be frequency shifted. Although the contribution from each scatterer is only on the scale of nanometres, the effect is accumulative over the whole optical pathlength, and therefore it can have a significant effect.

Both of these mechanisms lead to the development of an acoustic sideband in the electric fields of modulated photons, which is either side of the optical carrier frequency.

This sideband is itself broadened due to the residual motions of these optical scatterers within the tissue. Thus, these mechanisms modulate the phase of photons passing through the focal region of the ultrasound beam, and they become 'tagged'.

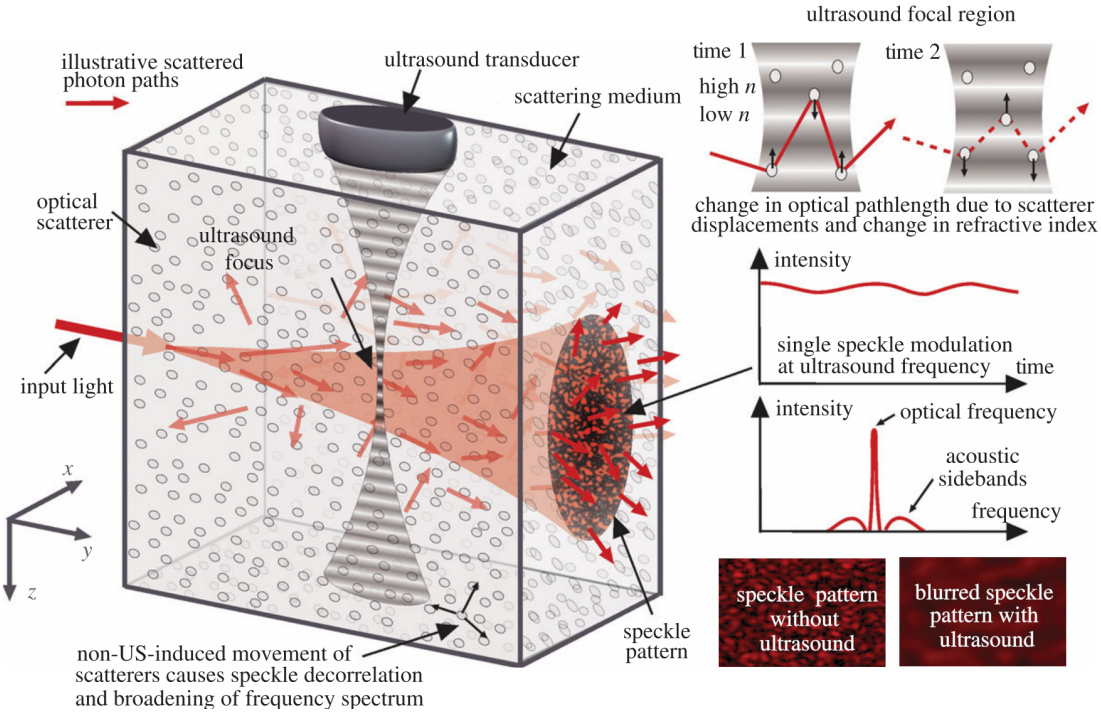

Figure 2.13: Origin of the acousto-optic signal. Reproduced with permission from [93]. © 2011 The Royal Society.

Resink *et al.* also detail four other incoherent phenomena which lead to UTL, but also describe how in many situations the variation in signal strength owing to these four mechanisms is often too low to be measured [120]:

- modulation of local optical properties, such as absorption;
- variation in position of scattering particles;
- variation in cross-section of scattering particles;
- variation in refractive index which causes Bragg diffraction patterns.

Ultrasound frequencies in the range of 1 - 5 MHz are typically used, as they provide a good compromise between depth penetration and spatial resolution (in terms of both axial and lateral resolution) [93].

Single-mode detection, using photodiodes (PDs) or PMTs for example [119], was one of the earliest reported strategies for AOT detection. However, the low levels of SNR available with single-mode detection, together with a low modulation depth at biologically safe ultrasound power levels, limits the viability of these single-point AOT

detection methods, especially *in vivo* [93]. To overcome the low SNR of single-mode detection, a confocal Fabry-Perot interferometer can be used to optically filter the incident background unmodulated light, so that the full dynamic range of the detector may be used. The advantages of this technique are that a large etendue[2] may be achieved, and that the technique is not affected by speckle decorrelation due to its use of incoherent light [93]. However, it is more effective at higher ultrasound modulations, which provide shallower imaging depths, and may therefore be more suited to thinner tissue samples. Gunther and Andersson-Engels describe that this technique is very sensitive to light incidence angle, and also describe that reports of its use within the field of AOT have not been published since 2011 [18].

Other techniques to enhance the sensitivity to the acoustic sideband include the use of spectral hole burning (SHB) and photorefractive (PR) crystals. The SHB technique uses a high-power pump laser to burn a spectral hole in a SHB crystal, which permits the passage of acoustically modulated photons and absorbs any incident unmodulated background light [18]. SHB crystals may be used at biologically relevant wavelengths around 800 nm, and the spectral hole, once burnt, persists for about 10 ms [93]. The main disadvantage of this technique is the cryogenic cooling that is required to keep the rare earth crystals at $\sim$4 K [120].

One variation of the group of PR crystal techniques involves frequency shifting a reference arm by the ultrasound modulation frequency, so that only the acoustically modulated component of the signal arm and the reference arm write the refractive index grating in the PR crystal. This results in the wavefronts of the shifted reference arm being matched with the wavefronts of the modulated signal, and a photodetector then records the heterodyne amplified modulated component of the signal arm [120]. The signal contribution for each speckle is then integrated on the photodetector, increasing both the etendue and the SNR of the experimental setup. However, one of the main challenges of this technique is the PR response time of the crystals (0.1 - 150 ms) [120], which must be fast relative to tissue decorrelation time (0.1 - 1.0 ms). In conjunction to having a sufficiently fast response time, PR crystals must also be responsive at biologically relevant wavelengths (i.e., in the NIR window). It has also been argued that the use of a strong reference beam, which is used to induce a large heterodyne gain term, may lead to an increased level of scattered background light at the photodetector [93]; however, the same could be argued of any interferometric technique.

Analogous to the multispeckle approaches that have been described within the context of DCS (Section 2.3.6.2), parallel detection techniques also boost measurement SNR within the context of AOT. These techniques can make use of the spatial statistics of ultrasound modulated speckle [18], parallel lock-in speckle detection [120], and heterodyne detection using digital holography [93] to infer flow within the insonified region.

[2]Etendue is the product of the surface area of detection and the detection solid angle [120, 121].

A concise introduction to the application of digital holography to multispeckle detection in general is given in Chapter 3.

As with traditional focused ultrasound imaging, the lateral resolution of AOT is equivalent to the width of the focal area of the ultrasound beam, W, which is determined by [46]

$$W = 1.41\lambda\frac{F}{2a}, \tag{36}$$

where λ is the wavelength of the ultrasound beam, F is the focal length, and a is half the width of the ultrasound array. Lateral resolution can thus be improved by using a higher frequency ultrasound transducer, but this will be at the expense of available imaging depth.

In general, axial resolution may be achieved by adding a time-dependence to the ultrasound frequency, phase, or amplitude, and typically axial resolutions of $\sim$1 mm can be achieved [93]. At the most basic level, an axial scan of a tissue sample may be achieved by resolving detected modulated signal intensity as a function of time during the propagation of pulsed ultrasound wavefronts. These short ultrasound pulses consist of a small number of ultrasound cycles, and will arrive at a depth of interest, z, at time $t_{\text{start}} = z/c_{\text{a}}$, where c_{a} is the speed of sound in the sample. The ultrasound pulse will finish passing through z at time

$$t_{\text{end}} = t_{\text{start}} + \frac{N\lambda}{c_{\text{a}}}, \tag{37}$$

where N is the number of cycles per ultrasound pulse. By recording the modulated AOT signal intensity between t_{start} and t_{end}, only the photons that have been modulated at a depth $z \pm (N\lambda)$ will be recorded.

This then presents a trade-off between axial resolution and SNR, with higher axial resolution requiring shorter ultrasound pulses, with consequently less available photons within a shorter time-gate, and a larger spread of energy in the frequency domain, which may not match the available bandwidth of the detector appropriately. The major drawback of this technique is that it is only possible using fast detectors.

The frequency sweep technique is the first method that was implemented to achieve axial resolution in the field of AOT [122]. This technique uses a short, chirped ultrasound wave, the frequency of which varies linearly with time according to

$$f(t) = a_{\text{start}} + bt, \tag{38}$$

where $f(t)$ is the frequency sweep at time t, a_{start} is the starting frequency, and b is the sweep rate. Photons along the axial acoustic axis are then modulated with a different frequency at each depth, and a Fourier transform of the detected signal will encode axial

information as frequency. The axial resolution achievable with this technique depends on both the chirp repetition rate and chirp duration.

Randomisation of the phases of ultrasound and optical illumination is a technique adopted by Lesaffre *et al.* [123] to achieve axial resolution, and is sometimes known as acousto-optic coherence tomography. This group used a dataset containing 512 randomly selected phases of either 0 or π, with a period of 1 ms, to modulate the ultrasound transducer and the optical illumination source. A time delay, τ, was applied to the optical illumination according to $\tau = z/c_a$, where z is the depth of interest along the acoustic axis, at which point the ultrasound and optical phases will be correlated and only acoustically modulated photons will be detected using a heterodyne gain system. The axial resolution for this technique is related to both c_a and the time required to change phase (i.e., 1 ms/512 = 1.95 μs in the case of this example).

Other techniques to improve spatial resolution include: construction of a synthetic focus by superposition of many unfocused wavefronts to increase lateral resolution [120]; the use of CEUS (see Section 2.2.5); the use of two ultrasound transducers and dual ultrasound frequencies; coded ultrasound [1, 124]; and nonlinear second harmonic imaging and pulse inversion [18]. The detection of nonlinear ultrasound effects is associated with higher sample contrast and spatial resolution [93].

BF and the movement of scatterers within the ultrasound focal region will decrease the temporal autocorrelation of the photons that pass through it, which is equivalent to decreasing and broadening the amplitude of the acoustically modulated frequency sideband. Therefore, as BF within a region increases, the cross correlation between the incident ultrasound pulse and the detected modulated photons will decrease, and vice versa, which can be used to infer BF [125]. However, this measurement technique suffers from signal contamination and decorrelation by intermediate layers between the imaging depth and the transmission/reception plane, and therefore tends to incorrectly assess CBF due to the contribution from extra-cerebral tissues. This led to the development of the 'differential spectral width' method, which is able to determine both the location and amplitude of flow patterns [1]. By modulating a sample with pulsed ultrasound, the spectral broadening around the acoustic sideband due to BF at a range of sample depths can be be acquired. This yields a 2D spectrogram, in which the time delay is associated with depth, and the spectral broadening is associated with volumetric flow rate. An example of a 2D spectrogram is shown in Figure 2.14(A) for simulated data by Tsalach *et al.* [1].

The spectral width, SW, as a function of imaging depth can then be calculated by normalising the area under the spectrogram curve, AUC, by the amplitude at the central

ultrasound carrier frequency $A(f_{\mathrm{US}})$

$$SW = \frac{AUC}{A(f_{\mathrm{US}})}, \tag{39}$$

which is shown in Figure 2.14(B).

The spectral broadening at a given depth can then be deduced by subtracting spectral widths of adjacent layers, thus providing a measure of net broadening caused by the relevant tissue layer, i.e., 'local broadening', 'differential spectral width', or BFI. This can be calculated as the first derivative of SW with respect to imaging depth

$$\mathrm{BFI} = \frac{\partial(SW)}{\partial z}, \tag{40}$$

which is shown in Figure 2.14(C).

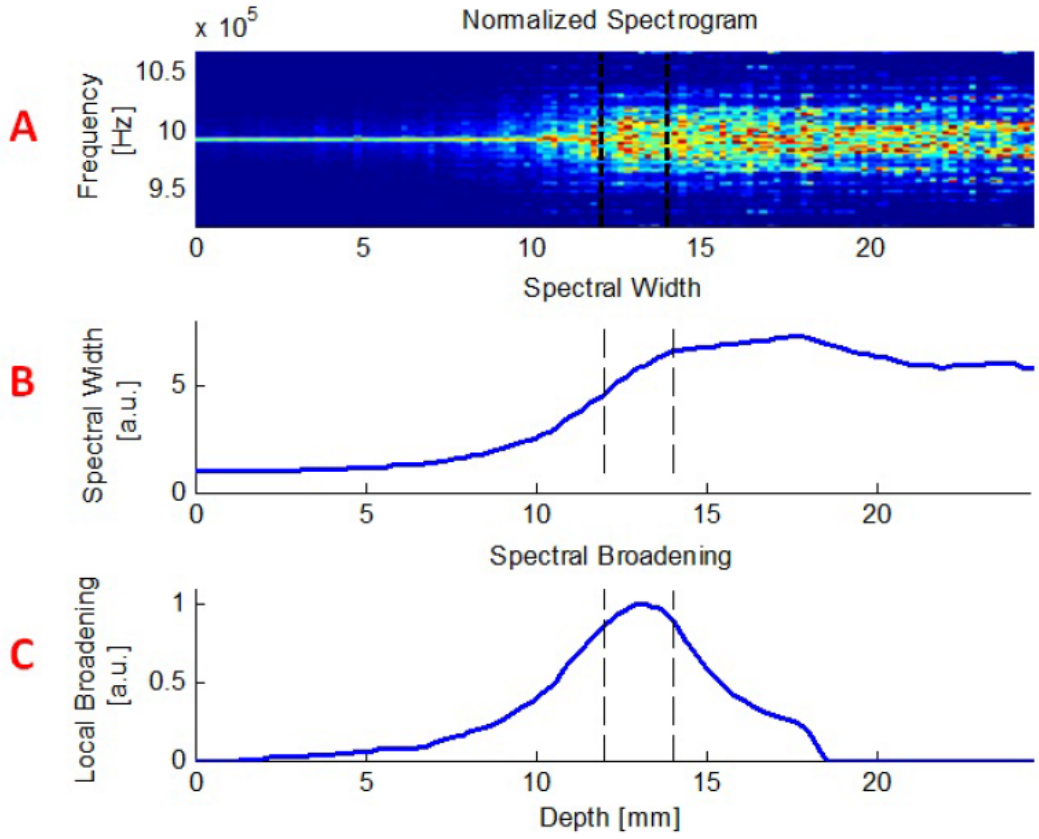

Figure 2.14: The differential spectral width method for simulated data. (A) Horizontal concatenation of power spectra yields a 2D spectrogram, in which colour denotes amplitude in arbitrary units. (B) The spectral width is the ratio of area under the curve and the amplitude at the ultrasound frequency, for each imaging depth. (C) BFI is the derivative of spectral width with respect to imaging depth. Reproduced with permission from [1]. © 2015 Optical Society of America.

The importance of depth-resolved flow measurement in AOT is highlighted by a recent study, which used the c-FLOW$^{\mathrm{TM}}$ AOT system (Ornim Medical Ltd), and found

that this device could indicate an apparently normally perfused brain in patients that had been pronounced brain dead [126]. The authors of this study attributed this to the failure of the device to remove signal contamination from superficial extra-cerebral flow, which can persist in the scalp after death, for example.

The first *in vivo* demonstration of an AOT signal was by Lev and Sfez in 2003 [127]. One of the main findings of this study is that *ex vivo* experiments suffer much less from speckle decorrelation noise than *in vivo* experiments. To the best of my knowledge there has been no published account of depth-resolved AOT CBF measurements being successfully made and validated *in vivo*. The main challenges for *in vivo* AOT applications are tissue decorrelation times and low light levels [120], and the compromises that must be made when addressing each of these two factors. Gunther and Andersson-Engels state that challenges facing AOT for *in vivo* imaging also include [18],

> 'improving resolution, reducing acquisition time, increasing contrast or SNR, increasing etendue, integrating relevant wavelengths for biological tissue, incorporating safety limitations, resolving optical and mechanical properties, and increasing imaging depth'.

Gunther *et al.* state that speckle contrast imaging, digital holography, SHB, and PR crystal systems hold the most promise for *in vivo* AOT imaging [128]. These authors highlight the promise of SHB systems, owing to their particularly high etendue, their immunity to speckle decorrelation noise, and their ability to efficiently suppress the unmodulated background light signal (which may be six orders of magnitude higher than the modulated light signal). SHB crystals with 60 dB suppression have been developed, but these have not yet been incorporated into AOT systems [129].

2.4.2 Photoacoustic tomography

PAT involves the use of a wide-beam laser pulse of a few nanoseconds duration, which is used to illuminate a sample, and which is then absorbed by chromophores. At this point the absorbed light is thermalised and converted to a pressure wave, which gives rise to an ultrasonic pulse [130]. This ultrasonic pulse can be measured by an array of ultrasound transducers on the surface of the sample. An image reconstruction algorithm can then be used to convert the measured acoustic pressure field into an initial acoustic pressure distribution, using a time reversal algorithm, for example, to produce a photoacoustic image [131]. The contrast in the image is related to optical absorption, and the benefit of recording ultrasound instead of diffuse light is that ultrasound is much less scattered than light in biological tissue.

A recent study has shown that AOT holds greater potential over PAT in terms of imaging depth, with simulated imaging depths of $\sim$6 cm and $\sim$3 cm, respectively, in

cardiac tissue [128, 132]. Additionally, for CBF measurements, there is the challenge of attenuation of ultrasound as it passes through the skull. In the case of AOT, *transmitted* ultrasound can be focused within the brain [133], which confers a significant advantage over the ultrasound *detection* of PAT.

PAT already has *in vivo* applications, but one of its main disadvantages in comparison to AOT is that the contrast in PAT is related to optical absorption, whereas AOT is sensitive to changes in absorption, scattering, and mechanical properties of tissue [18]. Additionally, when making BF measurements through the use of Doppler shift measurements, the comparatively long wavelength of the received ultrasound makes PAT relatively insensitive to the small optically generated Doppler shifts that are produced [76].

2.5 Chapter summary

This chapter serves to develop a description of the currently vacant niche for an inexpensive, continuous, noninvasive, portable, bedside, and non-ionising imaging/sensing modality with which to measure CBF. Of all the non-optical methods described, TCD has the greatest potential to fill this niche; however, TCD is highly operator dependent and measures macrovascular BF rather than making direct measurements of CBF itself.

Having offered a concise introduction to biomedical optics, in this chapter I have also described the various incoherent and coherent optical modalities which can be used to measure CBF, with a range of characteristic imaging depths. Diffuse optical techniques are required to image deeper into the brain; however, these techniques are marred by the low SNR that is associated with the SDS distances that are required to achieve deeper imaging. DCS is a promising CBF measurement technique, and many research groups have recently been investigating methods to improve the SNR, imaging depth, and spatial resolution of DCS. Such methods have included multispeckle, long wavelength, interferometric, depth discrimination, and time-domain approaches, and these methods inform the novel approach to DCS that is investigated in subsequent chapters of this thesis. iNIRS is perhaps the most comprehensive diffuse optical imaging modality to date, but it currently suffers from a lack of parallelised detection, which limits its application to the measurement of CBF.

AOT is an emerging hybrid imaging modality that makes use of the ultrasound modulation of light, and it has the potential to offer higher levels of SNR, imaging depth, and spatial resolution than purely diffuse optical methods. Despite early promise, spatially resolved flow measurement with both sufficient SNR and temporal resolution for *in vivo* AOT detection remains extremely challenging. Most of the research in the area of portable and non-invasive CBF measurement focuses on diffuse optical techniques.

3 Digital holography for *in vivo* multispeckle detection

3.1 Chapter contribution

In this chapter I introduce digital holography: an optical imaging modality that I propose can be incorporated into diffuse correlation spectroscopy (DCS) technology to make measurements of cerebral blood flow (CBF). After a brief introduction to digital holography in Section 3.2, I explain how this technique is particularly suitable for multispeckle detection, and describe previous examples of its use in biomedical optics in Section 3.3. I then introduce heterodyne parallel speckle detection (HPSD) in Section 3.4, which allows the measurement of the power spectral density (PSD) of an electric field using inexpensive low-frame rate cameras, simultaneously measured over multiple speckles, with narrow temporal frequency broadening. In Section 3.5, I give examples of the instrument response function (IRF) of an HPSD instrument, and describe how the Wiener-Khinchin theorem can be used to infer sample dynamics from HPSD measurements. This then allows me to pose the research question for this thesis, and some of the challenges to be overcome for *in vivo* detection, in Section 3.6.

3.2 Introduction to digital holography

Dennis Gabor proposed the concept of holography in 1948 [134]. Gabor recognised that when a mutually coherent reference wave, $A(x,y)$, of known amplitude and phase, interferes with the light scattered or diffracted by an object, $a(x,y)$, it is possible to record information about both the amplitude and phase of $a(x,y)$, even when using a recording medium which is sensitive to light intensity only. If we let $A(x,y) = |A(x,y)| \exp(i\phi(x,y))$ and $a(x,y) = |a(x,y)| \exp(i\psi(x,y))$, then the intensity of the sum of the two complex fields that is recorded is given by [135]

$$h(x,y) = |A(x,y)|^2 + |a(x,y)|^2 + 2|A(x,y)||a(x,y)| \cos(\phi(x,y) - \psi(x,y)) . \qquad (41)$$

The recorded interference pattern may be regarded as a hologram, and, provided that it is possible to separate each of the terms in Equation 41, $|A|^2 a(x,y)$ (or its conjugate, $|A|^2 a^*(x,y)$, the holographic twin-image) can be reconstructed by illuminating $h(x,y)$ with $A(x,y)$ or $A^*(x,y)$, respectively. An observer will then see a reconstructed 3D image of the object which displays all the effects of both perspective and depth of focus [136].

The term holography is used, as it is derived from the Greek words 'holos', meaning whole or entire, and 'graphein', meaning to write. As holography requires the use of a coherent light source, practical applications of optical holography only became possible with the invention of the laser in the 1960s. Holographic detection initially made use of

photographic films and plates, which require wet processing and are associated with a delay between recording and reconstruction steps. Digital holography, which involves digital sampling and *numerical* holographic reconstruction, obviates the need for wet processing and speeds up reconstruction times significantly.

The remainder of Section 3.2 is devoted to the demonstration of numerical holographic reconstruction using the Fresnel approximation as an illustrative example of digital holography. The Fresnel technique is the least computationally expensive of the holographic reconstruction algorithms, and is primarily used for larger objects and longer observation distances. However, the image resolution of this technique can be arbitrarily scaled by zero padding or upsampling recorded holograms. Alternative reconstruction techniques include convolution and angular spectrum approaches, which are slower and are typically used for small objects and short observation distances [137].

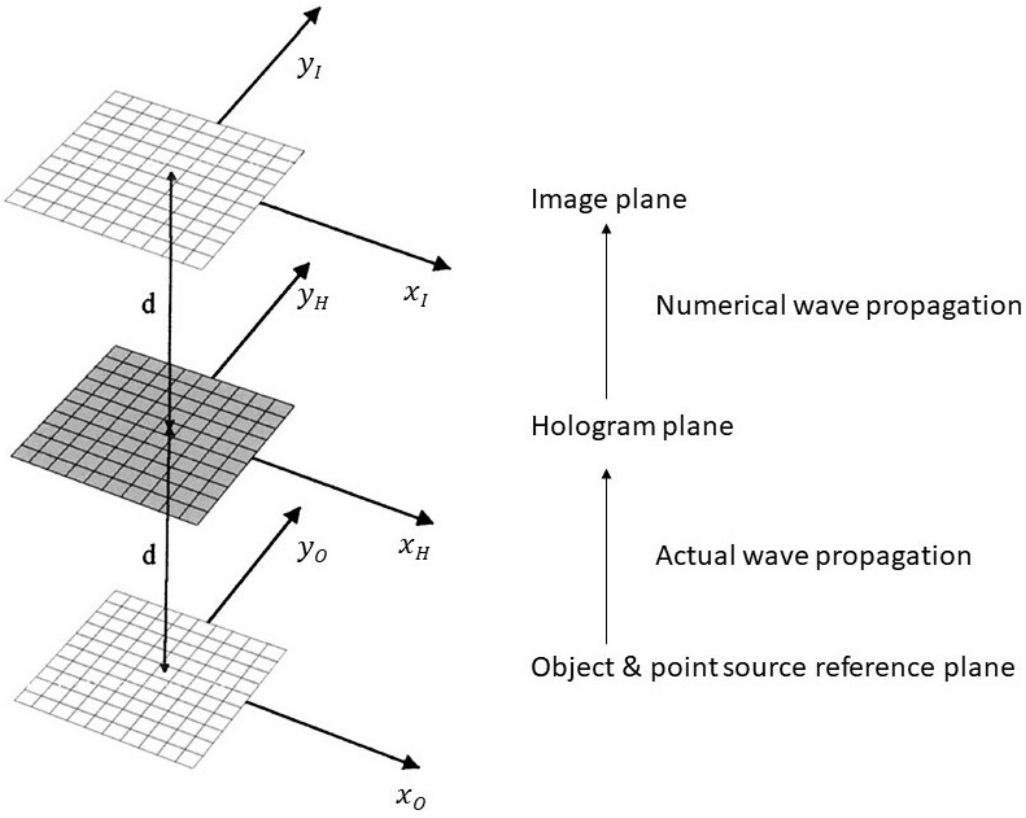

Figure 3.1: Coordinate systems for digital lensless Fourier holography. Adapted from [138, 139].

Using the coordinate systems depicted in Figure 3.1, a light wave diffracted by a hologram, $h(x_H, y_H)$, perpendicular to an incoming reference beam, $A(x_H, y_H)$, can be

described by

$$a(x_I, y_I) = \frac{i}{\lambda d} \exp\left(-i\frac{2\pi}{\lambda}d\right) \exp\left(-i\frac{\pi}{\lambda d}\left[x_I^2 + y_I^2\right]\right) \times \cdots \\ \mathcal{F}^{-1}\left\{h(x_H, y_H) A(x_H, y_H) \exp\left(-i\frac{\pi}{\lambda d}\left[x_H^2 + y_H^2\right]\right)\right\}, \quad (42)$$

where $\mathcal{F}^{-1}$ denotes the inverse Fourier transform. The interested reader is referred to [136, 140] for a complete derivation of Equation 42, which makes use of both the Fresnel-Kirchhoff integral and the Fresnel approximation. Noting that

$$C = \frac{i}{\lambda d} \exp\left(-i\frac{2\pi}{\lambda}d\right) \quad (43)$$

is a complex valued constant, Equation 42 becomes

$$a(x_I, y_I) = C \exp\left(-i\frac{\pi}{\lambda d}\left[x_I^2 + y_I^2\right]\right) \times \cdots \\ \mathcal{F}^{-1}\left\{h(x_H, y_H) A(x_H, y_H) \exp\left(-i\frac{\pi}{\lambda d}\left[x_H^2 + y_H^2\right]\right)\right\}. \quad (44)$$

The factors outside the argument of the inverse Fourier transform in Equation 44 only affect the overall phase, and can be neglected if it is only the intensity of the object that is of interest [136, 140]. Equation 44 then simplifies to

$$a(x_I, y_I) = \mathcal{F}^{-1}\left\{h(x_H, y_H) A(x_H, y_H) \exp\left(-i\frac{\pi}{\lambda d}\left[x_H^2 + y_H^2\right]\right)\right\}. \quad (45)$$

For the specific geometry of lensless Fourier holography, the effect of the spherical phase factor associated with the Fresnel diffraction pattern of the object is eliminated by using a spherical reference wave with the same average curvature

$$A(x_H, y_H) = \exp\left(i\frac{\pi}{\lambda d}\left[x_H^2 + y_H^2\right]\right). \quad (46)$$

This can be achieved in practice by using a reference wave that approximates a point source located in the plane of the object. Substituting Equation 46 into Equation 45 we have

$$a(x_I, y_I) = \mathcal{F}^{-1}\left\{h(x_H, y_H)\right\}, \quad (47)$$

and the intensity of the object can be reconstructed as $|a(x_I, y_I)|^2$.

Lensless Fourier holography reconstructs both holographic twin-images in the same plane, and therefore a technique to separate these two images is required. The geometry of lensless Fourier holography maintains an approximately constant angle between the object beam and the reference beam over the whole area of the sensor, thus utilising its full spatial bandwidth and decreasing sensor resolution requirements [138, 141]. Lens-

less Fourier holography is fast, as it requires only one Fourier transform, and the spatial resolution of the reconstructed image can be increased by zero padding or upsampling $h(x_H, y_H)$.

3.3 Digital holography for blood flow measurement

As digital holography is a lensless technique, it is free from aberrations by imaging devices [136]. Digital holography is inherently interferometric, and the use of area sensors also allows for multispeckle detection as well as facilitating the implementation of tomographic and depth discrimination techniques. In Section 2.3.6, I outlined that interferometric and multispeckle detection are approaches that have recently been investigated to improve the signal-to-noise ratio (SNR) and depth specificity of DCS. It is clear that both of these approaches can be combined into one detection modality in a digital holography system. Additionally, shot noise limited detection can be achieved in digital holography by combining an appropriate temporal filtering strategy with the spatial filtering that is facilitated by off-axis interference of object and reference arms [34, 142], which can lead to further SNR gains. Digital holography can also be used to implement long wavelength approaches, as near-infrared (NIR) enhanced silicon cameras and InGaAs cameras can be employed for detection. Speckle detection systems must use a coherent light source, and therefore the requirement for coherence that digital holography presents does not represent an additional hardware cost for speckle detection. Finally, when compared to single photon avalanche detectors (SPADs) and superconducting nanowire single-photon detection (SNSPD), cameras offer an extremely low relative cost of detection.

Digital holography is therefore an attractive modality with which to detect speckle patterns in biomedical optics; indeed, it has been highlighted as a promising detection strategy for acousto-optic tomography (AOT) [128]. By shifting the frequency of the reference arm near to the acoustic sideband, it is possible to selectively detect tagged photons at the shot noise limit using off-axis holography [143, 144]. Most recently, Hussain *et al.* developed an analytical model for detection of an AOT signal using digital holography with a frequency shifted reference arm, which they implemented to successfully resolve flow in a dynamic flow phantom [76]. These authors showed that the AOT signal within the ultrasound focus was dependent on both the blood flow (BF) through that volume and the integration time of the camera, and were able to achieve *in vitro* depth-resolved flow measurements by analysing images captured using different integration times.

Interferometric speckle visibility spectroscopy (ISVS) is a technique that was developed and published during the time that the research for this thesis was being conducted [37]. ISVS uses off-axis holography to facilitate spatial filtering, and quantitatively assesses the contrast (or equivalent visibility factor) of time-integrated holograms,

rather than frequency shifting the reference arm, to access sample dynamics. A longer integration time, or shorter sample decorrelation time, will result in more blurring, and vice versa, and these authors derived a quantitative model to relate these three factors, similarly to the approach developed by Hussain *et al.* [76]. ISVS uses a lensless Fourier holography setup, and therefore only one Fourier transform is required to reconstruct the holographic terms of interest. Additionally, ISVS uses the interferometric nature of holography to compensate for camera noise, and, like interferometric near-infrared spectroscopy (iNIRS), access the electric field directly, thereby obviating the Siegert relationship, and the constraints therein. The ISVS system that these authors presented uses a sampling rate of 100 Hz, and was able to resolve CBF sample dynamics *in vivo* using source-detector separation (SDS) distances of 0.75 and 1.50 cm, using photon count rates that were not high enough to yield a detectable single-mode DCS signal. However, the off-axis setup that was used by these authors was not ideal, as it did not allow for sampling of the reference beam intensity from measured holograms [see Figure 7.1(A1-A2)]. This lack of calibration leads to noisier flow measurements when compared to like-for-like DCS flow measurements.

Laser Doppler holography (LDH) was presented by Puyo *et al.* in 2018, and is conceptually similar to laser Doppler flowmetry (LDF) (see Section 2.3.4.3), but the holographic implementation allows for full-field imaging of the retina [145]. To maximise the field of view, on-axis holography is used, and a fast detection frame rate (up to 75 kHz), rather than frequency shifting of the reference arm, is used to achieve sensitivity to sample dynamics with sufficiently high temporal resolution. In LDH, a 3D sliding window is moved along a consecutive time-stack of reconstructed holograms. The pixel-wise PSD of each sliding window is calculated using a short-time Fourier transform. This PSD is then integrated between two frequencies of interest to yield a single pixel-wise power Doppler image, an example of which is shown in Figure 3.2. These images can be acquired with a temporal resolution of 1.6 ms, when sampling over 512 $\times$ 512 pixels, which represents 2.4 $\times$ 2.4 mm^2 of the retina.

3.4 Heterodyne parallel speckle detection

The main limitations of digital holography for BF detection are the trade-off that exists between equipment cost and the detection frame rates that are required to resolve rapid sample fluctuations, and the temporal frequency bandwidth broadening that is caused by these high detection frame rates. Therefore, to sample the PSD of a rapidly fluctuating electric field, using low-cost and low-frame rate detection, a technique known as HPSD was developed [146]. Briefly, HPSD makes use of the spatiotemporal filtering that can be achieved using multi-frame off-axis digital holography, together with sweeping the reference arm frequency, to interrogate the PSD at discrete locations of interest. The term 'parallel' is used as HPSD allows the simultaneous measurement of

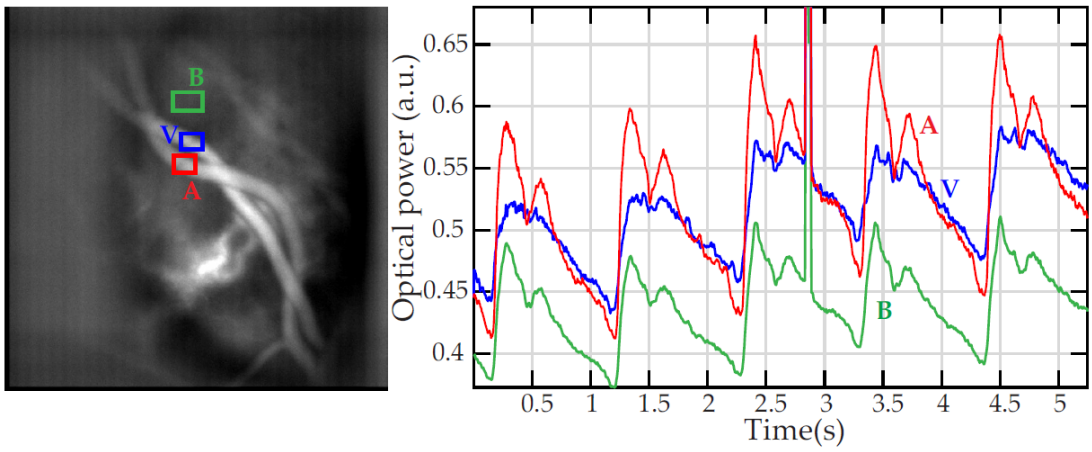

Figure 3.2: Time-averaged power Doppler image of the retina acquired using LDH (left). Red, blue, and green regions of interest (ROI), correspond to an artery (A), a vein (V), and background tissues (B), respectively. These ROIs are used to spatially average the power Doppler signal for the time-series plots (right). Reproduced with permission from [145] under the terms of the OSA Open Access Publishing Agreement. © 2018 Optical Society of America.

multiple speckles [144].

HPSD using digital holography has been well described in the literature since its inception in 2003 [142, 144, 147, 148]. The experimental configuration of an HPSD system consists of a Mach-Zehnder interferometer, where the reference and sample arms are recombined and interfere on a digital camera (see Figure 3.3). Temporal filtering occurs over the camera integration period, and the resulting images record the first-order PSD of the scattered electric field, S_1, at a particular frequency and with a certain bandwidth. By detuning the frequency of the reference arm of the interferometer by a pair of acousto-optic modulators (AOMs), S_1 may be sampled at discrete frequency shifts (Δf) from that of the input optical field, allowing the frequency spectrum of the scattered light to be acquired. The heterodyne gain and shot noise limited performance [142] of this technique permit illumination below the maximum permissible exposure limits of tissue, and it is therefore particularly suited to *in vivo* flow detection [120].

In general, interferometry techniques involve the recombination of a reference beam with a signal beam that has been transmitted through a sample. The source is split into two parts by a beamsplitter to form a signal beam and a reference beam. In the HPSD interferometry system described in this thesis, the frequency of the signal beam is unshifted, such that $\omega_S = \omega_L$, where ω_S is the optical frequency of the signal beam, and ω_L is the optical frequency of the laser source beam. The reference beam, ω_R, is shifted away from ω_L using a pair of AOMs. A pair of AOMs is used as the required frequency shift can be very small compared to the centre wavelength of the AOMs [93], and thus one AOM is used to produce a negative frequency shift (ω_{AOM1}), and the other AOM a positive frequency shift (ω_{AOM2}) of a slightly different magnitude. This results

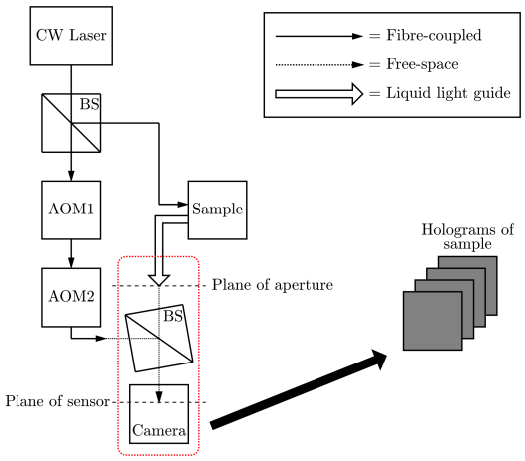

Figure 3.3: Schematic representation of the HPSD system that is described in this thesis. A continuous wave (CW) laser source is split into a reference arm and a sample arm in a fibre-coupled beamsplitter (BS). The reference arm is frequency shifted by a pair of acousto-optic modulators (AOM1 and AOM2). Light is collected from the sample in a reflectance mode geometry through the aperture of a liquid light guide (LLG). The two arms are recombined off-axis in a cube BS. A photograph of the experimental apparatus contained within the red dashed rectangle is shown in Figure 4.3.

in $\omega_R = \omega_L + \omega_{\text{AOM1}} + \omega_{\text{AOM2}}$.

Having passed through the sample, the signal field takes the form $\mathcal{E}_S(t) = E_S \exp^{i\omega_S t}$. The reference field takes the form of $\mathcal{E}_R(t) = E_R \exp^{i\omega_R t}$. The sample and reference beams are recombined in a beamsplitter and are interfered on a camera sensor. This recombination occurs slightly off-axis with respect to the camera sensor by a small tilt angle [148].

The intensity of the speckle interference pattern that is detected by the camera is then

$$I(t) = |\mathcal{E}_S(t) + \mathcal{E}_R(t)|^2, \tag{48}$$

which, analogously to Equation 41, expands to [148]

$$I(t) = |E_S|^2 + |E_\text{R}|^2 + E_S E_R^* \exp^{-i(\omega_R - \omega_S)t} + E_S^* E_R \exp^{+i(\omega_R - \omega_S)t}, \tag{49}$$

where the first two terms of Equation 49 correspond to the self-beating homodyne terms, and the third and fourth terms correspond to the heterodyne signal-reference cross terms. Therefore, the strength of the measured signal (i.e., the two heterodyne terms) depends on both the transmitted signal beam and the reference beam, according to

$$G = \frac{|\mathcal{E}_S \mathcal{E}_R|}{|\mathcal{E}_S|^2} \gg 1, \tag{50}$$

where G is heterodyne gain [143]. The use of a large reference beam intensity allows this technique to reach the shot noise limit, permitting optimum acquisition times [18,

93], enabling its use for *in vivo* imaging [120].

For a given value of ω_R, N_f camera frames are captured using a given camera exposure time, T, and camera frame rate, f_s. The off-axis recombination allows the spatial separation of the zero order of diffraction and the two heterodyne gain terms (which are a conjugate pair). This facilitates the *spatial* filtering component of HPSD, owing to the separation of the signal, shot noise, speckle decorrelation noise, and technical noise of the reference beam in the spatial frequency domain of the detected interference pattern [120], as is demonstrated in Figure 3.4(b).

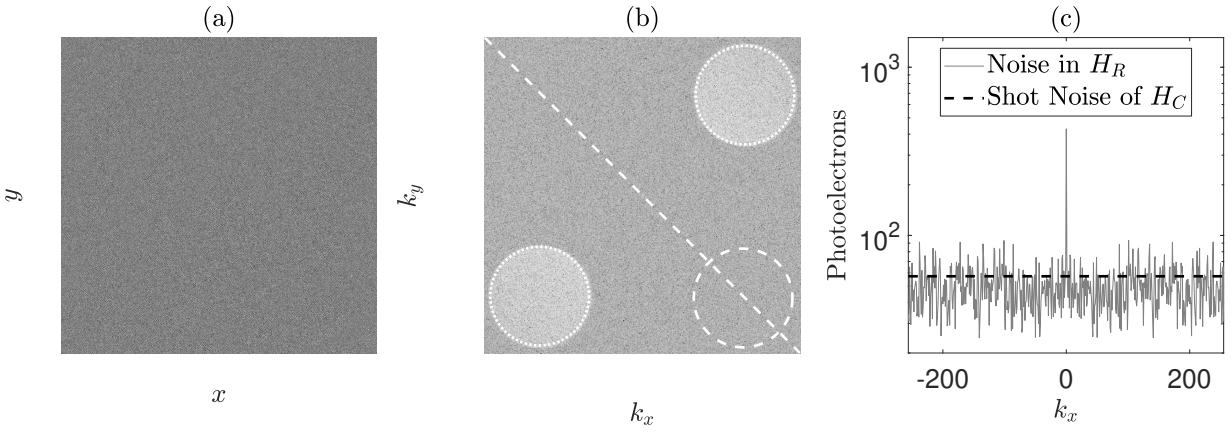

Figure 3.4: Imaging a speckle pattern through the 5 mm diameter aperture of the LLG depicted in Figure 3.3. (a) Camera plane hologram, H_C, formed using DC subtraction temporal filtering. (b) Arbitrary logarithmic representation of a reconstructed intensity hologram, H_R. The two heterodyne gain terms, $S(\pm\Delta\omega, k_x, k_y)$, are masked by the dotted circles (which are a conjugate pair), the shot noise mask, $N(\Delta\omega, k_x, k_y)$, is depicted by the dashed circle. (c) The thin grey solid line shows the value of the diagonal white dashed line that has been superimposed on H_R, averaged over ± 5 pixels in k_y. The thick dashed black line shows the average shot noise value of all the pixels in H_C for this image reconstruction.

As well as this spatial filtering, *temporal* filtering is also achieved by two methods. An inherent temporal filter is applied due to the integration time of the camera. Further temporal filtering is also achieved by constructing a hologram in the camera plane from two or more consecutive images. For example, using a DC subtraction temporal filtering method, the camera plane hologram, H_C, is constructed as the difference of two successive images (i.e., $N_f = 2$)

$$H_C = I_1 - I_2, \tag{51}$$

which removes the two homodyne terms, $|E_S|^2$ and $|E_\mathrm{R}|^2$ in Equation 49, from the hologram. Owing to the use of a lensless Fourier holography setup, the intensity hologram, H_R, is then reconstructed in the object plane by performing a 2D discrete Fourier trans-

form (DFT) of the camera plane hologram [136]

$$H_R = |\mathcal{F}_{2D}(H_C)|^2. \tag{52}$$

A masking operation can then be performed to sum over the two heterodyne signal terms and also to sum over a shot noise mask, which is implemented in one of the two 'quiet' corners of the reconstructed hologram [Figure 3.4(b)]. The *average* pixel value in each mask is then obtained, which is denoted by $\overline{S}(\pm\Delta\omega)$ for the two heterodyne masks, and $\overline{N}(\Delta\omega)$ for the shot noise mask. To avoid contamination by the technical noise of the reference beam and speckle decorrelation noise, none of the three masks should be placed in the low spatial frequency region of H_R [142]. The unnormalised first-order PSD at a given detuning frequency may then be calculated for each heterodyne term as [121, 149]

$$\overline{S}_1(\pm\Delta\omega) = \frac{\overline{S}(\pm\Delta\omega)}{\overline{N}(\Delta\omega)} - 1. \tag{53}$$

Phase-shifting holography (which is distinct from the DC subtraction temporal filtering method) involves offsetting one of the AOM detuning frequencies by f_s/N_f, so that multiple images of the interference pattern can be recorded which have slightly different phase offsets between the signal and reference beams [93]. This has the effect that, following temporal filtering, peak sensitivity to the first heterodyne gain term of the IRF will be at DC (see Figure 3.7). For phase-shifting with $N_f = 2$, H_C is constructed according to Equation 51, whilst for phase-shifting with $N_f = 4$, H_C is constructed as [148]

$$H_C = (I_1 - I_3) + i(I_2 - I_4). \tag{54}$$

Four-frame phase-shifting holography allows separation of the two heterodyne gain terms in the reconstructed hologram; however, this comes at the cost of increased acquisition time, which one group argues should ideally be less than the speckle decorrelation time of the sample [120]. However, another group argues that this 'decorrelation problem' does not exist, and that optimal sensitivity can be achieved by using a camera exposure time in the order of the speckle decorrelation time of the sample [143]. This is because the spatial filtering component of HPSD separates speckle decorrelation noise from the heterodyne signal terms in the reconstructed hologram, meaning that it is possible to measure flow using a camera exposure time that is longer than the sample decorrelation time, assuming that the flow rate is constant (as is demonstrated in Chapter 4 of this thesis). However, when measuring a sample in which the flow rate is *changing* (e.g., an *in vivo* pulsatile sample) then the total acquisition time to acquire a flow metric must be less than half the period of the change that is being measured, according to Nyquist-Shannon sampling theorem. Finally, compared to other more complicated

multiple-phase-shifting techniques, it has been shown that a DC subtraction technique is sufficient to reach the shot noise limit [34].

3.5 Instrument response function

The expression for the IRF, or the apparatus function, for the first and second heterodyne terms of an HPSD instrument is given by disregarding the sample arm fluctuations due to dynamic scattering, and can be found as [146, 147, 149]

$$B_{\pm\Delta\omega} = \left| \operatorname{sinc}\left(\frac{\Delta\omega}{2\pi}T\right) \sum_{k=1}^{k=N_f} \exp(-2ik\pi/N_f) \exp(\mp 2ik\pi\Delta\omega/\omega_s) \right|^2, \tag{55}$$

where ω_s is the angular frame rate of the camera and

$$\operatorname{sinc}(t) = \frac{\sin(\pi t)}{\pi t} \tag{56}$$

is the normalised sinc function. The summation term in Equation 55 has already been rigorously derived in [147] by demodulating an HPSD signal in the absence of fluctuations due to either the reference arm or dynamic sample scatterers, but the argument of the sinc term is not presented consistently in the relevant literature [146, 147, 149]. The correct form of this sinc filter can be derived by considering the Fourier transform of a time domain rectangular bandpass filter of width T. By normalising the area of this filter such that it has a height of $1/T$ and an area of one, this Fourier transform becomes

$$\frac{1}{T}\int_{-T/2}^{+T/2} \exp^{-2\pi i f t}\ \mathrm{d}t = \frac{\sin(\pi f T)}{\pi f T} = \operatorname{sinc}\left(\frac{\Delta\omega}{2\pi}T\right). \tag{57}$$

Equation 57 produces a sinc shaped low pass filter in the frequency domain, with a bandwidth (i.e., the distance between DC and first null) of $1/T$.

Characteristic examples of the HPSD IRF are shown in Figures 3.5, 3.6, and 3.7 for single frame, DC subtraction, and four-frame phase-shifting holography, respectively, using camera exposure parameters of T = 30 ms and f_s = 12 Hz [149].

The IRF thus provides the inherent temporal filtering that is associated with the camera's integration time and that is also partly associated with the temporal demodulation of the HPSD signal. The IRF will be broad when T is small, and the IRF will be narrow when T is large. Thus, broadening of measured power spectra will occur when using a relatively broad IRF, which is more likely to happen when using shorter camera exposure times, or when measuring the narrow power spectra of samples with slower dynamics.

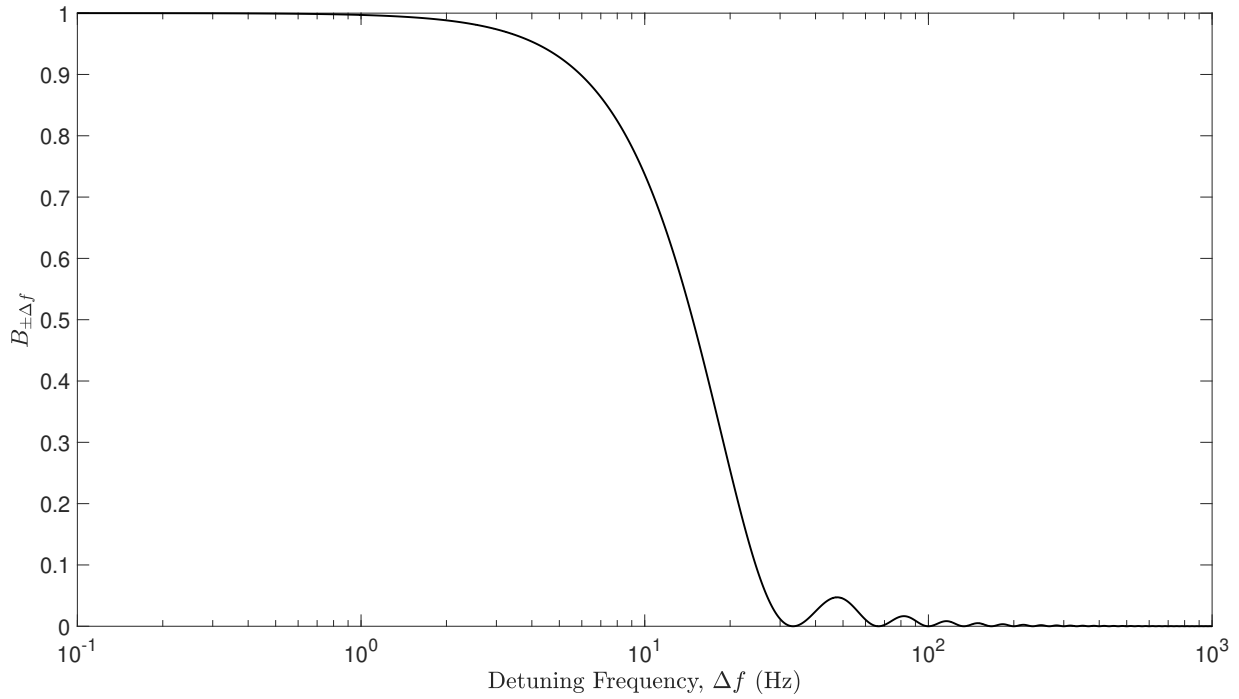

Figure 3.5: $B_{\pm\Delta\omega}$ for single frame holography (i.e., $N_f = 1$), T = 30 ms, and f_s = 12 Hz. The two heterodyne terms cannot be distinguished, and therefore $B_{\pm\Delta\omega}$ overlie each other.

According to the Wiener-Khinchin theorem, the first-order PSD, $s_1(\omega)$, of the field fluctuations is the Fourier transform pair of the field autocorrelation function, $g_1(\tau)$ [150]. Considering this, and by taking into account the effects of the IRF in the Fourier domain, the total *normalised* measured response of an HPSD instrument is then the Fourier domain counterpart of Equation 17 [146, 147]

$$s_1(\Delta\omega) = \alpha s_{1d}(\Delta\omega) * B_{\pm\Delta\omega} + (1-\alpha)B_{\pm\Delta\omega}, \tag{58}$$

where s_{1d} is the first order PSD of the field fluctuations due to *dynamic* scatterers, and $*$ is the convolution product. If the IRF is much narrower than the PSD that is being measured, Equation 58 can be simplified to [147, 149]

$$s_1(\Delta\omega) = \alpha s_{1d}(\Delta\omega) + (1-\alpha)B_{\pm\Delta\omega}. \tag{59}$$

As per Equation 18, if we make the assumption that a sample is composed entirely of dynamic scatterers, then Equation 59 becomes

$$s_1(\Delta\omega) = s_{1d}(\Delta\omega). \tag{60}$$

Likewise, if a sample is composed entirely of static scatterers, then Equation 59 becomes

$$s_1(\Delta\omega) = B_{\pm\Delta\omega}. \tag{61}$$

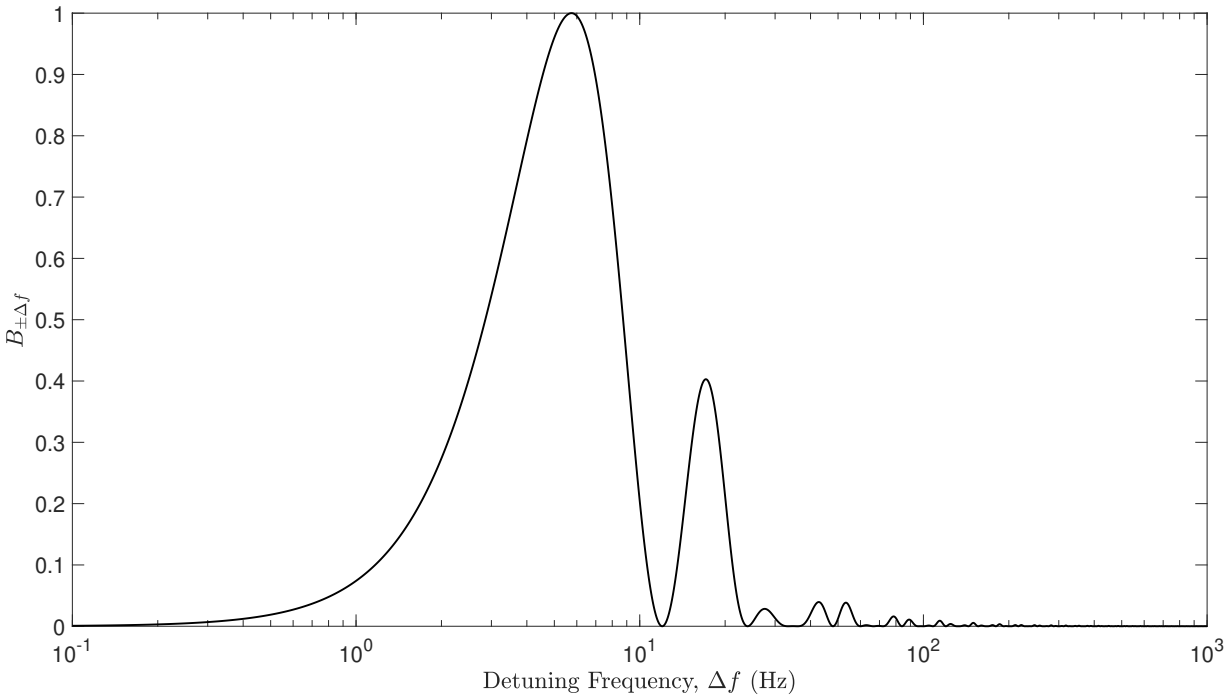

Figure 3.6: $B_{\pm\Delta\omega}$ for DC subtraction holography (i.e., $N_f = 2$), T = 30 ms, and f_s = 12 Hz. The two heterodyne terms cannot be distinguished (even when using phase-shifting), and therefore $B_{\pm\Delta\omega}$ overlie each other.

This can be related to Equation 19 by considering the normalised Fourier transform of an IRF in the limit that detection is continuous for the whole measurement, which is unity over the timescales of interest. Equations 58, 59, 60, and 61, together with their time domain counterparts, are summarised in Table 3.1.

Table 3.1: Summary of measured data types for BF detection in the time and frequency domains.

Data domain	**Time**	**Frequency**
Data type	$g_1(\tau)$	$s_1(\Delta\omega)$
Combined dynamic/static sample	$\alpha\lvert g_{1d}(\tau)\rvert + (1-\alpha)$	$\alpha s_{1d}(\Delta\omega) * B_{\pm\Delta\omega} + (1-\alpha)B_{\pm\Delta\omega}$
Abbreviated form	-	$\alpha s_{1d}(\Delta\omega) + (1-\alpha)B_{\pm\Delta\omega}$
Dynamic sample	$\lvert g_{1d}(\tau)\rvert$	$s_{1d}(\Delta\omega)$
Static sample	1	$B_{\pm\Delta\omega}$

The naïve approach to recovering flow information from HPSD data is simply to transform the data into the time domain, and use established theory to fit for an appropriate flow metric. However, although $g_1(\tau)$ and $s_1(\Delta\omega)$ are fundamentally equivalent, this approach will lead to errors owing to differences in the sampling of the data in the time and frequency domains, the effects of static scattering in an HPSD system, the nature of the measurement noise, and broadening by the IRF.

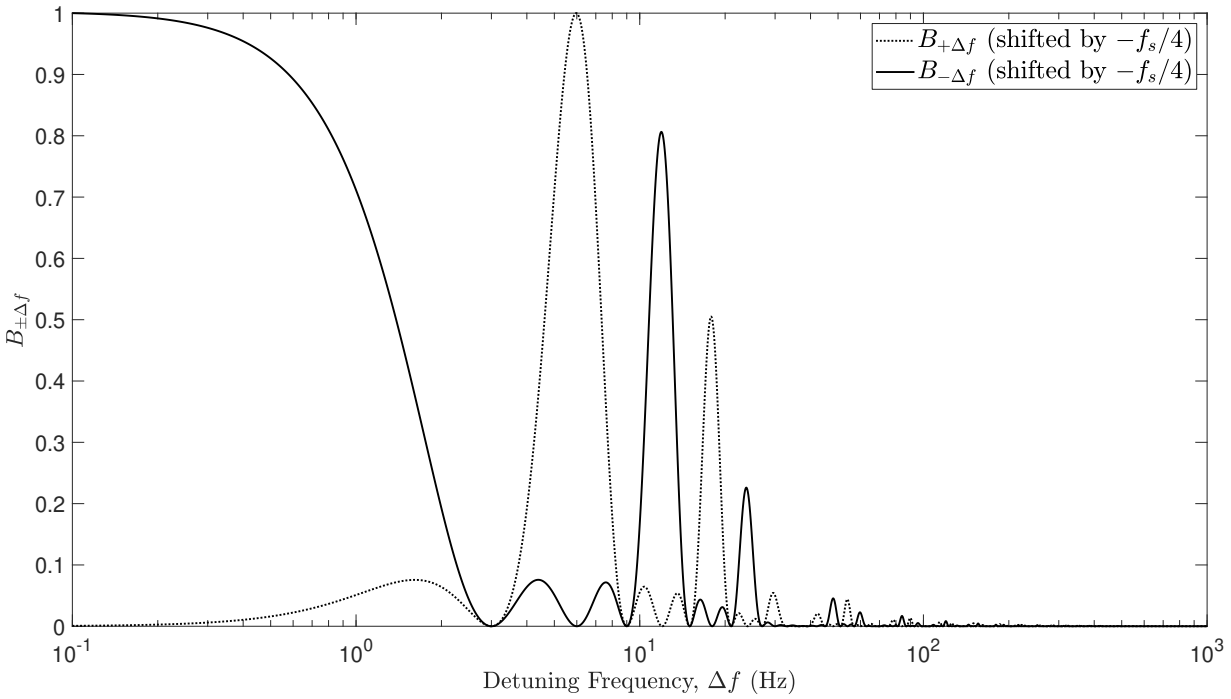

Figure 3.7: $B_{\pm\Delta\omega}$ for four-frame phase-shifting holography (i.e., $N_f = 4$), T = 30 ms, and f_s = 12 Hz. The two heterodyne terms can be distinguished using this technique, and the peak sensitivity to the first heterodyne gain term of the IRF will be at DC.

3.6 Research question and challenges for *in vivo* detection

It is hopefully now apparent to the reader that by using an HPSD instrument to collect DCS data in the frequency domain at a range of discrete frequencies, and fitting these data to Equations 58, 59, or 60 as appropriate, values of D_b and α could be obtained that will be entirely equivalent to that derived from a conventional DCS experiment. Indeed, in 1997 Boas and Yodh stated in their founding work on DCS that [21],

> 'Since our theoretical formulation and measurements have generally focused on the time-domain picture, we shall continue to adopt that picture throughout this paper. We note, however, that a line-shape analysis of the light spectrum obtained by the frequency-domain instruments will provide entirely equivalent information'.

In Section 2.3.6, I described the broad range of approaches that have recently been investigated to improve the sensitivity, spatial resolution, and imaging depth of DCS. Compared to conventional DCS, the potential benefits of implementing DCS using HPSD are multiple: SNR that scales linearly with the square root of the number of camera pixels used, order of magnitude reduction in detector cost, robustness to the effects of ambient light, shot noise limited interferometric detection using off-axis holography, potential for detector scalability and sensor partitioning (which could facilitate tomographic and depth discrimination techniques), and suitability to a range of design wavelengths (which could confer a further SNR advantage). Like iNIRS and

ISVS, HPSD interrogates the electric field directly, and it is therefore not constrained by the Siegert relationship. HPSD is also particularly suitable for the detection of AOT signals, owing to the ability to select an acoustic sideband by detuning the reference arm. HPSD could also be used to acquire time-of-flight (TOF) resolved measurements, in a similar fashion to iNIRS, by using a tunable laser source and detecting spectrally resolved intensity.

Despite the potential advantages of an HPSD implementation of DCS, such an approach has never been documented in the literature. The closest report of such a study was published by Magnain *et al.* in 2014 [149]. Cognisant of the benefits of sampling in the native domain of the data, this group used HPSD to measure convective flow rates *in vitro*, by fitting measured power spectra to a Fourier domain diffusing wave spectroscopy (DWS) model of convective motion in a backscattering configuration [149]. Diffusive Brownian motion was quantified by fitting measured data to the discrete Fourier transform of a DWS model of Brownian motion. The same study also measured localised superficial microvascular convective flow rates in the cerebral cortices of 2 mice and the retinas of 3 adult rats by imaging through a 5 mm $\times$ 5 mm aperture. However, this study used a camera exposure time of 30 ms and a camera frame rate of 12 Hz, which provided insufficient temporal resolution to resolve pulsatile flow *in vivo*, especially after frame averaging and frequency shifting. Additionally, it is well documented in the DCS literature that a Brownian diffusion model, rather than a convective motion model, provides a better fit to measured DCS data over a broad range of tissue types [8, 19].

In this thesis I therefore propose to investigate the implementation of DCS using HPSD, which I will refer to henceforth as holographic Fourier domain DCS (FD-DCS). Motivated by improvements of the sensitivity of DCS to CBF in typically non-ideal settings, holographic FD-DCS places a particular emphasis on scalability, affordability, and robustness to ambient light. HPSD has been highlighted as a promising detection strategy for AOT signals, and therefore holographic FD-DCS could also form an effective basis for acousto-optic modulated DCS (AOM-DCS). A comparative summary of conventional DCS and holographic FD-DCS is concisely detailed in Table 3.2.

Using holographic FD-DCS to measure flow, at rates sufficient to resolve pulsatile information, brings significant challenges. To employ holographic FD-DCS in a practical *in vivo* setting requires the use of short camera exposure times to minimise the effects of sample movement and external sources of vibration which disrupt the interferometric configuration, particularly when using multispeckle detection. Additionally, short exposure times are required to facilitate a high parameter output rate that can resolve fast pulsatile changes. However, reducing the exposure time comes at the cost of a wider IRF, which will result in a broadening of the measured power spectra, which in turn

Table 3.2: Comparison of conventional DCS and the proposed holographic FD-DCS technique.

Technique	**Conventional DCS**	**Holographic FD-DCS**
Data domain	Time	Frequency
Data type	Photon arrival time series used to derive autocorrelation functions	Power spectrum measurements at discrete frequency shifts
Speed of detection	∼10 MHz	∼100 Hz
Optical throughput	Single or few-mode	Thousands of modes
Potential for detector scalability and implementation of diffuse correlation tomography (DCT)	Low	High
Sensitivity to ambient light	Sensitive	Robust
Cost of detector	High	Low
Other cost considerations	Correlator (∼£5000)	Pair of AOMs (∼£7000) Interferometry (∼£1000)
Detection sensitivity	Close to shot noise limited, but no inherent gain	Shot noise limited, with heterodyne gain
Potential for ultrasound modulation	Yes, but with low SNR	Yes, with improved SNR
Potential for TOF resolved detection	Yes, requires a pulsed light source to implement time domain diffuse correlation spectroscopy (TD-DCS)	Yes, requires a tunable laser and detection of spectrally resolved intensity, similar to iNIRS
Suitability for long wavelength approaches	Detector suitability is particularly challenging at present	Detectors are readily available, but are less ideal
Constrained by Siegert relation	Yes	No

will increase the complexity of data sampling and interpretation. A related complication arises as whilst the true field autocorrelation, G_1, and PSD, S_1, of the scattered light form a Fourier transform pair, the data measured using conventional DCS and holographic FD-DCS systems will deviate due to differences in the nature of the measurement systems. These differences arise due to the nature of the sampling in the two domains, the effects of IRF broadening and static scatterers, and the differing effects of measurement noise between the two techniques.

Whilst holographic FD-DCS offers many advantages compared to conventional measurement techniques, data acquisition speed and processing load requirements are high, especially if real-time data acquisition at high parameter output rates is desired. There is also a trade-off to consider between speed of data acquisition, making use of

averaging to improve SNR, and sampling the measured power spectra at enough frequency shifts so as to permit robust fitting to a forward model.

Finally, no available FD-DCS model exists in the literature. The nature of measured DCS data in the time and frequency domains, although fundamentally equivalent, will deviate from each other. Therefore, the development of an FD-DCS model, which allows for native domain fitting of holographic FD-DCS data, is necessary in this regard.

3.7 Chapter summary

Digital holography is a coherent interferometric technique that involves the digital capture and numerical reconstruction of holographic images. When combined with off-axis interferometry and an appropriate temporal filtering strategy, digital holography can achieve shot noise limited detection. HPSD involves scanning the frequency of the reference arm of a digital holography instrument, which allows for the use of inexpensive low-frame rate cameras, with a narrow IRF, to sample the power spectrum of a rapidly fluctuating electric field at discrete locations of interest, through the simultaneous measurement of multiple speckles in parallel. By making use of the Wiener-Khinchin theorem, these measurements can be related to the Fourier transform of conventional time-domain models of motion to infer sample dynamics.

In this thesis, I propose to explore an alternative approach to conventional DCS that employs an HPSD detection method: holographic FD-DCS. Such an approach benefits from interferometric, multispeckle, and shot noise limited measurements that are not constrained by the Siegert relation. Holographic FD-DCS places a particular emphasis on scalability, affordability, and robustness to ambient light, and is particularly suitable for long wavelength approaches and the detection of AOT signals.

The main challenges for implementing holographic FD-DCS are the short camera exposure times that are necessary to resolve pulsatile flow *in vivo*, and the IRF broadening that results from this. Also, compared to conventional DCS, the data acquisition speed and processing load requirements of holographic FD-DCS are high. Finally, despite the validity of FD-DCS being recognised by the founders of DCS, an analytical model for this framework does not exist in the literature.

4 A digital holographic system for DCS

4.1 Chapter contribution

In this chapter I present a high speed holographic Fourier domain diffuse correlation spectroscopy (FD-DCS) instrument suitable for making *in vivo* measurements at a frame rate that permits the recovery of pulsatile flow. This approach employs heterodyne parallel speckle detection (HPSD) to allow averaging over thousands of modes to realise improvements in signal-to-noise ratio (SNR) (which are demonstrated *in vitro* in this chapter), and operates with continuous wave (CW) illumination without disturbance from ambient light. The system that I demonstrate can make measurements of the power spectral density (PSD) of a fluctuating electric field across $\sim$1300 speckles at 6 discrete frequency shifts, with an overall parameter output rate of 23.8 Hz.

In Section 4.2, I define a novel FD-DCS model which allows for parameter fitting in the native domain of the data, permitting extraction of flow parameters whilst respecting the nature of the noise in the measurement system. The architecture and implementation of the holographic FD-DCS instrument, which uses a highly parallel GPU-accelerated holographic demodulation pathway to manage the processing requirements for the technique, is described and validated in Sections 4.3 and 4.4. I describe a novel mixed motion diffuse correlation spectroscopy (DCS) model in Section 4.5, which is used together with a novel model for the temperature dependent properties of intralipid phantoms, to demonstrate accurate absolute interpretation of holographic FD-DCS data in their native domain, both at room temperature (Section 4.6) and over a physiologically relevant temperature range (Section 4.7). In Section 4.8, I demonstrate the SNR improvement that holographic FD-DCS offers compared to conventional DCS, as well as demonstrating its relative insensitivity to ambient light. Finally, in Section 4.9, I demonstrate the *in vivo* application of this inexpensive camera-based detection system by recovering pulsatile flow rates measured in the human forearm.

This chapter forms the basis for work that I published in the Biomedial Optics Express Biophotonics 2020 Feature Issue [151], in which the reviewers highlighted the novelty and significance of the work, as well as the potential impact of holographic FD-DCS to overcome the SNR limitations of conventional DCS. As a result of this publication, I was subsequently awarded the 2021 Robert Speller Prize for the best paper by a PhD student in the UCL Medical Physics and Biomedical Engineering Department, and I also presented related work at Photonics West SPIE BiOS 2020 [152].

4.2 Developing and validating a Fourier domain DCS model

The framework for conventional DCS has been described in Section 2.3.6, and is based on measurements of photon arrival time series, which are made in the time domain,

and which are used to derive autocorrelation functions. The motivation to develop an analytical FD-DCS model has been described in Chapter 3. In this section I define the FD-DCS models that I have developed for both Brownian and convective motion, which are suitable for holographic FD-DCS. Full derivations of these models, together with considerations for acousto-optic modulation, are included in Appendix A.

As was introduced in Section 3.5, it is well established according to the Wiener-Khinchin theorem that the first-order PSD, $S_1(\omega)$, and the field autocorrelation function, $G_1(\tau)$, are a Fourier transform pair [5, 21, 120, 146, 149, 150, 153]

$$S_1(\omega) = \int_{-\infty}^{+\infty} G_1(\tau) \exp^{-i\omega\tau} \, \mathrm{d}\tau. \tag{62}$$

The Fourier transform of $G_{1d}(\tau)$, which is the field autocorrelation function due to *dynamic* scatterers, Equation 28, is then

$$S_{1d}(\Delta\omega) = \frac{S_0}{4\pi D} \left[F(\Delta\omega, r_1) - F(\Delta\omega, r_2) \right], \tag{63}$$

where $\Delta\omega$ is angular detuning frequency. In the case of Brownian motion and $\Delta\omega > 0$, I find that

$$F_{[D_b]}(\Delta\omega_+, r) = \frac{1}{\Delta\omega^{3/2}} \left(\frac{1}{4} + \frac{i}{4} \right) \mu_s' \sqrt{6C} \exp\left(-\frac{D(\Delta\omega)}{2} - \frac{E(\Delta\omega)}{2} \right) \times \ldots \left(\exp\left(D(\Delta\omega)\right) \operatorname{erfc}\left(A_-(\Delta\omega)\right) - i \exp\left(E(\Delta\omega)\right) \operatorname{erfc}\left(A_+(\Delta\omega)\right) \right), \tag{64}$$

where the auxiliary function, $A_\pm(\Delta\omega)$, is defined as

$$A_\pm(\Delta\omega) = \frac{(2 \mp 2i)\Delta\omega \sqrt{\frac{\mu_a \mu_s'}{2C}} + (1 \pm i)\mu_s'^2 r \sqrt{6C}}{2\sqrt{2}\mu_s' \sqrt{\Delta\omega}}, \tag{65}$$

erfc is the complementary error function,

$$C = k_0^2 D_b, \tag{66}$$

$$D(\Delta\omega) = \frac{i\mu_a \Delta\omega}{\mu_s' C}, \tag{67}$$

and

$$E(\Delta\omega) = \frac{3i\mu_s'^2 C r^2}{\Delta\omega}. \tag{68}$$

$G_{1d}(\tau)$ is an even and real function, and therefore its Fourier transform is also real.

For convective motion I find that

$$F_{[V^2]}(\Delta\omega, r) = \sqrt{\frac{3\mu_a\mu_s'}{\mu_s'^2 k_0^2 V^2 r^2 + \Delta\omega^2}} K_1\left(\sqrt{3\mu_a\left(\mu_s' r^2 + \frac{\Delta\omega^2}{\mu_s' k_0^2 V^2}\right)}\right), \tag{69}$$

where K_1 is the first modified Bessel function of the second kind.

For a given set of arbitrary experimental parameters, examples of $s_1(\omega)$, which is the *normalised* $S_1(\omega)$, are plotted in subplot (a) of Figure 4.1, for both Brownian and convective motion (i.e., Equations 64 and 69, respectively). Examples of $g_1(\tau)$, which is the *normalised* $G_1(\tau)$, for the same experimental parameters as used in subplot (a), are shown in subplot (b). There is excellent agreement between the analytical expressions and the numerical Fourier transform of the novel FD-DCS analytical expressions, and I am thus confident of the accuracy of the two FD-DCS models that I have derived.

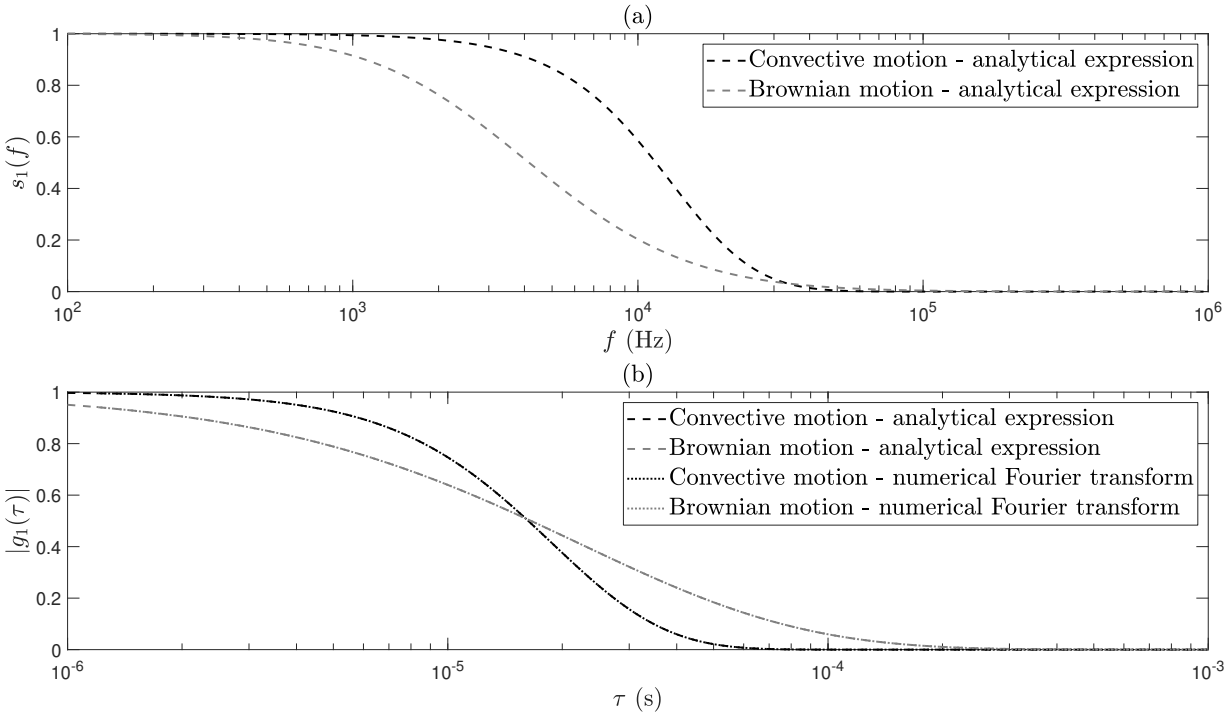

Figure 4.1: Numerical validation of novel analytical FD-DCS models. (a) Examples of $s_1(\omega)$ for both Brownian and convective motion. (b) Examples of $g_1(\tau)$, for the same experimental parameters as used in (a). There is excellent agreement between the analytical models for $g_1(\tau)$ and the numerical Fourier transforms of the novel FD-DCS models.

4.3 System design and integration

In addition to the introduction to HPSD given in Chapter 3, and having developed and validated the analytical framework with which to analyse FD-DCS data, I shall

now describe the specific architecture and implementation of the holographic FD-DCS system that I have developed.

A schematic of the experimental design has already been shown in Figure 3.3. All experiments were performed using a 785 nm CW long coherence length (∼9.5 m) laser (Toptica, iBeam Smart S WS), with a maximum optical output power of 120 mW. This near-infrared (NIR) light source is initially split into two parts by a 75:25 fibre coupler (Thorlabs, 1x2 75:25 narrowband coupler, TN785R3A1) to form a sample arm and a reference arm, respectively. The sample arm then illuminates the sample via a multimode source fibre (Thorlabs, FT200EMT).

In the instrument reported in this thesis, a pair of acousto-optic modulators (AOMs) is placed on the reference arm (Gooch & Housego, Fiber-Q, 150 MHz centre frequency, 785 nm, upshift & downshift), which then feed into a single-mode fibre that terminates in an antireflection-coated free-space connector (Thorlabs, P3-780AR-2). The signal field that has been scattered by the sample is collected in a reflection mode geometry through the aperture of a 5.0 mm diameter core liquid light guide (LLG), which has a numerical aperture of 0.52 (Thorlabs, LLG5-4Z). The sample and reference arms are recombined in a 50:50 cube beamsplitter (Thorlabs, CCM1-BS014/M), as illustrated in Figure 4.3. This recombination occurs slightly off-axis with respect to the camera sensor and the reference arm, which enables spatial filtering in the reconstructed hologram. The sCMOS camera (FLIR, BFS-U3-16S2M-CS) has a sensor size of 1440 × 1080 pixels, which is truncated to $2^n \times 2^n$ (where n is an integer between 3 and 10) so as to facilitate holographic reconstruction by the fast Fourier transform (FFT) algorithm, and I denote $N_{\text{pix}} = 2^n$.

To prevent multiple out of phase speckles illuminating a single pixel, I ensure that each speckle illuminates no less than one camera pixel. The camera has a pixel size, Δ_{pix}, of 3.45 μm. Therefore the minimum speckle size, S, is constrained, according to [154, 155]

$$S = \frac{(\lambda z)^2}{A_{\text{aperture}}} \geq \Delta_{\text{pix}}^2, \tag{70}$$

where z is the observation distance between the plane of the aperture and the plane of the camera sensor (as depicted in Figure 3.3), and A_{aperture} is the area of the aperture. This yields a minimum observation distance, z_{min}, of 19.5 mm. Additionally, by considering the maximum spatial frequency that can be resolved at the detector for a lensless Fourier holography setup, it has also been shown that [140]

$$z_{\text{min}} = \frac{\sqrt{2}\Delta_{\text{pix}} L}{\lambda}, \tag{71}$$

where L is the characteristic dimension of the aperture. This expression yields a value of

z_{min} = 31.1 mm. The experiments reported in this chapter use a value of z = 75 - 80 mm, which adheres to both of these constraints, and for which a single speckle occupies the area of ∼15 - 17 square pixels, respectively. ∼5200 speckles were sampled in each signal mask for $N_{\text{pix}} = 1024$, and ∼1300 speckles for $N_{\text{pix}} = 512$. Decreasing the value of z from 75 - 80 mm to 31.1 mm would increase the number of detected speckles on the camera sensor, but this would lead to sampling of the zero order DC term in the centre of the reconstructed hologram and is therefore avoided.

To maximise the use of the sensor layout, the size of the pixels, $\Delta\xi$, in the reconstructed hologram image is also considered [136]

$$\Delta\xi = \frac{\lambda z}{N_{\text{pix}}\Delta_{\text{pix}}}, \tag{72}$$

where N_{pix} is the number of pixels in 1D. Using a circular aperture, the maximum achievable diameter of one heterodyne term can be shown to be $N_{\text{pix}}\sqrt{2}/(3+\sqrt{2})$ (as has been independently corroborated by [37]), so as not to collect any signal at the zero order DC term, whilst ensuring that the aperture is fully contained within the reconstructed hologram (i.e., without spatial aliasing). This is equivalent to calculating the maximum diameter of four equally sized circles that are both aligned along the diagonal of a square and fully contained within the square. The motivation to maximise the size of the heterodyne term is twofold:

- the number of resolvable speckles within the signal mask will be increased;
- each of these speckles will be smaller, owing to the shorter observation distance, z.

Both effects will lead to an increase in the total number of speckles detected. For example, using a 512 x 512 sensor, and allowing for pixel discretisation, the optimal radius of the heterodyne term is 81 pixels, with a sensor layout as shown in subplot (a) of Figure 4.2.

A CAD designed and 3D-printed mount was designed with which to hold the beamsplitter and the LLG in an off-axis configuration, as shown in Figure 4.3. Rapid iterative prototyping meant that the following two parameters could then be optimised:

- the size of the reconstructed heterodyne term, which is inversely related to z;
- the location of the reconstructed heterodyne term in the xy plane, which is a function of the offset of the LLG from the optical axis of the beamsplitter.

A heterodyne term radius of 80 pixels was achieved, with no sampling of the zero order DC term and with no signal aliasing, as shown in subplot (b) of Figure 4.2.

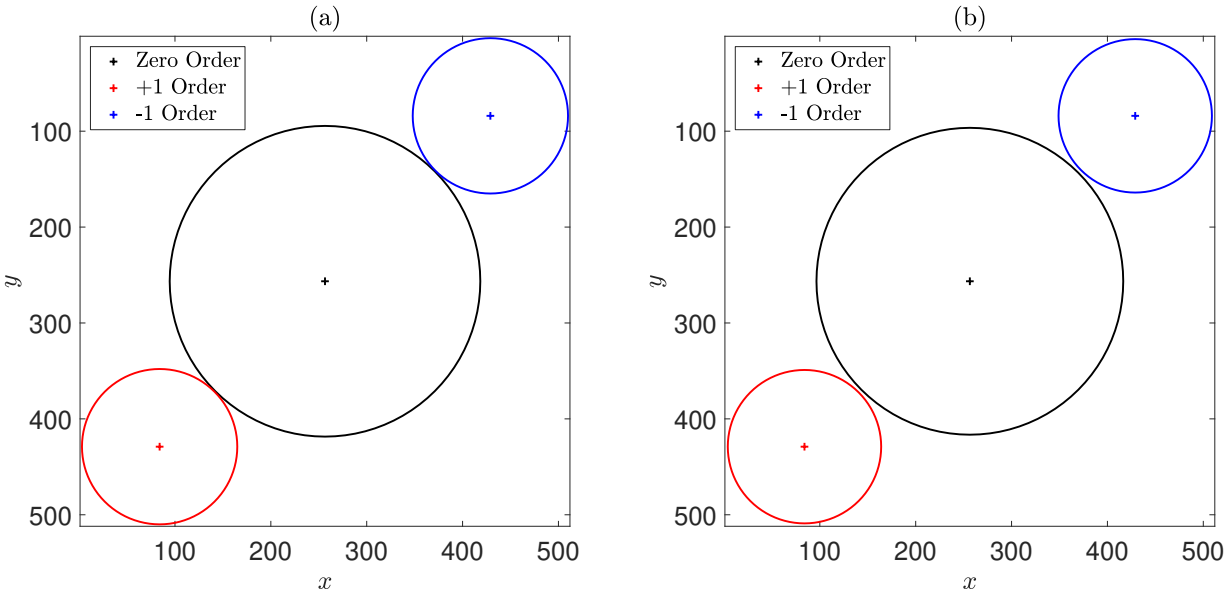

Figure 4.2: A 512 × 512 sensor with (a) ideal, and (b) achieved sensor layouts. Each of the two first orders of diffraction represent the holographic twin images [as shown in Figure 3.4(b)], which are used to image the sample, which, in this case, is the 5 mm diameter exit pupil of the LLG.

As introduced in Chapter 3, one of the main challenges for the application of holographic FD-DCS at high-frame rates is fast data acquisition and processing load: calculating an S_1 measurement requires frequency shifting, image capture, temporal filtering, 2D FFT, spatial filtering, and reduction. I have therefore designed a custom integrated holographic FD-DCS system with a high throughput, with the aim of achieving demodulation and data acquisition at fast imaging frame rates, a schematic of which is shown in Figure 4.4. The system consists of a camera, a workstation, and a control board. The following acquisition parameters are specified in a configuration file:

- camera exposure;
- camera frame rate;
- sensor dimensions;
- the amplitude at which to drive the AOMs;
- a vector of frequency shifts to be implemented by the AOMs;
- the number of camera frames to be acquired at each frequency shift;
- the holographic demodulation mode (i.e., DC subtraction, 2-phase, or 4-phase);
- the shape, size, and position of the noise mask and the two signal masks;
- the number of frequency sweeps to acquire (i.e., the number of D_b frames).

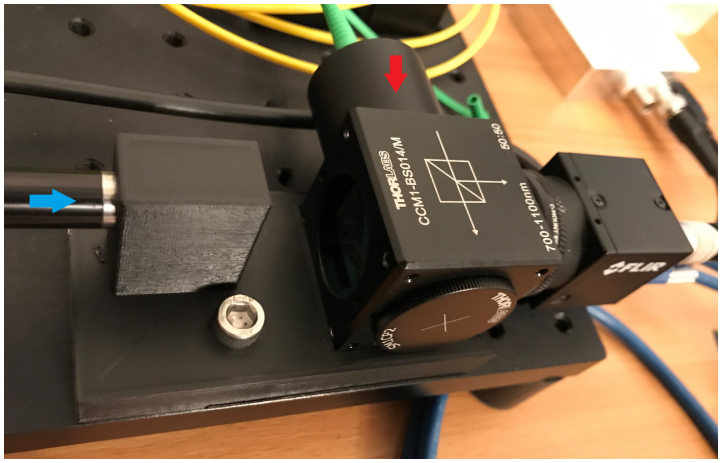

Figure 4.3: CAD designed and 3D-printed off-axis interferometry mount (as delineated by the red dashed rectangle in Figure 3.3). The reference arm (from top) is mounted to the beamsplitter via a lens tube (red arrow) and an externally threaded fibre adapter. This arrangement allows the observation distance of the reference arm to be adjusted to match that of the sample arm (from left, blue arrow), which is a requirement of lensless Fourier holography. N.B. A full system diagram is shown in Figure 3.3.

The use of camera frame preview images and demodulation preview images allows the assessment of camera saturation and the correct positioning of the demodulation masks, respectively.

The control board, which implements a Standard Commands for Programmable Instruments interface, receives instructions from the workstation. It then carries out the following three functions:

- generation of radio frequency waveforms for the AOMs using direct digital synthesis;
- control of the laser output;
- synchronisation of the overall experiment by generation of camera triggers and performing sweeps through the required frequency shifts.

Image data are then relayed to the workstation by a USB 3.0 connection, and then on to the GPU (nVidia Tesla K40, 12 GB memory, 288 GB/s bandwidth, 2880 CUDA cores), via a 16 lane Peripheral Component Interconnect express interface. Custom CUDA kernels execute the holographic demodulation pathway (i.e., calculation of S_1 values from raw camera frames, as described in Section 3.4) using the CUDA FFT library, which was implemented using Julia, a high-level programming language that has inbuilt GPU functionality. Demodulated data, together with log files specifying camera frame timestamps and serial commands to the instrument, are passed back to the workstation's system memory.

The use of this highly parallel GPU-accelerated demodulation pathway, together with a tightly synchronised instrument with minimal dead-time between frequency

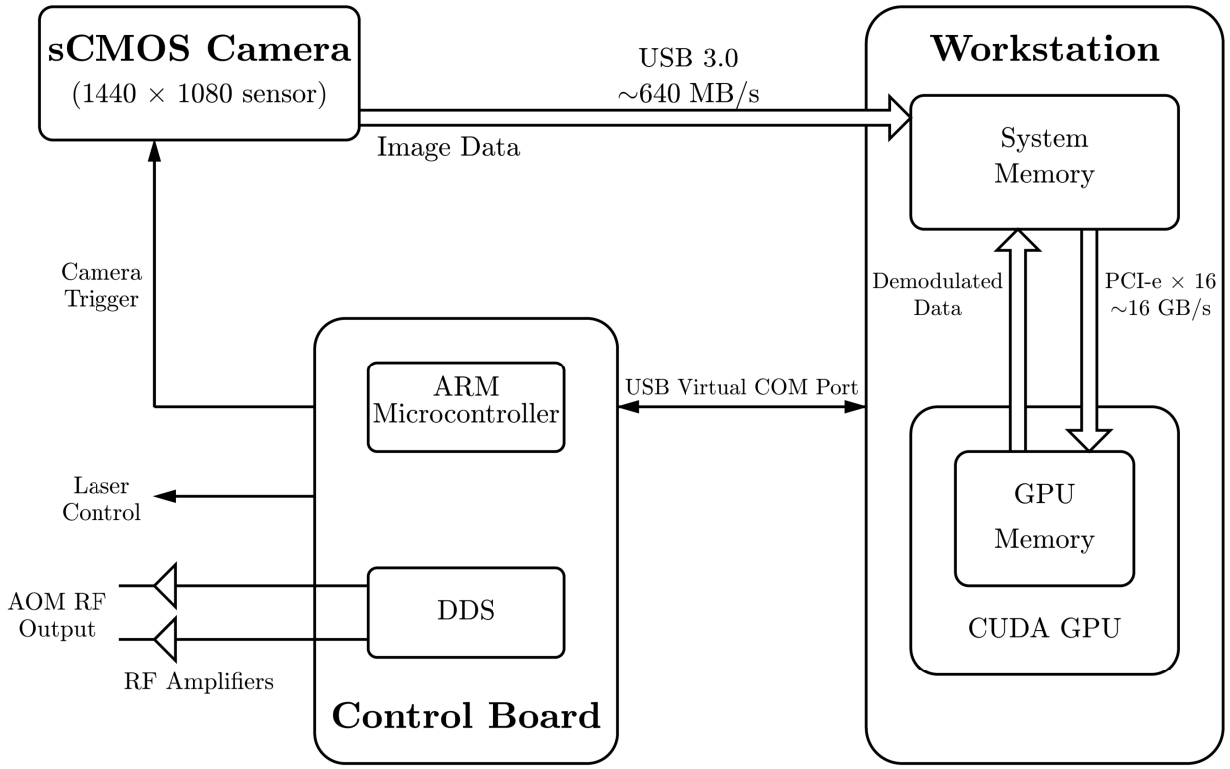

Figure 4.4: Integrated system architecture and data streaming via a highly parallel GPU-accelerated demodulation pathway. The control board synchronises experiments, holograms are relayed from the camera to the workstation's system memory, and custom CUDA kernels implement the holographic demodulation process.

shifts, allows the rapid measurement of the PSD of light scattered by a diffusing sample at a high parameter output rate (i.e., ~20 Hz [22]).

4.4 Validation of instrument response function

To validate the holographic FD-DCS instrument, as well as Equations 55 and 61, a series of 4-phase instrument response function (IRF) measurements was collected using a static polyester resin optical phantom, which was lent to me by Professor Jem Hebden. The optical properties of the illuminated region of this phantom were μ_a = 0.1 cm^{-1} and μ_s' = 8.5 cm^{-1} at 780 nm [156]. The IRF characterisation was performed for -100 Hz $\leq \Delta f \leq$ 100 Hz, as shown in Figure 4.5. In this figure, each IRF model has been normalised by its respective maximum value. Each measured IRF data set has been normalised according to a least squares fit to the normalised IRF model (Equation 55), allowing for a constant noise offset in each case. The IRF models in Figure 4.5 have been shifted by $-f_s/N_f$, as the peak sensitivity to the first heterodyne gain term of the IRF is at DC for phase-shifting holography. There is excellent agreement between the measured and modelled data in Figure 4.5, which serves to validate the design of the holographic FD-DCS instrument.

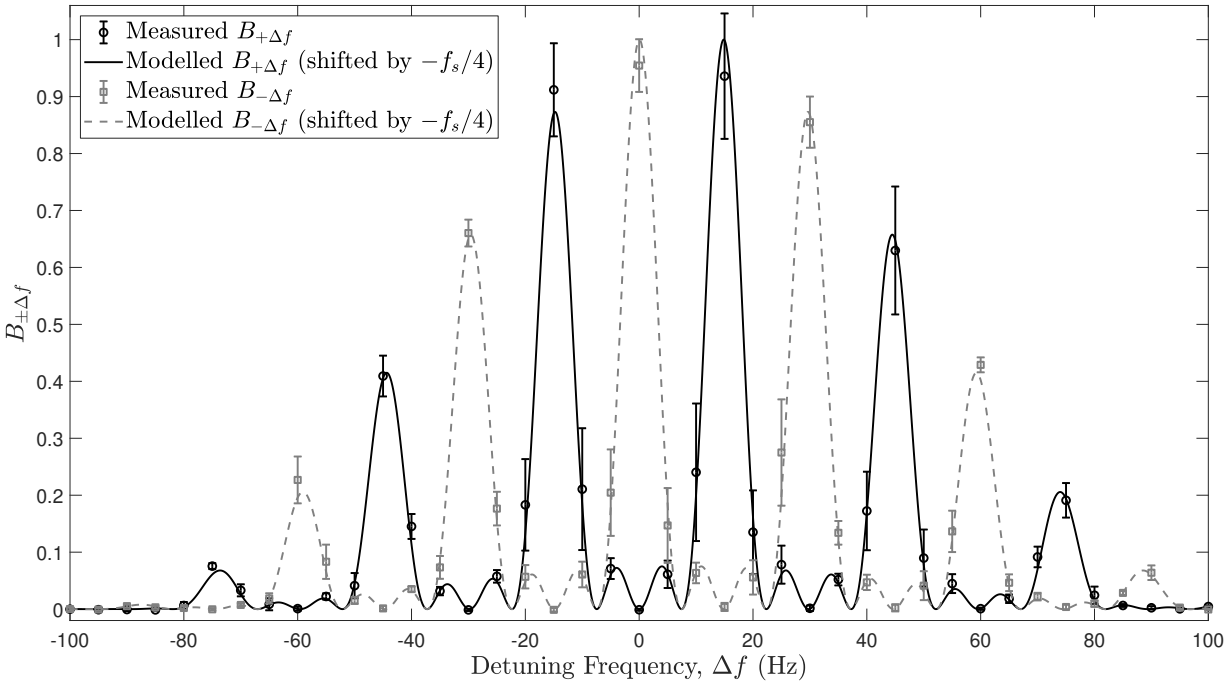

Figure 4.5: 4-phase IRF detection and validation against the IRF model for the first and second heterodyne terms ($T = 9.6$ ms, $f_s = 29.8$ Hz, $N_f = 4$). Error bars represent ± 1 standard deviation over 13 samples.

4.5 Mixed model fitting

This section describes the novel mixed motion model fitting process that was applied to measured DCS data in this chapter, both for conventional DCS data, and for holographic FD-DCS data. Conventional DCS data (g_2) were fit to Equation 16 by minimisation of the unweighted least squares objective function

$$\underset{[\beta,\langle\Delta r^2(\tau)\rangle]}{\operatorname{argmin}} \sum_{i=1}^{k} \left[g_2(\tau_i)_{\text{measured}} - g_2(\tau_i)_{\text{model}}\right]^2 \tag{73}$$

over k delay times. This was performed separately for both Brownian and convective motion models (i.e., paired vectors of $[D_b, \beta_{D_b}]$ and $[\langle V^2\rangle, \beta_{\langle V^2\rangle}]$ were optimised for separately). In a third and final optimisation step, the contribution of each of these two models to a mixed motion model could then be determined by optimising for a 'Brownian factor' (F_{Br}), which is constrained to have a value between 0 and 1. This was achieved by minimisation of the unweighted least squares objective function

$$\underset{[F_{\text{Br}}]}{\operatorname{argmin}} \sum_{i=1}^{k} \left[g_2(\tau_i)_{\text{measured}} - \left[F_{\text{Br}} \times g_2(\tau_i)_{\text{Brownian}} + (1 - F_{\text{Br}}) \times g_2(\tau_i)_{\text{convective}}\right]\right]^2. \tag{74}$$

The Brownian model fit and the extracted D_b value could then be scaled by the Brownian factor. Likewise, the convective model fit and the extracted $\langle V^2\rangle$ value could then be

scaled by (1 - Brownian factor). The mixed motion model fit is then then sum of these two scaled model fits, and it is assumed that flow parameters scale linearly with changes in Brownian factor [92]. An example of this mixed model fit is shown in Figure 4.6(a) and Figure 4.7(a).

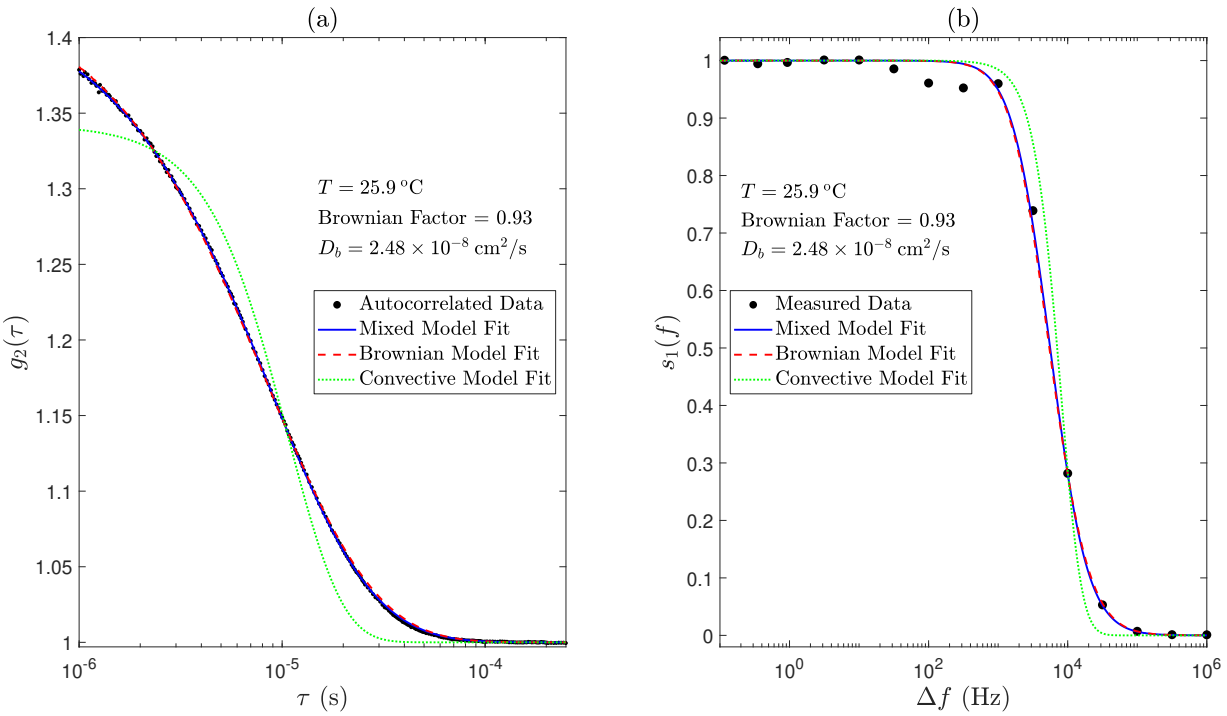

Figure 4.6: Application of (a) conventional DCS mixed model fitting, and (b) holographic FD-DCS mixed model fitting to data acquired using an intralipid optical tissue phantom. Magnified views are shown in Figure 4.7.

Similarly, measured S_1 data were fit to Equation 63; however, these data are implicitly unnormalised, and therefore fitting for a normalisation constant (C_{norm}) and noise floor parameter (N_{floor}) was also necessary. Flow parameters (i.e., D_b or $\langle V^2 \rangle$), C_{norm}, and N_{floor} were optimised for by minimisation of the weighted least squares objective function

$$\underset{[D_b/\langle V^2\rangle, C_{\mathrm{norm}}, N_{\mathrm{floor}}]}{\operatorname{argmin}} \sum_{i=1}^{k} w_i [C_{\mathrm{norm}}(S_{1d}(\Delta\omega_i)_{\mathrm{measured}} - N_{\mathrm{floor}}) - s_{1d}(\Delta\omega_i)_{\mathrm{model}}]^2, \qquad (75)$$

over k detuning frequencies, where w_i represents the weights. $s_{1d}(\Delta\omega)_{\mathrm{model}}$ is the forward model normalised by its maximum value (i.e., its value at the smallest measured positive detuning frequency), and w_i is calculated as $1/\sigma_i^2$, where σ_i is the standard deviation of the measured data at the i^{th} frequency step. Again, in a third and final optimisation step, the contribution of each of these two models of motion to a mixed motion model could then be determined by optimising for a Brownian factor (constrained to take a value between 0 and 1). This was achieved by minimisation of the weighted least

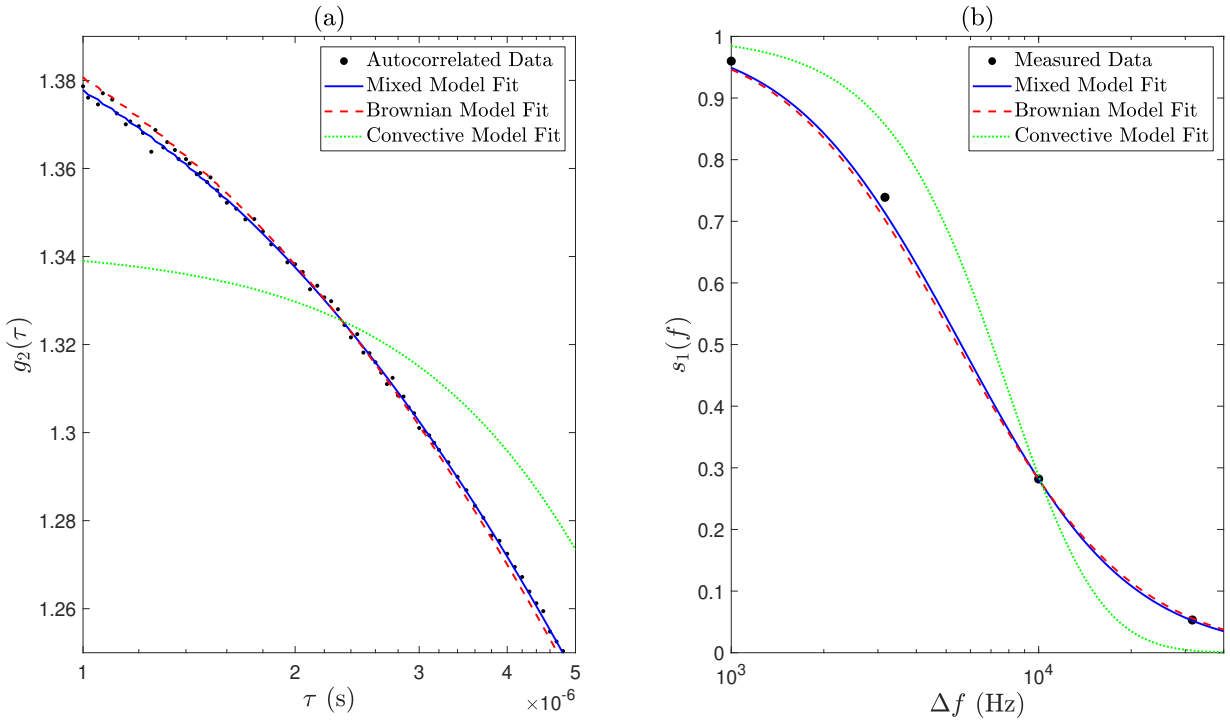

Figure 4.7: Magnified views of Figure 4.6 show that the mixed model fits the data better than either the Brownian model or the convective model alone, for both (a) conventional DCS, and (b) holographic FD-DCS.

squares function

$$\underset{[F_{\mathrm{Br}}]}{\operatorname{argmin}} \sum_{i=1}^{k} w_i [C_{\mathrm{norm}}(S_{1d}(\Delta\omega_i)_{\mathrm{measured}} - N_{\mathrm{floor}}) - \cdots$$
$$[F_{\mathrm{Br}} \times s_{1d}(\Delta\omega_i)_{\mathrm{Brownian}} + (1 - F_{\mathrm{Br}}) \times s_{1d}(\Delta\omega_i)_{\mathrm{convective}}]]^2. \quad (76)$$

The Brownian factor could then be used to weight the contribution of each of the two model fits to the mixed motion model, and to scale the values of D_b and $\langle V^2 \rangle$ accordingly. An example of this mixed model fit is shown in Figure 4.6(b) and Figure 4.7(b). This novel mixed model fitting process is validated, both for conventional DCS and holographic FD-DCS, in Section 4.7. In Figure 4.6(b) there is deviation from the model fit for the 6^{th}, 7^{th}, and 8^{th} detuning frequencies; it is possible that this deviation at these lower detuning frequencies could be due to contributions from the IRF, due to static scattering from the ferrule of the LLG. A similar effect is also visible for the lower detuning frequencies in Figure 4.9, which also shows that these detuning frequencies are noisier.

4.6 Absolute validation at room temperature

For the purposes of demonstrating absolute equivalence between the data obtained from conventional DCS and holographic FD-DCS techniques, I elected to use a relat-

ively long camera exposure time of 30 ms, together with a camera frame rate of 17.5 Hz, such that convolution of the true power spectra with the IRF could be ignored in the model fit process (as is detailed further below in this section and also displayed in Figure 4.9). This is the same camera exposure time that was used in [149] to accurately measure known convective *in vitro* flow rates using HPSD, which were controlled using a calibrated syringe pump.

Conventional DCS experiments used a single-mode detection fibre (Thorlabs, 780HP) coupled to a single photon avalanche detector (SPAD) with a typical dead time of 45 ns and a response time of 30 ns (Laser Components, COUNT-50N), giving a typical maximum detection rate of 13.3 MHz [22]. This is small compared to the 60 MHz system clock speed of the digital correlator (Correlator.com, Flex02-01D/C), which was used in single channel photon history recording mode to obtain photon arrival timestamps. These photon arrival timestamps were then autocorrelated in software using the Laurence algorithm [157]. The digital correlator was also used to autocorrelate photon arrival times in hardware using the multi-tau algorithm [19, 158] at 640 MHz, using a fixed value of 106 delay times per decade by default. However, my implementation of the Laurence algorithm provides more flexibility, as both the delay times of the autocorrelation function and the frame rate of the DCS measurement can defined in software.

An intralipid optical tissue phantom (Fresenius Kabi, Intralipid 20 %) was prepared which consisted of 25.62 mls of intralipid made up to 550 mls with deionised water, resulting in optical properties of μ_s' = 7.5 cm^{-1} (based on former in-house calibration measurements) and μ_a = 0.026 cm^{-1} at 20 ^{0}C [159] (assuming that the optical absorption of intralipid is primarily due to background water absorption, μ_a^{BKG}, as water is the main absorbing component of intralipid [160, 161]). This value of μ_s' is based on the measurement of the optical properties of the brain in three healthy volunteers in [22]. A temperature dependent model for the optical properties of combined intralipid/deionised water phantoms at 785 nm was constructed using the refractive index model of pure water presented in [162], the optical absorption coefficient model of pure water presented in [159], and the temperature coefficient for the reduced scattering coefficient of intralipid [160] (personal communication), having made scaling adjustments to allow for intralipid concentration differences. Intralipid is commonly used as an optical phantom to simulate the absorption and scattering properties of biological tissue; it has also been shown to have high temporal stability and negligible variation between batches [163].

The liquid phantom was contained within a glass beaker, which itself was immersed in a thermostatically controlled water bath, as depicted in Figure 4.8. It is important to control and account for the temperature of the phantom during absolute equivalence experiments, as not only does temperature affect the optical properties of the phantom, but it also affects the value of D_b in the phantom, according to the Stokes-Einstein equa-

tion [146, 149, 164, 165]

$$D_b = \frac{k_B T}{6\pi\eta r}, \tag{77}$$

where k_B is Boltzmann's constant, T is absolute temperature, η is dynamic viscosity, and r is the hydrodynamic radius of spherical particles diffusing through a liquid in the limit of a low Reynolds number. Furthermore, the dynamic viscosity of fluids also has a temperature dependence which is roughly exponential, $\eta \approx a\exp(-bT)$. However, a more accurate relationship can be modelled according to the empirical fit

$$\ln\left(\frac{\eta}{\eta_0}\right) = a + b\left(\frac{T_0}{T}\right) + c\left(\frac{T_0}{T}\right)^2, \tag{78}$$

where, for water, T_0 = 273.16 K, η_0 = 1.792 x 10^{-3} Kg/(m · s), and suggested coefficient values are a = -1.94 , b = -4.80 and c = 6.74 [166]. This model provides a better fit than a pure exponential decay model, and assumes the empirical result that $\ln(\eta)$ is quadratic in $1/T$, resulting in an accuracy of ± 1 %.

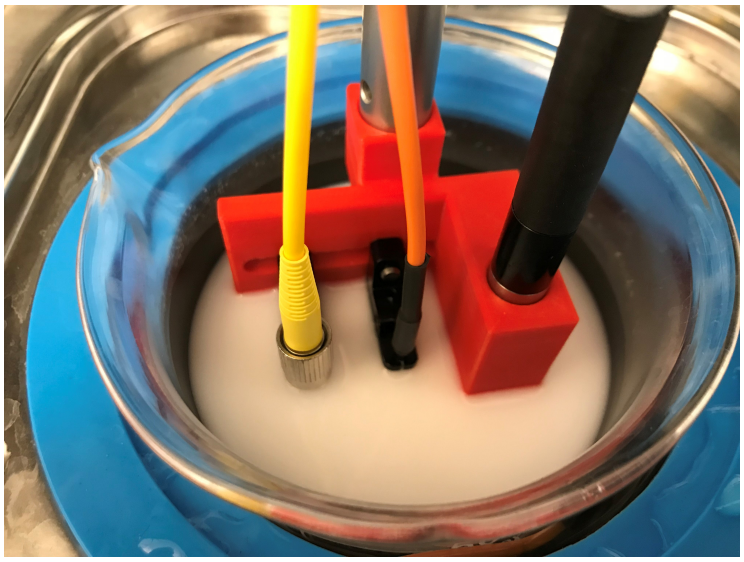

Figure 4.8: Semi-infinite reflection mode geometry used for absolute validation experiments. From left, single-mode detection fibre, multimode source fibre, and LLG, coupled to the intralipid phantom using a custom designed and 3D printed probe.

The source-detector separation (SDS) distance, as measured from the centre of the source fibre to the centre of the LLG, was set to 17.50 mm. The optical configuration was placed on the surface of the liquid phantom as shown in Figure 4.8. Holographic FD-DCS data were gathered by implementing a logarithmically spaced frequency sweep consisting of 15 steps between 0.1 Hz and 1 MHz, with 201 camera frames recorded at each frequency step, resulting in 200 data points at each detuning frequency for a DC subtraction temporal filtering method, and a total integration time of 90.45 seconds. The measured data were then fit directly to Equation 63 (as described by Equation 75), the results of which are depicted in Figure 4.9 and Figure 4.10(d). The former of these two

figures shows ± 1 standard deviation of the noise floor corrected and normalised data, together with the model fit to the FD-DCS model of Brownian motion. The average level of assumed Gaussian noise (as a percentage of mean s_1 value) was calculated at each detuning frequency, the median of which was determined to be 3.8 %. The half width at half maximum (HWHM) of the measured signal is two orders of magnitude larger than the HWHM of the main lobe of the IRF, and I therefore neglect the effects of IRF broadening in this experiment. Forward modelling simulations show that using these parameters, assuming 3.8 % Gaussian measurement noise averaged over 200 readings, an enforced condition of $\alpha = 1$, and a DC subtraction temporal filtering method, a final D_b estimation error of ~ 0.19 % is expected.

Conventional DCS data were gathered by collecting 30 seconds of multi-tau autocorrelated g_2 data, which were fit to Equation 16 assuming $\alpha = 1$ and a Brownian model of motion, the result of which is shown in Figure 4.10(a). The extracted value of D_b was input into the FD-DCS forward model of Brownian motion, the result of which is shown by the black dotted line in Figure 4.9. The remarkably close correspondence between the two power spectra shown in this figure further validates the instrument, as well as validating the novel FD-DCS model in terms of *absolute* D_b measurement.

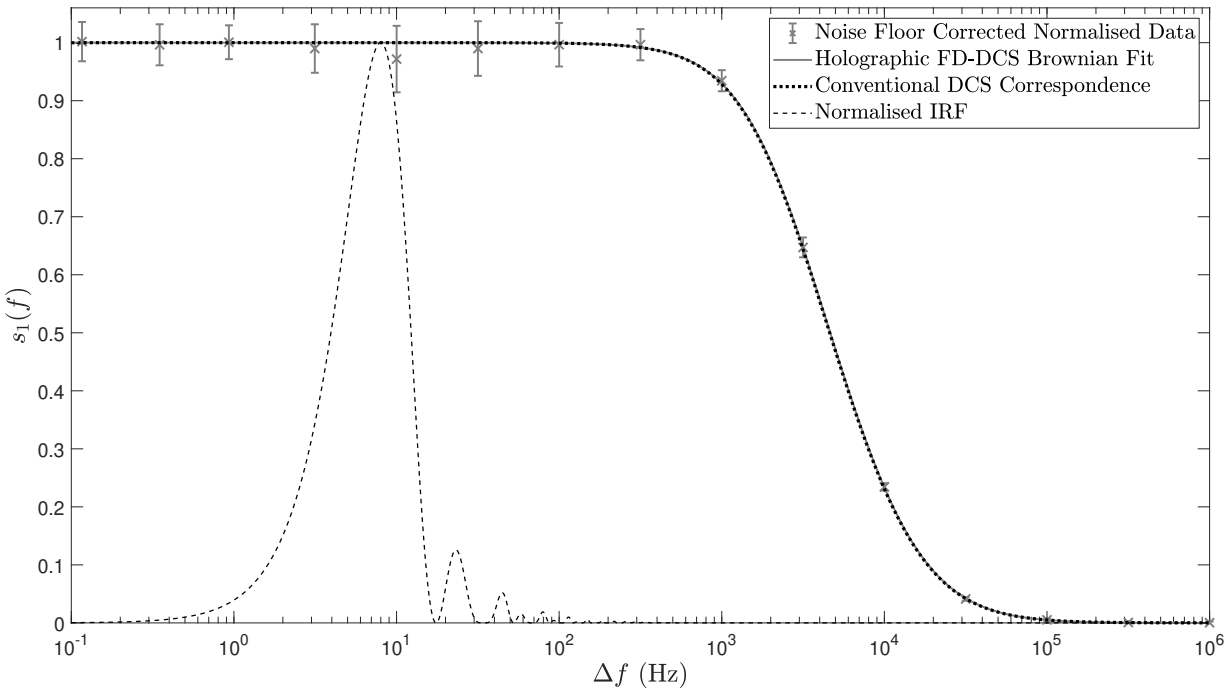

Figure 4.9: Fitting holographic FD-DCS data to the FD-DCS model (grey error bars and grey solid line), which is at least two orders of magnitude wider than the IRF (black dashed line). Error bars represent ± 1 standard deviation of measured data. The black dotted line represents synthetic data produced by forward modelling in the Fourier domain with the D_b value acquired from a conventional DCS setup.

The naïve approach to recovering flow information from Fourier domain data is to

numerically Fourier transform the data into the time domain, and to use established theory to fit for D_b. This approach is depicted in Figure 4.10(b), and would at first glance be considered acceptable under the conditions of this experiment: a sufficiently narrow IRF, a sample composed entirely of dynamic scatterers, and the ability to average out noise over a generously large data set. However, due to the logarithmic spacing of the measured data, linear resampling prior to numerical Fourier transform is required (using shape-preserving piece-wise cubic interpolation with a resolution of 0.1 Hz in this case). This two-step process is not immune to the presence of noise in the measured data, which results in sub-optimal fitting in the complementary domain: the D_b value acquired in Figure 4.10(b) is not in keeping with those acquired by fitting in the native domains, which are shown in Figure 4.10(a) and 4.10(d). This is confirmed by considering the time domain fit to the transformed Fourier domain native *model fit*, which produces a good D_b value correspondence (2.15×10^{-8} cm^2/s) to that of Figure 4.10(a).

Similarly, conventional DCS data were transformed into the Fourier domain, following linear resampling with a resolution of 0.5 μs, and were fit to the FD-DCS model of Brownian motion, the result of which is shown in Figure 4.10(c). The value of D_b produced by this model fit is also not in keeping with that acquired by fitting in the native domains; however, this can be rectified by considering the Fourier domain fit to the transformed time domain native *model fit*, which yields a much closer D_b value correspondence (2.13×10^{-8} cm^2/s) to that of Figure 4.10(d).

These results support the argument described above that, due to noise in the measured data, model fitting in the native domain is preferable to resampling, numerical transform, and fitting in the complementary domain. Whilst the deviations in D_b measurement using complementary domain fitting that are shown here are relatively small for these very slow acquisition times, they could be significant when optimising for fast acquisition times with a broader IRF, especially when imaging samples with a static scatterer component. Thus, fitting with a native model appears to be an appropriate technique to ensure accuracy in flow parameter measurements.

4.7 Absolute validation across a physiological temperature range

To show the absolute equivalence of conventional and holographic FD-DCS techniques over a physiologically relevant temperature range, as well as to demonstrate ground-truth validation from other measurement techniques, I repeated the validation experiment performed in Section 4.6 at 12 temperature steps during heating (in a step-wise fashion) between 17.1 ^{o}C and 40.5 ^{o}C. According to Equation 77, and using the novel temperature dependent model of the optical properties and dynamic viscosity of intralipid, the D_b value of the optical phantom will increase in a nonlinear fashion as its temperature is increased. Intralipid optical phantoms have previously been demonstrated to have good thermal stability, with scattering properties varying less than 0.5 %

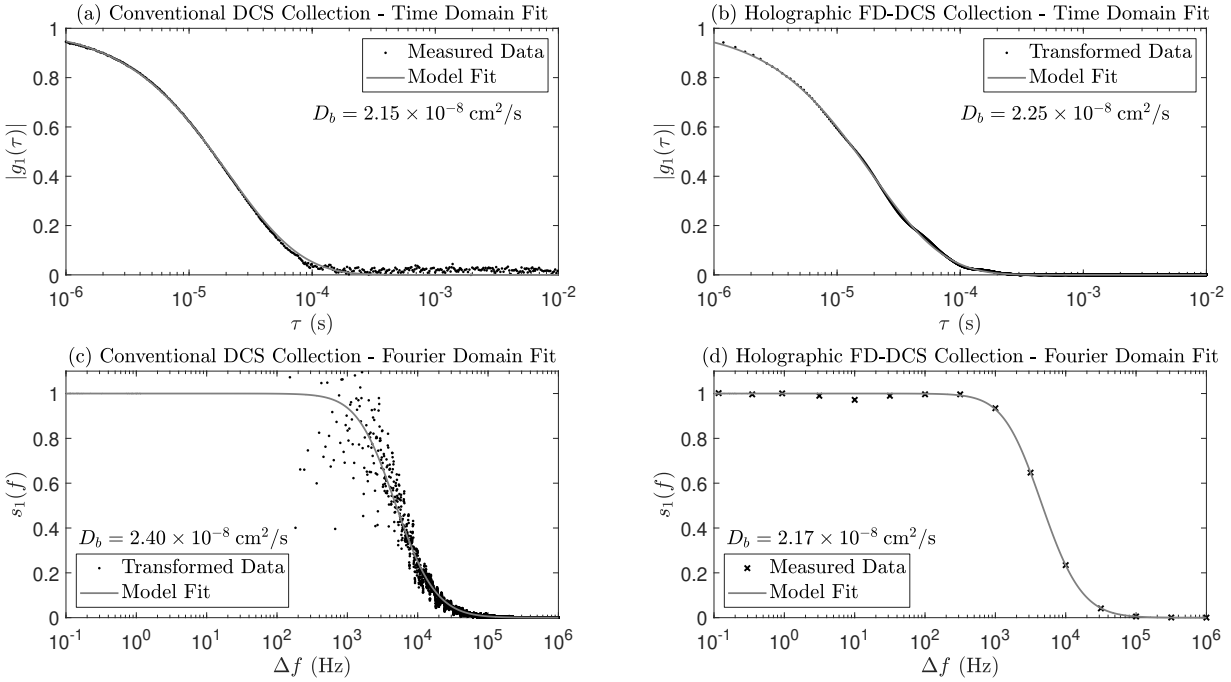

Figure 4.10: Fitting of measured data to native domain decorrelation models, for (a) conventional DCS collection, and (d) holographic FD-DCS collection. Model fitting in the complementary domain following numerical Fourier transform of measured data, for (b) holographic FD-DCS collection, and (c) conventional DCS collection. Due to noise in the measured data, DCS model fitting in the native domain is preferable to numerical transform and fitting in the complementary domain.

when held at 70 ^{o}C for 12 hours, and are therefore considered to be optically robust and stable when subject to elevated temperatures [163].

A thermostatically controlled waterbath was allowed to stabilise for 30 minutes before collecting each data set [160], and the phantom was manually stirred after each temperature increase to maintain homogeneity. Evaporative losses are to be expected when performing such an experiment, as such the optical probe was lowered slightly as need be before each measurement, to ensure good optical coupling with the phantom. Loss of water from the phantom will also alter its optical properties, by way of increasing the concentration of scatterers and decreasing the water concentration [161]; however, I deemed this effect to be minimal in my experimental setup due to both the original volume of the phantom and the relatively short span of time over which data were collected following the lowering of the optical probe. The laser source was turned off between readings to prevent any *undesired* heating of the phantom from occurring (the heating of the phantom therefore occurred solely due to the waterbath, as intended).

In addition to the data acquired in Section 4.6, 15 seconds of raw photon counting data were also collected at each temperature step (with the exception of the second temperature step, due to a corrupt data file). A time of 15 seconds was chosen as this was deemed long enough to average over, and to provide redundancy for postprocessing

of data. These data were autocorrelated using my implementation of the Laurence algorithm. Autocorrelated g_2 data were then fit to the conventional DCS mixed model, with the distribution of the mixed model D_b values and Brownian factors displayed in Figures 4.11 and 4.12, respectively (these two figures also show the corresponding multi-tau autocorrelated data). The 200 holographic FD-DCS frequency sweeps were averaged, and the D_b values acquired by fitting to the Fourier domain mixed motion model (as well as the corresponding Brownian factor at each temperature step) are also displayed in Figures 4.11 and 4.12. As the temperature of the phantom increases, I would expect there to be more convective flow within the phantom due to the temperature gradient induced and maintained by the waterbath. In this situation I would also expect that the Brownian factor should decrease with increasing temperature, as is demonstrated by the results presented in Figure 4.12. Although all three data sets shown in this figure demonstrate an inverse relationship between temperature and Brownian factor, there are marked differences between the specific Brownian factors for each temperature, and this disparity warrants further investigation. It is possible that this disparity could be due to the different flow profiles that occur across the 5 mm diameter aperture of the LLG and the ferrule opening of the single-mode fibre, especially at higher waterbath temperatures.

Figure 4.11 also shows the results of fitting the mixed motion model D_b values to the Stokes-Einstein equation, both in terms of the Stokes-Einstein model fits and the extracted intralipid particle radii, for all three data sets. There is close agreement between the Laurence algorithm, multi-tau algorithm, and holographic FD-DCS data, which yield an intralipid particle radius of 98, 102, and 98 nm, respectively. These values are all within a maximum 4 % deviation of each other. Furthermore, these values are in close agreement with previous measurements of intralipid by the same manufacturer using transmission electron microscopy (TEM) in [167], which suggest an average particle radius of 107 nm. By failing to account for a mixed model fit in this experiment (i.e., by using a Brownian motion model only), intralipid particle radii of 90, 94, and 88 nm are extracted for the Laurence algorithm data, multi-tau algorithm data, and holographic FD-DCS data, respectively, and a reduction in the goodness of model fitting to the Stokes-Einstein relation also occurs.

4.8 Comparing SNR performance with conventional DCS

I define the SNR of a D_b measurement to be the mean D_b value over N measurements, divided by the standard deviation in those measurements

$$\mathrm{SNR}_{D_b} = \frac{\mu(D_b)}{\sigma(D_b)}. \tag{79}$$

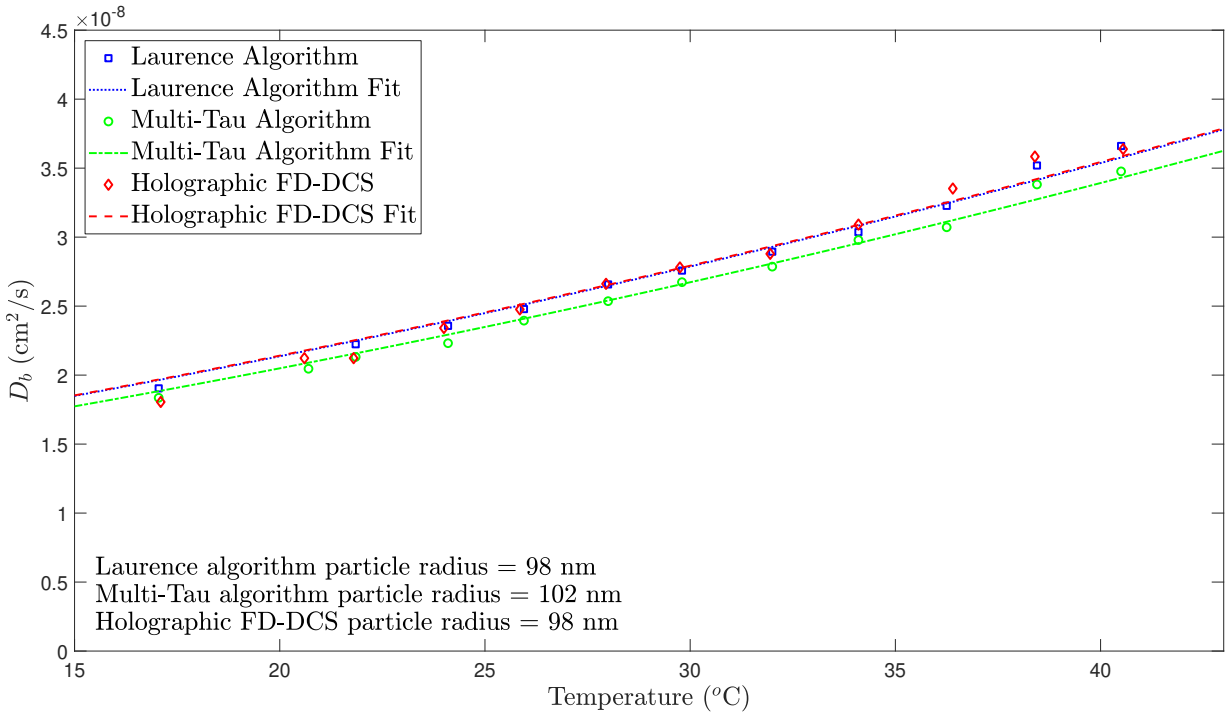

Figure 4.11: The distribution of D_b values for both conventional DCS and holographic FD-DCS over a temperature range in an optical tissue phantom using native domain mixed model fitting. Model fits to the Stokes-Einstein equation and extracted intralipid particle radii are also shown for all three data sets.

To assess the SNR_{D_b} benefit conferred by the holographic FD-DCS instrument under optical blackout conditions, I measured SNR_{D_b} (using a Brownian model of motion) over a range of flow parameter output rates in an intralipid phantom with optical properties similar to that of brain tissue ($\mu_a = 0.10$ cm^{-1} and $\mu_s' = 7.5$ cm^{-1} [22]), for an SDS distance of 15 mm and $N = 100$. This was achieved by the addition of Indian ink (Windsor & Newton, Liquid Indian Ink, 1010754) to an intralipid phantom, based on in-house dilution calibration experiments (using a PerkinElmer Lambda 750 S UV/Vis/NIR spectrophotometer). By varying the number of camera frames taken at each detuning frequency, the overall parameter output rate can be traded for the number frames to average, and thus the SNR_{D_b} in the measurement. For example, with measurement at 6 detuning frequencies, a camera exposure time of 0.299 ms and a camera frame rate of 303 Hz, an overall parameter output rate of 23.8 Hz can be obtained by capturing 2 camera frames per detuning frequency. Increasing the number of frames captured per detuning frequency to 11 effectively decreases the overall parameter output rate to 4.5 Hz.

I then performed equivalent analysis on conventional DCS data (autocorrelated using the Laurence algorithm) collected under matched conditions by collecting raw photon counting data and discretising it into N samples (each of length equal to T_{frame}, the *total* time required to acquire a D_b frame using the holographic FD-DCS instrument). Using a Brownian motion model fit to this data, I then calculated an SNR_{D_b} value for

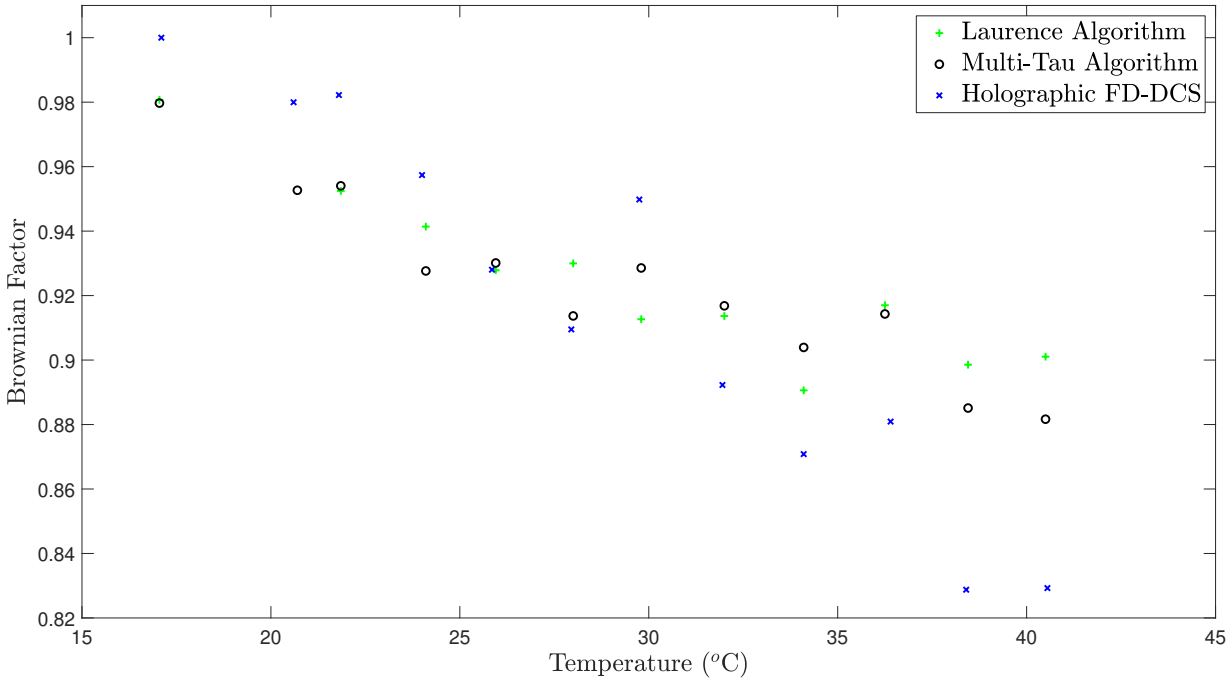

Figure 4.12: The distribution of Brownian factors for both conventional DCS and holographic FD-DCS over a temperature range in an optical tissue phantom using native domain mixed model fitting.

conventional DCS data at matched overall parameter output rates. For both holographic FD-DCS and conventional DCS data, I observed that SNR_{D_b} scales with $\sqrt{T_{\mathrm{frame}}}$, as is to be expected for a variable exhibiting Gaussian noise, as demonstrated in Figure 4.13.

The holographic FD-DCS instrument offered an improvement in SNR_{D_b} over conventional DCS by a mean factor of 2.3 over all 10 parameter output rates that were investigated. This is surprising considering that in the order of $\sim$1300 modes of light are detected for $N_{\mathrm{pix}} = 512$, which have undergone a heterodyne gain process. However, it must be considered that for this specific selection of exposure parameters the camera is operating at a 9.1 % duty cycle, whereas the SPAD is capable of detecting individual photon arrival times at a maximum rate of 13.3 MHz. Increasing this duty cycle is therefore motivated in the future work of this thesis, to further increase the SNR advantage of the system, which could be achieved by using a multiple camera setup, for example. Additionally, the camera has a quantum efficiency of $\sim$33 % at the operating wavelength of the laser, and a gain of 5.73 photoelectrons per digital count. Therefore, for every 100 photons incident upon a camera pixel, only 6 digital counts will be produced. However, the SPAD has a detection efficiency of $\sim$70 % at the operating wavelength of the laser. The use of a higher performance NIR-enhanced camera could therefore be considered to improve the relative SNR_{D_b} performance of the system, and this is discussed further in Chapter 7.

The results obtained by repeating this experiment under normal ambient lighting

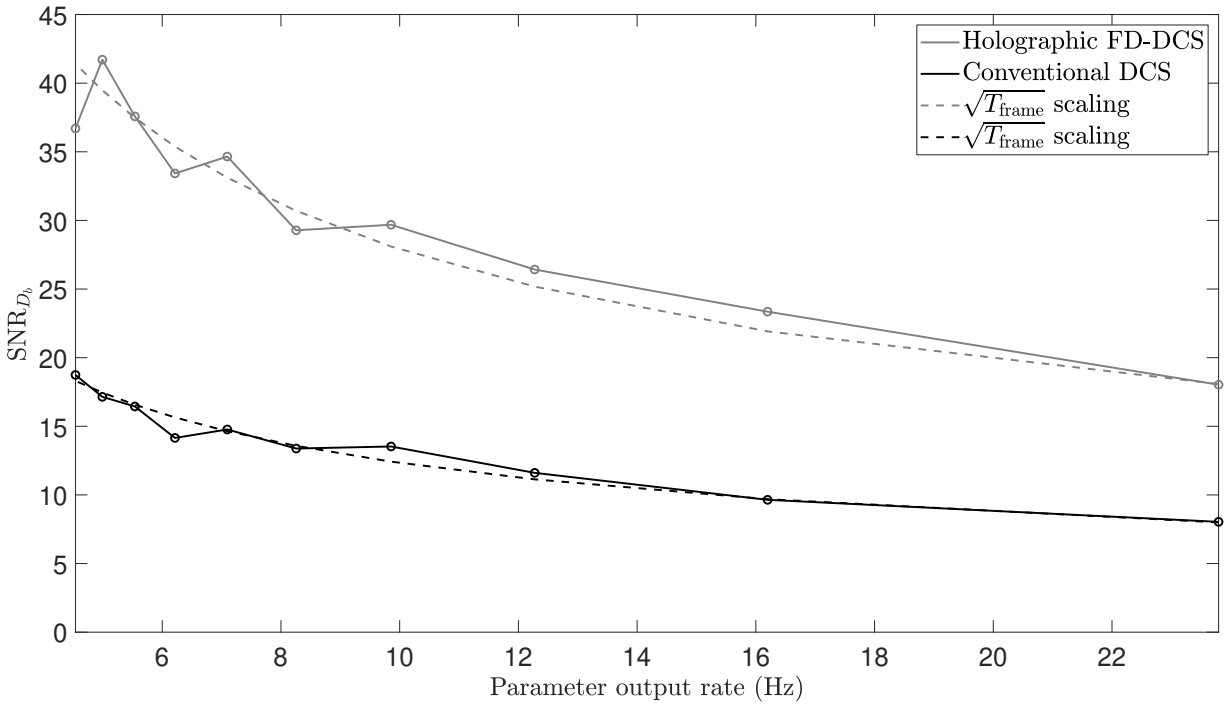

Figure 4.13: SNR_{Db} performance against overall parameter output rate for conventional DCS and holographic FD-DCS experiments, under optical blackout conditions.

conditions are shown in Figure 4.14. These experimental conditions result in an increase in the SNR_{D_b} mean improvement factor to 5.2, due to degradation of SNR_{D_b} associated with the conventional DCS technique. This confirms the relative insensitivity of the holographic FD-DCS technique to ambient light.

The *absolute* values of SNR_{Db} for the holographic FD-DCS data vary from Figure 4.13 to Figure 4.14, as, although performed under entirely equivalent experimental conditions, these experiments were performed on different samples, with possible drift in experimental apparatus between data collection sessions. However, the *relative* SNR_{Db} improvement of holographic FD-DCS with respect to conventional DCS for each of these two experiments is the key concern here, the behaviour of which is consistent with the prediction that holographic FD-DCS is relatively insensitive to ambient light.

4.9 Demonstrating *in vivo* feasibility

The challenges for the design of a holographic FD-DCS instrument for *in vivo* application were discussed in Sections 3.6 and 4.3. In addition to these considerations, patient safety limits must also be adhered to: the maximum permissible exposure of the skin to laser radiation at a wavelength of 785 nm is 2.96 mW/mm^2 [20]. I achieved this by making use of a fixed focus fibre collimator which produces a beam of 2.1 mm diameter (Thorlabs, F220APC-780), such that a maximum output power of 10.25 mW can be accepted at the end of the sample arm. To acceptably manage the risk of exposure of

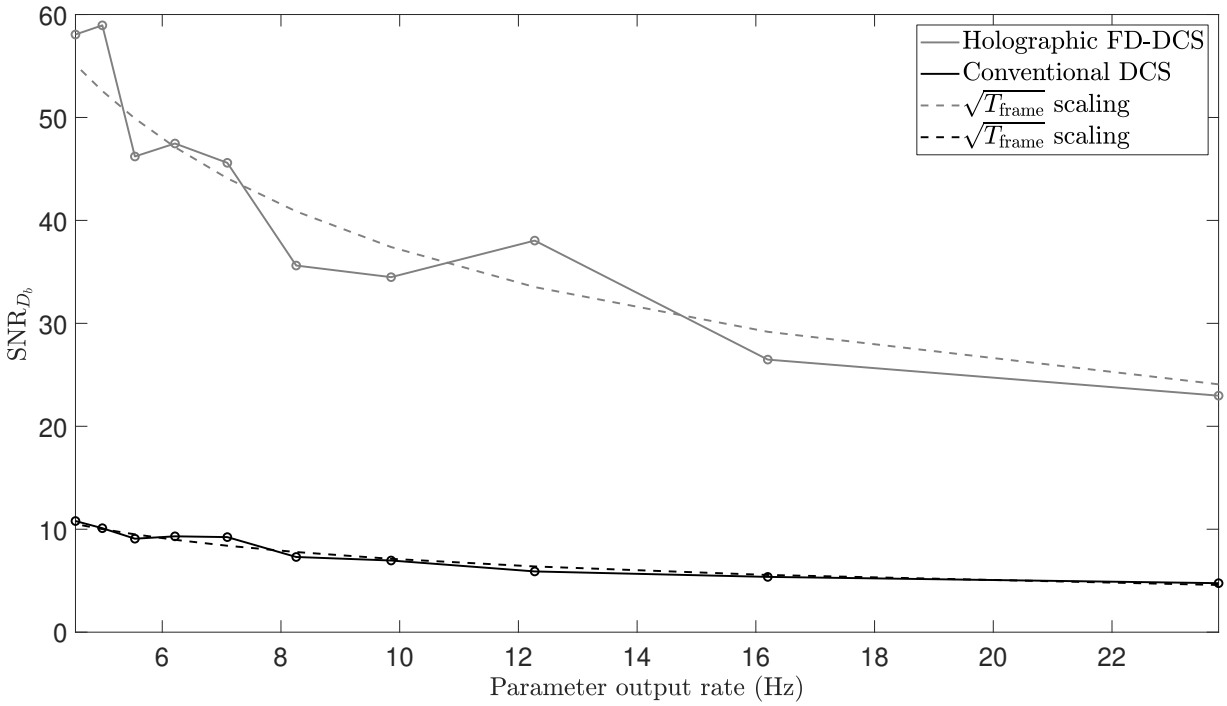

Figure 4.14: SNR_{Db} performance against overall parameter output rate for conventional DCS and holographic FD-DCS experiments, under ambient lighting conditions.

the naked eye to the collimated beam, safety glasses were worn by all persons present during acquisition of *in vivo* data.

The interferometric design of the system is highly sensitive to both sample movement and external sources of vibration. This can be ameliorated by selecting short camera exposures, and also by good experimental design. To this end, I designed a NIR opaque 3D printed probe with a neoprene sleeve to minimise the effects of stray light, as demonstrated in Figure 4.15. The LLG and collimator are both fixed in place with grub screws, and the lens of the collimator is held in contact against the skin by an optical mounting stage. The SDS distance of the probe is 11.3 mm, which provides an imaging depth of $\sim$ 3.8 - 5.7 mm.

By developing an understanding of the complex interplay between the parameters of the instrument and the flow values that are expected in a particular DCS geometry, I can determine the most appropriate camera exposure parameters for any given experiment. For example, when making forearm measurements I assume sample optical properties of $\mu_a = 0.25\ \text{cm}^{-1}$ and $\mu_s' = 4.27\ \text{cm}^{-1}$. These are the average of the measurements acquired from the forearm of three healthy volunteers at a wavelength of 788 nm by Wang *et al.* [22]. This group used sample optical properties measured at 788 nm to analyse data from DCS experiments of the same samples, which were undertaken using a 785 nm laser source. I therefore deem the values that I have selected to be appropriate estimates of the optical properties of the sample in this experiment, which also operates at 785 nm.

Figure 4.15: Top (left), and underside (right) views of a 3D printed *in vivo* probe with an SDS distance of 11.3 mm.

Using a conventional DCS system, these optical properties were used to recover the range of D_b values that would be expected in the sample. Then, for this particular experimental geometry, this allows the expected power spectra during both diastole (low flow) and systole (high flow) for Brownian motion to be modelled, as shown by Figures 4.16 and 4.17.

Inspection of Figure 4.17 shows that, for a camera exposure time of 2 ms and a camera frame rate of 200 Hz, the HWHM of the expected diastolic power spectrum and the HWHM of the IRF are equivalent, resulting in significant broadening of the measured diastolic spectrum (grey dotted line); however, this effect is much less pronounced during systole (black dotted line). I have chosen to sample at frequencies where the greatest measured change is expected over the cardiac cycle, and these are indicated by the circles on each of the measured power spectra in Figure 4.17. Additionally, since the camera exposure time is in the order of the expected tissue decorrelation time ($\sim$1 ms [18]), optimal detection sensitivity is expected [143]. The camera operates at a duty cycle of 40 % using these exposure parameters, which is an improvement over the 9.1 % duty cycle used in Section 4.8.

Selecting the location of detuning frequencies to sample at, and the number of camera frames to record at each of these frequencies, is a trade-off between the competing interests of the following two considerations:

- increased averaging for improved SNR, and picking more frequency points to make fitting to the FD-DCS analytical model more robust;
- the overall flow parameter output rate.

Choosing the 6 frequency points shown in Figure 4.17, with 3 camera frames at each point, gives an overall parameter output rate of 10.8 Hz for these camera exposure parameters, ensuring that pulsatile information can be accurately recovered, which we expect to contain significant frequency content at 1 - 2 Hz. Therefore, this information can be faithfully recovered by using a sampling rate of at least $\sim$ 4 Hz. However, I am

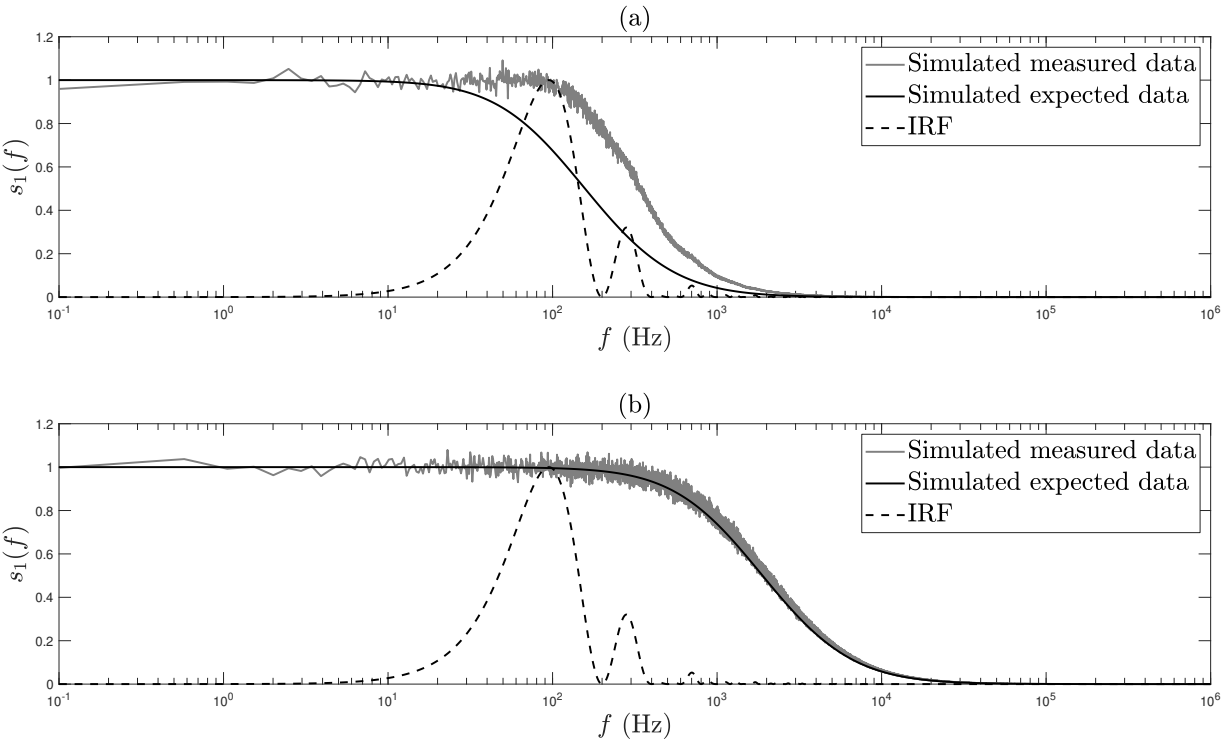

Figure 4.16: Simulated power spectra (black plots) expected during (a) diastole, and (b) systole. The IRF is shown by the black dashed plots, and the simulated measured power spectra, after IRF broadening, are shown by the grey plots. These simulated data were generated using a holographic FD-DCS forward modelling tool, using a camera exposure time of 2 ms, a camera frame rate of 200 Hz, a DC subtraction temporal filtering technique, 3.8 % Gaussian measurement noise, and averaging over two S_1 data sets.

motivated to sample even faster than this, for the reasons outlined in Section 2.3.6, and the overall parameter output rate of 10.8 Hz that I have achieved for this experiment therefore represents significant progress toward this goal.

Figure 4.18 validates the *in vivo* applicability of the instrument in the context of contact forearm measurements (this study was approved by the UCL Research Ethics Committee, project ID number: 1133/001). Subplot (a) of this figure shows the signal obtained from a the holographic FD-DCS instrument, with the resolution of pulsatile flow clearly visible in the signal. Subplot (b) of the same figure shows the conventional DCS signal for reference, at an equivalent overall parameter output rate (autocorrelated using the Laurence algorithm). Fourier transforms of these D_b time series, which were acquired using a Brownian model of motion, reveal peak content at 64.9 beats per minute (bpm) in both cases, as demonstrated in Figure 4.19. This was consistent with the resting heart rate of the volunteer in this study.

The mean value of the holographic FD-DCS D_b time series in Figure 4.18(a) is 1.13 $\times$ 10^{-8} cm^2/s, whereas the mean value of the conventional DCS D_b time series in Figure 4.18(b) is 0.58 $\times$ 10^{-8} cm^2/s. I attribute this to broadening of the measured signal by the

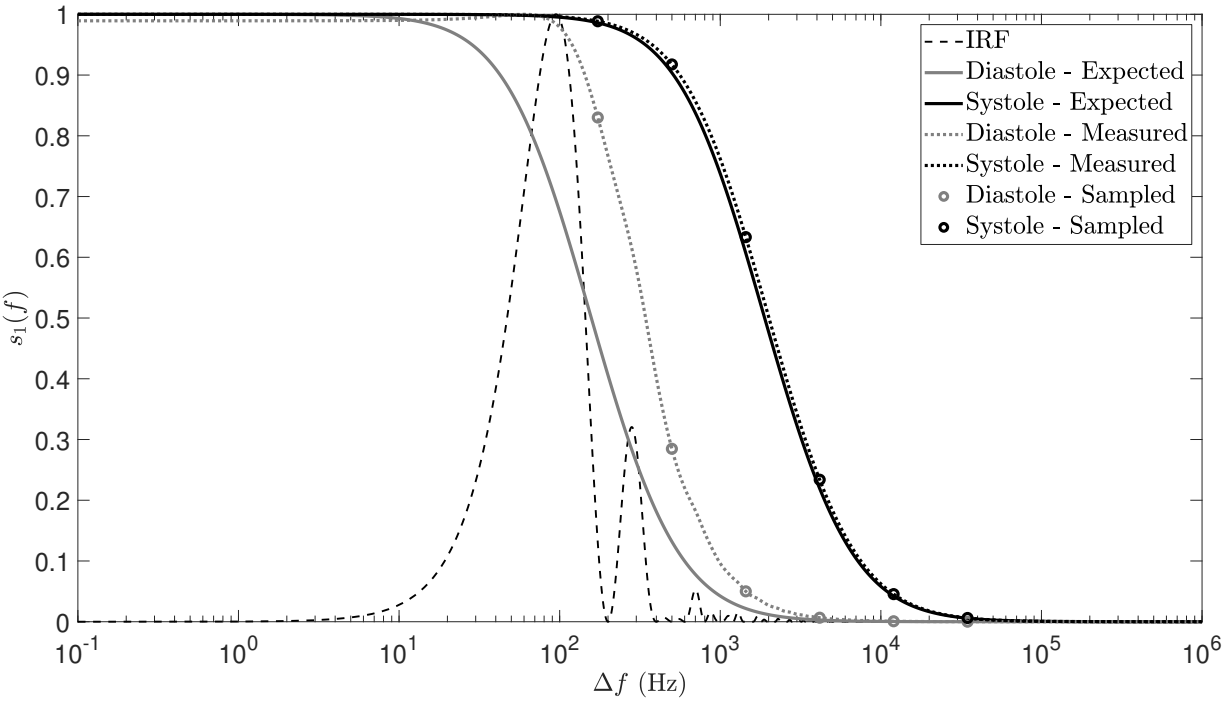

Figure 4.17: Simulated noiseless data, used to aid selection of appropriate detuning frequencies. The solid lines show the range of power spectra that are expected (using D_b values acquired from conventional DCS data collection). The dotted lines simulate the effects of IRF broadening on the expected power spectra. The simulated measured power spectra are then sampled where the greatest measured change is expected over the cardiac cycle (these sample points are depicted by the circles on each of the measured power spectra).

IRF of the system, as demonstrated in Figure 4.17, which artificially elevates the lower D_b values especially (as confirmed by fitting D_b values to the simulated measured data in Figure 4.17).

4.10 Chapter summary and discussion

The experiments performed in this chapter have shown that holographic FD-DCS can measure data that are entirely equivalent to conventional DCS, but with a higher optical throughput, a decreased cost of detector and a robustness to the effects of ambient light. Improved SNR has been demonstrated *in vitro*; however, this advantage is yet to be demonstrated *in vivo*. By developing and validating a mixed motion DCS Fourier domain model, as well as a temperature dependent model for the optical and dynamic properties of intralipid phantoms, I can achieve accurate interpretation of the data produced by the instrument in its native domain, which is fundamentally different to conventional DCS data. These differences arise due to the alternative sampling strategies of data in the time and frequency domains, the effects of static scattering in a holographic FD-DCS system, the nature of the noise, and broadening by the IRF, especially at high parameter output rates. These high output rates have been made possible by the design

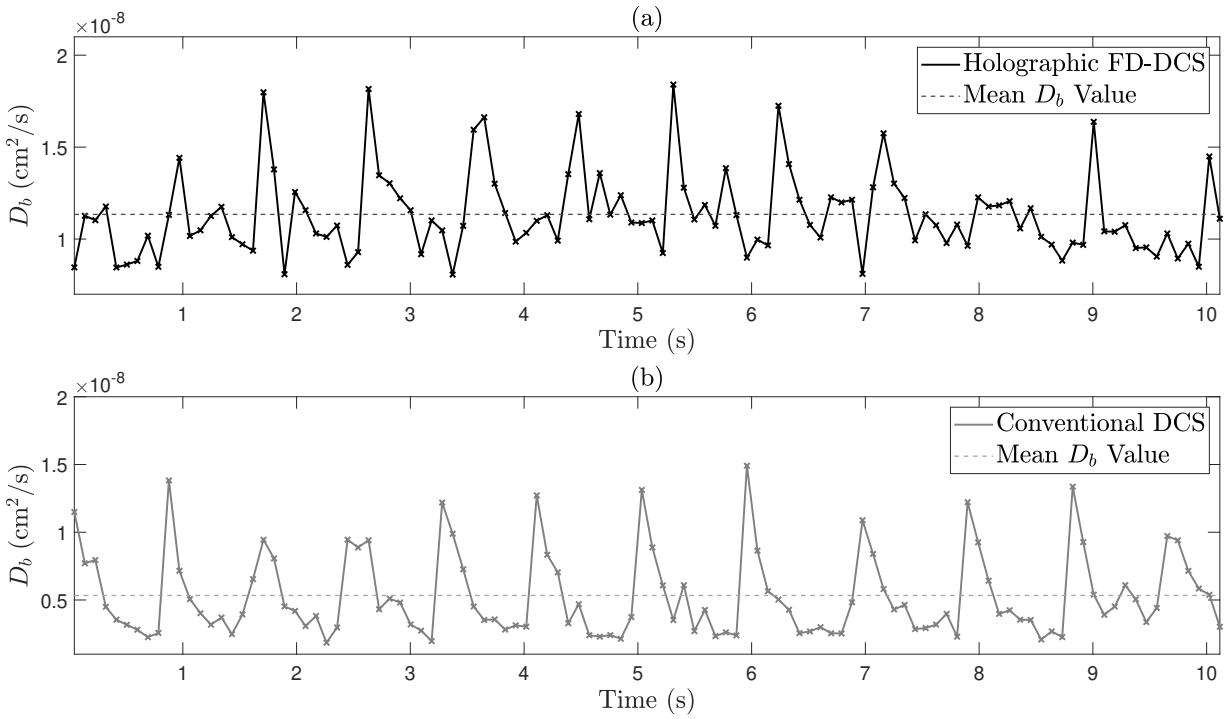

Figure 4.18: D_b time series for contact forearm measurements acquired at 10.8 Hz, using both (a) holographic FD-DCS, and (b) conventional DCS. The dashed horizontal lines represent the mean D_b value for each time series. Qualitatively, conventional DCS appears to have a better SNR than holographic FD-DCS, which I suspect is due to movement artefact and sub-optimal tissue coupling associated with an *in vivo* sample (this is discussed further in Sections 4.10 and 7.2.2).

of a custom instrument with a high throughput and minimal dead-time, which enables highly parallel GPU-accelerated holographic demodulation and is thus suited to *in vivo* application.

With reference to Figure 4.10, I conclude that, due to the noise in the measured data, DCS model fitting in the native domain is preferable to numerical transform and fitting in the complementary domain. Whilst the deviations in D_b measurement using complementary domain fitting that are shown in Figure 4.10 are relatively small for the very slow acquisition times used in the exemplar configuration of Section 4.6, they are significant when optimising for fast acquisition times with a broader IRF, especially when imaging samples with a static scattering component. Thus, fitting with a native model appears to be an appropriate technique to achieve accuracy in flow parameter measurements.

My mixed model fitting procedure has been rigorously validated by the results of Section 4.7. Compared to the Brownian model of motion, the mixed motion model D_b values shown in Figure 4.11 have an improved fit to the Stokes-Einstein relationship (Equation 77), and the extracted intralipid particle radii values are also in closer agreement with the TEM gold standard measurement [167]. This is because, although the speed of both the Brownian and convective components of the phantom increased as

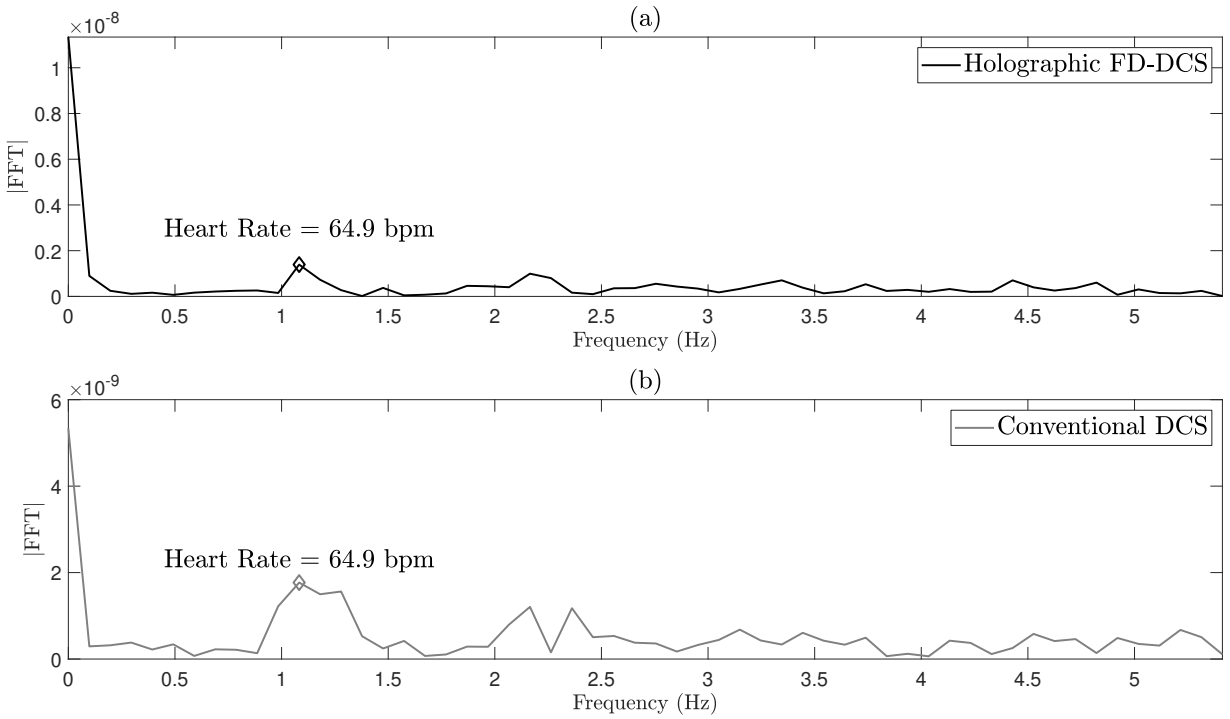

Figure 4.19: Fourier transform of the two time series in Figure 4.18 reveals peak frequency content at 65 bpm for both (a) holographic FD-DCS, and (b) conventional DCS.

the phantom was heated, the sample became less Brownian and more convective due to circulating currents within the waterbath (i.e., the Brownian factor decreased), and therefore allowing for this variation was important in revealing the underlying *absolute* D_b agreement between the conventional and holographic FD-DCS techniques. I therefore conclude that to show absolute equivalence between conventional DCS and holographic FD-DCS over a temperature range, the use of a mixed model fit to account for a Brownian factor variation is essential. However, the experiments in Sections 4.6, 4.8, and 4.9 do not make use of mixed model fitting, as the Brownian factor of the sample is not expected to vary within the course of each of these experiments.

Holographic FD-DCS is an inherently heterodyne and multispeckle detection technique. Conventional DCS has, until recently, been a homodyne single speckle detection technique. However, due to recent developments in the field [23, 31, 32], a fuller comparison of holographic FD-DCS (especially with regard to assessing SNR performance and robustness to ambient light) could be achieved by comparison to both single and multispeckle conventional heterodyne DCS techniques [i.e., interferometric diffuse correlation spectroscopy (iDCS), interferometric diffusing wave spectroscopy (iDWS), and multi-exposure iDWS (MiDWS)], and these comparisons form part of the future work of this thesis. However, the reduction in detector cost afforded by holographic FD-DCS, as well as the scalability of a detection strategy that operates at the shot noise limit, is a compelling advantage of this technique.

Despite validating and demonstrating the potential advantages of holographic FD-DCS, this chapter does not reflect the full potential of this technique. The short camera exposure times that were used in Section 4.9, which are necessary to sample fast enough to resolve pulsatile information, introduce a complication to the measured data. Spectral broadening by a relatively wide IRF artificially elevates the measured D_b values in Figure 4.18(a). Correcting for this, whilst sampling at only a limited number of detuning frequencies (especially in the presence of static scattering due to the skull, for example), represents a significant challenge, and this will form part of the future work of this thesis. Following on from this, the SNR advantage that was demonstrated *in vitro* in Section 4.8 was not achieved *in vivo* in Section 4.9. I suspect that this is in part due to movement artefact, which is a known problem of multimode detection [98], and sub-optimal tissue coupling in the system [96]. Therefore, experimentation into the effect of various collection optics and tissue coupling mechanisms, together with minimising other sources of movement and vibration in the system, is warranted. In light of this, a rigorous SNR performance characterisation of the holographic FD-DCS system for *in vitro* data collection is offered in Chapter 5.

Whilst the SDS distances used in this chapter (1.13 - 1.75 cm) are relatively short compared to the SDS distances of 2 - 3 cm typically used in human applications [4], this does not detract from the purpose of this proof of concept work, where the aim is to demonstrate the quantitative equivalence of measurements made using the holographic FD-DCS method. The future work of this thesis will assess the feasibility of the system to detect signals under the more challenging conditions provided by larger SDS distances, such as 3.5 cm (as was recently achieved by Zhou *et al.* [24]).

4.11 Conclusion

I have developed a new Fourier domain implementation of DCS by building an off-axis HPSD instrument. Rapid operation of this holographic FD-DCS instrument is enabled by a GPU-accelerated holographic demodulation system, which currently operates with a throughput of 79.4 M pixels per second when detecting ∼1300 modes in parallel. To show absolute equivalence between conventional DCS and holographic FD-DCS, the use of a novel mixed model fitting process, together with a novel temperature dependent model for the optical and dynamic properties of intralipid phantoms, is a key step. In this chapter I have also demonstrated the SNR_{Db} advantage that holographic FD-DCS yields compared to conventional DCS, as well as its relative insensitivity to ambient light. Finally, the feasibility of making *in vivo* measurements using holographic FD-DCS was demonstrated by acquiring forearm contact measurements. By considering the IRF of a holographic FD-DCS instrument, appropriate camera exposure parameters can be selected to allow for the high parameter output rates necessary to make *in vivo* measurements. The holographic FD-DCS system is limited by the duty cycles available with the

camera that is currently in use, especially when using very short camera exposure parameters. The future work of this thesis will therefore involve duty cycle optimisation, as well using higher performance NIR-enhanced cameras, and further development of a probe for *in vivo* detection.

To the best of my knowledge, this chapter represents the first time that a holographic FD-DCS technique has been used to recover *in vivo* flow measurements, at a fast enough sample rate to ensure the accurate recovery of pulsatile information. Additionally, this technology can readily be applied to longer wavelengths, which have previously been shown to improve SNR and depth sensitivity, but which are currently incompatible with existing detector technologies in conventional DCS. This offers exciting prospects not only for the potential of deeper multispeckle DCS measurements, but also for the potential of acquiring spatially resolved DCS measurements using acousto-optic tomography (AOT) techniques.

5 System performance characterisation

5.1 Chapter contribution

In this chapter I report on a systematic characterisation of the signal-to-noise ratio (SNR) performance of the holographic Fourier domain diffuse correlation spectroscopy (FD-DCS) instrument described in Chapter 4. In Section 5.2, I demonstrate and eliminate outliers in the measured data that are due to laser mode hopping, and I also correct for a model of the system's modulation transfer function (MTF) in Section 5.3. To the best of my knowledge, this is the first time that these two noise sources have been identified and removed from a digital holography experiment. In Section 5.4, I then describe the SNR performance problem that was encountered during initial performance characterisation of the instrument. By using spatiotemporal filtering as a validation tool in Section 5.4.1, I determine whether any given experimental setup is affected by limiting noise sources that compromise maximal SNR performance, and I use this to document the effects of varying laser source power in Section 5.4.2. In Section 5.4.3, I detail the final contribution of this chapter: a novel multispeckle denoising algorithm, the development of which has allowed the removal of spatiotemporally *uncorrelated* noise from the measured data, and which has also allowed the demonstration of a linear relationship between SNR gain and the square root of the number of speckles detected, as predicted by the theory of multispeckle detection. The denoising algorithm can also be used to go beyond this linear relationship by the removal of sampling noise, but this comes at a cost of decreased temporal resolution.

By bringing together the techniques outlined in this chapter, I achieve an *in vitro* SNR gain of 36, for a flow parameter output rate of 8.2 Hz, when detecting over $\sim$1290 heterodyne speckles for the inexpensive camera-based detection system described in this thesis. This is the highest SNR gain reported in the diffuse correlation spectroscopy (DCS) literature to date.

This chapter forms the basis for work that was recently accepted to be published in Biomedical Optics Express [168], in which the reviewers commended the SNR improvement that I have achieved as exciting, comprehensive, novel, and of high interest. I also presented work from this chapter at Photonics West SPIE BiOS 2022 [169]. Additionally, this chapter represents a pivot in the course of the research that was conducted for this thesis. Due to the Covid-19 pandemic, Section 5.3 and onward are the output of research that was carried out entirely remotely, and which could no longer be performed in a laboratory. Furthermore, the holographic FD-DCS instrument that I described in Chapter 4 was removed from UCL in July 2021. As such, I have not been able to perform any practical work since March 2020, and considerations for future practical work have been discussed in the remainder of this thesis where appropriate.

5.2 Elimination of multimode behaviour

Interferometric techniques inherently rely on splitting a light source into sample and reference arms. In my experimental setup, a fibre-coupled beamsplitter is used to achieve this (see Section 4.3), and I have found that back reflections from this beamsplitter into the laser cavity induce mode hopping that has deleterious effects on temporal filtering (as is confirmed later in this section). These effects are visible as negative going outliers in reconstructed $\overline{S}_1$ data, as shown in Figure 5.1(a), and occur at a rate of one in every 250 data points in this figure. Even though these outliers occur infrequently in this *in vitro* validation dataset, and could therefore easily be ignored, this would not be possible when detecting at the fast D_b parameter output rates that are required to resolve pulsatile flow *in vivo*, which limit the number of $\overline{S}_1$ values used to fit per D_b measurement. An outlying data point would be costly in this context and would negate the advantages of SNR improvement and goodness of model fitting that are offered by an increased number of camera frames.

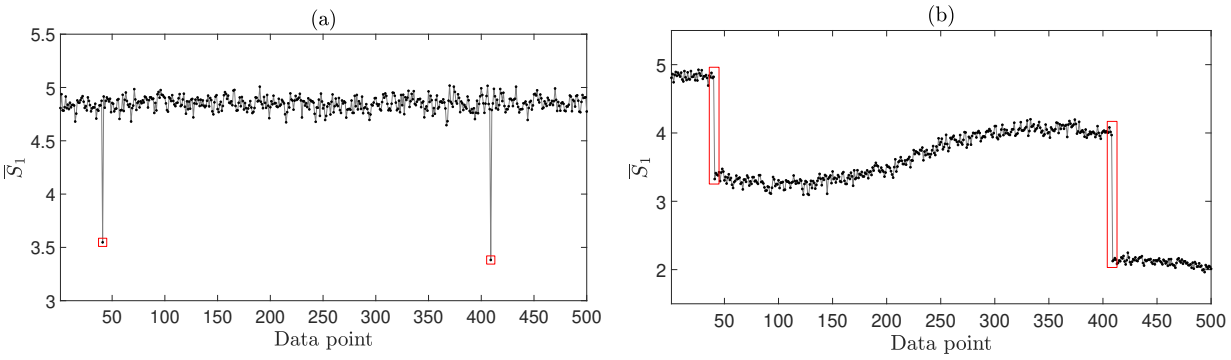

Figure 5.1: (a) Negative going outliers in $\overline{S}_1$ data (highlighted by the red squares). (b) Using an alternative temporal filtering strategy reveals discontinuities in intensity, which suggests that these outliers could be correlated with mode hopping (highlighted by the red rectangles).

The data presented in Figure 5.1(a) were acquired using a DC subtraction temporal filtering method (analogous to the approach recently presented in multi-exposure interferometric diffusing wave spectroscopy (MiDWS) [23]), in which the camera plane hologram, H_C, is constructed as the difference of two successive images

$$H_C = I_n - I_{n+1}, \tag{80}$$

which serves as a high pass filter that removes the contribution of what is assumed to be a temporally static contribution from the reference beam [34]. However, I hypothesise that if the laser were to mode hop between two successive images, then H_c would be formed from two mutually incoherent fields, which would result in an artefactual increase in $\overline{N}$, with a subsequent decrease in $\overline{S}_1$, according to Equation 53. To test this

theory, I used an alternative temporal filtering strategy

$$H_C = I_n - I_1, \tag{81}$$

where $n \neq 1$, which removes the contribution of the reference beam as it is recorded in the *first* camera frame of a measured series. The results of this analysis, shown in Figure 5.1(b), reveal discontinuities in intensity, which suggests that these outliers could be correlated with mode hopping [this behaviour can also be demonstrated using a singular value decomposition (SVD) approach - see Figure 5.9(b)].

Inspection of H_C, for both the most median data point and one of the two outliers in Figure 5.1(a), is also instructive in diagnosing this behaviour. Aberrations are present in H_C, as shown in Figure 5.2(g), for one of these outlying data points. These aberrations could occur due to camera frames I_n and I_{n+1} being derived from mutually incoherent fields for this data point, which is consistent with my hypothesis that the laser has mode hopped between these two camera frames.

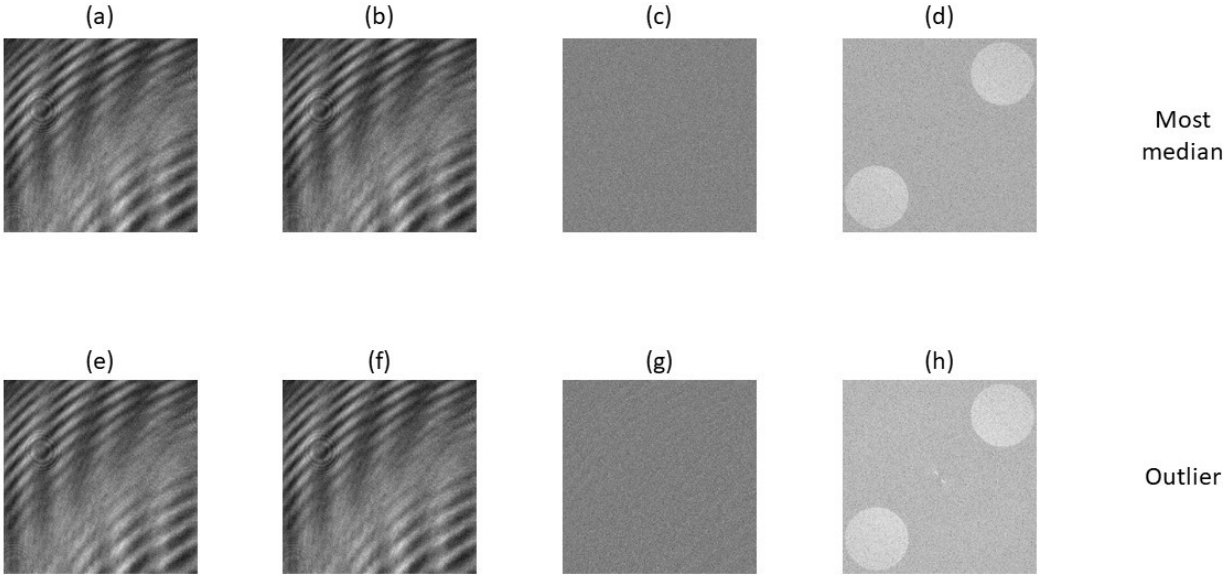

Figure 5.2: Top row: (a) I_n and (b) I_{n+1} are used to form (c) H_C, from which (d) H_R is reconstructed, for the most median data point in Figure 5.1(a). Bottom row: (e) I_n and (f) I_{n+1} are used to form (g) H_C, from which (h) H_R is reconstructed, for one of the two outlying data points in Figure 5.1(a). Aberrations are present in (g), because camera frames (e) and (f) are formed from mutually incoherent fields.

The light source in the system is a single-mode diode laser that incorporates a $\sim$35 dB optical isolator fitted at the laser head to minimise back reflections into the laser cavity. Back reflections from optical interfaces can cause the laser to mode hop unpredictably [110], and even with the use of a single-stage optical isolator it is still possible to encounter back reflections into the laser. By employing the laser manufacturer's proprietary feedback induced noise eraser (FINE) electronic feature, I am able to eliminate the outlying data points demonstrated in Figure 5.1(a), but at the expense of decreasing

the measured $\overline{S}_1$ values and introducing noise into the D_b measurement. For conventional DCS, the implementation of FINE decreased the measured β and D_b values, and I therefore suspect that FINE may reduce the coherence length of the laser.

By trimming the laser head to decrease back reflections into the main laser cavity, as well as incorporating a second optical isolator (Thorlabs, IO-F-780APC) to achieve $\sim$71 dB of total optical isolation at the laser head, I am able to eliminate outlying data points without employing FINE. Therefore, all three of FINE, laser head trimming, and dual-stage optical isolation were used as diagnostic tools to demonstrate the presence of mode hopping, but only the latter two were implemented as a solution in my experimental setup.

I confirmed that the back-reflections which caused mode hopping arose from the primary beamsplitter, by analysing data acquired under two experimental conditions: (a) removal of the reference arm, and (b) removal of both the reference arm and the primary beamsplitter. Under the experimental conditions of (a), the incidence of outliers was 167/3000; however, under the experimental conditions of (b), this incidence decreased to 2/3000. By modelling each of these two rates as a Poissonian distribution, they are statistically different at a significance level of $p < 0.0001$ using a chi-squared test.

5.3 Modulation transfer function

Due to effect of the finite size of the camera pixels $(\Delta x, \Delta y)$, the heterodyne detection efficiency within the space of H_R (k_x, k_y) is given by the MTF of the lensless digital Fourier holography instrument [138, 142, 170]. Here (k_x, k_y) refers to spatial frequency, which is a function of the rate of sampling and the number of samples in the spatial domain [170]. For example, $k_x = (N\Delta x)^{-1}$, where N is the number of camera pixels in the x dimension. The MTF is the Fourier transform pair of the spatial distribution of a single pixel in the camera plane

$$\mathrm{MTF}(k_x, k_y) = \left|\mathrm{sinc}(\sqrt{\alpha}\Delta x k_x)\mathrm{sinc}(\sqrt{\alpha}\Delta y k_y)\right|^2, \tag{82}$$

where α is the camera pixel fill factor, and

$$\mathrm{sinc}(t) = \frac{\sin(\pi t)}{\pi t} \tag{83}$$

is the normalised sinc function. Each of the terms $\Delta x k_x$ and $\Delta y k_y$ in Equation 82 is evaluated between ± 0.5 across each of the two dimensions of the camera sensor [142]. An example of the MTF for $\alpha = 0.72$ is shown in Figure 5.3(b). The MTF, which has rotational symmetry of order four, is centred on the reference beam (i.e., $k_x = k_y = 0$) and results in increasing attenuation for increasing heterodyne spatial frequencies

over the holographic twin images, but which does not affect the homodyne shot noise component [135]. I therefore update Equation 53 to become

$$S_1(\pm\Delta\omega, k_x, k_y) = \frac{\frac{S(\pm\Delta\omega,k_x,k_y)}{\overline{N}(\Delta\omega)} - 1}{\mathrm{MTF}(k_x, k_y)}, \tag{84}$$

and then proceed to take the average value within each heterodyne mask to make a measurement of $\overline{S}_1(\pm\Delta\omega)$, which, as both of the heterodyne terms are identical for the holographic detection schemes described in this chapter, I abbreviate to $\overline{S}_1(\Delta\omega)$.

As the optical tissue phantom is spatially invariant and has been imaged through the spatially incoherent core of a liquid light guide (LLG) of length 1.2 m, I expect to reconstruct a flat profile in Figure 5.3(a), which shows the average intensity of 500 reconstructed S_1 images. However, and as expected, the MTF of the instrument causes a distortion artefact whereby higher spatial frequencies are more strongly attenuated. By minimising the variance, σ^2, in the reconstructed S_1 image, for values of α in the range $[0, 1]$, I can determine the α value for the experimental setup to be 0.72, as is shown in Figure 5.4.

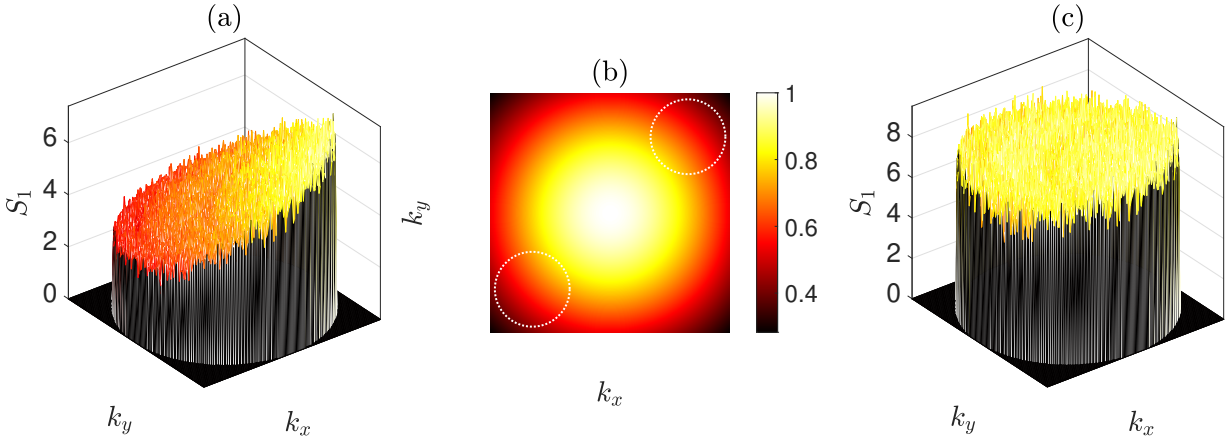

Figure 5.3: (a) Reconstructed average of 500 S_1 images without MTF correction. (b) MTF with $\alpha = 0.72$, the white dotted circles indicate the location of the twin holographic images, which lie in a common plane. (c) Reconstructed average of 500 S_1 images with MTF correction.

The manufacturer of the camera reports a camera pixel fill factor of 1.00, due to the microlenses that are used in the sensor array. The use of a microlens array will increase the light detection efficiency of the sensor; however, this does not consider the optical aberrations of the microlenses that are relevant to an *imaging* application. Additionally, the camera has a maximum quantum efficiency over visible wavelengths, and its microlenses will therefore have a wavelength response that is not designed for the near infrared. By modelling a value of $\alpha = 0.72$, as shown in Figure 5.3(b), the

flatness of the average reconstructed S_1 image in Figure 5.3(c) is optimised, and thus the distortion artefact caused by the MTF of the instrument is corrected for.

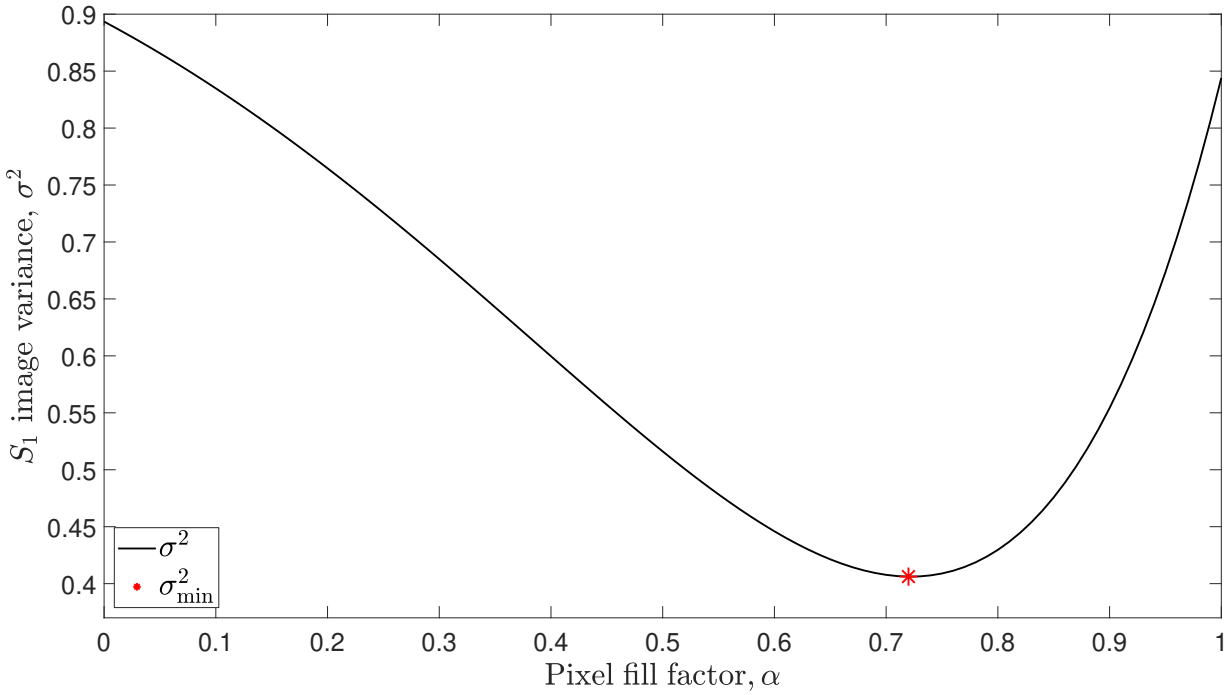

Figure 5.4: Choosing a value of $\alpha = 0.72$ minimises the variance, $\sigma^2_{\min}$, and thus maximises the flatness, of the average reconstructed S_1 image.

This optimisation process can be customised to the features of any particular experimental setup, and other appropriate optimisation targets for this experimental design could include radial symmetry, or the gradient of the radial average. I note that, in practice, it is unlikely that a fill factor of 1.00 can be achieved; for example, the use of an array of circular microlenses and square pixels will yield a maximum fill factor of $\pi/4 \approx 0.79$.

5.4 SNR scaling problem

Under the assumption of shot noise limited detection over the *entire* speckle pattern, and in the absence of detector noise and other experimental noise sources, the SNR of a speckle detection instrument should scale linearly with the square root of the number of detected speckles [25, 27, 66]. I therefore sought to verify this for the $\overline{S}_1$ values produced by my instrument, using the same intralipid optical phantom as used in Sections 4.6 and 4.7. Here I define the SNR in $\overline{S}_1$ to be the ratio of the mean value, μ, to the standard deviation, σ, of a sample of $\overline{S}_1$ values

$$\mathrm{SNR}_{\overline{S}_1} = \frac{\mu(\overline{S}_1)}{\sigma(\overline{S}_1)}, \tag{85}$$

over N repeats. For this experiment I use 501 camera plane holograms, which yields a value of $N = 500$ for DC subtraction temporal filtering, and note that the laser is being driven at its maximum rated output power of 120 mW. By varying the size of the signal mask in the holographic reconstruction process, the number of speckles that contribute to each $\overline{S}_1$ measurement can be controlled.

The resulting SNR values are plotted in Figure 5.5, where I expect to observe a linear relationship between SNR and mask radius (the square root of the number of modes is a linear function of mask radius). This shot noise limited regime is indeed observed for a mask radius of approximately 10 pixels and smaller in this figure. However, for larger mask radii, the SNR of $\overline{S}_1$ appears to form an asymptote, which suggests that another source of noise becomes limiting at this point.

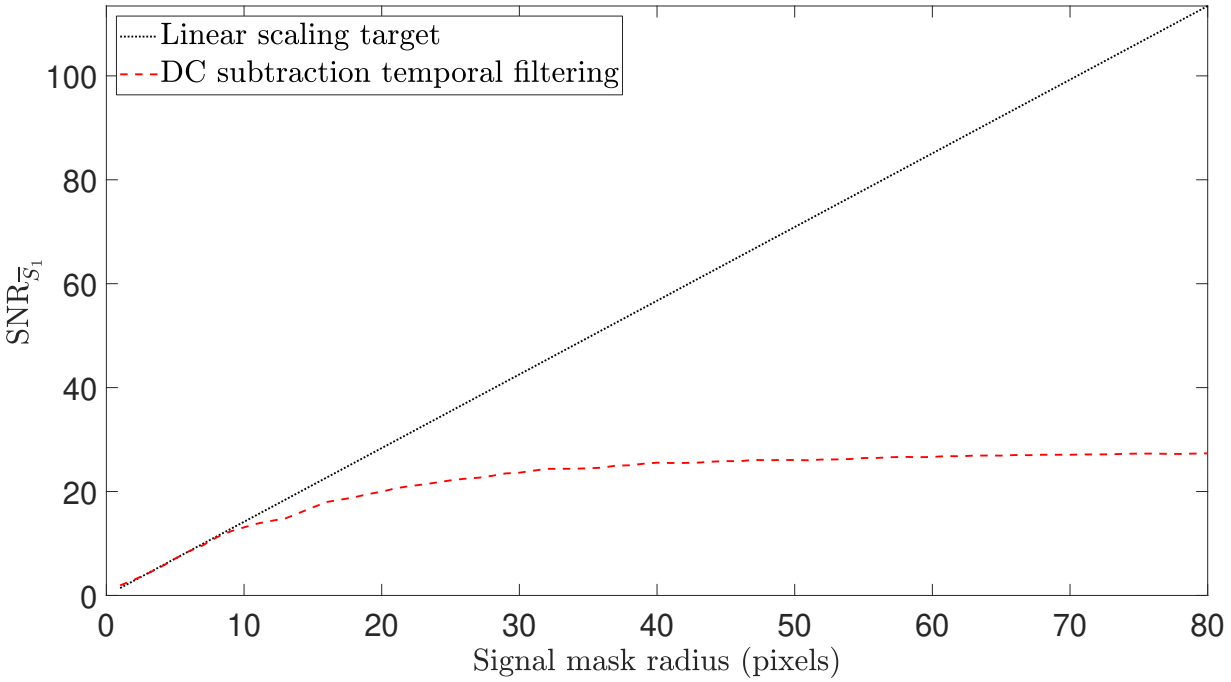

Figure 5.5: The red dashed line shows relationship between SNR$_{\overline{S}_1}$ and the radius of the demodulation mask for Δf = 0.1 Hz. The linear scaling target is shown by the dotted grey line, which is calculated from the data presented in Figure 5.11(b).

Further analysis has shown that this finding is consistent when using masks which are not centrally located within the reconstructed aperture, i.e., it is the size of the mask, not its location, which is important in determining this effect. It is fundamental that this problem is addressed, as one of the proposed advantages of holographic FD-DCS is SNR that scales with the square root of the number of pixels of relatively low-cost camera-based detection. Realisation of this proposed SNR advantage is a pre-requisite for achieving deeper imaging depths in DCS, and for the effective detection of acousto-optic tomography (AOT) signals. The remainder of Section 5.4 therefore describes the series of experiments and analysis that was performed to investigate this SNR scaling problem.

5.4.1 Singular value decomposition

The spatiotemporal filtering of holograms using an SVD approach has recently been presented in the field of laser Doppler holography (LDH) (see Section 3.3) to discriminate between the spatiotemporal characteristics of blood flow (BF), and unwanted clutter such as bulk tissue motion, camera jitter, parasitic reflections, and other physical flaws in the recording channel [171, 172]. The authors of the LDH technique achieved this by reconstructing holograms, having first performed an SVD of the holograms and setting the first n_c singular values to zero.

Within the context of multispeckle interferometric DCS (iDCS), a similar approach has also recently been presented by Robinson *et al.* [173]. These authors suggested that the largest singular values are also associated with movement artefacts and fluctuations in laser power, although the precise identity of the noise source is less important than the removal of a component of the measured data that is overly represented across the camera sensor, and which is therefore not due to the signal of an individual speckle.

The spatiotemporal filtering of holograms works by reshaping a series of n_t consecutive holograms, of spatial dimensions $n_x \times n_y$, into a 2D space-time matrix H, which has dimensions $n_x n_y \times n_t$. An SVD allows the matrix H to be described as the sum of n_t independent terms

$$H = \sum_{i=1}^{n_t} \lambda_i U_i V_i^*, \tag{86}$$

where λ_i are the singular values (ordered by decreasing value), U_i are the left singular vectors (which correspond to space), V_i are the right singular vectors (which correspond to time), and * denotes the complex conjugate transpose. This decomposition is depicted in Figure 5.6.

The basis of the spatiotemporal filtering approach is that the highest magnitude singular values correspond to variations in H with the strongest spatiotemporal correlations. Since speckle is expected to have weak spatiotemporal correlation, it is assumed that strong spatiotemporal correlations in H will be due to artefacts. In this section I propose to remove spatiotemporal clutter owing to channel noise in the experimental setup, that may be caused by laser instability and reflections at optical interfaces, for example. This is achieved by setting the first n_c singular values to zero, and reconstructing H using this updated vector of singular values. Spatiotemporal filtering is used as a validation tool against which to benchmark the SNR performance of any given experimental setup, and I demonstrate this approach in Section 5.4.2.

H is formed from 501 camera plane holograms, each of spatial dimensions 512×512 pixels. Thus, the dimensions of H are 262144×501. All 501 singular values of this matrix are computed, this first 100 of which are shown in Figure 5.7(a). The first 10 singular

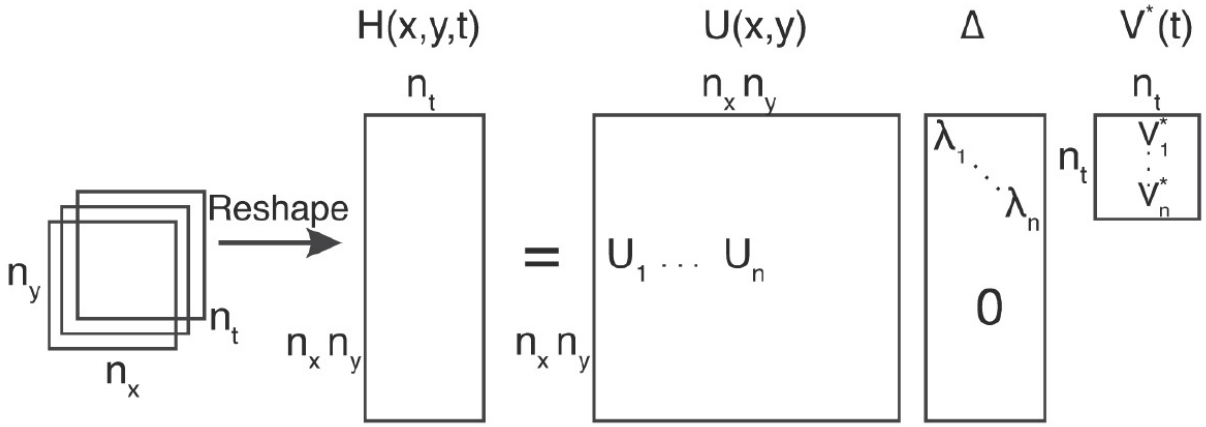

Figure 5.6: A 3D time-stack of camera frames is reshaped into a 2D space-time matrix, H. By performing an SVD, H can be described as the product of three matrices. U and V are the spatial and temporal singular vectors, respectively, and Δ is the diagonal matrix of singular values, λ_i. Reproduced with permission from [171] under the terms of the OSA Open Access Publishing Agreement. © 2020 Optical Society of America.

values are elevated due to spatiotemporally correlated noise, and a threshold value of $n_c = 10$ is therefore used. Speckle has inherently weak spatiotemporal correlation, and I make use of this fundamental property by reconstructing H having set the first n_c singular values equal to zero. As the SVD step has already implemented temporal filtering, this allows the formation of H_C using single frame holography, i.e.,

$$H_C = I_n, \tag{87}$$

and I then proceed to reconstruct each H_R according to Equation (52). The $\mathrm{SNR}_{\bar{S}_1}$ analysis is then repeated for this spatiotemporally filtered data, and it is found that the SNR performance is closer to the linear scaling target, as is depicted in Figure 5.7(b), with shot noise limited detection persisting up until a mask radius of approximately 25 pixels.

5.4.2 Laser source power

With a view to characterising the source of the noise that has been removed by the SVD step in Section 5.4.1, I repeated this analysis on data acquired using a reduced laser output power of 100 mW, the results of which are shown in Figure 5.8. This time, the spatiotemporal filtering approach results in similar SNR performance to the DC subtraction temporal filtering technique. I can therefore conclude that by reducing the laser output power, high frequency clutter has been removed from the measured data that is outside the stopband of a DC subtraction temporal filter. This can also be appreciated as a reduction in magnitude of some of the first 10 singular values in Figure 5.8(a), compared to Figure 5.7(a). Furthermore, as spatiotemporal filtering and DC subtrac-

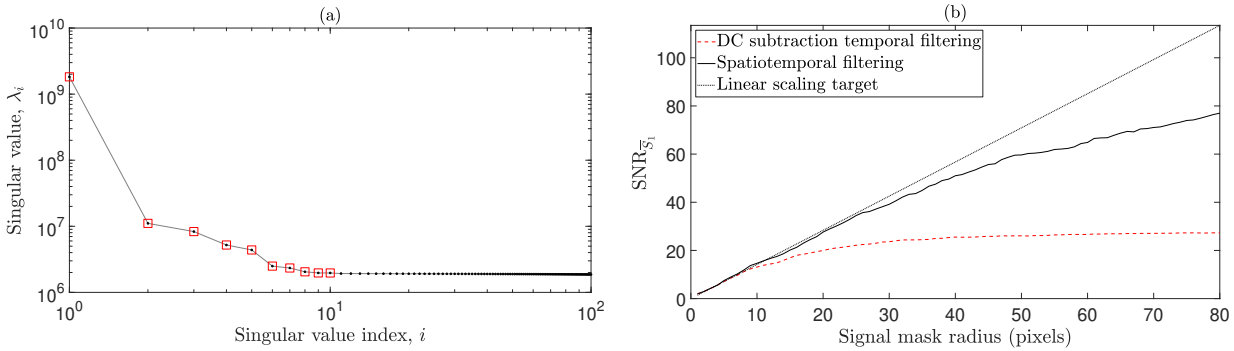

Figure 5.7: 120 mW laser output power. (a) Singular values that result from the SVD of H. The first 10 singular values (highlighted in red) are elevated and thus correlated with spatiotemporal noise. (b) Spatiotemporal filtering (plotted in solid black) results in an improvement in SNR performance compared to DC subtraction temporal filtering alone (plotted in dashed red).

tion temporal filtering offer similar SNR performance for this dataset, I can conclude that they have similar efficacy at removing low frequency clutter, which is within the stopband of a DC subtraction temporal filter.

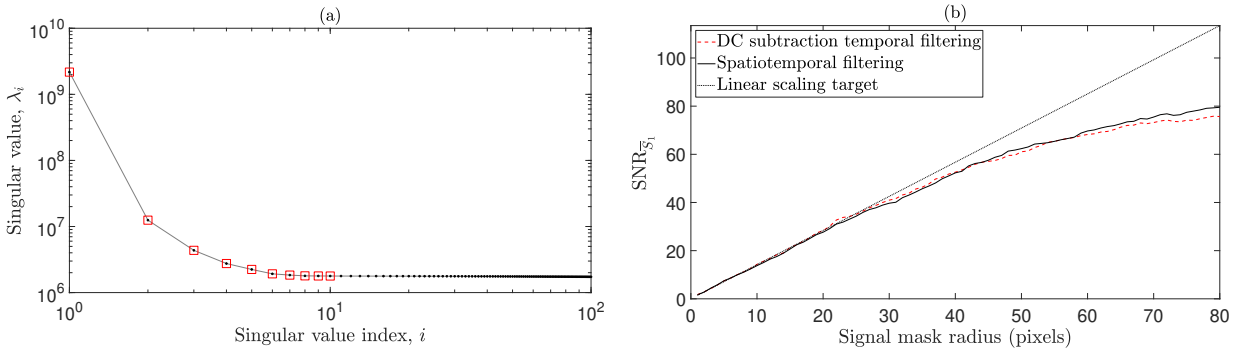

Figure 5.8: 100 mW laser output power. (a) Singular values that result from the SVD of H. The first 10 singular values (highlighted in red) are elevated and thus correlated with spatiotemporal noise. (b) Spatiotemporal filtering (plotted in solid black) results in a similar SNR performance to DC subtraction temporal filtering alone (plotted in dashed red).

As was also demonstrated by Puyo *et al.* [171], I have found that SVD provides a more robust basis than Fourier space to filter clutter from holograms. This is because high frequency clutter cannot be effectively removed using high pass temporal filtering alone. As this clutter is removed by decreasing the laser output power, it may be that the clutter is due to reflections that occur at optical interfaces within the experimental setup [110, 174]. Indeed, inspection of the temporal singular vectors associated with elevated singular values reveals the presence of beat notes when using a laser output power of 120 mW, as depicted in Figure 5.9(a), which implies that the laser is not achieving stable single-frequency operation at this power setting. Additionally, this technique can also be used to visualise mode hopping behaviour (see Section 5.2) when dual-stage optical

isolation is not used, as is shown in Figure 5.9(b).

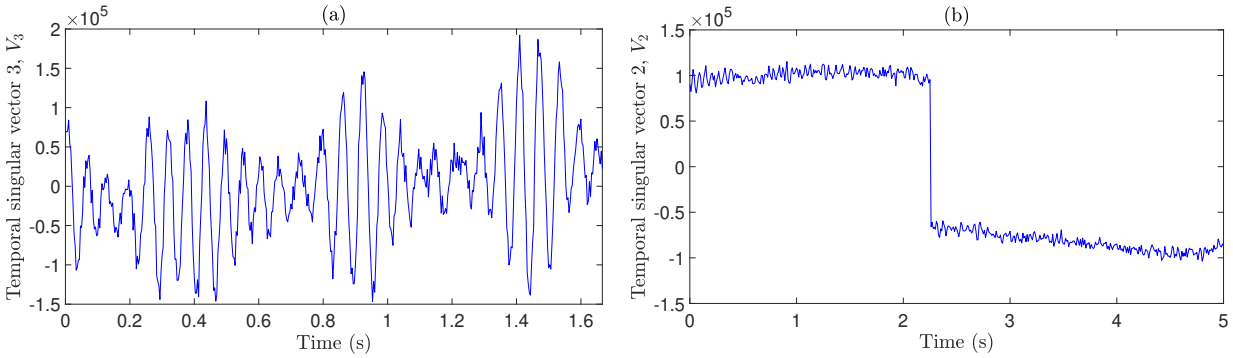

Figure 5.9: Temporal singular vector noise characterisation examples. (a) A beat note is evident when using a laser output power of 120 mW. (b) Mode hopping occurs when dual-stage optical isolation is not used.

It may also be that when pumping the laser at its maximum rated output power, phenomena such as increased spontaneous emission and technical noise (e.g., vibrations of the laser resonator, excess noise from the pump source, or temperature fluctuations) contribute noise to the measured data [175]. However, I use spatiotemporal filtering as a validation tool, rather than a final solution to implement in my signal processing pipeline, and therefore the precise identification of the sources of noise that spatiotemporal filtering removes is not imperative. The conclusion that DC subtraction temporal filtering, together with a sub-maximal laser output power, provides equivalent SNR performance to spatiotemporal filtering is key to validating the choice of DC subtraction as a temporal filtering strategy.

For these *in vitro* validation datasets, I have the luxury of computing singular values over a time-stack of $n_t = 501$ camera frames. Using this approach when detecting *in vivo* pulsatile flow rates places significant restrictions on the hardware that is used. For example, Puyo *et al.* [171] used a value of $n_t = 1024$ for their LDH technique, which was made possible by using a camera operating at a frame rate of 75 kHz. A DC subtraction temporal filtering strategy requires a minimum of only two camera frames, and is therefore a more appropriate choice for my experimental setup, which uses a camera operating at 200 Hz for *in vivo* experiments.

5.4.3 A novel multispeckle denoising algorithm

Noise due to detector nonidealities impacts the SNR performance of a multispeckle detection system [66], and in this section I demonstrate a novel algorithm to remove this noise from the measured data.

Having performed the SVD filtering step described in Sections 5.4.1 and 5.4.2, the remaining sources of noise demonstrably have no spatiotemporal correlation, and are therefore particularly challenging to remove, especially as the signal itself also has no

spatiotemporal correlation. In Figure 4(d) of [66], Xu *et al.* observed a similar phenomenon to that which I present in Figure 5.8(b) of this thesis. These authors postulated that the experimental SNR does not reach the predicted theoretical linear relationship with the square root of the number of detected speckles due to experimental imperfections, such as detector noise. The sources of noise that exist in a holographic reconstruction in lensless digital Fourier holography have been discussed in [140, 176], and these include detector nonidealities (such as quantisation noise, read noise, and pixel nonuniformity noise) and noise due to superimposed diffraction patterns caused by dust particles in the interferometric path.

In this section I present a method that allows the removal of this noise from the measured data. I start by constructing a 2D space-time matrix, as described in Section 5.4.1, but this time I reshape *reconstructed* holograms (which have undergone DC subtraction temporal filtering in the camera plane), and this matrix is denoted R. For this example, the same dataset that has been analysed in Figure 5.8 is used (i.e., a laser output power of 100 mW and a detuning frequency of 0.1 Hz). There are 20081 camera pixels within each of the signal masks shown in Figures 3.4(b) and 4.2(b), and the values within one of these signal masks is reshaped into a column vector. This is then repeated for $n_t = 500$ reconstructed holograms, and the resulting 500 column vectors are horizontally concatenated to form R, which has dimensions 20081×500, an example of which is shown in Figure 5.10(a). The formation of R does not alter the S_1 values within each reconstructed hologram, and, since this matrix of raw data is yet to be denoised (and it is to be used to test the efficacy of the denoising algorithm), it is referred to as 'control' data.

In theory, each column of R contains values sampled from the same distribution of S_1 values, but which has been independently randomised due to the nature of spatial speckle sampling (such that each column vector is therefore uncorrelated), and each column of R is therefore one in a series of independent and identically distributed random variables that has been drawn from the same probability density function (PDF). However, a further consideration is that each column of R has also been contaminated with both sampling noise and measurement noise. The next step of the multispeckle denoising algorithm involves independently sorting the elements of each column of R into ascending order, as is shown in Figure 5.10(b). This means that any temporal variation that exists between sorted holograms is due to both sampling noise, which is inherent to the speckle pattern that is measured, and also detection noise. As detector noise occurs as white noise in each camera plane hologram, its discrete Fourier transform (DFT) is a random walk and can be assumed to have speckle-like statistics [176], and therefore it can be treated as an additional speckle-like noise in the reconstruction plane. Thus I propose that speckle reduction techniques can be adapted to remove detector noise from the sorted S_1 data. In this thesis I propose median filtering, which has previously been employed to remove speckle noise from reconstructed holograms of static objects

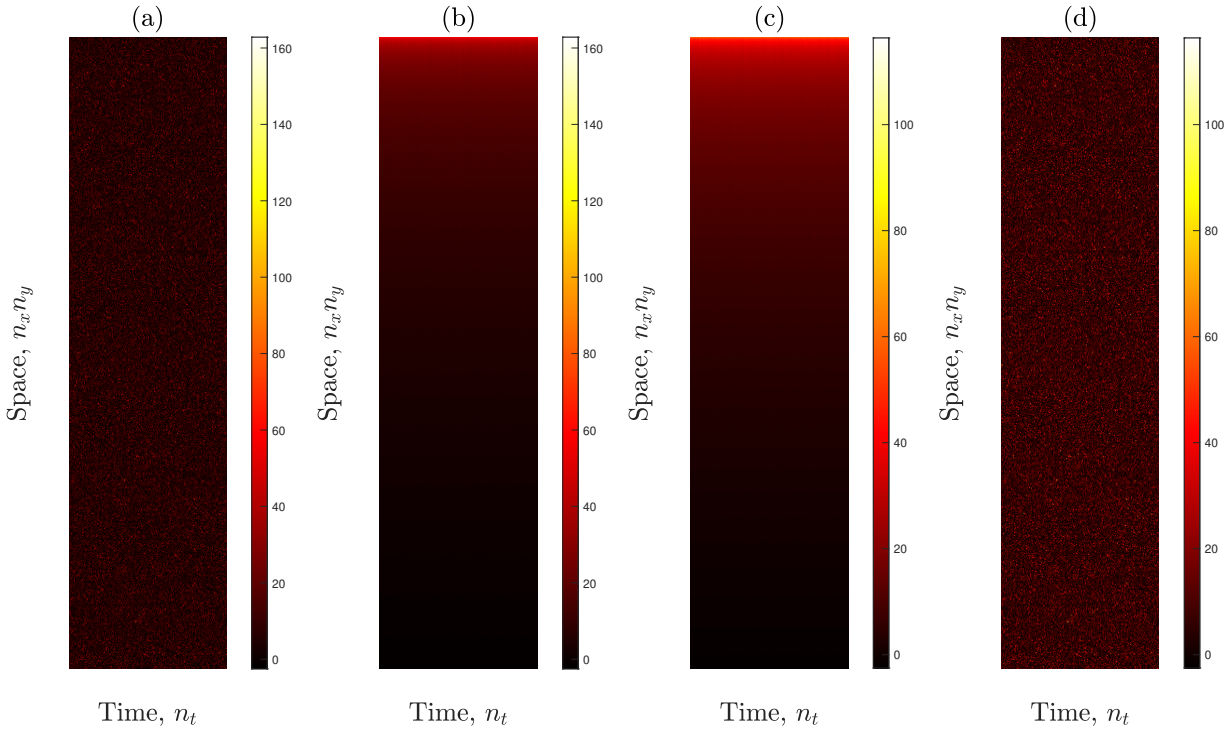

Figure 5.10: Novel multispeckle denoising algorithm. (a) The 2D space-time matrix, R. (b) Each column of R is sorted into ascending order. (c) R is then median filtered using a $[1 \times 3]$ neighbourhood. (d) The sorting is reversed.

[177].

By removing the inherently random nature of the *spatial* sampling of speckle within each column of R, *temporal* filtering can then be performed between each column of R to remove noise. This is done by filtering the sorted matrix using a $[1 \times n]$ neighbourhood (which refers to the space and time axes of R, respectively) and I choose a median filter, as discussed in the paragraph above, with a value of $n = 3$. I am motivated to use a low value of n so as not to compromise the temporal resolution of the measurement, and I have found that $n = 3$ is the lowest value of n that achieves the linear SNR scaling that multispeckle detection predicts, as depicted in Figure 5.13. The results of median filtering the sorted matrix are shown in Figure 5.10(c). The sorting of each column is then reversed to restore the random nature of spatial speckle sampling, as is shown in Figure 5.10(d), and this matrix is referred to as 'denoised' data.

The distribution of the $\overline{S}_1$ values of each column of the control data are shown by the red histogram in Figure 5.11(a), which also shows the distribution of the $\overline{S}_1$ values of each column of the denoised data by the black histogram. By applying the novel multispeckle denoising algorithm, the variance of the data has been decreased without disturbing its central tendency. The noise that has been removed from the control data is defined as the pixel-wise difference between the control data and the denoised data [i.e., the matrices in Fig 5.10(a) and Fig 5.10(d)]. The distribution of this noise is shown by the histogram in Figure 5.12; 99.95 % of the noise that has been removed from this

dataset has an absolute value less than the camera read noise (2.45 photoelectrons), and 99.99 % of the noise that has been removed has an absolute value less than the camera quantisation interval (5.73 photoelectrons). As almost all of the noise is contained within the read noise and quantisation interval of the camera, this suggests that the detector is a limiting noise source for this dataset, and I am thus confident that the final source of noise that has been removed by this denoising step is detector noise.

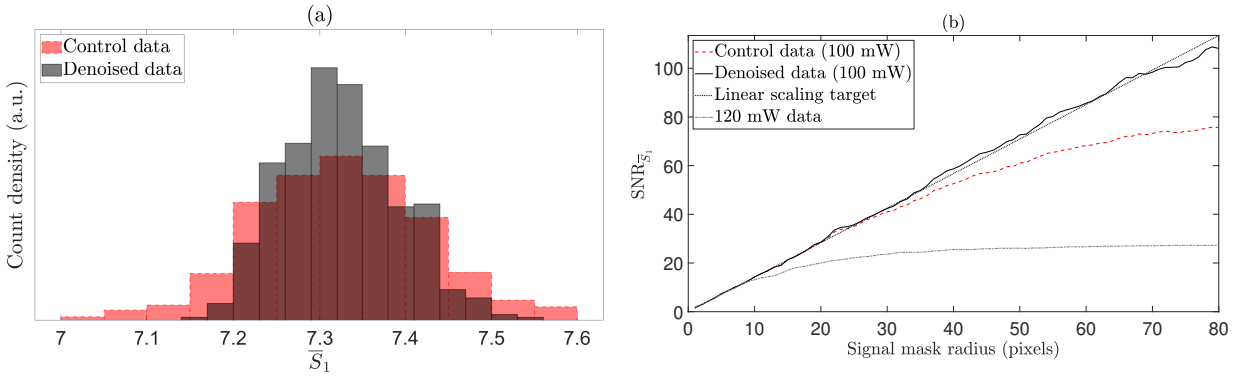

Figure 5.11: (a) Red and black histograms show the distribution of 500 $\overline{S}_1$ values for control and denoised data ($n = 3$), respectively. (b) Denoising achieves the theoretical linear scaling target (which is calculated as the linear line of best fit through the origin that includes the maximum number of data points possible whilst still retaining an R-squared value of at least 0.99) for SNR performance, as shown by the black solid line. For effective comparison, SNR performance achieved using 120 mW laser output power and DC subtraction temporal filtering is shown by the grey dash-dotted line.

I then reorder each of the columns of the denoised data back into the form of the native signal mask, and repeat the $\mathrm{SNR}_{\overline{S}_1}$ analysis that is given by Equation 85. The results of this are shown by the black solid line in Figure 5.11(b), which demonstrates that the theoretical linear scaling target for SNR performance has been achieved, and that the shot noise limited detection regime persists up until a maximum mask radius of 80 pixels. I repeat this validation for all six detuning frequencies for this dataset, as is shown in Figure 5.13. Additionally, to verify that the denoising process does not corrupt the power spectral density (PSD) measurement, D_b was fitted to both control and denoised data in Figure 5.14, which confirms that the signal is unchanged by the denoising process.

Finally, I define the SNR gain of my multispeckle detection system to be the ratio of $\mathrm{SNR}_{\overline{S}_1}$ achieved with multispeckle DCS to $\mathrm{SNR}_{\overline{S}_1}$ achieved with single speckle DCS, using detectors with the same performance [10] and at the same detuning frequency. The geometry of my experimental setup has been described in Chapter 4, and for the observation distance used in the current dataset ($z = 76.84$ mm), a single speckle occupies 15.6 pixels on the camera sensor. Figure 5.15 shows that, at a detuning frequency of 1 kHz and for a value of $n = 3$, the experimental SNR gain fits the theoretical prediction that SNR gain is equal to the square root of the number of detected speckles, and I

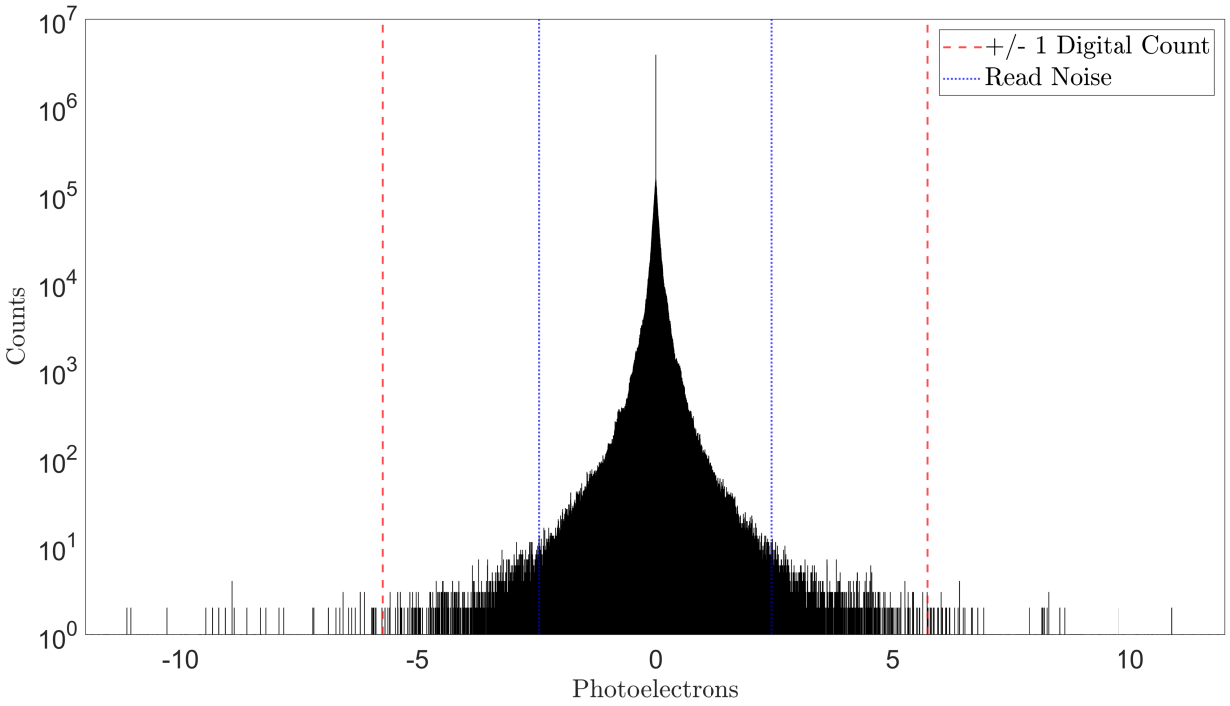

Figure 5.12: Noise distribution histogram, where noise is defined as the pixel-wise difference between the control data and the denoised data [i.e., the matrices in Fig 5.10(a) and Fig 5.10(d)]. 99.95 % of the noise has an absolute value less than the camera read noise (2.45 photoelectrons), and 99.99 % of the noise has an absolute value less than the camera quantisation interval (5.73 photoelectrons).

find that this relationship is validated at all six measured detuning frequencies for this dataset. I achieve an SNR gain of 36 when detecting ∼1290 speckles in parallel.

5.5 Chapter summary and discussion

The current state-of-the-art in SNR performance achieved by a multispeckle DCS system is described by Sie *et al.* [10], who reported an *in vitro* SNR gain of 32 when detecting *homodyne* speckles using a 1024 pixel single-photon avalanche diode camera, with a source-detector separation (SDS) distance of 11.0 mm (see Section 2.3.6.2). I have achieved an *in vitro* SNR gain of 36 when detecting over ∼1290 *heterodyne* speckles in parallel, with an SDS distance of 17.5 mm, using a detector that is two orders of magnitude less expensive. Additionally, compared to homodyne DCS, heterodyne DCS has been shown to offer an SNR gain of ∼2 for *in vitro* experiments [32] (see Section 2.3.6.4).

An *in vivo* SNR gain of 16 has recently been reported in a DCS system that has a design wavelength of 1064 nm, and which uses superconducting nanowire single-photon detection (SNSPD), with an SDS distance of 25.0 mm on the forehead of human subjects [30] (see Section 2.3.6.3). Although I have not reported *in vivo* results in this chapter, this, together with optimisation of an *in vivo* probe, will form part of the future work of this thesis, as has already been discussed in Chapter 4. The *in vivo* data that I

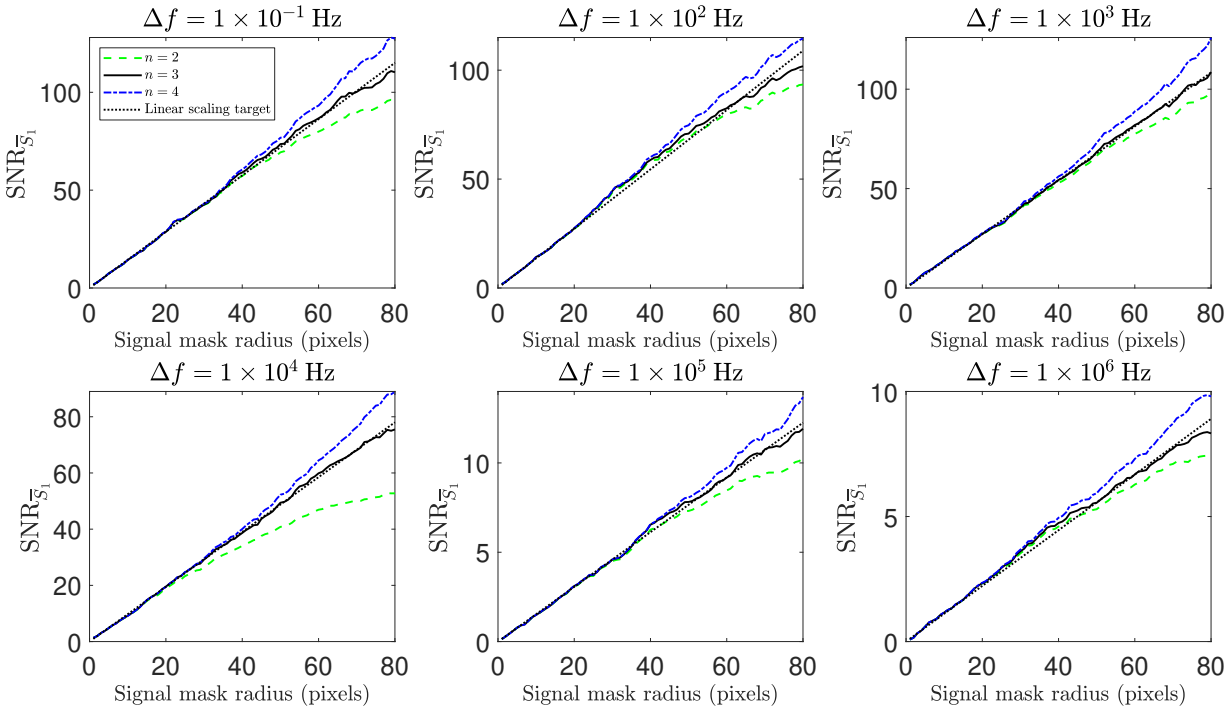

Figure 5.13: Denoising with $n = 3$ achieves the theoretical linear scaling target for SNR performance at all six detuning frequencies for this dataset, as shown by the black solid line in each subplot. Denoising with $n = 4$ outperforms the linear scaling target at a cost of decreased temporal resolution.

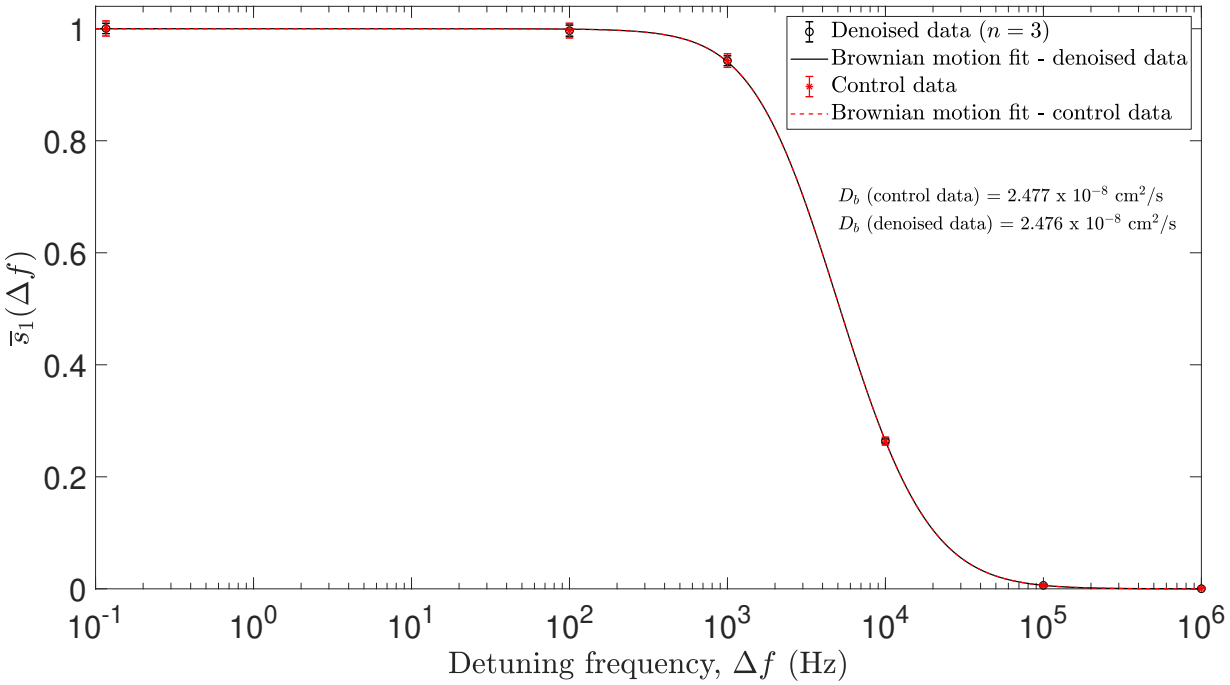

Figure 5.14: Denoising does not affect the signal contained within the PSD measurement. The D_b values fitted to control and denoised data are within 0.02 %, 0.02 %, and 0.01 % of each other for a Brownian motion fit, for values of $n = 2, 3$, and 4, respectively. Error bars represent ± 1 standard deviation of measured data.

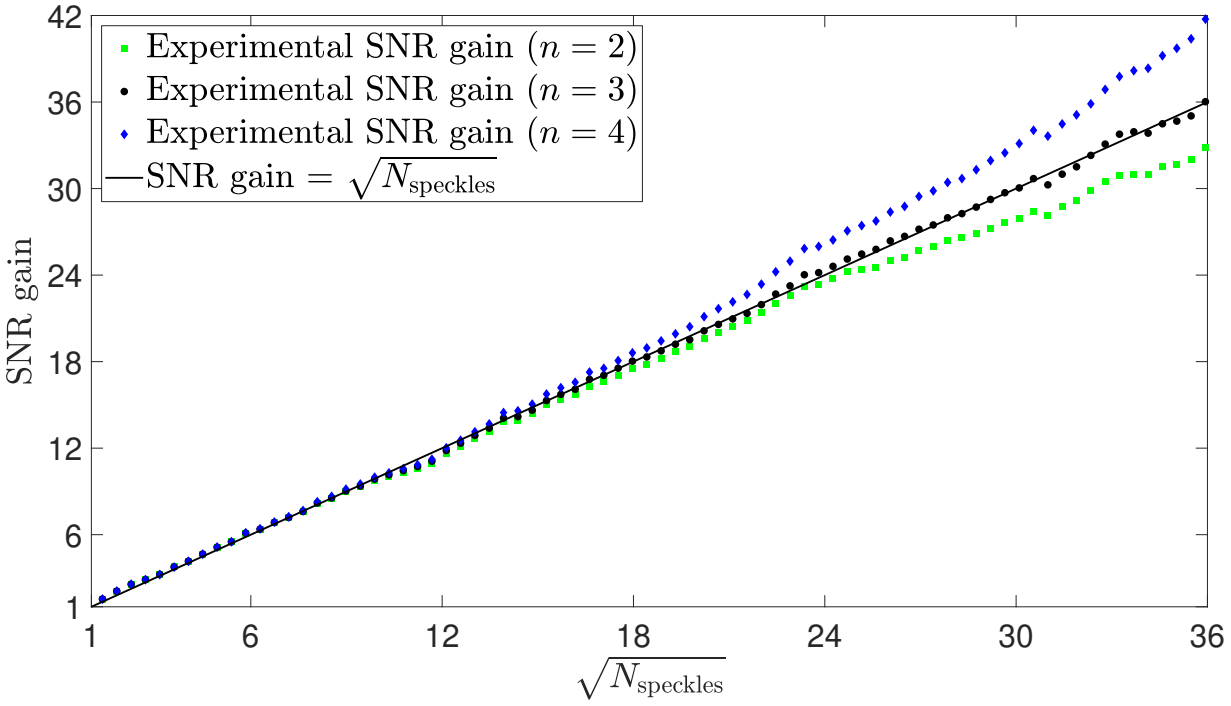

Figure 5.15: Experimental SNR gain for a detuning frequency of 1 kHz. Using a value of $n = 3$, the experimental data fit the theoretical prediction that SNR gain is equal to the square root of the number of detected speckles, $\sqrt{N_{\text{speckles}}}$. Using a value of $n = 4$ outperforms this linear prediction by reducing the independence of consecutive holograms, but at the cost of a decreased temporal resolution, which allows access to a broader range of temporal information, meaning that more speckles contribute to each measurement. The denoising algorithm does not achieve better performance than the theoretical shot noise limit, but rather its utility lies in demonstrating the distribution of noise that needs to be removed in order to achieve this fundamental limit, as demonstrated in Figure 5.12.

presented in Chapter 4 involved the capture of three camera frames at each detuning frequency, using a sub-maximal laser output power of 39 mW, with a subsequent D_b frame rate of 10.8 Hz for my current experimental setup. The multispeckle denoising algorithm requires the capture of four camera frames at each detuning frequency for $n = 3$, and doing so slows down the resulting D_b frame rate to 8.2 Hz. However, this frame rate is still sufficiently fast to recover pulsatile information.

The value of n that is used in the novel denoising algorithm represents a trade-off between temporal resolution and denoising performance. Indeed, I note that by using a value of $n > 3$, I can reduce the independence of consecutive holograms further, without perturbing the measured signal, thereby overcoming the linear SNR scaling limit imposed by sampling noise (as depicted in Figure 5.15) but at the cost of a decreased temporal resolution. For any given value of n, temporal averaging *without* sorting achieves the same magnitude SNR gain as temporal averaging *with* sorting, when evaluated at the maximum sampled mask radius. However, without sorting, the SNR gain does not scale as it should with the square root number of speckles, and therefore

leaves noise sources unaccounted for. In this chapter, I have found that median filtering with sorting, for a value of $n = 3$, yields the SNR statistics that are expected, and I have shown that this can be achieved by accounting for both spatiotemporally correlated noise sources and detector noise, which occurs as white noise in the camera plane. This could be further corroborated by using detectors with higher performance noise characteristics, and this will be addressed in future work.

The computational processing requirements of holographic FD-DCS are demanding, especially when operating at fast D_b frame rates. With a view to reducing the computational demand of conventional DCS experiments, deep learning techniques have recently been employed [112], resulting in a 23-fold increase in the speed of BF quantification. The application of deep learning techniques to holographic FD-DCS would be an interesting further study. The generation of training data could be performed using the algorithms that I present in Chapter 6 for the generation of wide-field two-dimensional time-integrated dynamic speckle patterns (2D-TIDSPs), which would serve as a forward model for that which is detected on the sample arm of the instrument. The development of such a forward model would also aid a fuller statistical analysis of the denoising algorithm presented in this chapter.

Finally, the SNR gain reported in this chapter has the potential to facilitate the measurement of acousto-optic modulated DCS (AOM-DCS) signals *in vivo*, which are weak at biologically safe power levels [18]. By using a heterodyne parallel speckle detection (HPSD) instrument, I obviate the need for high-frame rate detection, thus making my low-frame rate detection strategy suitable for this purpose. Therefore, the future work of this thesis will also involve the development of an acousto-optic modulated FD-DCS analytical model, as well as an exploration of depth-resolved flow measurement strategies using this technique.

5.6 Conclusion

I have systematically characterised the SNR performance of a holographic FD-DCS instrument. By bringing together the four methods detailed in this chapter, I have achieved an SNR gain which is equal to the square root of the number of measured speckles, and which is also the highest SNR gain reported in the DCS literature to date.

In this chapter I have characterised the effects of mode hopping and the MTF of my holographic FD-DCS instrument. To the best of my knowledge, this is the first time that either of these effects has been characterised in a digital holography experiment. I then used SVD filtering to remove spatiotemporally correlated source noise, before devising a novel multispeckle denoising algorithm to isolate and remove detector noise. This has been achieved using scalable low-cost camera-based detection that is robust to the effects of ambient light. This represents a significant step toward mitigating the trade-off that exists between SNR and brain specificity in conventional DCS, in typically non-

ideal clinical settings, as well as increasing the affordability of such a system.

6 Simulation of time-integrated dynamic speckle patterns

6.1 Chapter contribution

The simulation of statistically accurate time-integrated dynamic speckle patterns using a physics-based model that accounts for spatially varying sample properties is yet to be presented in biomedical optics, and in this chapter I propose a solution to this problem based on the Karhunen-Loève expansion of the electric field. In Section 6.2, I describe the motivation to simulate such images, and also detail why pre-existing methods in the literature are not used in this thesis. In this section I also detail two probability density function (PDF) solutions for time-integrated dynamic speckle patterns that have previously been proposed by Goodman [150]. In Section 6.3, I offer novel expressions for speckle contrast for various forms of field autocorrelation function, $g_1(\tau)$, that are commonly encountered in biomedical optics. I then use these expressions to validate the novel time-integrated dynamic speckle pattern simulation framework that I present in Section 6.4. In this section I then go on to show how the simulation framework that I propose can readily be extended to cases with spatially varying sample properties, that it can also be extended to include any form of $g_1(\tau)$ that results from various detection geometries, and that it can also include sample dynamic properties, as well as optical and acoustic parameters. Considerations for the use of the simulation framework presented in this chapter for the generation of a forward model of holographic Fourier domain diffuse correlation spectroscopy (FD-DCS) are then given in Section 6.5.

This chapter forms the basis for work that I published in Optics Letters [178], in which the reviewers praised the convincing and elegant nature of the simulation framework that I propose. I also presented work from this chapter at two conferences. The first of these was a presentation at IEEE IPC 2021 [179], for which I was nominated for the best student paper prize, and the second of these was an invited presentation at Photonics West SPIE BiOS 2022 [180].

6.2 Motivation and prior art

The measurement of wide-field two-dimensional time-integrated dynamic speckle patterns (2D-TIDSPs) for the purpose of blood flow (BF) measurement using inexpensive, low-frame rate cameras, is a task that is performed in a variety of modalities in biomedical optics. These modalities have all been introduced in Section 2.3; however, their relevance within the context of *time-integrated* measurement is briefly reviewed here.

The oldest example of these modalities is laser speckle contrast imaging (LSCI - Section 2.3.4.1), which was developed in the 1980s [78]. LSCI infers blood flow index (BFI) as $1/K^2$, where K is the speckle contrast of a 2D-TIDSP that has been backscattered from the sample [80]. A related technique, multiple exposure speckle imaging (MESI - Sec-

tion 2.3.4.2), is based on the acquisition of a series of 2D-TIDSPs using multiple camera exposure times [65].

Diffuse correlation spectroscopy (DCS - Section 2.3.6) is a modality that is able to measure BF at greater imaging depths than LSCI and MESI through the recovery of $g_1(\tau)$. This technique is traditionally limited to single-mode photon counting detection [3]; however, one group has recently demonstrated the feasibility of recovering equivalent information from multi-exposure 2D-TIDSPs through the use of the multi-step Volterra integral method (MVIM) [83], as introduced in Section 2.3.6.2. Additionally, in Chapters 5 and 6 of this thesis, I have presented a holographic FD-DCS instrument that makes use of low-frame rate camera-based detection in the Fourier domain to acquire DCS data using a heterodyne detection technique [151, 152].

Diffuse speckle pulsatile flowmetry (DSPF - Section 2.3.9) has recently been presented and is a technique that extends diffuse speckle contrast analysis (DSCA) from single-mode to multimode detection, with a subsequent improvement in the measurement rate of deep tissue BF that is equal to the camera frame rate [100]. Speckle contrast optical tomography (SCOT - Section 2.3.8) reconstructs 3D maps of deep tissue BF by utilising information from all the source-detector pairs that are detected by an array of detectors, such as that present within a camera [25].

The motivation to develop a forward model for holographic FD-DCS was introduced in Section 5.5: not only would such a model serve as a useful characterisation tool, but it would also find utility in aiding a fuller statistical analysis of the denoising algorithm presented in Section 5.4.3, as well as being suitable for the generation of training data for the application of deep learning techniques to holographic FD-DCS. Within a broader context, the motivation to simulate speckle patterns has also previously been put forward by Song *et al.* [181], who explained that simulation techniques are a useful complement to experimental investigation with regard to understanding speckle phenomena and their practical application [79, 154, 182]. Simulation is also a useful tool for evaluating data processing methods [81, 183] and for investigating the feasibility of novel applications of laser speckle.

Two techniques have been described in the literature to model the evolution of a speckle pattern between two statistically independent fully developed speckle patterns, based on the expected properties of $g_1(\tau)$. The first of these is the copula method [184], an empirical approach that was used [81, 182, 183] to simulate 2D-TIDSPs; however, the solutions offered by this technique do not model static scatterers and are restricted to only a few prescribed forms of $g_1(\tau)$. The second technique is a first principles approach [181] that allows for the generation of a series of fully developed speckle patterns with corresponding spatial variations in $g_1(\tau)$: the pre-defined correlation distribution method. This technique does not restrict the form of $g_1(\tau)$ that is used, and it is also able to model static scatterers. However, my investigations have shown that integrating

over time in such an evolution does not simulate a 2D-TIDSP with statistically accurate speckle contrast, the property from which sample motion may be inferred. This is because this approach does not take into account the number of statistically independent degrees of freedom (or temporal coherence lengths), $\mathcal{M}$, that influence a time-integrated speckle measurement [150].

Goodman employed the concept of independent degrees of freedom to generate an approximate solution for the PDF of a 2D-TIDSP, and also described an approach to obtain an exact solution for this problem that makes use of the Karhunen-Loève expansion of the electric field [150]. In this chapter I extend this latter approach and propose new insights to simulate 2D-TIDSP *images* in biomedical optics. By doing so, I build a robust forward model for the simulation of 2D-TIDSPs that accounts for spatial variation in $g_1(\tau)$ (with known scatterer motion and decorrelation time), camera integration time, contributions from dynamic and static scatterers, and the coherent transfer function (CTF) of the instrument.

The forward model that I have developed in this chapter is suitable for the simulation of a speckle pattern that is detected on the *sample arm* of a holographic FD-DCS instrument. Considerations for holographic image formation, numerical holographic reconstruction, and attenuation by detuning of the reference arm, are given in Section 6.5.

6.2.1 Copula method

The copula method was introduced in 2008, and works by first generating a pair of uniformly distributed and statistically independent random variables, $\mathbf{X}_1$ and $\mathbf{X}_2$, where bold notation indicates a 2D xy dependency. A copula is a function that links two individual distributions into a prescribed joint distribution function [184], and the authors of this method use a Gaussian copula to correlate $\mathbf{X}_1$ and $\mathbf{X}_2$, from which a sequence of correlated speckle patterns may be generated. Prior to using an FFT to scatter the resulting fields, a multiplicative phase factor, m, is used to modulate the rate of decorrelation of the sample, where a larger m value corresponds to a faster decorrelation. A 2D-TIDSP can then be simulated by averaging over a sequence of such frames [81].

As well as generating a sequence of speckle patterns for Gaussian forms of $g_1(\tau)$, the authors of the copula method also offer a solution for exponential forms of $g_1(\tau)$. However, these discrete solutions limit the flexibility of the copula method, as it can only accommodate forms of $g_1(\tau)$ for which analytical solutions are given. Additionally, whilst m is a useful tuning parameter when performing simulations, it does not physically represent any quantitative experimental parameter. Furthermore, the solutions offered by the copula method do not model static scatterers. For these reasons, the copula method was not used as a technique to simulate 2D-TIDSPs in this thesis, and other methods of achieving this goal were subsequently explored.

6.2.2 Pre-defined correlation distribution method

In 2016, Song *et al.* proposed an alternative method to link two statistically independent and uncorrelated random variables into a joint distribution: the pre-defined correlation distribution method [181]. These authors recognised that if two random variables $\mathbf{U}_1$ and $\mathbf{U}_2$ are uncorrelated, then a new variable $\mathbf{V}$ can be generated that has a specific correlation between $\mathbf{U}_1$ and $\mathbf{U}_2$, according to

$$\mathbf{V} = r\mathbf{U}_1 + \sqrt{1 - r^2}\mathbf{U}_2, \tag{88}$$

where r is the correlation coefficient factor between $\mathbf{V}$ and $\mathbf{U}_1$, and r takes a value in the range $[0, 1]$. By letting

$$\mathbf{U}_1 = \exp(-i\mathbf{\Omega}_1) \tag{89}$$

and

$$\mathbf{U}_2 = \exp(-i\mathbf{\Omega}_2), \tag{90}$$

where $\mathbf{\Omega}_1$ and $\mathbf{\Omega}_2$ are two 2D matrices that consist of independent uniformly distributed variables on the interval $(-\pi, \pi)$, it can be considered that $\mathbf{U}_1$ and $\mathbf{U}_2$ represent fields of random phasors in the object plane for instantaneous (or 'fully developed') speckle. Ignoring the effects of the CTF of an imaging system (i.e., by considering free-space propagation, or objective speckle), the expression for the observed intensity of an instantiation of a fully developed speckle pattern in a far field image plane is given by its Fraunhofer diffraction pattern [155]

$$\mathbf{I} = \left|\mathcal{F}\left[\mathbf{V}\right]\right|^2, \tag{91}$$

where $\mathcal{F}$ denotes the 2D Fourier transform. Incorporating the CTF of a coherent imaging system allows for the consideration of subjective, or imaged, speckle. Equation 91 then becomes

$$\mathbf{I} = \left|\mathcal{F}^{-1}[\mathcal{F}(\mathbf{V})\mathbf{H}]\right|^2, \tag{92}$$

where $\mathbf{H}$ is the CTF of the imaging system (i.e., the optical pupil function of the clear aperture), and $\mathcal{F}^{-1}$ denotes the 2D inverse Fourier transform. This then allows for the generation of a sequence of fully developed speckle patterns to be generated, each of which has a pre-defined correlation between both of the two seed variables, $\mathbf{U}_1$ and $\mathbf{U}_2$. If r is a 1D vector, then temporal decorrelation is specified. Alternatively, if r is a 2D matrix, then spatial decorrelation is specified. Finally, if r is a 3D matrix, then spatiotemporal decorrelation is specified.

Song *et al.* recognised that

$$g_1(\tau) = r^2(0, j) = \frac{\mathrm{cov}(\mathbf{I}_0, \mathbf{I}_j)}{\sigma(\mathbf{I}_0)\sigma(\mathbf{I}_j)}, \tag{93}$$

where $\mathbf{I}_0$ is the initial speckle pattern, $\mathbf{I}_j$ is the j^{th} speckle pattern at delay time τ, cov denotes covariance, and σ denotes standard deviation. These authors used the form of

$$g_1(\tau) = \exp\left(-\tau/\tau_c\right), \tag{94}$$

where τ_c is the decorrelation time of the sample, which is a commonly employed form $g_1(\tau)$ in LSCI, and which corresponds to single scattering from unordered motion or multiple scattering from ordered motion, when imaging medium sized vessels (i.e., with a diameter between 30 μm and 110 μm) [77, 80, 89]. Song *et al.* were therefore able to generate a series of fully developed speckle patterns that models the pre-defined spatiotemporal decorrelation from one fully developed speckle pattern to another, by accounting for any arbitrary form of $g_1(\tau)$, including the effects of both dynamic and static scatterers, at each pixel address within a speckle image. Further examples of the various forms of $g_1(\tau)$ used in LSCI, together with novel analytical expressions for speckle contrast, are expounded in Section 6.3.

Motivated to develop a technique to simulate a 2D-TIDSP, I explored the concept of integrating over time in such a series of fully developed speckle patterns. This was performed using two approaches: (a) a brute-force approach that involved the simulation of N images equally spaced over the camera exposure period, T, and (b) a more elegant approach that involved developing an analytical expression for a time-integrated measurement. Accordingly, for the form of $g_1(\tau)$ given by Equation 94, I find that

$$\begin{aligned}\mathbf{W} = \frac{1}{T}\Bigg[T\left(\mathbf{c}^2+\mathbf{d}^2\right) + \cdots \\ \tau_c\left(\mathbf{a}^2+\mathbf{b}^2-\mathbf{c}^2-\mathbf{d}^2\right) + \tau_c X\left(-\mathbf{a}^2-\mathbf{b}^2+\mathbf{c}^2+\mathbf{d}^2\right) - \cdots \\ \frac{2\tau_c Z(\mathbf{ac}+\mathbf{bd})\left[Y-1+Y\sqrt{1-Y}\tanh^{-1}\left(\sqrt{1-Y}\right)\right]}{\sqrt{Z\left(Y-1\right)}}\Bigg],\end{aligned} \tag{95}$$

where $\mathbf{W}$ is the intensity of a 2D-TIDSP, and where

$$x = T/\tau_c, \tag{96}$$

$$X = \exp\left(-x\right), \tag{97}$$

$$Y = \exp\left(x\right), \tag{98}$$

$$Z = \exp\left(-2x\right), \tag{99}$$

and where $\mathbf{a}$ and $\mathbf{c}$ are the real parts of $\mathbf{U}_1$ and $\mathbf{U}_2$, respectively, and $\mathbf{b}$ and $\mathbf{d}$ are the imaginary parts of $\mathbf{U}_1$ and $\mathbf{U}_2$, respectively (i.e., $\mathbf{U}_1 = \mathbf{a} + \mathbf{b}i$, and $\mathbf{U}_2 = \mathbf{c} + \mathbf{d}i$). The full

derivation of Equation 95 is given in Appendix B.

For these two approaches, I simulated a 2D-TIDSP using the simulation parameters presented by Song *et al.*: τ_c = 0.37 ms, T = 1.85 ms, an image size of 600 $\times$ 600 pixels, and **H** was modelled as a central circle function of radius 100 pixels [181]. The number of intermediate images used was $N = 2^n$, where n is an integer between 1 and 15. The equivalence of the intermediate image approach and the analytical expression approach is validated in Figure 6.1. Subplot (a) of this figure shows the sum of squared differences (SSD) between **W** acquired using intermediate image data and **W** acquired using the analytical expression; the reduction in error between the two images as N increases validates the accuracy of the analytical expression. Subplot (b) of this figure shows that as N is increased, the global speckle contrast of **W** acquired using intermediate image data converges on the global speckle contrast of **W** acquired using the analytical expression. The computational performance of these two approaches is compared in subplot (a) of Figure 6.2: the analytical expression approach offers a shorter computation time for all values of N. Finally, for a value of $N = 64$, the values of r^2 (calculated according to Equation 93) are plotted by the black crosses in subplot (b) of Figure 6.2, where excellent agreement between the simulated data and the underlying physical model of $g_1(\tau)$ is evident.

Having established both the accuracy and the computational advantage of the analytical expression that I developed, I then sought to verify the statistical accuracy of the speckle contrast of 2D-TIDSPs generated using this technique (for free-space propagation), according to Equation 4 of [65]

$$K(x) = \sqrt{\beta \left[\frac{\exp(-2x) - 1 + 2x}{2x^2} \right]}, \tag{100}$$

where $x = T/\tau_c$. This analysis is presented in Figure 6.3, in which the black crosses represent the global speckle contrast of 2D-TIDSPs acquired for a range of $= T/\tau_c$ values, and the black line plots the relationship that is expected, according to Equation 100. As can be seen from this figure, integrating over time using the pre-defined correlation distribution method fails to simulate a 2D-TIDSP with statistically accurate speckle contrast. Although the pre-defined correlation distribution method can model the spatiotemporal decorrelation between two fully developed speckle patterns over time, this approach does not work when considering a time-integrated measurement, as it does not consider the $\mathcal{M}$ value of the measurement. In this situation, many independent fluctuations of instantaneous intensity occur within the integration time. Song *et al.* allude to this limitation in their paper [181],

'The contrast profile of the simulated and experimental data fit well although

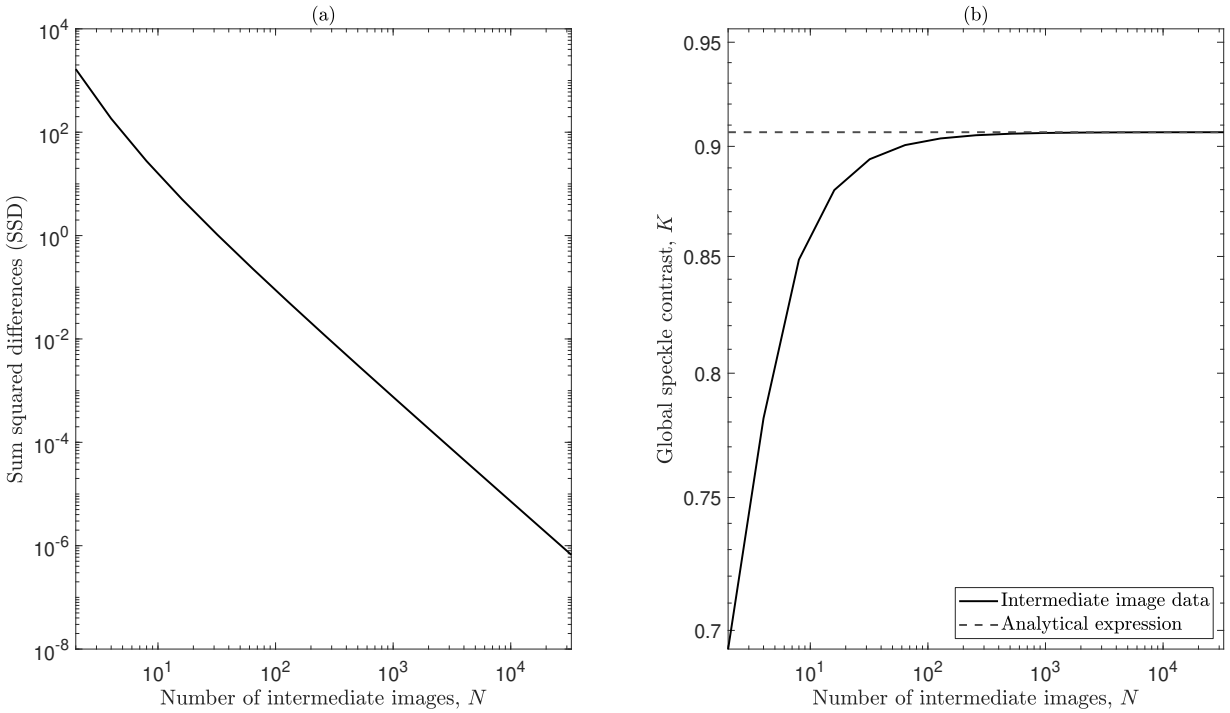

Figure 6.1: (a) The sum of squared differences (SSD) between **W** acquired using intermediate image data and **W** acquired using the analytical expression; the reduction in error between the two images as N increases validates the accuracy of the analytical expression. (b) As N is increased, the global speckle contrast of **W** acquired using intermediate image data converges on the global speckle contrast of **W** acquired using the analytical expression.

> the absolute values are different because the experimental images are not fully developed'.

The concept of $\mathcal{M}$ is explored further in Section 6.2.3.1.

6.2.3 Probability density function solutions

Although Goodman has not presented algorithms to simulate 2D-TIDSPs, he has presented solutions with which to obtain the PDF of a 2D-TIDSP [150, 155]. In this section I introduce both of Goodman's approaches to solve this problem: the approximate approach and the exact approach. Whilst both approaches will yield a PDF with the correct mean and variance, the approximate approach involves significant simplification, and only the exact approach yields a PDF with a statistically accurate distribution of intensities.

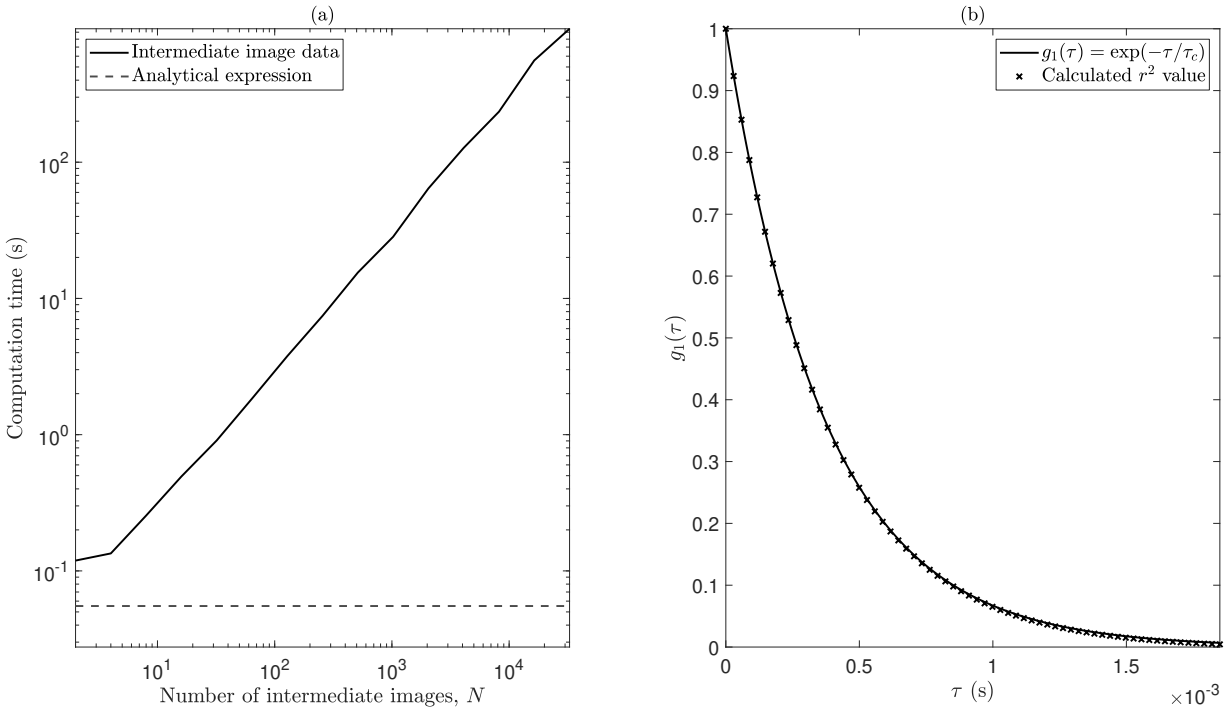

Figure 6.2: (a) Comparison of computational performance: the analytical expression approach offers a shorter computation time for all values of N. (b) For a value of $N = 64$, the values of r^2 are plotted by the black crosses, which show excellent agreement with the underlying physical model of $g_1(\tau)$.

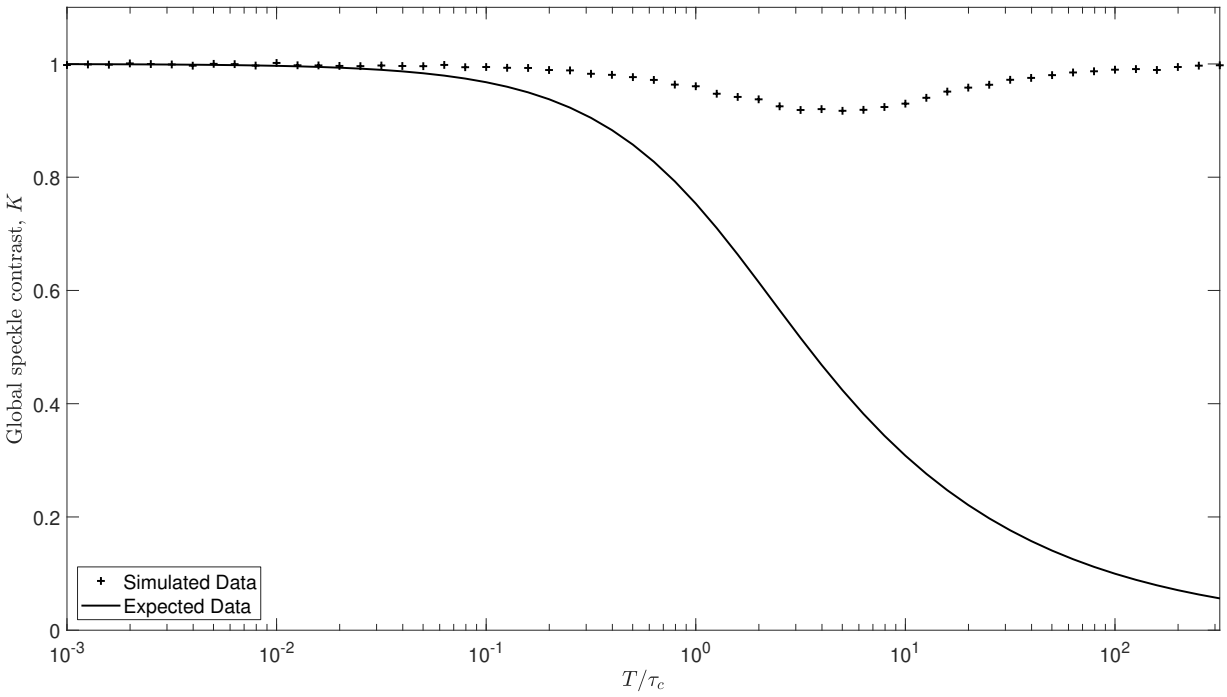

Figure 6.3: The black crosses represent the global speckle contrast of 2D-TIDSPs, simulated using the pre-defined correlation distribution method, and the black line plots the relationship that is expected, according to Equation 100, for a range of T/τ_c values.

6.2.3.1 Approximate solution

Goodman [150] developed the concept of the number of degrees of freedom, $\mathcal{M}$, contained within a finite integration period, T,

$$\mathcal{M} = \frac{1}{K^2} = \left[\frac{2\beta}{T} \int_0^T \left(1 - \frac{\tau}{T}\right) \left[g_1(\tau)\right]^2 d\tau \right]^{-1}, \tag{101}$$

for a fully polarised wave. By considering the limiting case that $T \gg \tau_c$, it can be shown that $\mathcal{M} \approx T/\tau_c$, and $\mathcal{M}$ is therefore equal to the number of temporal coherence lengths for a time-integrated measurement (and therefore the 'number of degrees of freedom' appears to be an appropriate name). Alternatively, by considering the limiting case that $T \ll \tau_c$, it can be shown that $\mathcal{M} \approx 1$, as there will always be at least one degree of freedom that contributes to a time-integrated measurement, even for the case of instantaneous speckle. The novel expressions for K, for various forms of $g_1(\tau)$ commonly employed in biomedical optics, that are presented in Section 6.3, can readily be re-expressed in terms of $\mathcal{M}$. These expressions can be used to find the asymptotes of $\mathcal{M}$ for $\lim_{T\to 0}$ and $\lim_{T\to\infty}$ for the forms of $g_1(\tau)$ presented.

Equation 101 will yield an exact expression for the mean and variance of a 2D-TIDSP; however, Goodman highlights the need to know the PDF of such a distribution, rather than just these two numerical parameters [150],

> 'In some applications, knowledge of only the mean and variance of the integrated intensity is not sufficient. Rather, the entire probability density of this quantity is desired'.

Within the context of this thesis, this statement is applicable to the accurate simulation of a 2D-TIDSP for the purpose of generating a forward model for holographic FD-DCS, for example.

Goodman's approximate approach involves replacing the smoothly varying instantaneous intensity, $\mathbf{I}(t)$, by a boxcar function on the interval $t = 0$ to $t = T$, which is divided into $\mathcal{M}$ equal subintervals. $\mathbf{I}(t)$ is assumed to be constant within each subinterval, and it is also assumed to be statistically independent of all other subintervals. The integrated intensity is then the area under the boxcar function

$$\mathbf{W} = \int_0^T \mathbf{I}(t)\, dt \approx \sum_{j=1}^{\mathcal{M}} \mathbf{I}_j \Delta t = \frac{T}{\mathcal{M}} \sum_{j=1}^{\mathcal{M}} \mathbf{I}_j, \tag{102}$$

where $\Delta t = T/\mathcal{M}$ (i.e., the width of each subinterval), and $\mathbf{I}_j$ is the value of the boxcar in the j^{th} subinterval. By considering the resulting characteristic function of $\mathbf{W}$, Goodman

showed that the PDF of $\mathbf{W}$ takes the form of a gamma PDF of order $\mathcal{M}$

$$p(\mathbf{W}) = \begin{cases} \frac{\left(\mathcal{M}/\overline{\mathbf{W}}\right)^{\mathcal{M}} \mathbf{W}^{\mathcal{M}-1} \exp\left(-\mathcal{M}\mathbf{W}/\overline{\mathbf{W}}\right)}{\Gamma(\mathcal{M})} & \mathbf{W} \geq 0 \\ 0 & \text{otherwise,} \end{cases} \tag{103}$$

where Γ is the gamma function. For a mean normalised distribution, such that $\overline{\mathbf{W}} = 1$,

$$p(\mathbf{W}/\overline{\mathbf{W}}) = \begin{cases} \frac{\mathcal{M}^{\mathcal{M}} \mathbf{W}^{\mathcal{M}-1} \exp(-\mathcal{M}\mathbf{W})}{\Gamma(\mathcal{M})} & \mathbf{W} \geq 0 \\ 0 & \text{otherwise.} \end{cases} \tag{104}$$

For $\lim_{\mathcal{M}\to 1}$, this PDF simplifies to

$$p(\mathbf{W}/\overline{\mathbf{W}}) = \begin{cases} \exp\left(-\mathbf{W}\right) & \mathbf{W} \geq 0 \\ 0 & \text{otherwise,} \end{cases} \tag{105}$$

which is the negative exponential PDF (with a mean value of 1) of one fully developed speckle pattern. As $\mathcal{M}$ increases, according to the central limit theorem the PDF approaches a Gaussian distribution. For $\lim_{\mathcal{M}\to\infty}$, the PDF becomes a delta function at $\mathbf{W}/\overline{\mathbf{W}} = 1$. Examples of the PDFs generated using this approximate technique are shown in the bottom row of Figure 6.5.

If the parameters on the right hand side of Equation 101 are known (i.e., $g_1(\tau)$, β, and T), then a value of $\mathcal{M}$ can be acquired, from which it is possible to calculate the PDF of a 2D-TIDSP, and also to simulate a 2D-TIDSP by generating an array of random numbers from a gamma PDF (by using the `gamrnd` function in MATLAB, for example). This simulation technique is advantageous in that it allows for the parameterisation of β, and it will also yield a 2D-TIDSP which has the correct mean and variance. However, this technique does not incorporate the CTF, and also the PDF distribution is not statistically correct, as is described in Section 6.2.3.2.

6.2.3.2 Exact solution

Goodman then described an exact solution for the PDF of a 2D-TIDSP [150], which makes use of the Karhunen-Loève expansion of the electric field, $\mathbf{U}(t)$ [the Karhunen-Loève expansion is described in more detail in Section 6.4]. Starting from this expansion of the electric field, Goodman showed that the PDF of a 2D-TIDSP can be expressed as the sum of an infinite number of negative exponential distributions

$$p(\mathbf{W}) = \begin{cases} \sum_{n=1}^{\infty} d_n \left[\frac{1}{\lambda_n} \exp\left(\frac{-\mathbf{W}}{\lambda_n}\right)\right] & \mathbf{W} \geq 0 \\ 0 & \text{otherwise,} \end{cases} \tag{106}$$

where

$$d_n = \prod_{\substack{m=1 \\ m \neq n}}^{\infty} \left(1 - \frac{\lambda_m}{\lambda_n}\right)^{-1}, \tag{107}$$

and where $\lambda_{m/n}$ are the eigenvalues of $g_1(\tau)$ evaluated over the integration time, T. Examples of the PDFs generated using this exact technique are shown in the bottom row of Figure 6.5.

Whilst this method provides an exact PDF solution, it is approximate in that, unless an analytical solution and tabulated eigenvalues exist for any particular form of $g_1(\tau)$, the problem must be discretised and the eigenvalues found numerically (as is demonstrated in Section 6.4). This discretisation occurs with finite numerical accuracy using a certain sampling resolution, and decisions must be made about how many eigenvalues to use and retain. Compared to Goodman's approximate method, the exact method is computationally expensive, and it does not directly parameterise β.

To the best of my knowledge, the exact PDF technique has never been extended to the simulation of 2D-TIDSPs, and neither has it ever been applied to the forms of $g_1(\tau)$ commonly employed in biomedical optics. Therefore in the remainder of this chapter, I develop an approach to achieve this in Section 6.4, and I validate the results obtained from these simulations against novel expressions for speckle contrast, which I develop in Section 6.3.

6.3 Novel expressions for speckle contrast

In this section I develop novel analytical expressions for speckle contrast, which I use to validate the 2D-TIDSP simulation framework that I develop Section 6.4, both for varying types of sample motion and various camera integration times. During the time that the research for this thesis was being conducted, these expressions for speckle contrast were published independently and concurrently elsewhere [89].

As introduced in Sections 2.3.4.1 and 6.2.3.1, speckle contrast is the ratio of standard deviation, σ, to mean intensity, μ, of a sample of speckles and can be related to $\mathcal{M}$ and $g_1(\tau)$ through [77, 100]

$$K = \frac{\sigma}{\mu} = \frac{1}{\sqrt{\mathcal{M}}} = \left[\frac{2\beta}{T}\int_0^T \left(1 - \frac{\tau}{T}\right)\left[g_1(\tau)\right]^2 \, d\tau\right]^{1/2}. \tag{108}$$

Remembering that $g_1(\tau)$ has contributions from both dynamic and static scatterers [21]

$$g_1(\tau) = \alpha|g_{1d}(\tau)| + (1 - \alpha), \tag{109}$$

where α is the fraction of the dynamic scattering component, in this chapter I consider

$$g_{1d}(\tau) = \exp\left(-\left(\frac{\tau}{\tau_c}\right)^p\right), \tag{110}$$

for values of $p = [0.5, 1, 2]$. These three forms of $g_{1d}(\tau)$ can be used to model sample motion in LSCI experiments according to scattering regime (i.e., single or multiple), particle motion type (i.e., ordered or unordered) and approximate vessel size [77, 80, 89], and these forms of $g_{1d}(\tau)$ are summarised in Table 6.1. Values of $p = 1$ and $p = 2$ can also be used to model Brownian and convective motion in DCS experiments, respectively, under certain conditions [10].

Table 6.1: Form of $g_{1d}(\tau)$ for different scattering regimes, motion types, and approximate vessel sizes in LSCI, adapted from [89].

Form of $g_{1d}(\tau)$	**Scattering**	**Motion**	**Approximate vessel size**
$\exp\left(-\left(\frac{\tau}{\tau_c}\right)^{0.5}\right)$	Multiple	Unordered	Small ($\approx \oslash < 30$ μm)
$\exp\left(-\left(\frac{\tau}{\tau_c}\right)^{1}\right)$	Multiple	Ordered	Medium ($\approx 30 < \oslash < 110$ μm)
	Single	Unordered	
$\exp\left(-\left(\frac{\tau}{\tau_c}\right)^{2}\right)$	Single	Ordered	Large ($\approx \oslash > 110$ μm)

For the form of $g_{1d}(\tau)$ given by Equation 110, I find that the general solution to the right hand side of Equation 108 is

$$K_p = \sqrt{\beta}\sqrt{\frac{\alpha^2}{2x^2}A_p(x) + \frac{\alpha(1-\alpha)}{x^2}B_p(x) + (1-\alpha)^2}, \tag{111}$$

where $x = T/\tau_c$, and where $A_p(x)$ and $B_p(x)$ are auxiliary functions, for $p = [0.5, 1, 2]$. For $p = 0.5$, I find that (analogous to Equation 15 of [80])

$$A_{0.5}(x) = \exp(-2\sqrt{x})\left(3 + 6\sqrt{x} + 4x\right) - 3 + 2x, \tag{112}$$

and

$$B_{0.5}(x) = 16\left[\exp(-\sqrt{x})(3 + 3\sqrt{x} + x) - 3 + \frac{1}{2}x\right]. \tag{113}$$

The solution for $p = 1$ is (Equation 14 of [77])

$$A_1(x) = \exp(-2x) - 1 + 2x, \tag{114}$$

and

$$B_1(x) = 4\left[\exp(-x) - 1 + x\right]. \tag{115}$$

For $p = 2$, I find that (analogous to Equation 10 of [185])

$$A_2(x) = \exp\left(-2x^2\right) - 1 + \operatorname{erf}\left(x\sqrt{2}\right) x\sqrt{2\pi}, \tag{116}$$

and

$$B_2(x) = 2\left[\exp(-x^2) - 1 + \operatorname{erf}(x) x\sqrt{\pi}\right], \tag{117}$$

where erf is the error function.

This analysis can also be extended to interferometric DCS (iDCS) by considering that [32]

$$g_2(\tau) = 1 + \beta_1 \left[g_1(\tau)\right]^2 + \beta_2 g_1(\tau), \tag{118}$$

where β_1 and β_2 are defined by Equations 32 and 33 in Section 2.3.6.4. For this form of $g_2(\tau)$, it can be shown that

$$K = \sqrt{\frac{2}{T}\left[\beta_1 \int_0^T \left(1 - \frac{\tau}{T}\right) \left[g_1(\tau)\right]^2 d\tau + \beta_2 \int_0^T \left(1 - \frac{\tau}{T}\right) g_1(\tau)\, d\tau\right]}. \tag{119}$$

Thus expressions for K for an interferometric measurement, for the forms of $g_1(\tau)$ described in Table 6.1, can readily be obtained.

6.4 A novel multispeckle simulation algorithm

With a view to calculating an exact solution for 2D-TIDSP PDFs, I described in Section 6.2.3.2 Goodman's result that such a PDF can be represented as the sum of an infinite number of negative exponential distributions [150]. Here I extend this approach to the simulation of 2D-TIDSP *images* for fully polarised light. The measured intensity of a 2D-TIDSP is evaluated as

$$\mathbf{W} = \int_0^T \mathbf{U}(t)\mathbf{U}^*(t)\, dt, \tag{120}$$

where $\mathbf{U}(t)$, the complex valued field, is a random process that has autocorrelation function $g_1(\tau)$, where τ is the delay time $t_2 - t_1$, and $g_1(\tau)$ measures the statistical similarity of $\mathbf{U}(t_1)$ and $\mathbf{U}(t_2)$ over a measured spatial ensemble. I first consider Goodman's starting point for his exact PDF solution: the inverse Karhunen-Loève expansion of $\mathbf{U}(t)$ on the interval $(0, T)$ into a weighted sum of basis vectors

$$\mathbf{U}(t) = \sum_{n=1}^{\infty} \phi_n(t) \hat{\mathbf{U}}_n, \tag{121}$$

which at this stage is a general expression, and where $\phi_n(t)$ is a set of orthonormal and complete functions, such that

$$\int_0^T \phi_n(t)\phi_m^*(t)\,dt = \begin{cases} 1 & n = m \\ 0 & n \neq m, \end{cases} \tag{122}$$

and the expansion coefficients $\hat{\mathbf{U}}_n$ are uncorrelated modes given by

$$\hat{\mathbf{U}}_n = \int_0^T \phi_n^*(t)\mathbf{U}(t)\,dt. \tag{123}$$

By design, the Karhunen-Loève expansion maximally decorrelates the expansion coefficients $\hat{\mathbf{U}}_n$, and thus for a zero mean process it is required that

$$E[\hat{\mathbf{U}}_n\hat{\mathbf{U}}_m^*] = \begin{cases} \lambda_n & n = m \\ 0 & n \neq m, \end{cases} \tag{124}$$

which can be achieved when the set $\{\phi_n(t)\}$ satisfies the integral equation

$$\int_0^T g_1\left(t_2 - t_1\right)\phi_n(t_1)\,dt_1 = \lambda_n\phi_n(t_2), \tag{125}$$

i.e., $\phi_n(t)$ and λ_n are the set of eigenfunctions and eigenvalues, respectively, of the integral equation that has $g_1\left(\tau\right)$ as its kernel [186].

Substituting Equation 121 into Equation 120,

$$\mathbf{W} = \sum_{n=1}^{\infty}\sum_{m=1}^{\infty}\hat{\mathbf{U}}_n\hat{\mathbf{U}}_m^*\int_0^T \phi_n(t)\phi_m^*(t)\,dt, \tag{126}$$

which, using Equation 122, simplifies to

$$\mathbf{W} = \sum_{n=1}^{\infty}\hat{\mathbf{U}}_n\hat{\mathbf{U}}_n^*, \tag{127}$$

and $\mathbf{W}$ has been expressed as the sum of an infinite number of uncorrelated and statistically independent modes. Each $\hat{\mathbf{U}}_n\hat{\mathbf{U}}_n^*$ represents a statistically independent instantiation of the instantaneous intensity of fully polarised light, which adheres to negative exponential statistics and is statistically equivalent to a fully developed speckle pattern [150].

I therefore propose that the time-integrated signal as a function of space (i.e., one 2D-TIDSP) may be simulated as the weighted sum of N uncorrelated and statistically independent fully developed 2D speckle patterns, each of which has a corresponding mean value of $E[\hat{\mathbf{U}}_n\hat{\mathbf{U}}_n^*] = \lambda_n$. I consider first the case of homogeneous fields (i.e.,

spatially invariant λ_n) in Section 6.4.1; however, I relax this assumption later in the chapter when considering spatially heterogeneous fields in Section 6.4.2.

An introduction to the simulation of fully developed speckle patterns was given in Section 6.2.2; however, I now specify adaptations to this that are required for the proposed simulation method. The intensity of an instantiation of a fully developed speckle pattern follows negative exponential statistics, the weighted spatial sampling of which can be modelled by [155, 181]

$$\mathbf{I}_n = \left|\hat{\mathbf{U}}_n\right|^2, \tag{128}$$

where,

$$\hat{\mathbf{U}}_n = \mathcal{F}\left[\exp\left(-i\boldsymbol{\Omega}_n\right)\right]\sqrt{\lambda_n} \tag{129}$$

is the corresponding field, where $\mathcal{F}$ denotes the 2D discrete Fourier transform and each $\boldsymbol{\Omega}_n$ is an independent instantiation of uniformly distributed random variables in a 2D matrix on the interval $(-\pi, \pi)$. Incorporating the CTF of a coherent imaging system, Equation 128 becomes [155, 181, 185]

$$\mathbf{I}_n = \left|\mathcal{F}^{-1}\left[\hat{\mathbf{U}}_n\mathbf{H}\right]\right|^2, \tag{130}$$

where $\mathbf{H}$ is the CTF. In this chapter, I model 600×600 pixel images and all simulations model $\mathbf{H}$ as a central circle function of diameter 200 pixels [181]; I therefore expect each modelled speckle to occupy a square region with a width of three pixels.

To compute the values of λ_n, I adapt the routine described by Goodman [150, 155]. $g_1(\tau)$ (Equation 109) is linearly discretised over the camera exposure period, T, by sampling the function $g_1(|t_2 - t_1|)$ over a 2D $N \times N$ matrix, for values of $t_1 = (0, T/(N-1), \ldots, T)$ on one matrix axis, and for values of $t_2 = (0, T/(N-1), \ldots, T)$ on the other matrix axis. λ_n are then the N eigenvalues of this $g_1(\tau)$ square sampling matrix, each of which is scaled by $1/N$, and in this chapter I use a value of either $N = 500$ or $N = 1000$. An example of this process is shown in Figure 6.4, whilst Figure 6.6 demonstrates how the individual λ_n values vary as a function of T/τ_c. The exact nature of this solution becomes approximate due to this discretisation; however, I have found that using these values of N provides a sufficient level of accuracy for the range of T/τ_c ratios used in the simulations presented in this chapter. The impact of the choice of N on the computational performance of this algorithm, together with considerations on how to optimise performance, are discussed in Section 6.5.

6.4.1 Homogeneous field

For homogeneous field simulations I use a value of $\tau_c = 0.37$ ms [181], and simulated 2D-TIDSPs for such fields are shown in the top row of Figure 6.5 for $p = 1$, $\alpha = 0.9$ and

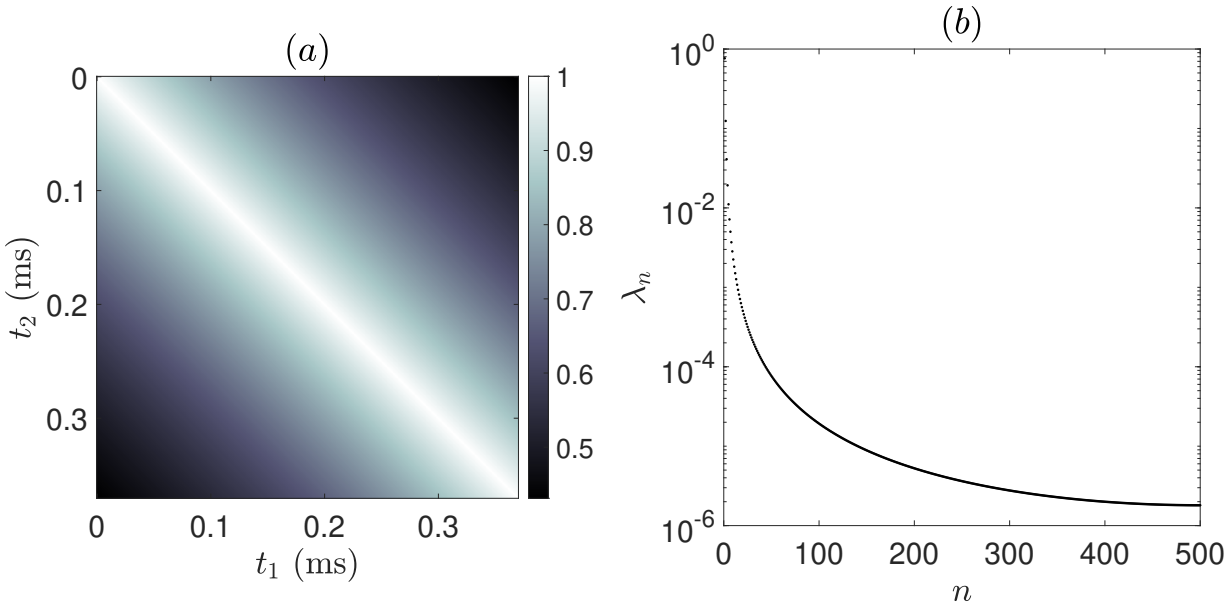

Figure 6.4: (a) Sampling of $g_1(|t_2 - t_1|)$ for T = 0.37 ms, τ_c = 0.37 ms, α = 0.9, p = 1, and N = 500. (b) The N eigenvalues, λ_n, of the square matrix (a).

various camera integration times. The bottom row of this figure shows the corresponding image histograms of the mean normalised 2D-TIDSPs. In each case there is excellent agreement with Goodman's exact PDF solution [150], which serves to validate the proposed simulation method in terms of intra-image statistics. At short integration times, the PDF takes the form of a negative exponential distribution (i.e., one fully developed speckle pattern). As the integration time increases, the PDF converges on a Gaussian distribution as an increasing amount of speckle blurring occurs, as is expected according to the central limit theorem. In this figure I also show Goodman's approximate PDF solution, which deviates from the simulated data, especially at intermediate values of T/τ_c.

Figure 6.6 shows the first five eigenvalues of $g_1(\tau)$ for $p = 1$ and $\alpha = 1$. At very short integration times the measurement is dominated by one mode. As the integration time increases this dominance decreases and the modes have an increasingly equal contribution to the time-integrated measurement, which results in blurring.

I then sought to validate the proposed simulation method against the novel analytical expressions for speckle contrast that were presented in Section 6.3. This was performed for different types of scatterer motion by simulating 2D-TIDSPs with homogeneous fields for $p = [0.5, 1, 2]$ and $\alpha = 0.9$, for the range of T/τ_c ratios shown in Figure 6.7. The global speckle contrast of each 2D-TIDSP was calculated, and (for each value of p) the resulting values of K_p were fit to the respective form of Equation 111 by minimisation of the least squares objective function

$$\underset{(\tau_c,\beta,\alpha)}{\operatorname{argmin}} \sum_{i=1}^{x} \left[K_p(T_i)_{\text{simulated}} - K_p(T_i)_{\text{model}}\right]^2 \tag{131}$$

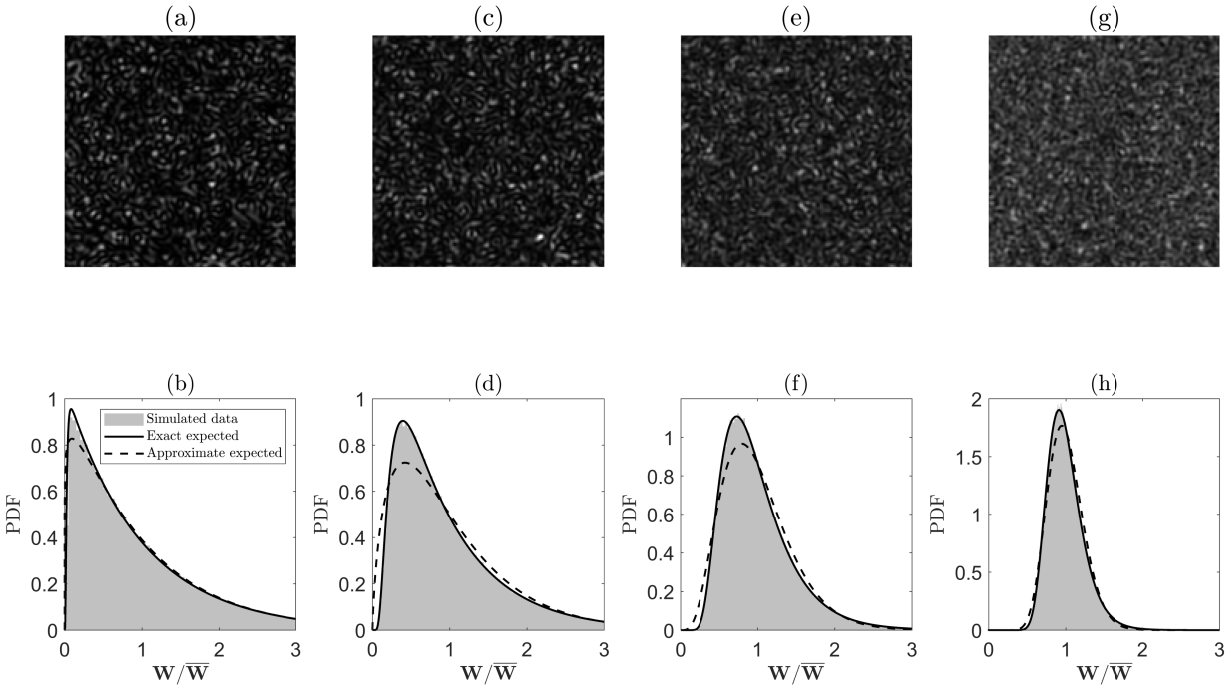

Figure 6.5: Simulated 2D-TIDSPs and their corresponding image histograms for $p = 1$, $\alpha = 0.9$, $\tau_c = 0.37$ ms, (a-b) $T/\tau_c = 0.1$, (c-d) $T/\tau_c = 1.0$, (e-f) $T/\tau_c = 5.0$, and (g-h) $T/\tau_c = 25.0$. The top row shows a 150×150 pixel region of interest (ROI) of each 2D-TIDSP. Exact and approximate expected PDFs [150] are superimposed on the image histograms.

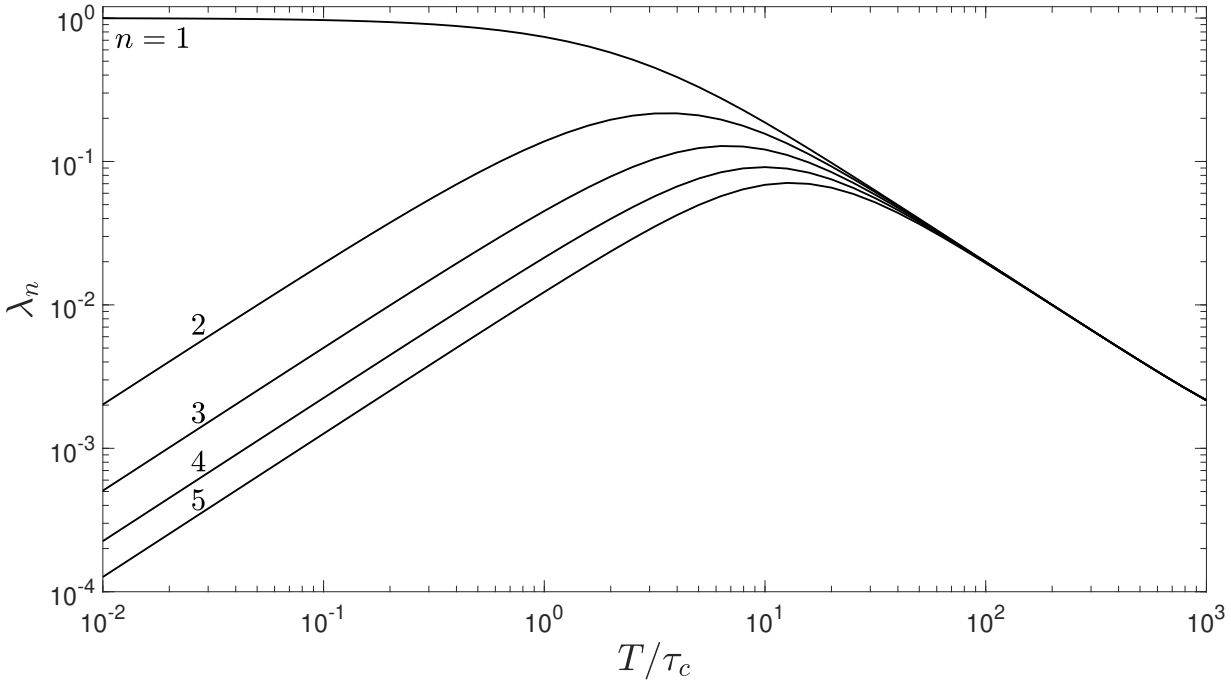

Figure 6.6: The first five eigenvalues of $g_1(\tau)$ for $p = 1$, $N = 1000$, $\alpha = 1$, $\tau_c = 0.37$ ms, and variable ratios of T/τ_c.

over x values of T. The resulting model fits and extracted parameter values shown in Figure 6.7 are in excellent agreement with the chosen simulation parameters and simu-

lated data. The proposed simulation framework has therefore been validated in terms of both intra-image and inter-image statistics, for a range of different motion types commonly encountered in biomedical optics. Although each speckle is expected to occupy nine image pixels for this fully polarised model, this is not a perfect mapping, and some pixels will have contributions from more than one speckle. The fitted values of β shown in Figure 6.7 are therefore slightly less than 1.

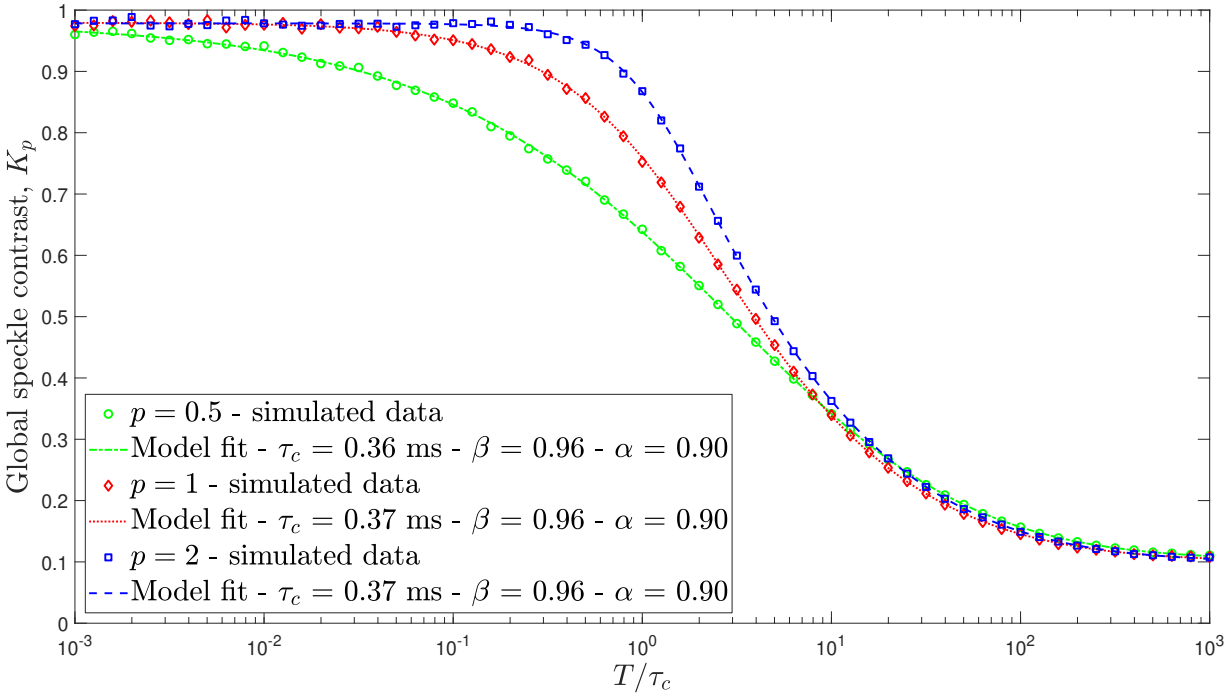

Figure 6.7: Global speckle contrast values of simulated 2D-TIDSPs for $p = [0.5, 1, 2]$, $\alpha = 0.9$, $\tau_c = 0.37$ ms, and variable ratios of T/τ_c. Model fits to the respective form of Equation 111 and extracted parameter values are also shown.

6.4.2 Heterogeneous field

I now consider the case of spatial variations in $g_1(\tau)$, which are treated by allowing λ_n to have a spatial dependence. This is done by partitioning the sample into labelled sub-domains, each having uniform $g_1(\tau)$ and, therefore, λ_n. Equation 129 is then evaluated for each sub-domain, where the support of each $\hat{\mathbf{U}}_n$ is given by the corresponding sub-domain. The smooth transition between adjacent tissue types can be modelled by increasing the number of labels (N_{label}); however, the incorporation of the CTF into the simulation will also perform this smoothing function. For each heterogeneous field simulation, λ_n is a 2D matrix of size $N_{\text{label}} \times N$ which need only be computed once. This λ_n 2D matrix is then distributed across N fully developed speckle patterns according to a $N_{\text{label}} \times 600 \times 600$ logical 3D matrix (each layer of this 3D matrix acts as a binary mask for each tissue label and for each fully developed speckle pattern).

To demonstrate this approach for a realistic yet arbitrary *in vivo* sample, I adap-

ted with permission the *in vivo* optical-resolution photoacoustic microscopy (OR-PAM) image from Figure 5(a) of [187], which shows an 8 mm $\times$ 8 mm field of view of the microvasculature of a mouse ear. Using an approach similar to that demonstrated by Song *et al.* [181], the image was partitioned into five greyscale labels, as shown in Figure 6.8(a), and arbitrary yet realistic values of τ_c in the range 0.05 - 1.0 ms [89] were assigned to each label. The image was sectioned to a 3.4 mm $\times$ 3.4 mm region of interest, and it was assumed that areas of higher optical absorption in the OR-PAM image correspond to areas of higher flow. Thus values of $\tau_c = [0.05, 0.10, 0.20, 0.50, 1.00]$ ms were used, which corresponded to labels [1,2,3,4,5], respectively. Modelling values of $p = [1, 1, 1, 1, 0.5]$ and $\alpha = [1, 1, 1, 1, 0.8]$ for each label, I simulated 30 2D-TIDSPs using an exposure time of 20 ms [81]. By running the validation presented in Figure 6.7, it was found that a value of $N = 1000$ is necessary to ensure statistical accuracy for these simulation parameters. An example of a simulated 2D-TIDSP generated using the spatially varying λ_n for these specified simulation parameters is shown in Figure 6.8(b). A temporal speckle contrast image was computed from this stack of 30 simulated 2D-TIDSPs, and this is shown in Figure 6.8(c), where the speckle contrast values correspond well with the spatial distribution of τ_c.

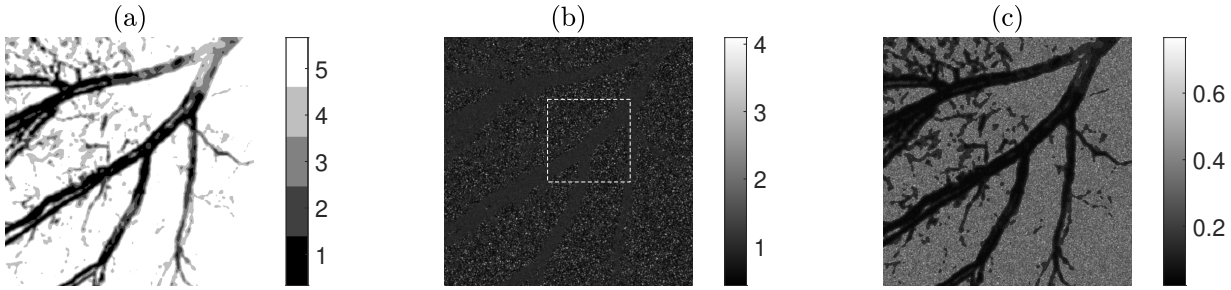

Figure 6.8: (a) Partitioned OR-PAM image of mouse ear vasculature. (b) Example of one simulated 2D-TIDSP. A magnified view of the ROI within the white dashed square is shown in Figure 6.9. (c) Temporal speckle contrast image computed from 30 simulated 2D-TIDSPs.

Figure 6.9 shows a magnified view of the 200 $\times$ 200 pixel ROI delineated by the white dashed square in Figure 6.8(b), which depicts an edge between a large vessel and its surrounding parenchyma. Each of the five labels in Figure 6.8(b) is composed of the weighted sum of the same 1000 fully developed speckle patterns, but in which the weights differ for each label. By allowing for this spatially variant λ_n, local changes in the ratio of dynamic and static scatterers, the type of motion encountered, and decorrelation time can all be modelled. This is enabled by using a suitably high number of labels, and by incorporating the CTF into the simulation.

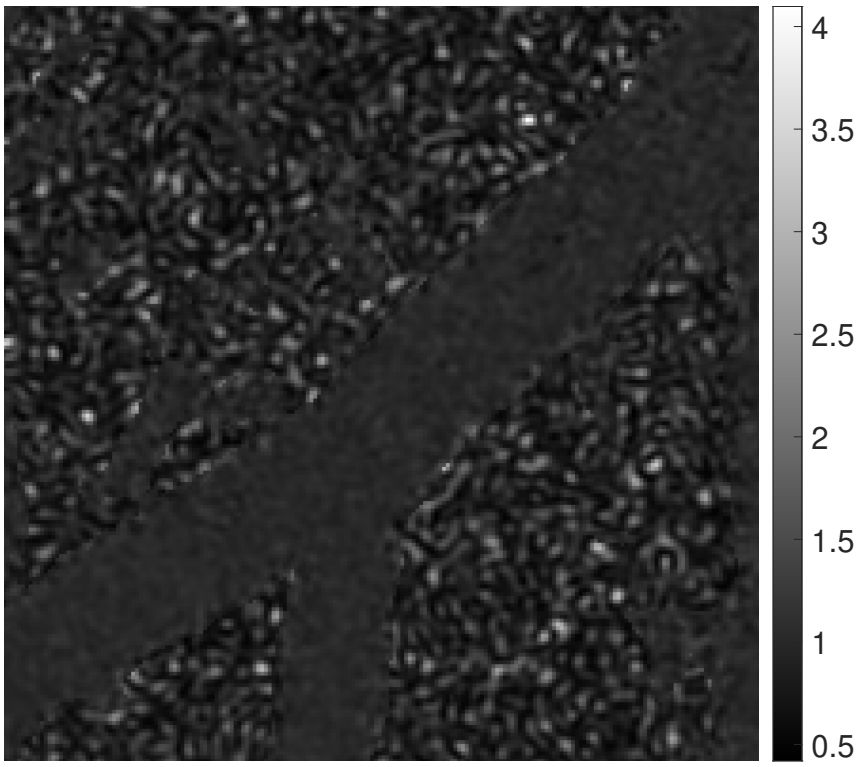

Figure 6.9: Magnified view of the 200 × 200 pixel ROI delineated by the white dashed square in Figure 6.8(b).

6.4.3 Acousto-optic modulation

The simulations presented thus far in this chapter have specified sample dynamic properties, for both homogeneous and heterogeneous fields. In this section I demonstrate that it is also possible to specify optical and acoustic parameters. As discussed in Section 2.3.6, conventional DCS is a useful tool for measuring BF in continuous, non-invasive, and portable settings; however, it is hindered by relatively poor depth penetration and spatial resolution. In order to overcome this, acousto-optic modulated DCS (AOM-DCS) (see Section 2.3.6.7) has been proposed as a technique to facilitate deeper imaging with improved spatial resolution, which makes use of an ultrasound modulated component of $g_1(\tau)$, according to

$$g_2(\tau) = 1 + \beta \left| \left[1 - \frac{M}{2} + \frac{M}{2} \cos(\omega_a \tau) \right] g_1(\tau) \right|^2, \tag{132}$$

where ω_a is acoustic radial frequency, and M is modulation depth (or modulation amplitude). According to Equation 132, $g_1(\tau)$ is modulated by $\cos(\omega_a \tau)$ between values of 1 and $(1 - M)$ [33].

I have done some preliminary work in determining the ultrasound modulated component of the Brownian signal in an AOM-DCS experiment, as shown in Figures 6.10 and 6.11, when modelling a semi-infinite detection geometry. This experiment made

use of a circular single element ultrasound transducer, with a diameter of 13.5 mm and an ultrasound centre frequency of 2 MHz. The source-detector separation (SDS) distance was measured to be 20.5 mm, and the same room temperature intralipid phantom that was described in Chapter 4 was used, but this time with continuous wave (CW) insonification.

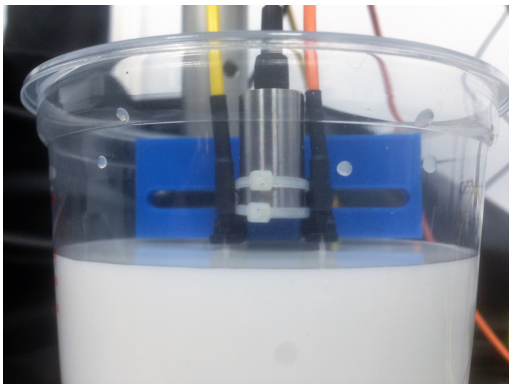

Figure 6.10: AOM-DCS with single-mode detection, using the intralipid phantom described in Chapter 4, but with CW insonification.

Photon arrival times were autocorrelated using the multi-tau algorithm, the results of which are shown by the blue dots in Figure 6.11. In this figure, the green line shows the result of fitting to Equation 132, which yields a modulation depth of $M = 0.078$, and excellent agreement between the measured data and the modulated model fit is seen. The red line shows the DCS Brownian motion model fit that would be expected in the absence of ultrasound modulation.

Modelling a camera exposure time of 10 μs (which is in the order of that presented in [31]), both of these fitted $g_1(\tau)$ functions were sampled in two 500 $\times$ 500 matrices, as shown in subplots (a) and (b) of Figure 6.12, for DCS and AOM-DCS, respectively. Subplot (c) of this figure shows the 500 eigenvalues of each $g_1(\tau)$ function, which were then used to simulate two 2D-TIDSPs, which are shown in subplots (a) and (b) of Figure 6.13. Although these two images are not visually distinct, the AOM-DCS image is more blurred as it has a lower speckle contrast value, $K_{\mathrm{AOM-DCS}}$, of 0.66, compared to the DCS image, which has a speckle contrast value, K_{DCS}, of 0.72. This is because the added time-varying process of the ultrasound perturbation (2 MHz) causes the speckle pattern to change more quickly than due to sample motion alone (typically 1 - 20 kHz for *in vivo* samples [89]), which causes a blurring effect when imaged (as was introduced in Figure 2.13 in Section 2.4.1), and this is validated analytically below.

Inspection of the PDFs of both of these images, shown in Figure 6.13(c) reveals that the AOM-DCS component, shown in solid green, is right-shifted away from a negative exponential distribution, and toward a Gaussian of mean value 1, when compared to the DCS component, shown in dashed red. Furthermore, modulation depth can be

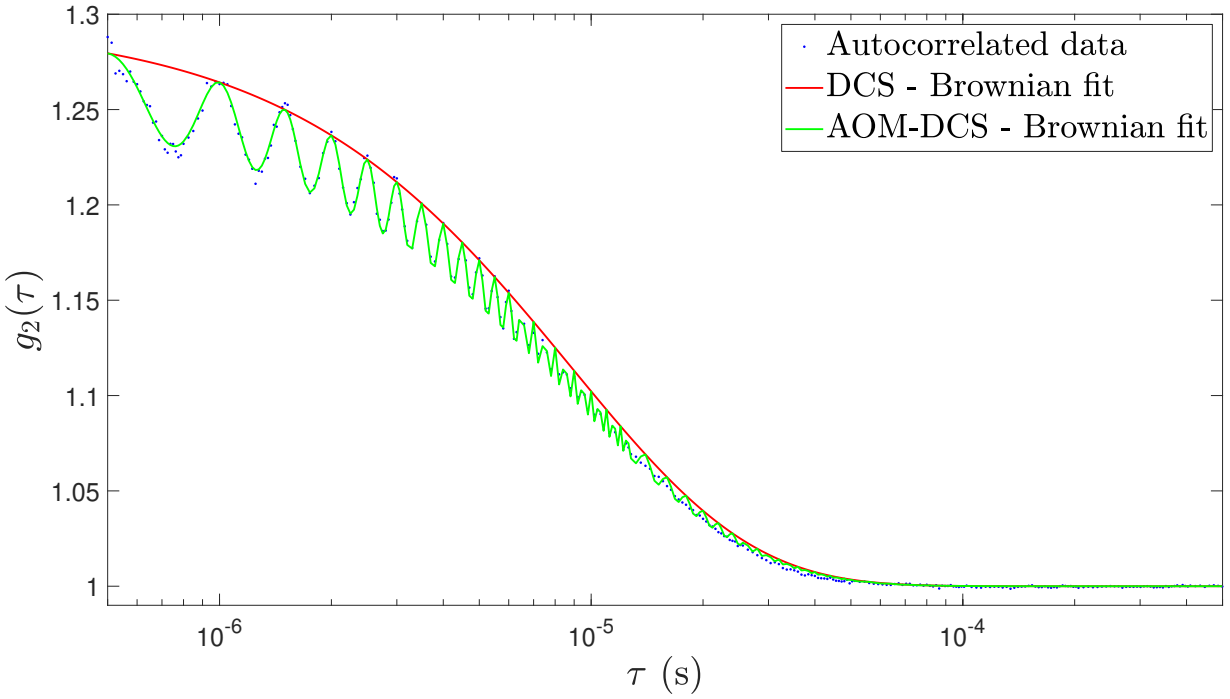

Figure 6.11: Fitting an AOM-DCS Brownian motion model (green line) to autocorrelated data (blue dots). The red line shows the DCS Brownian motion model fit without ultrasound modulation.

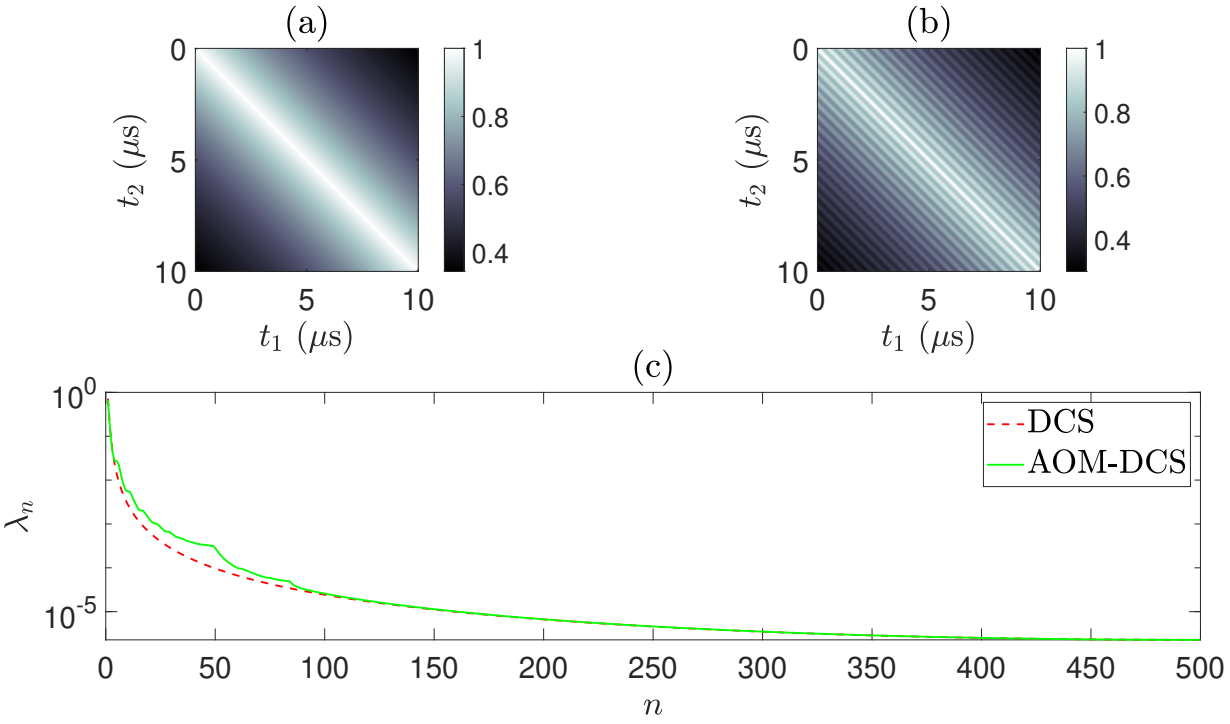

Figure 6.12: Sampling of $g_1(|t_2 - t_1|)$ for (a) DCS, and (b) AOM-DCS. (c) The 500 eigenvalues, λ_n, of the square matrices (a) and (b).

calculated by considering the speckle contrast of these two images, according to [18]

$$M \approx \frac{K_{\text{DCS}}}{K_{\text{AOM-DCS}}} - 1, \tag{133}$$

provided that the condition $T \gg 1/\omega_a$ is met, to ensure that the exposure time is long enough to sample the ultrasound modulation, which is adhered to in this simulation. Equation 133 yields a value of $M = 0.080$ for the two simulated 2D-TIDSPs shown in Figure 6.13, which is in good agreement with the value of $M = 0.078$ that is yielded by fitting experimental $g_2(\tau)$ data to Equation 132.

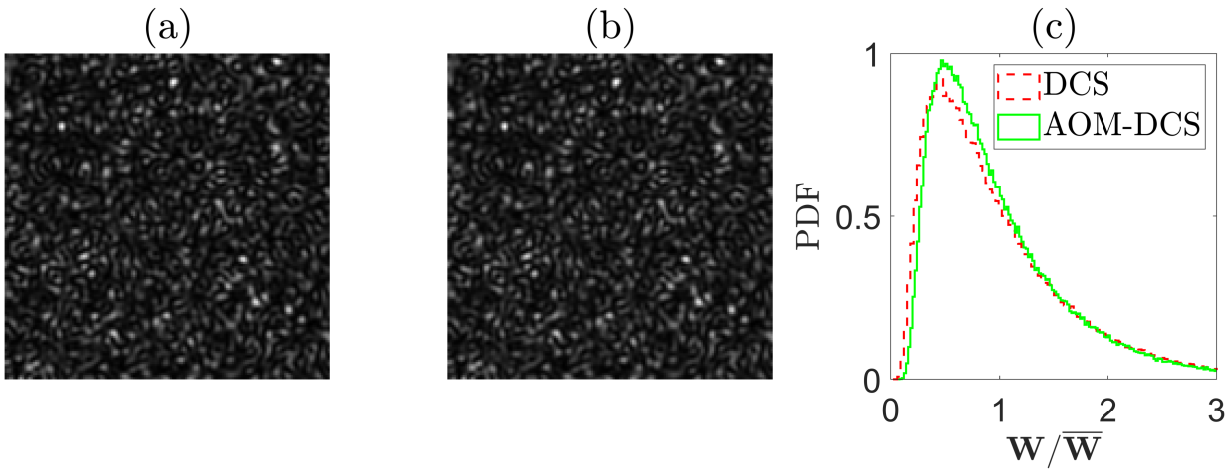

Figure 6.13: Simulated 2D-TIDSPs for (a) DCS, and (b) AOM-DCS. PDFs of both mean-normalised images are shown in (c).

I have therefore validated the statistical accuracy of simulated 2D-TIDSPs not only when incorporating sample dynamic properties, but also when incorporating optical and acoustic parameters too, and for both infinite and semi-infinite detection geometries. The simulation framework that I have presented in this chapter can readily be extended to include any form of $g_1(\tau)$, for example that which results from mixed motion models (see Section 4.5), including those where the edges between different types of motion are not sharp [80] (i.e., p exists on a spectrum between 0.5 and 2, for LSCI). Although the simulation framework does not model flow propagation due to velocity profiles in larger vessels, this is something that could be incorporated into the model by adjusting the simulation parameters. Further limitations of the simulation framework are discussed in Section 6.5 and Chapter 7.

6.5 Chapter summary and discussion

A major consideration when using the simulation technique presented in this chapter is that a larger ratio of T/τ_c results in a narrower $g_1(\tau)$ function, which requires a larger N value in order to sample $g_1(\tau)$ with sufficient accuracy. This accuracy can be ensured by running the validations presented in Figure 6.7, for a particular set of simulation parameters. However, a larger N value will increase the computational demand of the simulation; the choice of N (and also the number of eigenvalues to retain) therefore reflects a compromise between accuracy and performance. That being said, the simula-

tion framework presents a modest computational task when compared with full-wave modelling, for example.

In this chapter I have described that the edges that exist between two different tissue labels in a simulated 2D-TIDSP are smoothed by the CTF. The accuracy and spatial resolution of the simulation could be increased by increasing the value of N_{label} that is used, which would allow for gradual spatial transitions to be modelled more explicitly. However, this would increase the computational expense of the simulation and also rely on a sufficiently accurate partitioning of the initial image. Using MATLAB 2020a on a PC with 32 GB RAM and a 2.6 GHz processor with $N = 1000$ and $N_{\text{label}} = 5$, 0.3 seconds are required to compute the λ_n matrix used in the *in vivo* simulation presented in Figure 6.8, and a further 86 seconds are required to simulate each of the 30 2D-TIDSPs. If sufficient memory were available, it would be preferable to use pre-computed libraries of fully developed speckle patterns in the above calculation. Additionally, GPU acceleration and lower-level programming languages could also be employed.

A limitation of the simulation framework presented in this chapter is that it does not allow for the parameterisation of β. Although it is trivial to simulate the effect of two orthogonal polarisation states by taking the sum of two 2D-TIDSPs, simulating the effect of other factors that influence β (such as coherence length and stability of the laser light source, stray light, detector stability, and sample coupling) is more complex and would be an interesting further study. I have successfully modelled the CTF of a coherent imaging system, but variations in speckle to pixel size ratio could be further modelled by upsampling or downsampling of the simulated 2D-TIDSPs [154]. If the inclusion of β into a 2D-TIDSP is necessary, then it is possible to achieve this by extending Goodman's approximate PDF solution. However, such a 2D-TIDSP will have inaccurate second order statistics, and neither will it incorporate the effects of the CTF.

The addition of specific models of measurement noise (such as that due to shot noise, read noise, dark noise, and hot pixels [25]) to simulated 2D-TIDSPs, together with experimental validation of this combined technique, would be a useful and interesting further study. However, this is not within the scope of this chapter, which has addressed the more fundamental validation of the proposed simulation framework against previously published solutions for the exact PDF of time-integrated intensity for coherent light [150]. Furthermore, I have validated the simulation framework (both in terms of intra-image and inter-image statistics) against novel expressions for speckle contrast for different forms of homogeneous field. The correctness of these novel expressions has also been independently corroborated elsewhere [89].

The simulation framework presented in this chapter can simulate the 2D-TIDSP that is detected on the sample arm of a holographic FD-DCS instrument. By rearranging

Equation 84, the forward model for a reconstructed holographic FD-DCS image is

$$S_{(\pm\Delta\omega,k_x,k_y)} = \left[S_{1_{(\pm\Delta\omega,k_x,k_y)}} N_{(\Delta\omega,k_x,k_y)} \mathrm{MTF}_{(k_x,k_y)}\right] + N_{(\Delta\omega,k_x,k_y)}. \tag{134}$$

$S_{1_{(\pm\Delta\omega,k_x,k_y)}}$ may be simulated according to the 2D-TIDSP framework presented in this chapter, with an intensity attenuation according to the analytical solutions for FD-DCS that I presented in Chapter 4. $\mathrm{MTF}_{(k_x,k_y)}$ may be modelled according to the theory presented in Chapter 5, and $N_{(\Delta\omega,k_x,k_y)}$ may be modelled as a fully developed speckle pattern, of mean intensity equal to the shot noise of the reference beam [142]. An alternative approach to generate holographic FD-DCS images would be to use the 2D-TIDSPs simulated in this chapter as inputs to computer generated holography algorithms [188]. Investigation of these simulation approaches forms part of the future work of this thesis.

6.6 Conclusion

To the best of my knowledge, the work presented in this chapter represents the first time that a statistically accurate algorithm for the simulation of 2D-TIDSPs, with specified temporal and spatial correlations, including the effects of sample dynamics, optical and acoustic parameters, and a range of detection geometries, has been presented in the field of biomedical optics. The proposed simulation technique is efficient and adaptable, and can readily be extended to include any form of $g_1(\tau)$. I therefore expect the technique presented here to be a powerful and useful simulation tool for the biomedical optics community for the purposes of understanding the practical application of speckle phenomena, evaluating data processing methods of speckle images, and assessing the feasibility of novel applications of laser speckle.

7 Conclusions and discussion

7.1 Thesis summary and contribution to knowledge

In Chapter 1, I detail the motivation to measure cerebral blood flow (CBF), as well as the currently vacant niche to measure CBF using a continuous, noninvasive, and portable bedside device. Motivated by this challenge, I then described the project aims of this thesis, and enumerated the research objectives that I planned to investigate. Chapter 1 closes with a concise thesis overview and a summary of the thesis contribution.

In this thesis, I have explored the feasibility of fusing the fields of heterodyne parallel speckle detection (HPSD) and diffuse correlation spectroscopy (DCS), with a view to mitigating the trade-off between imaging depth and signal-to-noise ratio (SNR) that is inherent to conventional DCS. This has been motivated by the literature review undertaken in Chapter 2, in which I offer a concise and critical review of CBF measurement techniques.

DCS is the archetypal optical imaging modality to measure deep flow, however the SNR performance of conventional DCS is fundamentally limited by the use of single speckle detection, which can be expensive and impractical to scale-up. Given the potential that DCS has to achieve real-time, deep, and spatially-localised CBF monitoring, several approaches have been investigated to improve the sensitivity of DCS to CBF, and these are all introduced in Chapter 2. These approaches can be divided into: multispeckle detection strategies, long wavelength approaches, interferometric approaches, depth discrimination techniques, time-of-flight (TOF) resolved detection, and acousto-optic tomography (AOT). Most of the research in the area of portable and non-invasive CBF measurement using DCS focuses on the first five of these approaches (i.e., all-optical methods).

In Chapter 3, I then introduced the concept of digital holography, and described previously and concurrently published examples of its use in biomedical optics. Having introduced the specific example of HPSD in detail, I then describe the feasibility of applying an HPSD approach to DCS: holographic Fourier domain DCS (FD-DCS). Such an approach would have all the advantages of multispeckle and interferometric detection that has been investigated by other groups, and it could also be extended to include long wavelength detection, depth discrimination techniques, and the detection of acousto-optic tomography (AOT) signals. Furthermore, holographic FD-DCS would offer shot noise limited and scalable detection, using inexpensive detectors, which is not constrained by the Siegert relation. The main drawback of the proposed technique is that it does not offer TOF resolved detection. Additionally, the measurement of pulsat-

ile flow *in vivo* using holographic FD-DCS is particularly challenging, owing to the short camera exposure times that are required, the complexity of system integration, and the data processing requirements of the technique.

Having been informed by the wider context of the literature review in Chapter 2, in Chapter 3, I synthesise the connection of previously unrelated facts with a view to advancing the field of DCS. This is subsequently achieved in Chapters 4, 5, and 6, in which I demonstrate a distinct and significant contribution to biomedical optics though the development of new theory and ideas, the discovery of new knowledge, and the implementation of new practical applications.

Chapter 4 starts by defining the novel FD-DCS analytical models that I have developed, both for Brownian and convective motion in DCS experiments. Despite the utility of such a framework being recognised by the founders of DCS in the 1990s, a solution to this problem has not been forthcoming until the research for this thesis was carried out. Whilst the assembly of an off-axis HPSD instrument, as well as its application to measure *in vivo* flow at low temporal resolution, has been described before, the application of such an instrument to the formalism of DCS is novel.

By conducting a series of temperature controlled waterbath experiments, I validated both the holographic FD-DCS instrument and the analytical FD-DCS models that were developed in this thesis. As my understanding of this series of experiments evolved, I understood the need to develop a novel temperature dependent model for the optical, mechanical, and dynamic properties of intralipid optical tissue phantoms. Furthermore, I also developed a novel mixed motion model of DCS (which is applicable to both conventional DCS and holographic FD-DCS), which accounts for variation in both the predominance of the type of motion (i.e., the Brownian factor), and the speed of each type of motion within the sample. I used this series of experiments to show that holographic FD-DCS can measure data that are entirely equivalent to a conventional DCS instrument, but with a higher optical throughput and a decreased cost of detector. By developing and validating this mixed motion model for FD-DCS, I achieved accurate interpretation of the data produced by the holographic FD-DCS instrument in its native domain, which are fundamentally different to conventional DCS data.

I then demonstrated the *in vitro* SNR_{D_b} advantage that holographic FD-DCS has over conventional DCS, as well as its relative insensitivity to ambient light, by conducting a series of experiments using an intralipid phantom with optical properties resembling that of brain tissue. This robustness to ambient light is a particularly important consideration for the use of DCS in typical clinical settings, in which optical isolation of the imaged areas of a patient would be impractical.

In addition to the novelty described above, the application of an off-axis HPSD instrument to measure at parameter output rates sufficient to resolve pulsatile flow *in vivo*,

which was achieved in Chapter 4, is also novel. From a theoretical perspective, achieving this required the development of a deep understanding of the interplay between the exposure parameters of the system, the instrument response function (IRF), and the dynamic and optical properties of the *in vivo* sample. Whilst these factors could be gleaned from the literature, their synthesis and subsequent validation has not been demonstrated before. From a hardware perspective, these high output rates were made possible by the design of an instrument with a high throughput and minimal dead-time between frequency shifts, and which enables highly parallel GPU-accelerated holographic demodulation and is thus suited to *in vivo* application. The considerations presented in this paragraph are perhaps the most fundamental limitations for the application of holographic FD-DCS to *in vivo* settings, and these are evaluated further in Section 7.2.

Chapter 5 is concerned with the characterisation and optimisation of the holographic FD-DCS instrument that was described and validated in Chapter 4. Chapter 5 can be subdivided into four major investigations: the diagnosis and elimination of laser mode hopping, correction for the modulation transfer function (MTF) of a holographic FD-DCS instrument, using a singular value decomposition (SVD) spatiotemporal filtering approach to characterise and remove source noise, and the development of a novel multispeckle denoising algorithm to characterise and remove detector noise. By undertaking this rigorous and systematic SNR performance assessment, I demonstrate the highest SNR gain reported in the DCS literature to date, which has been achieved using scalable and low-cost camera-based detection.

The use of DC subtraction temporal filtering has been well described in the digital holography literature: it is a strategy that can achieve shot noise limited detection with only two camera frames. In Chapter 5, I document the vulnerability of such a technique to laser mode hopping, which has not been documented in the literature before. This investigation evolved through various stages to show that negative going outlying data points were caused by laser mode hopping. Whilst these outliers could easily be ignored when analysing *in vitro* validation datasets, this is not possible when detecting at the high parameter output rates that are necessary for *in vivo* detection, and thus it is preferable to eliminate them at source using hardware based techniques.

Whilst a model for the MTF of a lensless digital Fourier holography instrument is accepted within the relevant literature, its incorporation and validation within an HPSD experiment has not been reported before. In Chapter 5, I therefore revise the reconstruction of an unnormalised power spectral density (PSD) measurement using HPSD, in order to include the MTF of the instrument. This was motivated by the need to investigate an attenuation that I initially observed over the reconstructed holographic twin images. However, I then had to consider the effect of the camera pixel fill-factor on the

gradient of the MTF, and I found that modelling a camera pixel fill-factor of 0.72 appropriately compensated for the MTF of the instrument. To best of my knowledge, this is the first time that this inclusion has been validated in a digital holography experiment.

I then developed an SVD spatiotemporal filtering approach to denoising, which was adapted from the related fields of laser Doppler holography (LDH) and multispeckle interferometric DCS (iDCS). In this thesis, I specifically exploit the weak spatiotemporal correlation of speckle, and use this knowledge to justify the removal of the first n_c singular values of a hologram time-stack. When pumping the laser at its maximum rated output power of 120 mW, SVD filtering offers an improved SNR performance that is closer to that which the theory of multispeckle detection predicts (compared to when SVD filtering is not used). However, the same SNR improvement can also be achieved by decreasing the laser source power from 120 mW to 100 mW, and I therefore hypothesise that by pumping the laser at its maximum rated output power, effects such as increased spontaneous emission and technical noise decrease SNR performance. However, SVD filtering is costly in terms of the number of camera frames that it requires, especially in a holographic FD-DCS instrument (which is designed to exploit low-frame rate detection). I therefore propose that, within the context of holographic FD-DCS, SVD filtering be used as a validation tool, rather than a final solution in the signal processing pipeline, to confirm that any particular experimental setup is not impacted by spatiotemporally correlated noise sources.

The final contribution of Chapter 5 is a novel multispeckle denoising algorithm, which has yielded the demonstration of a linear relationship, and beyond, between SNR and the square root of the number of speckles detected. This algorithm takes advantage of the knowledge that a series of a two-dimensional time-integrated dynamic speckle patterns (2D-TIDSPs) represents a series of independent and identically distributed random variables, each of which has been drawn from the same probability density function (PDF). Therefore, once the randomness of spatial speckle sampling has been corrected for, the resulting distribution of sampled intensities should be identical between consecutive holograms. This means that temporal filtering can be applied to remove noise sources, before restoring the random nature of spatial speckle sampling. By applying this technique to experimental data, I have found that this algorithm can not only be used to characterise and remove detector noise, but it can also be used to remove sampling noise, which can be thought of as another form of noise that can be identified and removed from a shot noise limited distribution. However, there is a trade-off between SNR gain and temporal resolution when using this algorithm, and this is discussed further in Section 7.2.

By bringing together the four investigations described in Chapter 5, I achieve an *in vitro* SNR gain of 36, for a flow parameter output rate of 8.2 Hz, when detecting over $\sim$1290 heterodyne speckles, using scalable and low-cost detection. This is the highest

SNR gain reported in the DCS literature to date, and represents a significant step toward mitigating the trade-off that exists between SNR and imaging depth in conventional DCS, and toward increasing the affordability of such a system.

Chapter 6 is concerned with the simulation of statistically accurate 2D-TIDSPs in biomedical optics, which is motivated by the development of a forward model for holographic FD-DCS. Such a forward model would not only aid system characterisation, but it could also be used to generate training data for the application of deep learning techniques to holographic FD-DCS, and to aid a fuller statistical analysis of the denoising algorithm presented in Chapter 5. I start Chapter 6 by detailing why existing speckle simulation algorithms are not appropriate for use in this thesis. The copula method lacks the flexibility necessary to account for any arbitrary type of speckle decorrelation (including that due to static scatterers). I also undertake an investigation to extend the pre-defined correlation distribution method to the simulation of 2D-TIDSPs, and report the negative result that such an extension is not appropriate, as it yields 2D-TIDSPs with statistically inaccurate speckle contrast.

I then introduce Goodman's approximate and exact solutions for the PDF of a 2D-TIDSP and describe the advantages and disadvantages of each solution. The former is based on the principle of the number of degrees of freedom, $\mathcal{M}$, within a time-integrated speckle measurement, and the latter is based on the Karhunen-Loève expansion of the electric field. Goodman's exact PDF solution has never been used to simulate 2D-TIDSPs before, and neither has it ever been applied to forms of $g_1(\tau)$ commonly encountered in biomedical optics. The main contribution of Chapter 6 is therefore the extension of Goodman's exact PDF solution to the development of a new theoretical framework for the simulation of a statistically accurate 2D-TIDSPs in biomedical optics. In Chapter 6, I also offer novel expressions for speckle contrast for various forms of $g_1(\tau)$ that are used in biomedical optics (which were also reported independently and concurrently elsewhere during the time that the research for this thesis was being conducted), and describe how expressions for speckle contrast can also be obtained for an iDCS measurement.

I robustly validate the 2D-TIDSP simulation framework that I develop in Chapter 6 in terms of intra-image statistics and inter-image statistics, in part by using the expressions for speckle contrast that I have developed, for various sample motion types and camera exposure times. I also show that, by using a suitably high number of tissue labels, and by incorporating the coherent transfer function (CTF) into the framework, the simulation technique can readily be extended to samples with spatially varying sample properties. The work presented in Chapter 6 represents a distinct and significant contribution to the understanding of spatiotemporally sampled speckle in biomedical optics, and was indeed instructive when devising the novel multispeckle denoising algorithm

presented in Chapter 5.

The final contribution of Chapter 6 showcases the versatility of the 2D-TIDSP simulation framework that I have developed by applying it to an acousto-optic modulated DCS (AOM-DCS) model of $g_1(\tau)$, which incorporates dynamic, optical, and acoustic parameters in a semi-infinite detection geometry. Using this approach, I validate the speckle contrast of simulated AOM-DCS 2D-TIDSPs against experimentally measured $g_1(\tau)$ data. In fact, the 2D-TIDSP simulation framework that I propose can be used to model *any* form of $g_1(\tau)$, and I therefore expect it to become a powerful and useful simulation tool for the biomedical optics community.

7.2 Discussion and future work

In this section I discuss the findings of my research within the context of similar work by other researchers, the limitations of the research, and the future work that could extend the investigations in this thesis. This is done for each novel chapter in turn.

7.2.1 Chapter 4

The multispeckle aspect of holographic FD-DCS that I propose in this thesis is closely related to the multispeckle detection strategies of other research groups. The system that I have proposed detects over $\sim$1290 speckles for the *in vivo* detection setup that I have described; the work of Sie *et al.* [10] and Liu *et al.* [27] detects over 1024 speckles using a 32×32 single-photon avalanche diode (SPAD) array, and interferometric diffusing wave spectroscopy (iDWS) detects over $\sim$96 speckles using a high speed line-scan camera. Multispeckle techniques which use low cost 2D detector arrays [23, 26, 37] do no not specify the number of detected speckles. Perhaps this is because it is assumed that achieving a one-to-one pixel to speckle ratio can be achieved, and that the relatively low cost per pixel of these detectors means that scaling up to an arbitrary level of multispeckle detection is readily feasible. Indeed, the authors of the interferometric speckle visibility spectroscopy (ISVS) technique state that 'a speckle pattern recorded by using a detector array can contain thousands to millions of speckle grains' [37]. The largest number of pixels per detector that has been reported was by Zhou *et al.*, who used 1700×280 pixels (476000) for their multi-exposure interferometric diffusing wave spectroscopy (MiDWS) instrument [23]. When combined with techniques that exploit low-frame rate detection and relatively long camera exposure times, such as holographic FD-DCS, ISVS and MiDWS, the use of low-cost camera-based detection represents a particularly effective way to scale SNR whilst maintaining affordability.

The considerations for multispeckle detection documented above lead into a limitation of my experimental design: sensor layout and light collection efficiency. Xu *et al.* [37] used a rectangular aperture for their digital lensless Fourier holography ISVS setup,

which, by inspection of Figure 7.1(A2), makes use of 50 % of the space of the reconstructed hologram. The experimental design reported in this thesis uses a circular aperture, which, as I describe in Chapter 4, has a maximum diameter of $A = N_{\text{pix}}\sqrt{2}/(3+\sqrt{2})$, as measured in the space of the reconstructed hologram. It can be shown that this only makes use of $\pi/(11+6\sqrt{2}) \approx 16$ % of the space of the reconstructed hologram. Therefore, the use of a rectangular aperture means that the number of pixels used to detect the holographic twin images is increased by a factor of 3.1. However, the use of a rectangular aperture means that the shot noise on the reference beam [which is contained within the grey region of Figure 7.1(B2)] cannot be sampled in the space of the reconstructed hologram, and Xu *et al.* observed that this introduced noise into their measurements [37]. These authors note that this could be mitigated by sampling the intensity fluctuations from a tap off the reference beam and using this to correct for fluctuations in signal intensity.

In this thesis, I present experiments in which the camera operates with a duty cycle ranging from 3.0 % (Section 5.4.2) to 52.5 % (Sections 4.6 and 4.7), with shorter duty cycles corresponding to shorter camera exposure times. Whilst I have demonstrated that these shorter camera exposure times are necessary for the detection of pulsatile flow *in vivo*, the measurement duty cycle could be increased by using a multiple camera setup, for example. Furthermore, the camera used for the experiments described in this thesis is designed for the detection of visible wavelengths, and has a quantum efficiency of $\sim$33 % at 785 nm. The use of a near-infrared (NIR) enhanced sensor could therefore also increase light collection efficiency (for example the Thorlabs Kiralux 1.3 MP NIR-Enhanced CMOS Camera, CS135MUN, has a quantum efficiency of $\sim$45 % at 785 nm, which would provide a gain of $\sim$37 % over the sensor that is currently used). The improvement of sensor layout, detector duty cycle, and detector quantum efficiency is therefore future work.

The interferometric nature of holographic FD-DCS plays an important role in determining the SNR gain of the technique, and as such, all the experiments reported in this thesis were calibrated so as to make full use of the reference arm SNR boost, without saturating the detector. That being said, there is only one report in the literature of an iDCS system that does not also make use of multispeckle detection. This work, by Robinson *et al.* [32], reports an SNR gain of $\sim$2, over all lag times, compared to a homodyne conventional DCS system. It would therefore seem prudent to combine the advantages of both interferometric and multispeckle detection when attempting to increase SNR performance in DCS.

Whilst it is established that larger source-detector separation (SDS) distances will lead to a deeper imaging depth (see Section 2.3.6.1), and that a higher SNR gain (such as that achieved in this thesis) is necessary to measure at larger SDS distances, in this thesis I have not explicitly demonstrated the sensitivity of holographic FD-DCS to deeper flow.

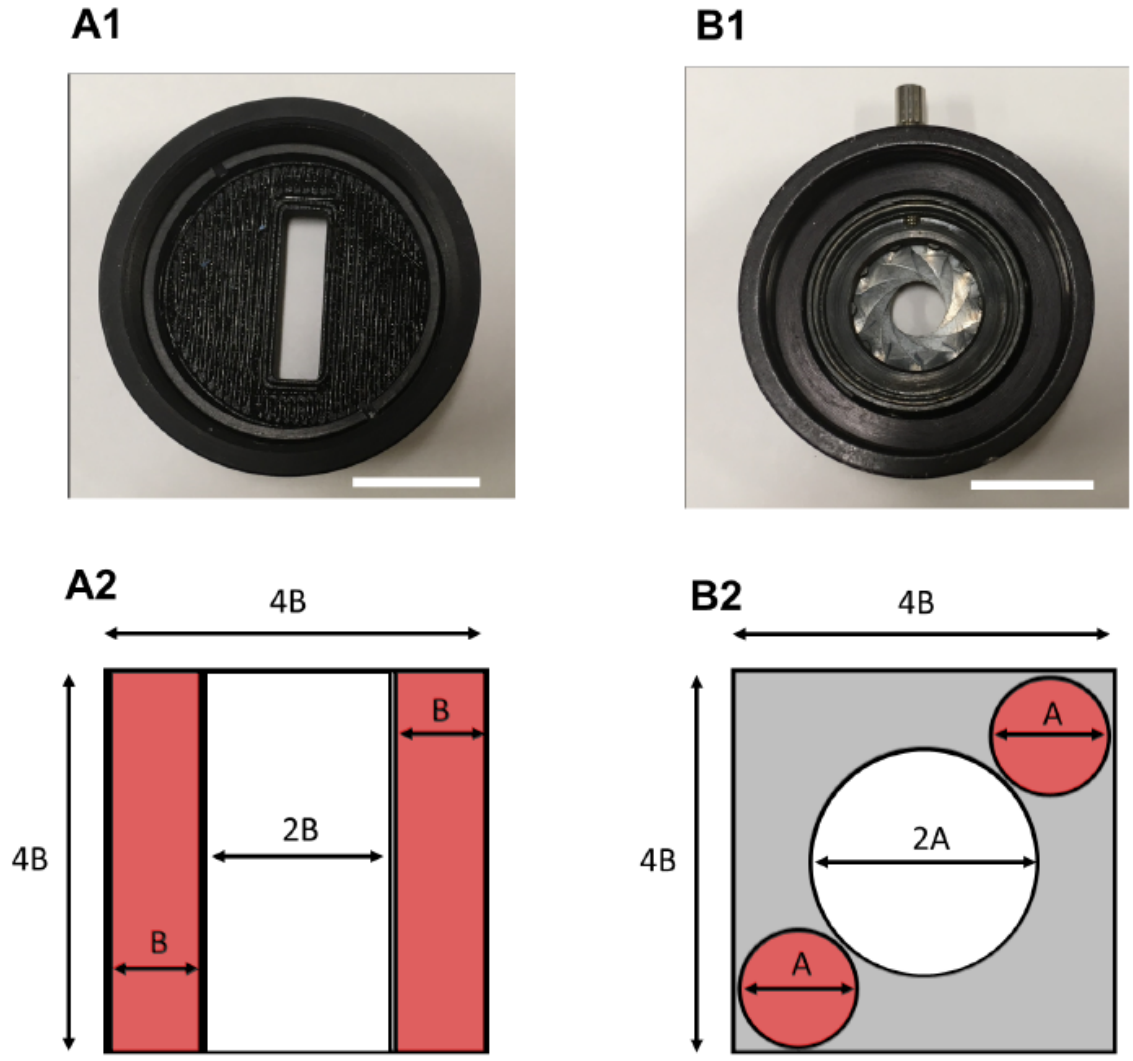

Figure 7.1: Aperture design considerations for off-axis holography. (A1) Rectangular aperture in the camera plane, and (A2) the respective holographic twin images in the reconstruction plane, shown by the two red rectangles, which occupy 50 % of the sensor. (B1) Circular aperture in the camera plane, and (B2) the respective holographic twin images in the reconstruction plane, shown by the two red circles, which occupy $\pi/(11+6\sqrt{2}) \approx 16$ % of the sensor. Reproduced with permission from [37] under the terms of a Creative Commons Attribution 4.0 License. © Xu, Jahromi, Brake, Robinson, and Yang 2020.

Future work to demonstrate this would necessitate the use of phantoms that are more sophisticated than the homogeneous intralipid phantoms used in this thesis. Improved phantoms could include two layer designs (e.g., using silicone oil and intralipid, which are immiscible and will have different D_b values, or phantoms which have a static superficial layer and a deeper dynamic layer, which could be used to simulate the skull and the brain, respectively). Furthermore, a dynamic flow phantom could also be constructed, so as to validate measurements of flow that is occurring at both a known depth

and convective speed.

Unlike other multispeckle DCS studies, in this thesis I have chosen to use a liquid light guide (LLG) to detect speckles, rather than a multimode fibre, since this provides an optical aperture of appropriate dimensions to enable the use of digital lensless Fourier holography without any additional optical elements. This allows for the most robust and stable optical configuration with minimal alignment requirements. If desired, a multimode fibre could be employed by introducing a microscope objective and associated imaging lenses, and, whilst this was not a priority for this thesis, this would be an interesting further study. Indeed, this would be a useful experiment to investigate the differences in Brownian factor measurements between conventional DCS and holographic FD-DCS, which are shown in Figure 4.12.

Like ISVS [37] and interferometric near-infrared spectroscopy (iNIRS) [116], holographic FD-DCS interrogates the electric field directly, rather than intensity, and therefore the Siegert relation, and the assumptions therein, do not constrain holographic FD-DCS. The Siegert relation assumes that a scattered field obeys Gaussian statistics and is violated in the presence of static scatterers or stray light at the sensor. Obviating the Siegert relation is therefore an advantage when performing measurements in typical clinical settings, in which optical isolation of imaged areas from ambient light may be impractical.

A fundamental limitation of holographic FD-DCS to the application of *in vivo* measurement is the requirement to obtain a series of very short exposure camera frames, at a series of discrete frequency shifts, all at a fast enough sample rate so as to ensure the accurate recovery of pulsatile information. These short camera exposure times come at the cost of broadening of the signal in the Fourier domain, and make the data more difficult to interpret, especially in the presence of static scatterers. Whilst the investigation of IRF deconvolution and static scatterer compensation techniques could be one way to solve this problem, another solution could be to adopt the approach used by ISVS, for example. This technique works by assessing the amount of *blurring* within recorded holograms, rather than using *frequency shifting*, to access sample dynamics.

Compared to time-domain DCS (TD-DCS) and iNIRS, holographic FD-DCS is limited in that it does not offer TOF resolved detection. However, by modifying a holographic FD-DCS instrument with the addition of a tunable laser, it is possible to use frequency shifting to isolate individual beat frequencies, each of which encodes a particular photon pathlength. The disadvantage of this approach, however, would be the reduction in speed owing to the frequency shifting.

To conclude the comparison of holographic FD-DCS with other approaches aimed at improving the performance of DCS, holographic FD-DCS is a potential candidate for the detection of both long wavelength DCS and AOM-DCS signals, which can be used to improve SNR and spatial resolution, respectively. Therefore, the future work

of this thesis also includes investigating long wavelength holographic FD-DCS, and the development of an AOM FD-DCS analytical model, as well as an exploration of depth-resolved flow measurement strategies using this combined technique.

Finally, it is important to consider the potential clinical translation of holographic FD-DCS. For this to be achieved, sensitivity to CBF would need to be demonstrated, and this could be achieved by developing acousto-optically modulated FD-DCS, or by extension to a superficial regression technique or tomographic approach. With further experimental effort it would be possible to measure multiple source-detector pairs on the same sensor (by using a spatially coherent fibre bundle or multiple detector fibres, for example), and these investigations also form part of the future work of this thesis. Having achieved CBF sensitivity, the use of a longer design wavelength (i.e., 1064 nm), continued work on the development of a suitable *in vivo* probe, and scaling up the number of sample arms and detectors to improve head coverage, would all need to be considered before taking the instrument through to clinical trials and application.

7.2.2 Chapter 5

Whilst the use of a low laser power [28] and optical isolation stages [110] have been advocated in the DCS literature to reduce the incidence of mode hopping, it is surprising that the effects of mode hopping described in Chapter 5 are not observed and accounted for elsewhere in the the digital holography literature. Additionally, any coherent multiple camera frame technique will be vulnerable to mode hopping in the way that I have described in this thesis, and it would be interesting to observe if a similar phenomenon has been encountered in techniques such as MiDWS [23] and ISVS [37], for example. It is also surprising that the MTF of a digital holography instrument (in this thesis a *lensless* digital Fourier holography instrument) has not been experimentally validated and corrected for in the literature before. Although the MTF will not vary from camera frame to camera frame, and therefore does not affect absolute validation experiments, it does increase the variance of the data and therefore introduce noise. ISVS [37] and LDH [145] both make use of digital holography to recover quantitative flow parameters in biomedical optics, and yet neither of these two techniques describes MTF correction in its signal processing pipeline. I hope that the work presented in this thesis leads to the more commonplace inclusion of the MTF in image reconstructions in digital holography.

Although inspired by the LDH technique of Puyo *et al.* [145], my implementation of SVD spatiotemporal filtering is different to that implemented in LDH. The authors of the LDH technique compute singular values over a short-time window of 1024 frames, when running their camera at 75 kHz, which yields an integration time of 14 ms. Whilst this is fast enough to resolve pulsatile flow *in vivo*, the holographic FD-DCS experiments reported in this thesis use low-frame rate measurement (i.e., 200 Hz), which means that

the high-frame requirement of SVD spatiotemporal filtering is not appropriate when detecting rapidly changing signals. Furthermore, in this thesis I have not investigated the impact of SVD spatiotemporal filtering on absolute measurement value (as was done by Robinson *et al.* [173]), nor have I considered methods for automating the thresholding of singular values. However, I have used SVD spatiotemporal filtering as a validation tool with which to analyse *in vitro* validation datasets, and to confirm that any particular experimental setup is not impacted by spatiotemporally correlated noise sources. I have also been able characterise some of these noise sources by inspection of the temporal singular vectors associated with elevated singular values.

Two research groups have recently investigated the relationship between multispeckle DCS detection and SNR performance. Sie *et al.* observed an SNR gain that was equal to the square root of the number of detected speckles, when detecting 1024 speckles using a 32×32 SPAD camera [10]. Xu *et al.* were not able to achieve this linear SNR scaling target when detecting $\sim$3000 speckles using a CMOS camera [66]; these authors attributed this deficit to experimental imperfections, such as detector noise and imperfect control of the speed of the sample. Given the findings of Sie *et al.*, and also the findings of the denoising algorithm that I present in Chapter 5, I suspect that this deficit is mainly due to the noise performance of CMOS sensors. The denoising algorithm that I present is unprecedented in the field of multispeckle DCS detection, and, as it can be used to both characterise and remove noise sources, I hope that other researchers will find it useful when denoising multispeckle DCS measurements.

The spatiotemporal filtering aspect of off-axis digital holography is instrumental in achieving shot noise limited detection when using inexpensive and relatively noisy detectors, which I have demonstrated in Figure 3.4(c). Although this figure demonstrates shot noise limited performance for a single frame, I have found that this effect does not persist over the whole multispeckle pattern when using temporal SNR statistics. In order to achieve this linear SNR scaling target over the whole multispeckle pattern, I have shown in Figure 5.11(b) that both source noise and detector noise must be accounted for, and this is a consideration that has been expounded in neither the DCS nor the digital holography literature before. Whilst I have shown that the multispeckle denoising algorithm that I have presented can remove both detector noise and sampling noise from a time-series of multispeckle DCS measurements, the major limitation of this algorithm is the trade-off between SNR gain and temporal resolution.

In this thesis I have characterised the SNR performance of a holographic FD-DCS instrument without trialling the use of different detectors. Experimenting with different detectors would be useful in corroborating the impact of detector noise on SNR performance that I documented in Chapter 5. The future work of this thesis also includes developing a forward model for holographic FD-DCS, which could be achieved using the simulation framework presented in Chapter 6. Such a forward model would

have three main functions. Firstly, it could be used as a system characterisation tool. Secondly, it could be used to aid a fuller statistical analysis of the multispeckle denoising algorithm that I have presented. Thirdly, it could be used to generate training data for the application of learning approaches to holographic FD-DCS. Robinson *et al.* highlight that camera-based approaches to DCS have the disadvantages of requiring software postprocessing and less manageable data volumes, especially for longer recordings [32]. These factors affect the ability to achieve real-time measurement, and learning approaches have already been used in conventional DCS to speed up blood flow (BF) quantification 23-fold [112]. I therefore propose that the application of learning approaches to holographic FD-DCS would be useful in compensating for the software postprocessing and data volumes that are required by the technique.

Other further work that leads from Chapter 5 is the improvement of the *in vivo* probe that was developed in Chapter 4. The SNR performance characterisation that was described in Chapter 5 was performed on *in vitro* data, and, in Chapter 4, I demonstrated how an *in vitro* SNR advantage did not translate into an *in vivo* SNR advantage (Figure 4.18). This may well be due to patient movement artefact and sub-optimal tissue coupling, and improvements to the *in vivo* probe therefore warrant further investigation. Whilst all of the research objectives that are enumerated in Section 1.2 have been achieved in this thesis, the further work that is described in this paragraph addresses a potential shortcoming related to research objective 2 (i.e., the holographic FD-DCS instrument that I have developed is not suitable for repeatable high SNR *in vivo* measurement in its current form).

In Chapter 5, I have also inferred various physical properties of the holographic FD-DCS instrument based on data analysis. For example, by compensating for the MTF of the instrument I have inferred a camera pixel fill-factor of 72 %, and, by inspection of the temporal singular values of SVD spatiotemporal filtering, I have inferred that the laser does not achieve stable single-frequency output when being pumped at its maximum output power. Inspection of the microlens array using an optical microscope would therefore be a useful further investigation, as would assessing the laser beam at various output powers using an optical spectrum analyser.

7.2.3 Chapter 6

Chapter 6 draws together literature relating not only to previous speckle simulation algorithms [181, 184], but also that relating to time-integrated speckle PDF solutions [150, 155], the forms of $g_1(\tau)$ commonly encountered in biomedical optics and how they relate to speckle contrast [80, 89], and also AOM-DCS [18, 33]. The context of the speckle simulation algorithm that I have developed within this literature is embedded throughout Chapter 6.

The main limitation of the speckle simulation framework that I present in Chapter 6

is that narrower $g_1(\tau)$ functions require sampling with a higher N value, which requires the addition of more fully developed speckle patterns, and subsequently decreases the computational performance of the simulation. Future work to mitigate this could include the use of pre-computed libraries of fully developed speckle patterns, GPU acceleration, and lower level programming languages. Another limitation of the technique is that it does not parameterise the coherence factor, β, although, in Chapter 6, I do discuss how the technique can be extended to include two orthogonal polarisation states, and I describe how Goodman's approximate PDF simulation technique can be adapted if the parameterisation of β is necessary.

A potential limitation of the work presented in Chapter 6 is that it does not consider how faithfully the simulation framework operates under conditions of experimental noise, and that the framework has not been validated by experimental results. Whilst I appreciate this concern, it overlooks the fundamentally novel and impactful contribution of this chapter. The proposed simulation technique aims to simulate the signal of a 2D-TIDSP; prior to this thesis the simulation of the signal of a statistically accurate 2D-TIDSP that accounts for any arbitrary $g_1(\tau)$ function was an unsolved problem. In addition to this, previous speckle simulation studies [181, 184] do not explicitly model the inclusion of experimental noise into the simulation of speckle patterns. However, the addition of specific models of experimental noise (such as shot noise, read noise, dark noise, and hot pixels [25], as well as noise models unique to any arbitrary speckle measurement system) would be a useful and interesting further study that is unfortunately outside the scope of this thesis. In this thesis I robustly validate my proposed technique against previously published solutions for the exact PDF of time-integrated intensity for coherent light. I further validate my technique (both in terms of intra-image and inter-image statistics) against expressions for speckle contrast for different forms of homogeneous field.

Following on from this concern, the quality of the simulation is limited by the *knowledge* of $g_1(\tau)$ of the sample, including its spatial variation. It is not within the remit of the simulation framework to predict what $g_1(\tau)$ will be at each pixel. The simulations in this thesis have focussed on the generation of LSCI images, which only contain information relating to superficial scatterers, by discretising the sample into a 2D matrix. It is possible to extend the simulation framework to consider the scattering that is detected at the sample surface due to scatterers *within* the volume of the sample, by discretising the sample into a 3D matrix and assigning properties to each element. This would allow for the use of more complicated forms of $g_1(\tau)$ that include depth dependent information (such as that used to model the correlation diffusion equation in a semi-infinite geometry in DCS experiments, for example), as well as the consideration of the interaction of multiple source-detector pairs (i.e., diffuse correlation tomography [DCT]). If the form of $g_1(\tau)$ is known, then, by incorporating a suitably high number of tissue labels

within the sample volume, as well as the CTF of the instrument, local changes in sample properties can be modelled, which can incorporate any form of $g_1(\tau)$. Experimental validation of these simulations would indeed be a useful and interesting further study, but the validation that I have demonstrated in this thesis proves the potential impact of the technique.

Appendix A Developing a Fourier domain DCS model

A.1 Brownian motion

The time domain expression that we wish to Fourier transform is

$$G_{1d}(\tau) = \frac{S_0}{4\pi D}\left[\frac{\exp^{-K(\tau)r_1}}{r_1} - \frac{\exp^{-K(\tau)r_2}}{r_2}\right], \tag{135}$$

where

$$K(\tau) = \sqrt{3\mu_a\mu_s' + \mu_s'^2 k_0^2 6D_b|\tau|}, \tag{136}$$

for a Brownian motion model. The term outside the square brackets in Equation 135 has no dependence on τ, and the terms inside the square brackets can be split. Then, having made simplifying substitutions, the following expression can be arrived at to undergo Fourier transform

$$f(\tau) = \frac{\exp\left(-R\sqrt{AB + B^2F|\tau|}\right)}{R}. \tag{137}$$

As $G_{1d}(\tau)$ is a real and even function, i.e., symmetrical about $\tau = 0$, its Fourier transform is also real. Thus, only the real part of the full Fourier transform could be used. Alternatively, a Fourier cosine transform can be performed from the outset, which takes advantage of the Fourier transform property

$$\int_{-\infty}^{+\infty} g(|\tau|)\exp(i\omega\tau)\,d\tau = 2\int_0^{+\infty} g(\tau)\cos(\omega\tau)\,d\tau, \tag{138}$$

to arrive at

$$F(\omega) = \frac{2}{\sqrt{2\pi}}\int_0^{+\infty} \frac{\exp\left(-R\sqrt{AB + B^2F\tau}\right)}{R}\cos(\omega\tau)\,d\tau. \tag{139}$$

An integration by substitution approach was employed to solve Equation 139, where

$$Z = AB + B^2F\tau, \tag{140}$$

such that

$$\tau = \frac{Z - AB}{B^2F}, \tag{141}$$

and

$$d\tau = \frac{dZ}{B^2F}, \tag{142}$$

and the lower and upper integration limits of Equation 139 become AB and $+\infty$, respectively.

After applying the substitutions given by Equations 140, 141, and 142, Equation 139

becomes

$$F(\omega) = \frac{2}{\sqrt{2\pi}RB^2F}\int_{AB}^{+\infty}\exp(-R\sqrt{Z})\cos\left(\omega\frac{Z-AB}{B^2F}\right)\,dZ, \tag{143}$$

which was evaluated in Mathematica as

$$F(\omega) = \frac{2}{\sqrt{2\pi}RB^2F}\times\ldots \left(\left[\int_0^{+\infty}\exp(-R\sqrt{Z})\cos\left(\omega\frac{Z-AB}{B^2F}\right)\,dZ\right]-\ldots \left[\int_0^{AB}\exp(-R\sqrt{Z})\cos\left(\omega\frac{Z-AB}{B^2F}\right)\,dZ\right]\right), \tag{144}$$

with the assumptions

$$\{A,B,F,R\}\in\mathbb{R}_{>0},\quad Z\in\mathbb{R}_{\geq 0},\text{ and}\quad \omega\in\mathbb{R}.$$

The result of Equation 144 is then

$$\frac{B\sqrt{F}\omega\exp\left(-\frac{iA\omega}{BF}-\frac{iB^2FR^2}{4\omega}\right)}{4\left|\omega\right|^{7/2}\operatorname{sgn}(\omega)}\times\ldots \left[\exp\left(\frac{iB^2FR^2}{2\omega}\right)\left[-(1-i)\sqrt{\omega}\sqrt{|\omega|}\operatorname{erf}\left[T_+(\omega)\right]+|\omega|-i\omega\right]+\ldots \exp\left(\frac{2iA\omega}{BF}\right)\left[-(1+i)\sqrt{\omega}\sqrt{|\omega|}\operatorname{erf}\left[T_-(\omega)\right]+|\omega|+i\omega\right]\right], \tag{145}$$

where the auxiliary function, $T_\pm(\omega)$, is defined as

$$T_\pm(\omega) = \frac{(2\mp 2i)\omega\sqrt{\frac{AB}{F}}+(1\pm i)B^2\sqrt{F}R}{2\sqrt{2}B\sqrt{\omega}}, \tag{146}$$

and where, for real x,

$$\operatorname{sgn}(x) = \begin{cases} -1 & x<0 \\ 0 & x=0 \\ 1 & x>1, \end{cases} \tag{147}$$

and where the error function is the integral of the Gaussian distribution

$$\operatorname{erf}(z) = \frac{2}{\sqrt{\pi}}\int_0^z \exp^{-t^2}\,dt. \tag{148}$$

Equation 145 can be simplified, for the case of $\omega > 0$, to

$$\frac{1}{\omega^{3/2}}\left(\frac{1}{4}+\frac{i}{4}\right)B\sqrt{F}\exp\left(-\frac{iA\omega}{BF}-\frac{iB^2FR^2}{4\omega}\right)\times\ldots \\ \left[-i\exp\left(\frac{iB^2FR^2}{2\omega}\right)\operatorname{erfc}\left[T_+(\omega)\right]+\exp\left(\frac{2iA\omega}{BF}\right)\operatorname{erfc}\left[T_-(\omega)\right]\right], \quad (149)$$

and, for the case of $\omega < 0$, to

$$\frac{1}{\omega}\left(\frac{1}{4}+\frac{i}{4}\right)B\sqrt{-\frac{F}{\omega}}\exp\left(-\frac{iA\omega}{BF}-\frac{iB^2FR^2}{4\omega}\right)\times\ldots \\ \left[-\exp\left(\frac{iB^2FR^2}{2\omega}\right)\operatorname{erfc}\left[T_+(\omega)\right]+\ldots \right. \\ \left.\exp\left(\frac{2iA\omega}{BF}\right)\left(\operatorname{erfi}\left(\frac{\left(\frac{1}{2}+\frac{i}{2}\right)\left(B^2\sqrt{F}R+2i\omega\sqrt{\frac{AB}{F}}\right)}{\sqrt{2}B\sqrt{\omega}}\right)+i\right)\right], \quad (150)$$

where the complementary error function

$$\operatorname{erfc}(z) = 1-\operatorname{erf}(z), \quad (151)$$

and where the imaginary error function

$$\operatorname{erfi}(z) = \operatorname{erf}(iz)/i. \quad (152)$$

Equation 145 is undetermined for the case of $\omega = 0$, and I have therefore been unable to implement a *normalised* Brownian FD-DCS model, which would be given by

$$s_{1d}(\omega) = \frac{F(\omega,r_1)-F(\omega,r_2)}{F(0,r_1)-F(0,r_2)}. \quad (153)$$

The Fourier transform of Equation 135 that I implement in the Brownian FD-DCS forward model is then

$$S_{1d}(\omega) = \frac{S_0}{4\pi D}\left[F(\omega,r_1)-F(\omega,r_2)\right], \quad (154)$$

where ω is detuning frequency (rads/s). For practical purposes, I limit the expression for $F(\omega,r)$ that I have developed to the case of $\omega > 0$, having reversed the substitutions

used in Equation 137

$$F_{[D_b]}(\omega_+, r) = \frac{1}{\omega^{3/2}}\left(\frac{1}{4}+\frac{i}{4}\right)\mu_s'\sqrt{6k_0^2 D_b}\times\ldots \exp\left(-\frac{i\mu_a\omega}{2\mu_s' k_0^2 D_b}-\frac{3i\mu_s'^2 k_0^2 D_b r^2}{2\omega}\right)\times\ldots \left[-i\exp\left(\frac{3i\mu_s'^2 k_0^2 D_b r^2}{\omega}\right)\operatorname{erfc}\left[A_+(\omega)\right]+\ldots \exp\left(\frac{i\mu_a\omega}{\mu_s' k_0^2 D_b}\right)\operatorname{erfc}\left[A_-(\omega)\right]\right], \quad (155)$$

where the auxiliary function, $A_\pm(\omega)$, is defined as

$$A_\pm(\omega) = \frac{(2\mp 2i)\omega\sqrt{\frac{\mu_a\mu_s'}{2k_0^2 D_b}}+(1\pm i)\mu_s'^2 r\sqrt{6k_0^2 D_b}}{2\sqrt{2}\mu_s'\sqrt{\omega}}, \quad (156)$$

as given by Equations 64, 65, 66, 67, and 68 in Chapter 4.

A.2 Convective motion

The initial problem formulation is identical to that adopted when solving for Brownian motion: the time domain expression that we wish to Fourier transform is Equation 135; however, the following form of Equation 136 is considered for convective motion

$$K(\tau) = \sqrt{3\mu_a\mu_s' + \mu_s'^2 k_0^2 V^2\tau^2}. \quad (157)$$

Equation 157 yields the following expression to undergo Fourier transform

$$f(\tau) = \frac{\exp\left(-R\sqrt{AB+B^2F\tau^2}\right)}{R}, \quad (158)$$

which can be manipulated as follows

$$f(\tau) = \frac{1}{R}\exp\left(-R\sqrt{B^2F\left[\frac{A}{BF}+\tau^2\right]}\right), \quad (159)$$

$$f(\tau) = \frac{1}{R}\exp\left(-R\sqrt{B^2F}\sqrt{\left[\frac{A}{BF}+\tau^2\right]}\right), \quad (160)$$

$$f(\tau) = \frac{1}{R}\exp\left(-RB\sqrt{F}\sqrt{\left[\frac{A}{BF}+\tau^2\right]}\right). \quad (161)$$

Equation 161 is of the general form

$$f(x) = \exp\left(-\beta\sqrt{\alpha^2 + x^2}\right), \tag{162}$$

where the Fourier cosine transform of $f(x)$ is [189]

$$F(\omega) = \sqrt{\frac{2}{\pi}}\frac{\alpha\beta}{\sqrt{\beta^2 + \omega^2}}K_1\left[\alpha\sqrt{\beta^2 + \omega^2}\right], \tag{163}$$

for

$$\{\alpha, \beta\} \in \mathbb{R}_{>0}, \tag{164}$$

and where K_1 is the first modified Bessel function of the second kind.

If the following substitutions are performed

$$\beta = RB\sqrt{F}, \tag{165}$$

$$\alpha = \sqrt{\frac{A}{BF}}, \tag{166}$$

$$x = t, \tag{167}$$

then the Fourier cosine transform of Equation 161 is

$$F(\omega, R) = \sqrt{\frac{2}{\pi}}\sqrt{\frac{AB}{B^2FR^2 + w^2}}K_1\left[\sqrt{A\left(BR^2 + \frac{w^2}{BF}\right)}\right], \tag{168}$$

where

$$F(0, R) = \sqrt{\frac{2}{\pi}}\frac{AK_1\left[\sqrt{AB}R\right]}{R\sqrt{ABF}}. \tag{169}$$

The Fourier transform of the unnormalised expression $G_{1d}(\tau)$ (Equation 135) is then

$$S_{1d}(\omega) = \frac{S_0}{4\pi D}\left[F(\omega, r_1) - F(\omega, r_2)\right], \tag{170}$$

the normalised expression of which is

$$s_{1d}(\omega) = \frac{F(\omega, r_1) - F(\omega, r_2)}{F(0, r_1) - F(0, r_2)}. \tag{171}$$

By reversing the substitutions of Equations 158, 165, 166, and 167,

$$F_{[V^2]}(\omega, r) = \sqrt{\frac{3\mu_a\mu_s'}{\mu_s'^2k_0^2V^2r^2 + \omega^2}}K_1\left(\sqrt{3\mu_a\left(\mu_s'r^2 + \frac{\omega^2}{\mu_s'k_0^2V^2}\right)}\right), \tag{172}$$

which is given by Equation 69 in Chapter 4, and

$$S_{1d}(\omega, r_1, r_2) = \frac{S_0}{2\sqrt{2}\pi^{3/2}D} \times \ldots \left[\sqrt{\frac{3\mu_a\mu_s'}{\mu_s'^2 k_0^2 V^2 r_1^2 + \omega^2}} K_1 \left(\sqrt{3\mu_a \left(\mu_s' r_1^2 + \frac{\omega^2}{\mu_s' k_0^2 V^2} \right)} \right) - \ldots \sqrt{\frac{3\mu_a\mu_s'}{\mu_s'^2 k_0^2 V^2 r_2^2 + \omega^2}} K_1 \left(\sqrt{3\mu_a \left(\mu_s' r_2^2 + \frac{\omega^2}{\mu_s' k_0^2 V^2} \right)} \right) \right], \quad (173)$$

and

$$s_{1d}(\omega, r_1, r_2) = \frac{\sqrt{\mu_s'} k_0 V r_1 r_2}{\sqrt{3\mu_a} \left[r_2 K_1 \left(\sqrt{3\mu_a\mu_s'} r_1 \right) - r_1 K_1 \left(\sqrt{3\mu_a\mu_s'} r_2 \right) \right]} \times \ldots \left[\sqrt{\frac{3\mu_a\mu_s'}{\mu_s'^2 k_0^2 V^2 r_1^2 + \omega^2}} K_1 \left(\sqrt{3\mu_a \left(\mu_s' r_1^2 + \frac{\omega^2}{\mu_s' k_0^2 V^2} \right)} \right) - \ldots \sqrt{\frac{3\mu_a\mu_s'}{\mu_s'^2 k_0^2 V^2 r_2^2 + \omega^2}} K_1 \left(\sqrt{3\mu_a \left(\mu_s' r_2^2 + \frac{\omega^2}{\mu_s' k_0^2 V^2} \right)} \right) \right], \quad (174)$$

for

$$\sqrt{\frac{3\mu_a}{\mu_s' k_0^2 V^2}} \in \mathbb{R}_{>0},$$
$$r_1 \mu_s' k_0 V \in \mathbb{R}_{>0},$$
$$r_2 \mu_s' k_0 V \in \mathbb{R}_{>0},$$

for convective motion.

A.3 Acousto-optic modulation

By considering the acoustic modulation of Equation 135,

$$G_{1(d+a)}(\tau) = \frac{S_0}{4\pi D} \left[\frac{\exp^{-K(\tau)r_1}}{r_1} - \frac{\exp^{-K(\tau)r_2}}{r_2} \right] \cos(n\omega_a \tau), \quad (175)$$

where the subscript $(d + a)$ refers to dynamic scatterers and acoustic modulation, n corresponds to the harmonic of acoustic modulation, and ω_a is the ultrasound radial frequency [18]. The Fourier cosine transform of Equation 175 is then

$$2 \int_0^{+\infty} G_{1d}(\tau) \cos(n\omega_a \tau) \cos(\omega\tau) \, \mathrm{d}\tau. \quad (176)$$

The trigonometric product-sum identity states

$$\cos(x)\cos(y) = \frac{1}{2}[\cos(x+y) + \cos(x-y)], \tag{177}$$

which I use to rearrange Equation 176 to

$$\int_0^{+\infty} G_{1d}(\tau)\cos([\omega + n\omega_a]\tau)\,\mathrm{d}\tau + \int_0^{+\infty} G_{1d}(\tau)\cos([\omega - n\omega_a]\tau)\,\mathrm{d}\tau. \tag{178}$$

I have already derived the results to these Fourier cosine transforms, for Brownian and convective motion in Appendices A.1 and A.2, respectively. These results can be used directly to state

$$F_a(\omega, \omega_a, r, n) = F(\omega + n\omega_a, r) + F(\omega - n\omega_a, r). \tag{179}$$

The Fourier transform of Equation 175 is then

$$S_{1(d+a)}(\omega, \omega_a, n) = \frac{S_0}{4\pi D}\left[F_a(\omega, \omega_a, r_1, n) - F_a(\omega, \omega_a, r_2, n)\right], \tag{180}$$

the normalised expression of which is

$$s_{1(d+a)}(\omega, \omega_a, n) = \frac{[F_a(\omega, \omega_a, r_1, n) - F_a(\omega, \omega_a, r_2, n)]}{[F_a(0, \omega_a, r_1, n) - F_a(0, \omega_a, r_2, n)]}. \tag{181}$$

Note that this logic for acoustic modulation can be applied to both Brownian and convective models of motion.

Appendix B Time-integrated pre-defined correlation distribution

This appendix details the mathematical derivation of an expression for a two-dimensional time-integrated dynamic speckle pattern (2D-TIDSP), $\mathbf{W}$, using the pre-defined correlation distribution method approach that is described in Section 6.2.2. I start by substituting Equation 88 into Equation 92

$$\mathbf{I} = \left| \mathcal{F}^{-1} \left[\left[r\mathcal{F}\left[\mathbf{U}_1\right] + \sqrt{1-r^2}\mathcal{F}\left[\mathbf{U}_2\right] \right] \mathbf{H} \right] \right|^2, \tag{182}$$

multiplying out the inner square brackets

$$\mathbf{I} = \left| \mathcal{F}^{-1} \left[r\mathbf{H}\mathcal{F}\left[\mathbf{U}_1\right] + \sqrt{1-r^2}\mathbf{H}\mathcal{F}\left[\mathbf{U}_2\right] \right] \right|^2, \tag{183}$$

which, due to the linearity property of the inverse Fourier transform, can be expressed as

$$\mathbf{I} = \left| r\mathcal{F}^{-1}\left[\mathbf{H}\mathcal{F}\left[\mathbf{U}_1\right]\right] + \sqrt{1-r^2}\mathcal{F}^{-1}\left[\mathbf{H}\mathcal{F}\left[\mathbf{U}_2\right]\right] \right|^2, \tag{184}$$

which can be simplified to

$$\mathbf{I} = \left| r\mathbf{A} + \sqrt{1-r^2}\mathbf{B} \right|^2, \tag{185}$$

where $\mathbf{A} = \mathcal{F}^{-1}\left[\mathbf{H}\mathcal{F}\left[\mathbf{U}_1\right]\right]$ and $\mathbf{B} = \mathcal{F}^{-1}\left[\mathbf{H}\mathcal{F}\left[\mathbf{U}_2\right]\right]$. $\mathbf{A}$ and $\mathbf{B}$ are two constant and complex valued 2D matrices, each of which has no dependence on r.

Considering an element-wise decomposition of $\mathbf{I}$ into real and imaginary components, let $\mathbf{A} = \mathbf{a} + \mathbf{b}i$, and $\mathbf{B} = \mathbf{c} + \mathbf{d}i$. Equation 185 can then be expressed as

$$\mathbf{I} = \left| r\mathbf{a} + r\mathbf{b}i + \sqrt{1-r^2}\mathbf{c} + \sqrt{1-r^2}\mathbf{d}i \right|^2, \tag{186}$$

collecting real and imaginary terms

$$\mathbf{I} = \left| r\mathbf{a} + \sqrt{1-r^2}\mathbf{c} + r\mathbf{b}i + \sqrt{1-r^2}\mathbf{d}i \right|^2, \tag{187}$$

calculating the complex magnitude

$$\mathbf{I} = \left[\sqrt{\left(r\mathbf{a} + \sqrt{1-r^2}\mathbf{c} \right)^2 + \left(r\mathbf{b} + \sqrt{1-r^2}\mathbf{d} \right)^2} \right]^2, \tag{188}$$

simplifying

$$\mathbf{I} = \left(r\mathbf{a} + \sqrt{1-r^2}\mathbf{c} \right)^2 + \left(r\mathbf{b} + \sqrt{1-r^2}\mathbf{d} \right)^2, \tag{189}$$

multiplying out brackets

$$\mathbf{I} = r^2\mathbf{a}^2 + 2r\mathbf{a}\sqrt{1-r^2}\mathbf{c} + \mathbf{c}^2(1-r^2) + r^2\mathbf{b}^2 + 2r\mathbf{b}\sqrt{1-r^2}\mathbf{d} + \mathbf{d}^2(1-r^2), \tag{190}$$

multiplying out brackets and collecting terms

$$\mathbf{I} = r^2\left(\mathbf{a}^2 + \mathbf{b}^2 - \mathbf{c}^2 - \mathbf{d}^2\right) + 2r\sqrt{1-r^2}\left(\mathbf{ac} + \mathbf{bd}\right) + \mathbf{c}^2 + \mathbf{d}^2. \tag{191}$$

Using the form of r presented in Equation 16 of [181]

$$r^2 = \exp\left(-\frac{\tau}{\tau_c}\right), \tag{192}$$

$$r = \sqrt{\exp\left(-\frac{\tau}{\tau_c}\right)}, \tag{193}$$

and substituting Equations 192 and 193 into Equation 191, the expression for instantaneous intensity is

$$\begin{aligned}\boldsymbol{I}(\tau) = \exp\left(-\frac{\tau}{\tau_c}\right)\left(\mathbf{a}^2 + \mathbf{b}^2 - \mathbf{c}^2 - \mathbf{d}^2\right) + \cdots \\ 2\sqrt{\exp\left(-\frac{\tau}{\tau_c}\right)}\sqrt{1-\exp\left(-\frac{\tau}{\tau_c}\right)}\left(\mathbf{ac} + \mathbf{bd}\right) + \mathbf{c}^2 + \mathbf{d}^2.\end{aligned} \tag{194}$$

We therefore wish to solve

$$\mathbf{W} = \frac{1}{T}\int_0^T \boldsymbol{I}(\tau)\, d\tau, \tag{195}$$

where $\mathbf{W}$ is the intensity of a 2D-TIDSP, and where T is the integration time of the camera.

The indefinite integral of Equation 194 with respect to τ is

$$\begin{aligned}\int \boldsymbol{I}(\tau)\, d\tau = \tau\left(\mathbf{c}^2 + \mathbf{d}^2\right) + \tau_c \exp\left(-\frac{\tau}{\tau_c}\right)\left(-\mathbf{a}^2 - \mathbf{b}^2 + \mathbf{c}^2 + \mathbf{d}^2\right) - \cdots \\ \left[\exp\left(\frac{\tau}{\tau_c}\right) + \exp\left(\frac{\tau}{\tau_c}\right)\sqrt{1-\exp\left(\frac{\tau}{\tau_c}\right)}\tanh^{-1}\left(\sqrt{1-\exp\left(\frac{\tau}{\tau_c}\right)}\right) - 1\right] \times \cdots \\ \frac{2\tau_c \exp\left(-\frac{2\tau}{\tau_c}\right)\left(\mathbf{ac} + \mathbf{bd}\right)}{\sqrt{\exp\left(-\frac{2\tau}{\tau_c}\right)\left(\exp\left(\frac{\tau}{\tau_c}\right) - 1\right)}}.\end{aligned} \tag{196}$$

For $\lim_{\tau \to 0}$, Equation 196 converges on

$$\int \boldsymbol{I}(\tau)\, d\tau = \tau_c \left(-\mathbf{a}^2 - \mathbf{b}^2 + \mathbf{c}^2 + \mathbf{d}^2 \right). \tag{197}$$

and the definite integral over the camera exposure period evaluates to

$$\begin{aligned} \mathbf{W} = \frac{1}{T} \Bigg[& T \left(\mathbf{c}^2 + \mathbf{d}^2 \right) + \cdots \\ & \tau_c \left(\mathbf{a}^2 + \mathbf{b}^2 - \mathbf{c}^2 - \mathbf{d}^2 \right) + \tau_c X \left(-\mathbf{a}^2 - \mathbf{b}^2 + \mathbf{c}^2 + \mathbf{d}^2 \right) - \cdots \\ & \frac{2\tau_c Z(\mathbf{ac} + \mathbf{bd}) \left[Y - 1 + Y\sqrt{1-Y} \tanh^{-1}\left(\sqrt{1-Y} \right) \right]}{\sqrt{Z\,(Y-1)}} \Bigg], \end{aligned} \tag{198}$$

where

$$x = T/\tau_c, \tag{199}$$

$$X = \exp\left(-x\right), \tag{200}$$

$$Y = \exp\left(x\right), \tag{201}$$

$$Z = \exp\left(-2x\right). \tag{202}$$

Bibliography

1. Tsalach, A. *et al.* Depth selective acousto-optic flow measurement. *Biomedical Optics Express* **6,** 4871–4886 (2015).
2. Lang, E. W. *et al.* A Review of Cerebral Autoregulation: Assessment and Measurements. *Australian Anaesthesia,* 161–172 (2005).
3. Durduran, T. & Yodh, A. G. Diffuse correlation spectroscopy for non-invasive, micro-vascular cerebral blood flow measurement. *NeuroImage* **85,** 51–63 (2014).
4. Buckley, E. M., Parthasarathy, A. B., Grant, P. E., Yodh, A. G. & Franceschini, M. A. Diffuse correlation spectroscopy for measurement of cerebral blood flow: future prospects. *Neurophotonics* **1,** 011009 (2014).
5. Fantini, S., Sassaroli, A., Tgavalekos, K. T. & Kornbluth, J. Cerebral blood flow and autoregulation: current measurement techniques and prospects for noninvasive optical methods. *Neurophotonics* **3,** 031411 (2016).
6. Smith, M. Monitoring intracranial pressure in traumatic brain injury. *Anesthesia and Analgesia* **106,** 240–248 (2008).
7. Steiner, L. A. & Andrews, P. J. Monitoring the injured brain: ICP and CBF. *British Journal of Anaesthesia* **97,** 26–38 (2006).
8. Durduran, T., Choe, R., Baker, W. B. & Yodh, A. G. Diffuse optics for tissue monitoring and tomography. *Reports on Progress in Physics* **73,** 076701 (2010).
9. Tavakoli, S., Peitz, G., Ares, W., Hafeez, S. & Grandhi, R. Complications of invasive intracranial pressure monitoring devices in neurocritical care. *Neurosurgical Focus* **43,** E6 (2017).
10. Sie, E. J. *et al.* High-sensitivity multispeckle diffuse correlation spectroscopy. *Neurophotonics* **7,** 035010 (2020).
11. DeSantis, C. E. *et al.* International Variation in Female Breast Cancer Incidence and Mortality Rates. *Cancer Epidemiology, Biomarkers & Prevention* **24,** 1495–1506 (2015).
12. Durduran, T. *et al.* Diffuse optical measurement of blood flow in breast tumors. *Optics Letters* **30,** 2915–1917 (2005).
13. Zhou, C. *et al.* Diffuse optical monitoring of blood flow and oxygenation in human breast cancer during early stages of neoadjuvant chemotherapy. *Journal of Biomedical Optics* **12,** 051903 (2007).
14. Sunar, U. *et al.* Noninvasive diffuse optical measurement of blood flow and blood oxygenation for monitoring radiation therapy in patients with head and neck tumors: a pilot study. *Journal of Biomedical Optics* **11,** 064021 (2006).

15. Yu, G. *et al.* Real-time *In Situ* Monitoring of Human Prostate Photodynamic Therapy with Diffuse Light. *Photochemistry and Photobiology* **82,** 1279–1284 (2006).

16. Yu, G. *et al.* Noninvasive Monitoring of Murine Tumor Blood Flow During and After Photodynamic Therapy Provides Early Assessment of Therapeutic Efficacy. *Clinical Cancer Research* **11,** 3543–3552 (2005).

17. Cheatle, T. R. *et al.* Near-infrared spectroscopy in peripheral vascular disease. *British Journal of Surgery* **78,** 405–408 (1991).

18. Gunther, J. & Andersson-Engels, S. Review of current methods of acousto-optical tomography for biomedical applications. *Frontiers of Optoelectronics* **10,** 211–238 (2017).

19. Yu, G., Durduran, T., Zhou, C., Cheng, R. & Yodh, A. G. in *Handbook of Biomedical Optics* 1st, 195–216 (CRC Press, 2011).

20. The British Standards Institution. BS EN 60825-1:2014 - Safety of laser products (2017).

21. Boas, D. A. & Yodh, A. G. Spatially varying dynamical properties of turbid media probed with diffusing temporal light correlation. *Journal of the Optical Society of America A* **14,** 192–215 (1997).

22. Wang, D. *et al.* Fast blood flow monitoring in deep tissues with real-time software correlators. *Biomedical Optics Express* **7,** 776–797 (2016).

23. Zhou, W., Zhao, M., Kholiqov, O. & Srinivasan, V. Multi-exposure interferometric diffusing wave spectroscopy. *Optics Letters* **46,** 4498–4501 (2021).

24. Zhou, W. *et al.* Functional interferometric diffusing wave spectroscopy of the human brain. *Science Advances* **7,** eabe0150 (2021).

25. Varma, H. M., Valdes, C. P., Kristoffersen, A. K., Culver, J. P. & Durduran, T. Speckle contrast optical tomography: A new method for deep tissue three-dimensional tomography of blood flow. *Biomedical Optics Express* **5,** 1275–1289 (2014).

26. Murali, K. & Varma, H. M. Multi-speckle diffuse correlation spectroscopy to measure cerebral blood flow. *Biomedical Optics Express* **11,** 6699–6709 (2020).

27. Liu, W. *et al.* Fast and sensitive diffuse correlation spectroscopy with highly parallelized single photon detection. *APL Photonics* **6,** 026106 (2021).

28. Sutin, J. *et al.* Time-domain diffuse correlation spectroscopy. *Optica* **3,** 1006–1013 (2016).

29. Carp, S. A. *et al.* Diffuse correlation spectroscopy measurements of blood flow using 1064 nm light. *Journal of Biomedical Optics* **25,** 097003 (2020).

30. Ozana, N. *et al.* Superconducting nanowire single-photon sensing of cerebral blood flow. *Neurophotonics* **8,** 035006 (2021).

31. Zhou, W., Kholiqov, O., Chong, S. P. & Srinivasan, V. J. Highly parallel, interferometric diffusing wave spectroscopy for monitoring cerebral blood flow dynamics. *Optica* **5,** 518–527 (2018).

32. Robinson, M. B., Boas, D. A., Sakadzic, S., Franceschini, M. A. & Carp, S. A. Interferometric diffuse correlation spectroscopy improves measurements at long source–detector separation and low photon count rate. *Journal of Biomedical Optics* **25,** 097004 (2020).

33. Robinson, M. B. *et al.* Characterization of continuous wave ultrasound for acousto-optic modulated diffuse correlation spectroscopy (AOM-DCS). *Biomedical Optics Express* **11,** 3071–3090 (2020).

34. Gross, M., Atlan, M. & Absil, E. Noise and aliases in off-axis and phase-shifting holography. *Applied Optics* **47,** 1757–1766 (2008).

35. Zhou, C. *et al.* Diffuse optical correlation tomography of cerebral blood flow during cortical spreading depression in rat brain. *Optics Express* **14,** 1125–1144 (2006).

36. Selb, J. *et al.* Prolonged monitoring of cerebral blood flow and autoregulation with diffuse correlation spectroscopy in neurocritical care patients. *Neurophotonics* **5,** 045005 (2018).

37. Xu, J., Jahromi, A. K., Brake, J., Robinson, J. E. & Yang, C. Interferometric speckle visibility spectroscopy (ISVS) for human cerebral blood flow monitoring. *APL Photonics* **5,** 126102 (2020).

38. Wintermark, M. *et al.* Comparative overview of brain perfusion imaging techniques. *Stroke* **36,** e83–e99 (2005).

39. Kety, S. S. & Schmidt, C. F. The Determination Of Cerebral Blood Flow In Man By The Use Of Nitrous Oxide In Low Concentrations. *American Journal of Physiology* **143,** 53–66 (1945).

40. Tierradentro-García, L. O. *et al.* Cerebral Blood Flow of the Neonatal Brain after Hypoxic-Ischemic Injury. *American Journal of Perinatology* (2021).

41. Wietasch, G. J. K. *et al.* Bedside Assessment of Cerebral Blood Flow by Double-indicator Dilution Technique. *Anesthesiology* **92,** 367–375 (2000).

42. Buxton, R. B. The physics of functional magnetic resonance imaging (fMRI). *Reports on Progress in Physics* **76,** 096601 (2013).

43. Schmid, W. *et al.* Review of wearable technologies and machine learning methodologies for systematic detection of mild traumatic brain injuries. *Journal of Neural Engineering* **18,** 041006 (2021).

44. Kim, S.-G. Quantification of Relative Cerebral Blood Flow Change by Flow-Sensitive Alternating Inversion Recovery (FAIR) Technique: Application to Functional Mapping. *Magnetic Resonance in Medicine* **34,** 293–301 (1995).

45. Yerworth, R. *Anatomy and Physiology with Biomedical Applications - Lecture Notes* (University College London, 2015).

46. Cox, B. *Ultrasound in Medicine - Lecture Notes* (University College London, 2017).

47. Lu, J., Mamun, K. A. & Chau, T. Online transcranial Doppler ultrasonographic control of an onscreen keyboard. *Frontiers in Human Neuroscience* **8,** 199 (2014).

48. Lipnick, M. S., Cahill, E. A., Feiner, J. R. & Bickler, P. E. Comparison of Transcranial Doppler and Ultrasound-Tagged Near Infrared Spectroscopy for Measuring Relative Changes in Cerebral Blood Flow in Human Subjects. *Anesthesia & Analgesia* **126,** 579–587 (2017).

49. Nowaczewska, M. & Kaźmierczak, H. Cerebral Blood Flow in Low Intracranial Pressure Headaches—What Is Known? *Brain Sciences* **10,** 2 (2020).

50. Hwang, M. *et al.* Novel Contrast-Enhanced Ultrasound Evaluation in Neonatal Hypoxic Ischemic Injury: Clinical Application and Future Directions. *Journal of Ultrasound in Medicine* **36,** 2379–2386 (2017).

51. Charbel, F. T., Gonzales-Portillo, G., Hoffman, W. E., Ostergren, L. A. & Misra, M. Quantitative assessment of vessel flow integrity for aneurysm surgery. *Journal of Neurosurgery* **91,** 1050–1054 (1999).

52. Cox, B. *Biomedical Optics - Lecture Notes* (University College London, 2018).

53. Yun, S. H. & Kwok, S. J. J. Light in diagnosis, therapy and surgery. *Nature Biomedical Engineering* **1,** 0008 (2017).

54. Pinti, P. *et al.* Using Fiberless, Wearable fNIRS to Monitor Brain Activity in Real-world Cognitive Tasks. *Journal of Visualized Experiments* **106,** e53336 (2015).

55. Lloyd-Fox, S. *et al.* Functional near infrared spectroscopy (fNIRS) to assess cognitive function in infants in rural Africa. *Scientific Reports* **4,** 4740 (2014).

56. Hebden, J. C. in *Webb's Physics of Medical Imaging* 2nd, 665–685 (CRC Press, 2012).

57. Cheong, W.-F., Prahl, S. A. & Welch, A. J. A Review of the Optical Properties of Biological Tissues. *IEEE Journal of Quantum Electronics* **26,** 2166–2185 (1990).

58. Scholkmann, F. *et al.* A review on continuous wave functional near-infrared spectroscopy and imaging instrumentation and methodology. *NeuroImage* **85,** 6–27 (2014).

59. Henyey, L. G. & Greenstein, J. L. Diffuse Radiation In The Galaxy. *The Astrophysical Journal* **93,** 70–83 (1941).

60. Arridge, S. R. Optical tomography in medical imaging. *Inverse Problems* **15,** R41–R93 (1999).

61. Kaltenbach, J.-M. *Frequency- and time-domain modelling of light transport in random media* in *Medical Optical Tomography: Functional Imaging and Monitoring* (ed Mueller, G. J.) **10311** (SPIE, 1993), 65–86.

62. Contini, D., Martelli, F. & Zaccanti, G. Photon migration through a turbid slab described by a model based on diffusion approximation. I. Theory. *Applied Optics* **36,** 4587–4599 (1997).

63. Haskell, R. C. *et al.* Boundary conditions for the diffusion equation in radiative transfer. *Journal of the Optical Society of America A* **11,** 2727–2741 (1994).

64. Patterson, M., Madsen, S., Moulton, J. & Wilson, B. *Diffusion Equation Representation Of Photon Migration In Tissue* in *IEEE MTT-S International Microwave Symposium Digest* (1991), 905–908.

65. Parthasarathy, A. B., Tom, W. J., Gopal, A., Zhang, X. & Dunn, A. K. Robust flow measurement with multi-exposure speckle imaging. *Optics Express* **16,** 1975–1989 (2008).

66. Xu, J., Jahromi, A. K. & Yang, C. Diffusing wave spectroscopy: A unified treatment on temporal sampling and speckle ensemble methods. *APL Photonics* **6,** 016105 (2021).

67. Lemieux, P.-A. & Durian, D. J. Investigating non-Gaussian scattering processes by using *n*th-order intensity correlation functions. *Journal of the Optical Society of America A* **16,** 1651–1664 (1999).

68. Dong, L., He, L., Lin, Y., Shang, Y. & Yu, G. Simultaneously Extracting Multiple Parameters via Fitting One Single Autocorrelation Function Curve in Diffuse Correlation Spectroscopy. *IEEE Transactions on Biomedical Engineering* **60,** 361–368 (2013).

69. Eggebrecht, A. T. *et al.* Mapping distributed brain function and networks with diffuse optical tomography. *Nature Photonics* **8,** 448–454 (2014).

70. Hoshi, Y. & Yamada, Y. Overview of diffuse optical tomography and its clinical applications. *Journal of Biomedical Optics* **21,** 091312 (2016).

71. Hebden, J. C. Exploring the feasibility of wavelength modulated near-infrared spectroscopy. *Journal of Biomedical Optics* **25,** 110501 (2020).

72. White, B. R., Liao, S. M., Ferradal, S. L., Inder, T. E. & Culver, J. P. Bedside optical imaging of occipital resting-state functional connectivity in neonates. *NeuroImage* **59,** 2529–2538 (2012).

73. Tak, S. & Ye, J. C. Statistical analysis of fNIRS data: A comprehensive review. *NeuroImage* **85,** 72–91 (2014).

74. James, E. *An Analysis of Spatial Resolution in Continuous Wave Diffuse Optical Tomography* MA thesis (University College London, 2018).

75. Boas, D. A., Dale, A. M. & Franceschini, M. A. Diffuse optical imaging of brain activation: approaches to optimizing image sensitivity, resolution, and accuracy. *NeuroImage* **23,** S275–S288 (2004).

76. Hussain, A., Steenbergen, W. & Vellekoop, I. M. Imaging blood flow inside highly scattering media using ultrasound modulated optical tomography. *Journal of Biophotonics* **11,** e201700013 (2017).

77. Boas, D. A. & Dunn, A. K. Laser speckle contrast imaging in biomedical optics. *Journal of Biomedical Optics* **15,** 011109 (2010).

78. Fercher, A. F. & Briers, J. D. Flow Visualization By Means Of Single-Exposure Speckle Photography. *Optics Communications* **37,** 326–330 (1981).

79. Fredriksson, I. & Larsson, M. On the equivalence and differences between laser Doppler flowmetry and laser speckle contrast analysis. *Journal of Biomedical Optics* **21,** 126018 (2016).

80. Postnov, D. D., Tang, J., Erdener, S. E., Kılıç, K. & Boas, D. A. Dynamic light scattering imaging. *Science Advances* **6,** eabc4628 (2020).

81. Qiu, J. *et al.* Spatiotemporal laser speckle contrast analysis for blood flow imaging with maximized speckle contrast. *Journal of Biomedical Optics* **15,** 016003 (2010).

82. Dragojević, T. *et al.* Compact, multi-exposure speckle contrast optical spectroscopy (SCOS) device for measuring deep tissue blood flow. *Biomedical optics express* **9,** 322–334 (2018).

83. Murali, K., Nandakumaran, A. K., Durduran, T. & Varma, H. M. Recovery of the diffuse correlation spectroscopy data-type from speckle contrast measurements: towards low-cost, deep-tissue blood flow measurements. *Biomedical Optics Express* **10,** 5395–5413 (2019).

84. Safi, A. M. *et al. Quantitative Cerebral Blood Flow Imaging with Synthetic Single-Shot Multi-Exposure Laser Speckle Imaging* in *Biophotonics Congress 2021* (Optica Publishing Group, 2021), BW3B.4.

85. Clough, G., Chipperfield, A., Byrne, C., de Mul, F. & Gush, R. Evaluation of a new high power, wide separation laser Doppler probe: Potential measurement of deeper tissue blood flow. *Microvascular Research* **78,** 155–161 (2009).

86. Kolkman, R. G. M., Hondebrink, E., Bolt, R. A., Steenbergen, W. & de Mul, F. F. M. *Pulsed laser-Doppler flowmetry for monitoring deep perfusion* in *Hybrid and Novel Imaging and New Optical Instrumentation for Biomedical Applications* (eds Boccara, A.-C. & Oraevsky, A. A.) **4434** (SPIE, 2001), 204–207.

87. Binzoni, T., Leung, T. S., Boggett, D. & Delpy, D. Non-invasive laser Doppler perfusion measurements of large tissue volumes and human skeletal muscle blood RMS velocity. *Physics in Medicine and Biology* **48,** 2527–2549 (2003).

88. Lee, S. C., Chen, J. F. & Lee, S. T. Continuous regional cerebral blood flow monitoring in the neurosurgical intensive care unit. *Journal of Clinical Neuroscience* **12,** 520–523 (2005).

89. Liu, C., Kılıç, K., Erdener, S. E., Boas, D. A. & Postnov, D. D. Choosing a model for laser speckle contrast imaging. *Biomedical Optics Express* **9,** 3571–3583 (2021).

90. Du Le, V. N. & Srinivasan, V. J. Beyond diffuse correlations: deciphering random flow in time-of-flight resolved light dynamics. *Optics Express* **28,** 11191–11214 (2020).

91. Zhou, C. *et al.* Diffuse optical correlation tomography of cerebral blood flow during cortical spreading depression in rat brain. *Optics Express* **14,** 1125–1144 (2006).

92. Boas, D. A. *et al.* Establishing the diffuse correlation spectroscopy signal relationship with blood flow. *Neurophotonics* **3,** 031412 (2016).

93. Elson, D. S., Li, R., Dunsby, C., Eckersley, R. & Tang, M. X. Ultrasound-mediated optical tomography: a review of current methods. *Interface Focus* **1,** 632–648 (2011).

94. Rudin, M. *Molecular Imaging: Basic Principles and Applications in Biomedical Research* 2nd (Imperial College Press, 2013).

95. Dietsche, G. *et al.* Fiber-based multispeckle detection for time-resolved diffusing-wave spectroscopy: characterization and application to blood flow detection in deep tissue. *Applied Optics* **46,** 8506–8514 (2007).

96. He, L., Lin, Y., Shang, Y., Shelton, B. J. & Yu, G. Using optical fibers with different modes to improve the signal-to-noise ratio of diffuse correlation spectroscopy flow-oximeter measurements. *Journal of Biomedical Optics* **18,** 037001 (2013).

97. Gisler, T. *et al.* Mode-selective dynamic light scattering: theory versus experimental realization. *Applied Optics* **34,** 3546–3553 (2009).

98. Carp, S. A. *Novel Approaches for Increased Sensitivity to Cerebral Blood Flow Using Diffuse Correlation Spectroscopy* in *Biophotonics Congress: Biomedical Optics 2020 (Translational, Microscopy, OCT, OTS, BRAIN)* (Optica Publishing Group, 2020), BTh3C.1.

99. Johansson, J. D., Portaluppi, D., Buttafava, M. & Villa, F. A multipixel diffuse correlation spectroscopy system based on a single photon avalanche diode array. *Journal of Biophotonics* **12,** e201900091 (2019).

100. Bi, R. *et al.* Fast pulsatile blood flow measurement in deep tissue through a multimode detection fiber. *Journal of Biomedical Optics* **25,** 055003 (2020).

101. Murali, K., Nandakumaran, A. K. & Varma, H. M. On the equivalence of speckle contrast-based and diffuse correlation spectroscopy methods in measuring *in vivo* blood flow. *Optics Letters* **45,** 3993–3996 (2020).

102. Blackwell, M. *et al. Novel detector solutions for diffuse correlation spectroscopy at 1064 nm (Conference Presentation)* in *Dynamics and Fluctuations in Biomedical Photonics XVII* (eds Tuchin, V. V., Leahy, M. J. & Wang, R. K.) **11239** (SPIE, 2020).

103. Robinson, M. *et al.* Diffuse correlation spectroscopy beyond the water peak enabled by cross-correlation of the signals from InGaAs/InP single photon detectors. *IEEE Transactions on Biomedical Engineering* (in press - DOI: 10.1109/TBME.2021.3131353).

104. Verdecchia, K. *et al.* Assessment of a multi-layered diffuse correlation spectroscopy method for monitoring cerebral blood flow in adults. *Biomedical Optics Express* **7,** 3659–3674 (2016).

105. Baker, W. B. *et al.* Pressure modulation algorithm to separate cerebral hemodynamic signals from extracerebral artifacts. *Neurophotonics* **2,** 035004 (2015).

106. Mazumder, D. *et al.* Optimization of time domain diffuse correlation spectroscopy parameters for measuring brain blood flow. *Neurophotonics* **8,** 035005 (2021).

107. Samaei, S. *et al.* Performance assessment of laser sources for time-domain diffuse correlation spectroscopy. *Biomedical Optics Express* **12,** 5351–5367 (2021).

108. Chandran, R. S., Devaraj, G., Kanhirodan, R., Roy, D. & Vasu, R. M. Detection and estimation of liquid flow through a pipe in a tissue-like object with ultrasound-assisted diffuse correlation spectroscopy. *Journal of the Optical Society of America A* **32,** 1888–1897 (2015).

109. Ling, H., Gui, Z., Hao, H. & Shang, Y. Enhancement of diffuse correlation spectroscopy tissue blood flow measurement by acoustic radiation force. *Biomedical Optics Express* **11,** 301–315 (2020).

110. Biswas, A., Moka, S., Muller, A. & Parthasarathy, A. B. Fast diffuse correlation spectroscopy with a low-cost, fiber-less embedded diode laser. *Biomedical Optics Express* **12,** 6686–6700 (2021).

111. Safi, A. M., Moka, S., Harrah, M., Cini, S. & Parthasarathy, A. B. *Quantitative Measurement of Static and Dynamic Tissue Optical Properties with Continuous Wave Pathlength Resolved Diffuse Correlation Spectroscopy* in *Biophotonics Congress 2021* (Optica Publishing Group, 2021), BTh1B.6.

112. Poon, C.-S., Long, F. & Sunar, U. Deep learning model for ultrafast quantification of blood flow in diffuse correlation spectroscopy. *Biomedical Optics Express* **11,** 5557–5564 (2020).

113. Zhang, P., Gui, Z., Guo, G. & Shang, Y. Approaches to denoise the diffuse optical signals for tissue blood flow measurement. *Biomedical Optics Express* **9,** 6170–6185 (2018).

114. Xu, S., Yang, X., Konda, P. C. & Horstmeyer, R. *Rapid imaging of deep-tissue motion with parallelized diffuse correlation spectroscopy* in *Biophotonics Congress 2021* (Optica Publishing Group, 2021), BTh1B.3.

115. Borycki, D., Kholiqov, O., Chong, S. P. & Srinivasan, V. J. Interferometric Near-Infrared Spectroscopy (iNIRS) for determination of optical and dynamical properties of turbid media. *Optics Express* **24,** 329–354 (2016).

116. Kholiqov, O., Zhou, W., Zhang, T., Du Le, V. N. & Srinivasan, V. J. Time-of-flight resolved light field fluctuations reveal deep human tissue physiology. *Nature Communications* **11,** 391 (2020).

117. Valdes, C. P. *et al.* Speckle contrast optical spectroscopy, a non-invasive, diffuse optical method for measuring microvascular blood flow in tissue. *Biomedical Optics Express* **5,** 2769–2784 (2014).

118. Bi, R., Dong, J. & Lee, K. Deep tissue flowmetry based on diffuse speckle contrast analysis. *Optics Letters* **38,** 1401–1403 (2013).

119. Marks, F. A., Tomlinson, H. W. & Brooksby, G. W. *Comprehensive approach to breast cancer detection using light: photon localization by ultrasound modulation and tissue characterization by spectral discrimination* in *Photon Migration and Imaging in Random Media and Tissues* (eds Chance, B. & Alfano, R. R.) **1888** (SPIE, 1993), 500–510.

120. Resink, S. G., Boccara, A. C. & Steenbergen, W. State-of-the art of acousto-optic sensing and imaging of turbid media. *Journal of Biomedical Optics* **17,** 040901 (2012).

121. Gross, M. *et al.* Heterodyne detection of multiply scattered monochromatic light with a multipixel detector. *Optics Letters* **30,** 1357–1359 (2005).

122. Wang, L. V. Ultrasound-mediated biophotonic imaging: A review of acousto-optical tomography and photo-acoustic tomography. *Disease Markers* **19,** 123–138 (2004).

123. Lesaffre, M., Farahi, S., Boccara, A. C., Ramaz, F. & Gross, M. Theoretical study of acousto-optical coherence tomography using random phase jumps on ultrasound and light. *Journal of the Optical Society of America A* **28,** 1436–1444 (2011).

124. Levi, A. *et al.* Increased SNR in acousto-optic imaging via coded ultrasound transmission. *Optics Letters* **45,** 2858–2861 (2020).

125. Racheli, N. *et al. Non-invasive blood flow measurements using ultrasound modulated diffused light* in *Photons Plus Ultrasound: Imaging and Sensing 2012* (eds Oraevsky, A. A. & Wang, L. V.) **8223** (SPIE, 2012), 438–445.

126. Caccioppola, A. *et al.* Ultrasound-tagged near-infrared spectroscopy does not disclose absent cerebral circulation in brain-dead adults. *British Journal of Anaesthesia* **121,** 588–594 (2018).

127. Lev, A. & Sfez, B. *In vivo* demonstration of the ultrasound-modulated light technique. *Journal of the Optical Society of America A* **20,** 2347–2354 (2003).

128. Gunther, J., Walther, A., Rippe, L., Kröll, S. & Andersson-Engels, S. Deep tissue imaging with acousto-optical tomography and spectral hole burning with slow light effect: a theoretical study. *Journal of Biomedical Optics* **23,** 071209 (2018).

129. Kinos, A., Li, Q., Rippe, L. & Kröll, S. Development and characterization of high suppression and high étendue narrowband spectral filters. *Applied Optics* **55,** 10442–10448 (2016).

130. Changhui, L., Kim, C. & Wang, L. V. in *Handbook of Biomedical Optics* 419–442 (CRC Press, 2011).

131. Doktofsky, D., Rosenfeld, M. & Katz, O. Acousto optic imaging beyond the acoustic diffraction limit using speckle decorrelation. *Communications Physics* **3,** 5 (2020).

132. Walther, A., Rippe, L., Wang, L. V., Andersson-Engels, S. & Kröll, S. Analysis of the potential for non-invasive imaging of oxygenation at heart depth, using ultrasound optical tomography (UOT) or photo-acoustic tomography (PAT). *Biomedical Optics Express* **8,** 4523–4536 (2017).

133. Legon, W. *et al.* Transcranial focused ultrasound modulates the activity of primary somatosensory cortex in humans. *Nature Neuroscience* **17,** 322–329 (2014).

134. Gabor, D. A New Microscopic Principle. *Nature* **161,** 777–778 (1948).

135. Goodman, J. W. *Introduction to Fourier Optics* 4th (Macmillan Learning, 2017).

136. Schnars, U. & Jüptner, W. P. Digital recording and numerical reconstruction of holograms. *Measurement Science and Technology* **13,** R85–R101 (2002).

137. Nehmetallah, G., Aylo, R. & Williams, L. *Analog and digital holography with MATLAB®* 1st (SPIE, 2015).

138. Wagner, C., Seebacher, S., Osten, W. & Jüptner, W. Digital recording and numerical reconstruction of lensless Fourier holograms in optical metrology. *Applied Optics* **38,** 4812–4820 (1999).

139. Sharma, A., Sheoran, G., Jaffery, Z. A. & Moinuddin. Improvement of signal-to-noise ratio in digital holography using wavelet transform. *Optics and Lasers in Engineering* **46,** 42–47 (2008).

140. Schnars, U., Falldorf, C., Watson, J. & Jüptner, W. *Digital Holography and Wavefront Sensing - Principles, Techniques and Applications* 2nd (Springer, 2010).

141. Javidi, B. *et al.* Roadmap on digital holography. *Optics Express* **29,** 35078–35118 (2021).

142. Verpillat, F., Joud, F., Atlan, M. & Gross, M. Digital holography at shot noise level. *Journal of Display Technology* **6,** 455–464 (2010).

143. Gross, M. Selection of the tagged photons by off axis heterodyne holography in ultrasound-modulated optical tomography. *Applied Optics* **56,** 1846–1854 (2017).

144. Gross, M., Goy, P. & Al-Koussa, M. Shot-noise detection of ultrasound-tagged photons in ultrasound-modulated optical imaging. *Optics Letters* **28,** 2482–2484 (2003).

145. Puyo, L., Paques, M., Fink, M., Sahel, J.-A. & Atlan, M. *In vivo* laser Doppler holography of the human retina. *Biomedical Optics Express* **9,** 4113–4129 (2018).

146. Atlan, M., Desbiolles, P., Gross, M. & Coppey-Moisan, M. Parallel heterodyne detection of dynamic light-scattering spectra from gold nanoparticles diffusing in viscous fluids. *Optics Letters* **35,** 787–789 (2010).

147. Atlan, M. & Gross, M. Spatiotemporal heterodyne detection. *Journal of the Optical Society of America A* **24,** 2701–2709 (2007).

148. Gross, M. Heterodyne holography with full control of both the signal and reference arms. *Applied Optics* **55,** A8–A16 (2016).

149. Magnain, C. *et al.* Holographic laser Doppler imaging of microvascular blood flow. *Journal of the Optical Society of America A* **31,** 2723–2735 (2014).

150. Goodman, J. *Statistical Optics* 2nd (Wiley, 2015).

151. James, E. & Powell, S. Fourier domain diffuse correlation spectroscopy with heterodyne holographic detection. *Biomedical Optics Express* **11,** 6755–6779 (2020).

152. James, E. & Powell, S. *Diffuse correlation spectroscopy in the Fourier domain with holographic camera-based detection* in *Dynamics and Fluctuations in Biomedical Photonics XVII* (eds Tuchin, V. V., Leahy, M. J. & Wang, R. K.) **11239** (SPIE, 2020), 29–35.

153. Brown, J. C. Optical correlations and spectra. *American Journal of Physics* **51,** 1008–1011 (1983).

154. Kirkpatrick, S. J., Duncan, D. D. & Wells-Gray, E. M. Detrimental effects of speckle-pixel size matching in laser speckle contrast imaging. *Optics Letters* **33,** 2886–2888 (2008).

155. Goodman, J. *Speckle Phenomena in Optics - Theory and Applications* 2nd (SPIE, 2020).

156. Schmidt, F. E. W. *et al.* Multiple-slice imaging of a tissue-equivalent phantom by use of time-resolved optical tomography. *Applied Optics* **39,** 3380–3387 (2000).

157. Laurence, T. A., Fore, S. & Huser, T. Fast, flexible algorithm for calculating photon correlations. *Optics Letters* **31,** 829–831 (2006).

158. Schätzel, K., Drewel, M. & Stimac, S. Photon correlation measurements at large lag times: improving statistical accuracy. *Journal of Modern Optics* **35,** 711–718 (1988).

159. Buiteveld, H., Hakvoort, J. H. M. & Donze, M. *Optical properties of pure water* in *Ocean Optics XII* (ed Jaffe, J. S.) **2258** (SPIE, 1994), 174–183.

160. Cletus, B., Künnemeyer, R., Martinsen, P. & McGlone, V. A. Temperature-dependent optical properties of Intralipid® measured with frequency-domain photon-migration spectroscopy. *Journal of Biomedical Optics* **15,** 017003 (2010).

161. McGlone, V. A., Martinsen, P., Künnemeyer, R., Jordan, B. & Cletus, B. Measuring optical temperature coefficients of Intralipid®. *Physics in Medicine and Biology* **52,** 2367–2378 (2007).

162. Bashkatov, A. N. & Genina, E. A. *Water refractive index in dependence on temperature and wavelength: a simple approximation* in *Saratov Fall Meeting 2002: Optical Technologies in Biophysics and Medicine IV* (ed Tuchin, V. V.) **5068** (SPIE, 2003), 393–395.

163. Rowe, P. I. *et al.* Thermal Stability of Intralipid Optical Phantoms. *Applied Spectroscopy* **67,** 993–996 (2013).

164. Einstein, A. On the motion of small particles suspended in liquids at rest required by the molecular-kinetic theory of heat. *Annalen der Physik* **17,** 208 (1905).

165. Edward, J. T. Molecular volumes and the Stokes-Einstein equation. *Journal of Chemical Education* **47,** 261–270 (1970).

166. White, F. M. *Fluid Mechanics* 8th, 28 (McGraw-Hill, 2016).

167. Kodach, V. M., Faber, D. J., van Marle, J., van Leeuwen, T. G. & Kalkman, J. Determination of the scattering anisotropy with optical coherence tomography. *Optics Express* **19,** 6131–6140 (2011).

168. James, E., Powell, S. & Munro, P. Performance optimisation of a holographic Fourier domain diffuse correlation spectroscopy instrument. *Biomedical Optics Express* (in press, DOI: 10.1364/BOE.454346).

169. James, E., Powell, S. & Munro, P. *Performance characterisation of a holographic Fourier domain diffuse correlation spectroscopy instrument* in *Dynamics and Fluctuations in Biomedical Photonics XIX* (eds Tuchin, V. V., Leahy, M. J. & Wang, R. K.) **PC11959** (SPIE, 2022).

170. Kreis, T. M. Frequency analysis of digital holography. *Optical Engineering* **41,** 771–778 (2002).

171. Puyo, L., Paques, M. & Atlan, M. Spatio-temporal filtering in laser Doppler holography for retinal blood flow imaging. *Biomedical Optics Express* **11,** 3274–3287 (2020).

172. Atlan, M., Touminet, A., Andal, T., Puyo, L. & Pâques, M. *Image-based digital motion and aberration compensation in laser Doppler holography of the eye fundus (Conference Presentation)* in *Adaptive Optics and Wavefront Control for Biological Systems VI* (eds Bifano, T. G., Gigan, S. & Ji, N.) **11248** (SPIE, 2020).

173. Robinson, M. B., Carp, S., Peruch, A., Ozana, N. & Franceschini, M. *High frame-rate, InGaAs camera for interferometric diffuse correlation spectroscopy (iDCS) beyond the water peak (Conference Presentation)* in *Dynamics and Fluctuations in Biomedical Photonics XVIII* (eds Tuchin, V. V., Leahy, M. J. & Wang, R. K.) **11641** (SPIE, 2021).

174. Colomb, T. *et al.* Polarization imaging by use of digital holography. *Applied Optics* **41,** 27–37 (2002).

175. Peng, J. *et al.* Principles, Measurements and Suppressions of Semiconductor Laser Noise - A Review. *IEEE Journal of Quantum Electronics* **57,** 2000415 (2021).

176. Pandey, N. & Hennelly, B. Quantization noise and its reduction in lensless Fourier digital holography. *Applied Optics* **50,** B58–B70 (2011).

177. Garcia-Sucerquia, J., Ramírez, J. A. H. & Prieto, D. V. Reduction of speckle noise in digital holography by using digital image processing. *Optik* **116,** 44–48 (2005).

178. James, E., Powell, S. & Munro, P. Simulation of statistically accurate time-integrated dynamic speckle patterns in biomedical optics. *Optics Letters* **46,** 4390–4393 (2021).

179. James, E., Powell, S. & Munro, P. *Simulation of time-integrated dynamic speckle patterns in biomedical optics* in *2021 IEEE Photonics Conference (IPC)* (2021).

180. James, E., Powell, S. & Munro, P. *Simulation of statistically accurate time-integrated dynamic speckle patterns in biomedical optics* in *Dynamics and Fluctuations in Biomedical Photonics XIX* (eds Tuchin, V. V., Leahy, M. J. & Wang, R. K.) **PC11959** (SPIE, 2022).

181. Song, L., Zhou, Z., Wang, X., Zhao, X. & Elson, D. S. Simulation of speckle patterns with pre-defined correlation distributions. *Biomedical Optics Express* **7,** 798–809 (2016).

182. Thompson, O. B. & Andrews, M. K. Tissue perfusion measurements: multiple-exposure laser speckle analysis generates laser Doppler–like spectra. *Journal of Biomedical Optics* **15,** 027015 (2010).

183. Zhang, H. *et al.* Correcting the detrimental effects of nonuniform intensity distribution on fiber-transmitting laser speckle imaging of blood flow. *Optics Express* **20,** 508–517 (2012).

184. Duncan, D. D. & Kirkpatrick, S. J. The copula: a tool for simulating speckle dynamics. *Journal of the Optical Society of America A* **25,** 231–237 (2008).

185. Duncan, D. D. & Kirkpatrick, S. J. Can laser speckle flowmetry be made a quantitative tool? *Journal of the Optical Society of America A* **25,** 2088–2094 (2008).

186. Davenport, W. B. & Root, W. L. in *An Introduction to the Theory of Random Signals and Noise* 1st, 87–111 (McGraw-Hill, 1958).

187. Guggenheim, J. A. *et al.* Ultrasensitive plano-concave optical microresonators for ultrasound sensing. *Nature Photonics* **11,** 714–719 (2017).

188. Vijayakumar, A. & Bhattacharya, S. in *Design and Fabrication of Diffractive Optical Elements with MATLAB®* 1st, 145–175 (SPIE, 2017).

189. Erdélyi, A., Magnus, F., Oberhettinger, F. & Tricomi, F. G. in *Tables of Integral Transforms - Volume I* 1st, 14–17 (McGraw-Hill, 1954).

‘The whole problem with the world is that fools and fanatics are always so certain of themselves, and wiser people so full of doubts.’

Bertrand Russell (1872 - 1970)